



International School for Advanced Studies

# Spectra of Extragalactic Radio Sources After *Planck*

**Laura Bonavera**

Supervisors:

Prof. C. Baccigalupi

Prof. G. De Zotti

Prof. R. D. Ekers

A thesis submitted for the degree of

*Doctor Philosophiæ*

September 2011

---

# Contents

<b>List of Figures</b>	<b>vii</b>
<b>List of Tables</b>	<b>xvii</b>
<b>1 Introduction</b>	<b>1</b>
<b>2 The <i>Planck</i> View of Extragalactic Sources</b>	<b>7</b>
2.1 Overview . . . . .	7
2.2 The <i>Planck</i> On-Flight Forecaster (POFF) . . . . .	12
2.2.1 The <i>Planck</i> Scanning Strategy . . . . .	12
2.2.2 The Focal Plane . . . . .	14
2.2.3 The Code . . . . .	16
2.3 The Early Release Compact Source Catalog (ERCSC) . . . . .	17
2.4 Extragalactic Radio Sources at <i>Planck</i> Frequencies . . . . .	22
2.4.1 Peaked Spectrum Sources . . . . .	24
2.4.1.1 Compact Symmetric Objects . . . . .	24
2.4.1.2 Broad Peaked Radio Sources . . . . .	26
2.4.2 Flat and Multicomponent Spectrum Sources . . . . .	28
2.4.3 Upturning Spectrum Sources . . . . .	30
2.5 Radio Sources in the ERCSC . . . . .	30
2.5.1 Validation of the ERCSC . . . . .	32
2.5.2 Number Counts . . . . .	33
2.5.3 Spectral Index Distribution . . . . .	37

## CONTENTS

---

<b>3</b>	<b>Ground-based Observations</b>	<b>41</b>
3.1	The Simultaneous Medicina- <i>Planck</i> Experiment (SiMPIE) . . . . .	42
3.1.1	The Sample . . . . .	42
3.1.2	The observations . . . . .	44
3.1.3	The data reduction . . . . .	46
3.1.4	The Northern Sample Catalogue . . . . .	48
3.2	The <i>Planck</i> -ATCA Co-eval Observations (PACO) . . . . .	49
3.2.1	The Sample . . . . .	49
3.2.2	The Observations . . . . .	52
3.2.3	The Calibrators . . . . .	55
3.2.4	The Data Reduction . . . . .	57
3.2.4.1	Loading the Raw Data . . . . .	57
3.2.4.2	Editing . . . . .	59
3.2.4.3	Calibration . . . . .	60
3.2.5	Extended Sources . . . . .	64
3.2.6	Flux Density Estimation . . . . .	66
3.2.7	Quality Assessment . . . . .	68
3.2.7.1	Flux Density Error Estimation . . . . .	69
3.2.8	Catalogues . . . . .	70
<b>4</b>	<b>Data Analysis</b>	<b>73</b>
4.1	Spectral Analysis . . . . .	73
4.2	Source Counts . . . . .	98
4.3	Variability . . . . .	100
4.3.1	The PACO Bright Sample . . . . .	100
4.3.2	Comparison of PACO with AT20G measurements . . . . .	103
4.4	The SiMPIE Northern Sample . . . . .	107
4.5	Calibration Issues . . . . .	108
<b>5</b>	<b>Multi-frequency SEDs of PACO Sources</b>	<b>111</b>
5.1	Combining PACO with ERCSC data . . . . .	111
5.2	Global SEDs of Blazars . . . . .	123
5.2.1	Sample Selection . . . . .	123
5.2.2	Analysis . . . . .	126

<b>6 Conclusions</b>	<b>141</b>
<b>Appendix A Script for a general ATCA-CABB Continuum Data Reduction Pipeline</b>	<b>145</b>
<b>References</b>	<b>149</b>

## **CONTENTS**

---

# List of Figures

- 2.1 A map ([http://www.esa.int/esaMI/Planck/SEM5CMFWNZF\\_1.html](http://www.esa.int/esaMI/Planck/SEM5CMFWNZF_1.html)) of the sky at optical wavelengths shows a prominent horizontal band which is the light shining from our own Milky Way. The superimposed strip shows the area of the sky mapped by *Planck* during the First Light Survey. The colour scale indicates the magnitude of the deviations of the temperature of the Cosmic Microwave Background from its average value, as measured by *Planck* at a frequency close to the peak of the CMB spectrum (red is hotter and blue is colder). . . . . 8
- 2.2 The footprint of the *Planck* field-of-view: the ellipticities seen are representative of the shape of the beam at full-width-half maximum. The black crosses indicate the orientation of the pairs of linearly polarised detectors within each horn ([Planck Collaboration, 2006](#)). . . . . 10
- 2.3 RMS of the CMB fluctuations, and the frequency coverage of the *Planck* channels. Also indicated are the spectra of other sources of fluctuations in the microwave sky. Dust, synchrotron, and free-free temperature fluctuation (i.e., unpolarized) levels correspond to the levels of fluctuations when the brightest part of the Galaxy (15%) has been cut out (*WMAP* Kp2 mask; [Bennett et al., 2003b](#)). The CMB and Galactic fluctuation levels depend on angular scale, and are shown for  $\sim 1^\circ$ . On small angular scales, extragalactic sources dominate. The minimum in diffuse foregrounds and the clearest window on CMB fluctuations occurs near 70 GHz. The highest HFI frequencies are primarily sensitive to dust ([Planck Collaboration, 2006](#)). . . . . 11

## LIST OF FIGURES

---

2.4	In the upper and middle panel the POFF output is shown as a function of time and <i>Planck</i> frequency channels for the South and North Ecliptic Pole positions, respectively. The lower panel is a zoom in the upper one for the first period of observability of the North Ecliptic Pole position. The scheme of the <i>Planck</i> focal plane has been plotted for comparison: the sequence of frequencies of observations corresponds to the sequence with which aligned beams scan through the sky position. Note that the distances between beams is not to scale for plotting purposes (Massardi and Burigana, 2010). . . . .	15
2.5	I/O flow chart of the POFF code by Massardi and Burigana (2010). . .	16
2.6	Scheme of observability of the PACO sources (see Section 3.2) according to the <i>Planck</i> scanning strategy. Different colours correspond to different <i>Planck</i> channels. Sources are sorted by right ascension from the bottom (0h) to the top of the scheme (24h). Notice the equatorial pole region over-density for $4 < RA < 8$ . Day 0 corresponds to August 13th, 2009. .	18
2.7	The <i>Planck</i> ERCSC flux density limit quantified as the faintest ERCSC source at $ b  < 10^\circ$ (dashed black line) and at $ b  > 30^\circ$ (solid black line) is shown relative to other wide area surveys. Also shown are the spectra of known sources of foreground emission as red lines; these include a $F_\nu \sim \nu^{-0.7}$ synchrotron component, $\nu^{-0.1}$ free-free component, a Rayleigh-Jeans component and a $\nu^2$ emissivity of temperature 18 K. The ERCSC sensitivity is worse in the Galactic Plane due to the strong contribution of ISM emission especially at sub-millimetre wavelengths. In the radio regime, the effect is smaller. The faintest <i>WMAP</i> 7 year $5\sigma$ sources are derived from the catalogue of Gold et al. (2011). Although the flux density limits of <i>WMAP</i> and <i>Planck</i> appear to be comparable at the lowest frequencies, the <i>Planck</i> ERCSC is more complete. The GB6 sensitivity value is from Gregory et al. (1996), the AT20G flux limit is from Murphy et al. (2010), the SCUBA-2 All Sky Survey (SASSy) limit is from the Joint Astronomy Centre website while the IRAS flux density limits are from the IRAS explanatory supplement (Beichman et al., 1988). From Planck Collaboration (2011b). . . . .	21
2.8	The unified model of radio sources (de Zotti et al., 2010). . . . .	23

<p>2.9 SED of a known CSO source, J2022+6137. <i>Planck</i> measurements are shown in red, <i>WMAP</i>-7yr flux densities in blue, new VLA measurements in pink, and archival data obtained from NED in green (<a href="#">Planck Collaboration, 2011d</a>).</p>	25
<p>2.10 VLA, Metsahovi, IRAM, Effelsberg and <i>Planck</i> measurements of two known GHz-peaked blazars: J1800+782 (upper panel), and J0423-0120 (bottom panel). While the former shows only small signs of variability, the latter is clearly variable while preserving its spectral shape, pointing to helical or precessing jet. Asterisks identify epochs within 10 days from <i>Planck</i> observations at any of the LFI channels. For both sources, the <i>Planck</i> ERCSC data are a superposition of two scans separated by 3 and 6 months, respectively (<a href="#">Planck Collaboration, 2011d</a>).</p>	27
<p>2.11 Two examples of clearly multi-component spectra. <i>Planck</i> measurements are shown by filled circles; AT20G data by open diamonds (<a href="#">Massardi et al., 2011b</a>); PACO data, with their dense sampling in frequency space, are shown by open squares (<a href="#">Bonavera et al., 2011</a>; <a href="#">Massardi et al., 2011a</a>). Asterisks identify epochs within 10 days from <i>Planck</i> observations. The multi-valued spectra in J2035-6846 are a clear sign that this source is variable on time scales less than two weeks (see text) (<a href="#">Planck Collaboration, 2011d</a>).</p>	29
<p>2.12 <i>Planck</i> sources with an upturn in the spectrum. Upper panel: J0047-7310 in the SMC. Central panel: <i>Planck</i> spectrum of a familiar star-forming system, NGC253. Bottom panel: The star-burst galaxy M82 (<a href="#">Planck Collaboration, 2011d</a>).</p>	31

## LIST OF FIGURES

---

- 2.13 Euclidean normalized differential number counts at the LFI frequencies. The red circles with Poisson error bars show the counts of sources with counterparts in the reference 30 GHz sample. In each panel, the solid curves show the total number counts of extragalactic radio sources predicted by the [de Zotti et al. \(2005\)](#) model. Also shown are: the counts estimated at 31 GHz from DASI (grey dashed box; [Kovac et al., 2002](#)) and at 33 GHz from the VSA data (grey box; [Cleary et al., 2005](#)); the counts from the PACO (grey diamonds; [Bonavera et al., 2011](#)) and the *WMAP* 5-yr surveys (grey squares; [Massardi et al., 2009](#)), at the closest frequencies, and the counts estimated by [Waldram et al. \(2007\)](#) (grey dashed line), exploiting multi-frequency follow-up observations of the 15 GHz 9C sources. The vertical dashed magenta line in the upper panel indicates the estimated flux density completeness limit, 1.0 Jy ([Planck Collaboration, 2011g](#)). . . . . 34
- 2.14 Euclidean normalized differential number counts at the HFI frequencies (100, 143, and 217 GHz). The red circles with Poisson error bars show the counts of sources with counterparts in the reference 30 GHz sample. At 143 and 217 GHz the blue diamonds (shifted to the left by half of the bin size, for clarity) show the counts obtained after removing sources with 143-217 GHz spectral index indicative of dust emission. Again, in each panel, the solid curves show the total number counts of extragalactic radio sources predicted by the [de Zotti et al. \(2005\)](#) evolution model (it should be noticed that the model fail at 100-1000 mJy). Also shown are the SPT (grey squares; [Vieira et al., 2010](#)) and ACT (grey stars; [Marriage et al., 2011](#)) counts of radio sources. At 100 GHz we also show the estimated counts by [Sadler et al. \(2008\)](#) from follow-up observations of a sample of sources selected from the 20 GHz ATCA survey (grey dashed line) ([Planck Collaboration, 2011g](#)). . . . . 35
- 2.15 The distribution of spectral indices between adjacent *Planck* frequencies for sources above 30° of the Galactic Plane, likely to be dominated by extragalactic sources ([Planck Collaboration, 2011b](#)). . . . . 38

2.16 Spectral index distributions for different frequency intervals calculated by taking into account all sources selected at 30 GHz with $S_\nu > 1$ Jy. There is clear evidence for a steepening above 70 GHz (Planck Collaboration, 2011g). . . . .	39
3.1 The SiMPIE sample: the Northern Sample (diamonds) covers the area with $\delta > 45^\circ$ ; asterisks show the Southern Sample; squares indicate the central positions of the mapped sky patches (Procopio et al., 2011). . .	43
3.2 Fit of a sub-scan by a Gaussian (solid line) plus linear left and right baselines (dashed). From Procopio et al. (2011). . . . .	47
3.3 Polar projection of the Southern sky, showing the distribution of the PACO samples (RA=0 h is at the top and the RA increases counter-clockwise). The dotted lines indicate the Galactic plane and bound the area with Galactic latitude $ b  < 5^\circ$ . Sources in these regions were excluded from the PACO samples. The PACO faint sample (open pink diamonds) occupies the area with $3 < \text{RA} < 9$ h. The PACO bright sample (filled blue diamonds) covers the whole area at $\delta < -30^\circ$ . The spectrally selected sample (green squares), the blazars and the Australia telescope calibrator sources (black asterisks) are spread over the whole southern sky. From Massardi et al. (2011a). . . . .	51
3.4 A schematic illustration of the CABB configurations in the ATCA receiver bands. The scheme is only for explanatory reasons, the channels in this figure are not the ones used in the PACO project. The blue bars correspond to the frequency coverage of each receiver band. The orange bars correspond to the CABB bands (2 GHz bandwidth). From <a href="http://www.narrabri.atnf.csiro.au/observing/CABB.html">www.narrabri.atnf.csiro.au/observing/CABB.html</a> . . . . .	52
3.5 VIS display showing output during PACO observations. . . . .	53
3.6 Model for PKS 1934-638 in the frequency range between 4.5 and 40 GHz, as it is in the Miriad version we used. From Massardi et al. (2011a). . .	57
3.7 Data reduction pipeline diagram. Names in capital letters indicate the Miriad tasks used. From Massardi et al. (2011a). . . . .	59

## LIST OF FIGURES

---

3.8	Shadowing scheme for different array configurations: the blue area shows the region (hour angle and declination) not affected by shadowing. From ATCA User Guide ( <a href="http://www.narrabri.atnf.csiro.au/observing/users_guide/">www.narrabri.atnf.csiro.au/observing/users_guide/</a> ).	61
3.9	Scheme of the calibration performed with MIRIAD tasks. The indications in parenthesis refer to the case of Uranus as primary calibrator. The steps included in the dotted square have been applied only when a suitable leakage calibrator has been observed. (Massardi et al., 2011a).	65
4.1	SEDs of the sources in PACO bright sample. Asterisks of different colours correspond to different observing epochs. To avoid overcrowding we have not plotted the error bars that are in all the cases smaller than the symbol size. For comparison, the AT20G data (triangles) and, when available, <i>WMAP</i> data taken from the NEWPS_5yr catalogue (squares; Massardi et al., 2009) are also shown. From Massardi et al. (2011a).	74
4.2	Same of the previous figure, but for the PACO faint sample.	82
4.3	Images at each frequency for 0537-441 as observed on July 26th 2009 with the hybrid configuration H75, as an example of the quality of our data and a representation of the beam. Each panel measures $6 \times 6$ arcmin. Every 512-MHz sub-band for a given IF band is in a different column, so that frequencies increase from the left to the right and from the top to the bottom. From Massardi et al. (2011a).	89
4.4	Colour-colour plot comparing the spectral indices in the ranges 5-10 and 30-40 GHz for the PACO bright sample. The dotted lines show the boundaries adopted for our spectral classification. From Massardi et al. (2011a).	90
4.5	Distribution of PACO faint sources with $200 \text{ mJy} \leq S_{\text{AT20G}} < 500 \text{ mJy}$ in the $\alpha_5^{10}-\alpha_{30}^{40}$ plane. The dotted lines show the boundaries for the various spectral types. From Bonavera et al. (2011).	91
4.6	Distribution of peak frequencies of sources in the bright sample in the observer's frame (hatched histogram) and in the source frame (shaded) for sources with measured redshift. From Massardi et al. (2011a).	93
4.7	Distribution of $\alpha_5^{10}$ (shaded area) and $\alpha_{30}^{40}$ (hatched area) for the PACO bright sample.	93

4.8	Distribution of the differences between low- and high- frequency spectral indices ( $\alpha_5^{10} - \alpha_{30}^{40}$ ) for the PACO bright sample. From <a href="#">Massardi et al. (2011a)</a> . . . . .	94
4.9	Distributions of $\alpha_5^{10}$ (shaded area) and of $\alpha_{30}^{40}$ (hatched area) for the PACO faint sample ( $200 \leq S_{20GHz} \leq 500$ mJy). From <a href="#">Bonavera et al. (2011)</a> . . . . .	95
4.10	Distribution of the difference $\alpha_5^{10} - \alpha_{30}^{40}$ for the PACO faint sample ( $200 \leq S_{20GHz} \leq 500$ mJy). From <a href="#">Bonavera et al. (2011)</a> . . . . .	95
4.11	Distributions of spectral indices between 5 and 20 GHz (shaded) and between 20 and 40 GHz (hatched) for the PACO bright sample. . . . .	96
4.12	Distributions of $\alpha_5^{20}$ (shaded area) and of $\alpha_{20}^{40}$ (hatched area) for the PACO faint sample ( $200 \leq S_{20GHz} \leq 500$ mJy). . . . .	97
4.13	Differential source counts at 33 and 40 GHz (squares) compared with the <i>Planck</i> counts ( <a href="#">Planck Collaboration, 2011g</a> ) at 30 and 44 GHz (red asterisks), and with the DASI estimate ( <a href="#">Kovac et al., 2002</a> ) at 31 GHz (region bounded by dotted lines). The solid lines show the predictions of the <a href="#">de Zotti et al. (2005)</a> model. From <a href="#">Bonavera et al. (2011)</a> . . . . .	99
4.14	Contribution of extragalactic point sources to the CMB power spectrum (black solid line) for different flux density limits. In each panel the upper (dot-dashed) line refers to the ERCSC completeness limit (1 Jy at 33 GHz and 1.5 Jy 40 GHz), while the lower (dashed line) refers to the flux density limit of the PACO faint sample (200 mJy). From <a href="#">Bonavera et al. (2011)</a> . . . . .	101
4.15	Top: median variability index of the sample as a function of frequency; error bars are $\sigma/\sqrt{N-1}$ . Bottom: number of pairs. From <a href="#">Massardi et al. (2011a)</a> . . . . .	102
4.16	Comparison between the AT20G flux densities at 20 GHz and the PACO ones scaled to 20 GHz. The solid line corresponds to $S_{AT20G} = S_{PACO}$ and the dot-dashed lines correspond to $S_{PACO} = S_{AT20G,20GHz}(1 \pm \sigma_v)$ . From <a href="#">Bonavera et al. (2011)</a> . . . . .	104
4.17	Distribution of $\log_{10}(S_{PACO}/S_{AT20G})$ at $\simeq 20$ GHz. The dotted line is the Gaussian best-fit. The dashed lines are the mean and the mean $\pm \sigma$ of the distribution. From <a href="#">Bonavera et al. (2011)</a> . . . . .	105

## LIST OF FIGURES

---

4.18	Comparison between the AT20G flux densities at 4.8 GHz and the PACO ones at 4.744 GHz. The solid line corresponds to $S_{\text{AT20G}} = S_{\text{PACO}}$ and the dot-dashed lines correspond to $S_{\text{PACO},4.7\text{GHz}} = S_{\text{AT20G},4.8\text{GHz}}(1 \pm \sigma_v)$ . From <a href="#">Bonavera et al. (2011)</a> . . . . .	106
4.19	Distribution of spectral indices in the 5-8 GHz frequency ranges for the SiMPIE sample. From <a href="#">Procopio et al. (2011)</a> . . . . .	107
4.20	Distribution of spectral indices in the 5-30 (shaded area) and 30-70 GHz (hatched area) frequency ranges for the SiMPIE sample. From <a href="#">Procopio et al. (2011)</a> . . . . .	108
5.1	Comparison between the ERCSC flux densities at 30 GHz (left panel) and at 44 GHz (right panel) with the almost simultaneous ATCA measurements (PACO project) at 32.2 and 39.7 GHz, respectively. No correction for the slightly different frequencies has been applied. From <a href="#">Planck Collaboration (2011g)</a> . . . . .	112
5.2	Distribution of the angular distances (in arcmin) between the PACO and the ERCSC positions of PACO sources detected in the <i>Planck</i> channels. . . . .	113
5.3	Plot of the $\Delta_{RA} \cos(\delta_{\text{ERCSC}})$ and $\Delta_{\delta}$ (in arcmin) between the PACO and the ERCSC positions of PACO sources detected in the <i>Planck</i> channels (black asterisks). The red circle corresponds to the ideal case of $\Delta_{RA} \cos(\delta_{\text{ERCSC}}) = \Delta_{\delta} = 0$ and the green star to the median values of $\Delta_{RA} \cos(\delta_{\text{ERCSC}})$ and $\Delta_{\delta}$ . . . . .	114
5.4	SEDs determined combining the PACO (black asterisks) and ERCSC (red diamonds) data sets of sources for which ERCSC flux densities in at least three <i>Planck</i> channels are available. The position of each source is also specified according to PACO RA and DEC coordinates. . . . .	117
5.5	The area covered by the PACO faint sample is that bounded by the dashed lines, excluding the grey areas, i.e. the Galactic plane region ( $ b  \leq 5^\circ$ ) and the Large Magellanic Cloud (LMC) region (a circle of $4^\circ$ radius). The crosses show the positions of PACO sources, the circles those of ERCSC sources at 30, 44 and 70 GHz. . . . .	124

## LIST OF FIGURES

---

5.6	Distributions of the flux densities at 20 GHz in the AT20G catalogue of the PACO bright sample sources (white histogram) and of the bright sample sources with a match in the blazars catalogue (grey histogram).	125
5.7	SEDs constructed using the ASDC SED Builder tool. The red line is the fit to a third degree polynomial. . . . .	127
5.8	Redshift distribution of the sources for which it was possible to determine the synchrotron (grey histogram) and the Compton (hatched histogram) peak frequencies. . . . .	136
5.9	Distributions of the observed (hatched histogram) and rest-frame (grey histogram) synchrotron (top panel) and Compton (bottom panel) peak frequencies. The observed (dashed) and the rest-frame (dot-dashed) median values are also shown. . . . .	137
5.10	Compton against synchrotron peak frequencies in the source rest-frame.	138
5.11	Synchrotron (top panel) and Compton (bottom panel) peak luminosities vs peak frequencies . . . . .	138

## **LIST OF FIGURES**

---

# List of Tables

2.1	<i>Planck</i> channels parameters. . . . .	10
2.2	<i>Planck</i> ERCSC characteristics. The tables gives, for each channel, both the nominal frequency and wavelength, the sky coverage, the total number of sources and the number of sources with Galactic latitude $ b  < 30^\circ$ , the median flux density of the $> 10\sigma$ sources at $ b  > 30^\circ$ (where $\sigma$ is the photometric uncertainty of the source), the flux density of the faintest $> 10\sigma$ source at $ b  > 30^\circ$ , and the flux density of the faintest source at $ b  > 30^\circ$ (flux density limit) are also given. . . . .	22
2.3	Flux cut from the ERCSC used in the 6 fields in which the CIBA power spectrum was estimated. The shot noise due to radio galaxies (both in $Jy^2 sr^{-1}$ and in $\mu K_{CMB}^2$ ), appropriate for these cuts, is also shown. The computation is based on the radio galaxy evolution model by <a href="#">de Zotti et al. (2005)</a> . The values are given in two different units: $Jy^2 sr^{-1}$ and $\mu K_{CMB}^2$ . . . . .	37
2.4	Median and standard deviation of the spectral index distributions between 30 GHz and the selected frequency. We adopt the convention $S_\nu \propto \nu^\alpha$ . . . . .	38
3.1	Observational details used to plan the cross scans; in each scan the time on-source is of about 2.5 s. The high system temperature of the 8.3 GHz receiver was due to malfunctions in the receiver cryogenic system. . . . .	45
3.2	Array configuration description: the first line of each row lists the array name and the stations for antennas 1 to 6 respectively; the second line lists the baseline lengths available for each configuration in metres, in ascending order. . . . .	53

## LIST OF TABLES

---

3.3	The flux density values of the model for the primary calibrator PKS B1934-638 at the center of our observing frequency bands, as it is in the Miriad version we used. . . . .	56
3.4	The 63 good weather observational runs for the PACO project between July 2009 and August 2010. . . . .	58
3.5	The array configurations and their resolution properties. . . . .	67
4.1	Percentages of sources of each spectral type in the PACO faint sample ( $200 \text{ mJy} \leq S_{\text{AT20G}} < 500 \text{ mJy}$ ) and in the bright sample ( $S_{\text{AT20G}} \geq 500 \text{ mJy}$ ). . . . .	92
4.2	Matrix of median spectral indices calculated from the fitting double power-law function for the PACO bright sample. . . . .	97
4.3	Matrix of median spectral indices calculated from the fitting double power-law function for the PACO faint sample. . . . .	97
4.4	Fractions of PACO sources with $\simeq 19 \text{ GHz}$ (more precisely, at $18.768 \text{ GHz}$ ) flux densities (mJy) within the bins indicated in the first column, found in the $32.768$ (upper panel) and $39.768 \text{ GHz}$ (lower panel) bins listed in the first row. The values in parenthesis are the number of sources in each $19 \text{ GHz}$ bin. . . . .	98
4.5	Source counts at $32.744$ (second column) and $39.768 \text{ GHz}$ (third column), with their errors, obtained by extrapolating the AT20G source counts. . . . .	100
4.6	Median variability index of the PACO bright sample at varying frequency and time lag range. . . . .	101
4.7	The $7 \text{ mm}$ flux densities for the point-like calibrators in the PACO sample selected as those having $S_{\text{AT20G}} > 5 \text{ Jy}$ as observed in epochs simultaneous to the <i>Planck</i> satellite observations. . . . .	110
5.1	Number of PACO sources present in the ERCSC and rms distances between ERCSC and PACO positions, for each frequency channel. . . . .	112
5.2	Mean, median and $\sigma$ values for $\Delta_{RA} \cos(\delta_{\text{ERCSC}})$ and $\Delta_{\delta}$ for all <i>Planck</i> channels. . . . .	116

5.3	We give, for each <i>Planck</i> channel, the number of PACO faint sources in the ERCSC, the number of PACO faint sources in the ERCSC but not in the PACO bright sample, those which that have $S_{PACO} > 500$ mJy at 18.7 GHz, the percentage of missed sources when using the bright sample only. . . . .	123
5.4	Summary of the properties of the bright sample sources with a match in the BZcat ( <a href="#">Massaro et al., 2009</a> ) and $S_{AT20G}$ at 20 GHz greater than 1.5 Jy. . . . .	139

## **LIST OF TABLES**

---

# Chapter 1

## Introduction

ESA's *Planck* satellite is surveying the sky in nine frequency bands 30, 44, 70 GHz for the Low Frequency Instrument (LFI) and 100, 143, 217, 353, 545, 857 GHz for the High Frequency Instrument (HFI) with the beam full width at half-maximum (FWHM) ranging from 33 to 5 arcmin (Planck Collaboration, 2011f). At the HFI frequencies it will provide the first all-sky surveys ever, while at LFI frequencies its higher sensitivity and resolution will allow a significant improvement over the Wilkinson Microwave Anisotropy Probe (*WMAP*; Gold et al., 2011; Leach et al., 2008; Massardi et al., 2009; Planck Collaboration, 2006, 2011f). *Planck* thus offers a unique opportunity to carry out an unbiased investigation of the spectral properties of radio sources in a poorly explored frequency range, partially inaccessible from the ground.

*Planck* science yields can be greatly increased by simultaneous (i.e. reducing the effect of variability) ground-based observations at lower frequencies as well as at frequencies overlapping with *Planck* channels. Simultaneous observations at overlapping frequencies are important to transfer the *Planck* flux density calibration, which at frequencies up to 353 GHz is based on the cosmic microwave background (CMB) dipole, to the primary calibrators used by the ground-based radio telescopes (The Planck HFI Core Team, 2011b; Zacchei et al., 2011). These observations can also be used to help with the validation of sources detected by *Planck*.

At present, the flux density scales for ground-based telescopes are well determined for frequencies up to 10 GHz but there are known problems at the higher frequencies. The difficulty occurs because the radio interferometers, which can make the most precise flux density measurements at high frequencies, need point sources to calibrate

## 1. INTRODUCTION

---

and the strong point sources are mostly highly variable active galactic nuclei (AGNs). This has led to the use of the planets, Mars and Uranus, as primary calibrators. Their flux densities are estimated using relatively complex atmospheric models. In the case of Uranus there is a further complication because of the known orbital change in flux density as our view changes from equatorial to polar during the Uranian year. Simultaneous observations of very bright sources give a unique opportunity to tie all the high-frequency flux density scales together with the *Planck* calibration. It should be noted, however, that the source flux densities given in the Early Release Compact Source Catalogue (ERCSC; [Planck Collaboration, 2011b](#)) are averages over all observations, that may extend over several months. Therefore, they may be used for some statistical purposes, as in [Planck Collaboration \(2011g\)](#), while for calibration purposes we need to use the *Planck* time-ordered data, averaged over shorter periods, comparable with the time-scales of ground-based observations.

Source confusion is a serious issue for *Planck*, due to its rather large beam sizes. Sources near *Planck* detection limits may be strongly affected by the [Eddington \(1913\)](#) bias that leads to systematically overestimate the flux density ([Hogg and Turner, 1998](#)). Also, confusion fluctuations may produce high-intensity peaks that may be misinterpreted as real sources. Moreover, confusion can shift the positions of intensity peaks from the true source positions ([Hogg, 2001](#)), complicating their identification. Simultaneous ground-based observations, with much better resolution and signal to noise ratio, will allow an accurate control of these effects.

Spectral energy distributions (SEDs) of radio sources over a frequency range as large as possible are crucial in determining their physical properties and in identifying the different components that may contribute to their emission. Given that observations in the full *Planck* frequency range will not be repeated at least in the foreseeable future, it is essential not to lose the opportunity for near simultaneous observations while *Planck* is flying ([Planck Collaboration, 2011f](#)). Observations simultaneous with *Planck* can obviously be planned only for previously known sources.

The above considerations have motivated the simultaneous observations not only at radio frequencies, but also at mm, optical, UV, x-ray wavelengths ([Giommi et al., 2011](#); [Planck Collaboration, 2011c](#), where also  $\gamma$ -ray data were included in the analysis).

In this work we are going to focus on two major projects of radio observations simultaneous with *Planck*: the *Planck*-ATCA (Australia Telescope Compact Array)

---

Coeval Observations (PACO) project and the Simultaneous Medicina-*Planck* Experiment (SiMPIE). The former exploited the capabilities of the new ATCA Broadband Backend (CABB; Ferris, 2002; Wilson et al., 2011) system between 4.5 and 40 GHz and the latter used the Medicina single-dish telescope at 5, 8.3 and 22 GHz.

The PACO project consists of observations of 482 AT20G (The Australia Telescope 20 GHz Survey) extragalactic sources at Galactic latitude  $|b| > 5^\circ$  and outside a  $5^\circ$  radius circle centred at  $RA = 80.8939^\circ$ ,  $\delta = 69.7561^\circ$  (the LMC region). Of these, 344 sources form 3 partially overlapping complete sub-samples: the PACO bright sample, the PACO faint sample and the PACO spectrally-selected sample. The SiMPIE project complements PACO in the Northern Hemisphere. It consists of observations of 253 objects in the New Extragalactic *WMAP* Point Source (NEWPS) sample and 10 Galactic objects, not in the NEWPS catalogue, that may show strong outbursts during the *Planck* mission.

The plan of the work is as follows. Chapter 2 gives an overview of the *Planck* mission and of the *Planck* Early Release Compact Source Catalogue (ERCSC; Planck Collaboration, 2011b), focusing on the radio sources in the ERCSC. Chapter 3 describes the ground-based projects carried out simultaneously with *Planck*, focusing on the SiMPIE and PACO experiments. The analysis of the data collected with these observations is presented in Chapter 4 and 5 and summarized in Chapter 6.

Part of the work presented in this thesis has been reported in the following publications:

- P. Giommi, G. Polenta, A. Lähteenmäki, D. J. Thompson, M. Capalbi, S. Cutini, D. Gasparri, J. González-Nuevo, J. León-Tavares, M. López-Caniego, M. N. Mazziotta, C. Monte, M. Perri, S. Rainó, G. Tosti, A. Tramacere, F. Verrecchia, H. D. Aller, M. F. Aller, E. Angelakis, D. Bastieri, A. Berdyugin, A. Bonaldi, **L. Bonavera** et al. Simultaneous *Planck*, *Swift*, and *Fermi* observations of X-ray and  $\gamma$ -ray selected blazars. Submitted to *Astronomy and Astrophysics*, August 2011.
- M. Massardi, A. Bonaldi, **L. Bonavera**, M. López-Caniego, G. De Zotti, and R. D. Ekers. The *Planck*-ATCA Coeval Observations project: the bright sample. *Monthly Notices of the RAS*, 415:1597-1610, August 2011a.

## 1. INTRODUCTION

---

- **L. Bonavera**, M. Massardi, A. Bonaldi, J. González-Nuevo, G. de Zotti, and R. D. Ekers. The *Planck*-ATCA Co-eval Observations project: the faint sample. *Monthly Notices of the RAS*, pages 1034+, July 2011.
- P. Procopio, M. Massardi, S. Righini, A. Zanichelli, S. Ricciardi, P. Libardi, C. Burigana, F. Cuttaia, K. Mack, L. Terenzi, F. Villa, **L. Bonavera**, G. Morgante, C. Trigilio, T. Trombetti, and G. Umana. The Simultaneous Medicina-*Planck* Experiment (SiMPIE): data acquisition, reduction and first results. Submitted to *Monthly Notices of the RAS*, June 2011.
- Planck Collaboration and J. Aatrokoski, P. A. R. Ade, N. Aghanim, H. D. Aller, M. F. Aller, E. Angelakis, M. Arnaud, M. Ashdown, J. Aumont, C. Baccigalupi, A. Balbi, A. J. Banday, R. B. Barreiro, J. G. Bartlett, E. Battaner, K. Benabed, A. Benoît, A. Berdyugin, J. -. Bernard, M. Bersanelli, R. Bhatia, A. Bonaldi, **L. Bonavera** et al. *Planck* early results: Spectral energy distributions and radio continuum spectra of northern extragalactic radio sources. Submitted to *Astronomy and Astrophysics*, January 2011.
- Planck Collaboration and P. A. R. Ade, N. Aghanim, F. Argüeso, M. Arnaud, M. Ashdown, J. Aumont, C. Baccigalupi, A. Balbi, A. J. Banday, R. B. Barreiro, J. G. Bartlett, E. Battaner, K. Benabed, J. -. Bernard, M. Bersanelli, R. Bhatia, A. Bonaldi, **L. Bonavera** et al. *Planck* Early Results: Statistical properties of extragalactic radio sources in the *Planck* Early Release Compact Source Catalogue. Submitted to *Astronomy and Astrophysics*, January 2011.
- Planck Collaboration and P. A. R. Ade, N. Aghanim, M. Arnaud, M. Ashdown, J. Aumont, C. Baccigalupi, A. Balbi, A. J. Banday, R. B. Barreiro, J. G. Bartlett, E. Battaner, K. Benabed, A. Benoît, J. -. Bernard, M. Bersanelli, R. Bhatia, A. Bonaldi, **L. Bonavera** et al. *Planck* Early Results: The Early Release Compact Source Catalog. Submitted to *Astronomy and Astrophysics*, January 2011.
- A. Zacchei, D. Maino, C. Baccigalupi, M. Bersanelli, A. Bonaldi, **L. Bonavera** et al. *Planck* Early Results: The Low Frequency Instrument data processing. Submitted to *Astronomy and Astrophysics*, January 2011.

- 
- A. Mennella, M. Bersanelli, R. C. Butler, A. Curto, F. Cuttaia, R. J. Davis, J. Dick, M. Frailis, S. Galeotta, A. Gregorio, H. Kurki-Suonio, C. R. Lawrence, S. Leach, J. P. Leahy, S. Lowe, D. Maino, N. Mandolesi, M. Maris, E. Martínez-González, P. R. Meinhold, G. Morgante, D. Pearson, F. Perrotta, G. Polenta, T. Poutanen, M. Sandri, M. D. Seiffert, A. - . Suur-Uski, D. Tavagnacco, L. Terenzi, M. Tomasi, J. Valiviita, F. Villa, R. Watson, A. Wilkinson, A. Zacchei, A. Zonca, B. Aja, E. Artal, C. Baccigalupi, A. J. Banday, R. B. Barreiro, J. G. Bartlett, N. Bartolo, P. Battaglia, K. Bennett, A. Bonaldi, **L. Bonavera** et al. *Planck* early results: First assessment of the Low Frequency Instrument in-flight performance. Submitted to *Astronomy and Astrophysics*, January 2011.
  - Planck Collaboration and P. A. R. Ade, N. Aghanim, M. Arnaud, M. Ashdown, J. Aumont, C. Baccigalupi, A. Balbi, A. J. Banday, R. B. Barreiro, J. G. Bartlett, E. Battaner, K. Benabed, A. Benoît, J. - . Bernard, M. Bersanelli, R. Bhatia, K. Blagrove, J. J. Bock, A. Bonaldi, **L. Bonavera** et al. *Planck* Early Results: The Power Spectrum of Cosmic Infrared Background Anisotropies. Submitted to *Astronomy and Astrophysics*, January 2011.
  - Planck Collaboration and P. A. R. Ade, N. Aghanim, E. Angelakis, M. Arnaud, M. Ashdown, J. Aumont, C. Baccigalupi, A. Balbi, A. J. Banday, R. B. Barreiro, J. G. Bartlett, E. Battaner, K. Benabed, A. Benoît, J. P. Bernard, M. Bersanelli, R. Bhatia, A. Bonaldi, **L. Bonavera** et al. *Planck* Early Results: ERCSC Validation and Extreme Radio Sources. Submitted to *Astronomy and Astrophysics*, January 2011.

## 1. INTRODUCTION

---

## Chapter 2

# The *Planck* View of Extragalactic Sources

### 2.1 Overview

The first detection of intrinsic temperature fluctuations in the Cosmic Microwave Background (CMB) was performed by the COsmic Background Explorer (*COBE*; [Mather et al., 1990, 1999](#)): they were on angular scales larger than  $\sim 7^\circ$ , at a level  $\Delta T/T \sim 10^{-5}$  ([Bennett et al., 1992](#); [Kogut et al., 1992](#); [Smoot et al., 1992](#); [Wright et al., 1992](#)). A decade later the *WMAP* team announced results on scales of about  $15'$  with similar sensitivity per resolution element ([Bennett et al., 2003a,b](#)). To perform CMB measurements with even higher angular resolution and sensitivity, two space-based CMB experiments (COBRAS and SAMBA) were proposed to ESA, subsequently combined and renamed in honour of the German scientist Max Planck (1858-1947). The instruments for the *Planck* satellite (<http://www.esa.int/Planck>) are provided by two scientific Consortia funded by ESA member states (in particular the lead countries: France and Italy) with contributions from NASA (USA), and telescope reflectors provided in a collaboration between ESA and a scientific Consortium led and funded by Denmark.

The main objective of *Planck* is to measure the spatial anisotropies of the temperature of the CMB, with an accuracy set by fundamental astrophysical limits. *Planck* also measures with a higher accuracy with respect to previous measurement the polarisation of the CMB anisotropies. In addition, the *Planck* sky surveys will produce a wealth of

## 2. THE *PLANCK* VIEW OF EXTRAGALACTIC SOURCES

---

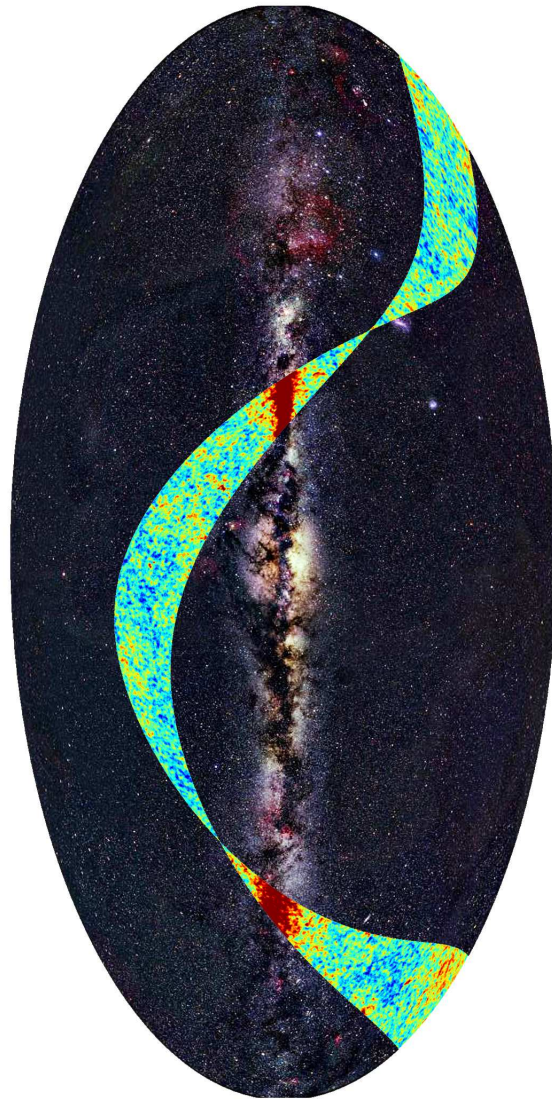


**Figure 2.1:** A map (<http://www.esa.int/esaMI/Planck/SEM5CMFWNZF.1.html>) of the sky at optical wavelengths shows a prominent horizontal band which is the light shining from our own Milky Way. The superimposed strip shows the area of the sky mapped by *Planck* during the First Light Survey. The colour scale indicates the magnitude of the deviations of the temperature of the Cosmic Microwave Background from its average value, as measured by *Planck* at a frequency close to the peak of the CMB spectrum (red is hotter and blue is colder).

information on the properties of extragalactic sources and on the dust and gas in our own Galaxy.

*Planck* was launched from the Centre Spatial Guyanais in Kourou (French Guyana) on 14 May 2009 on an Ariane 5 ECA rocket of Arianespace2 (Planck Collaboration, 2011f). ESA's Herschel observatory was launched on the same rocket. The Ariane rocket placed *Planck* with excellent accuracy (semi-major axis within 1.6% of prediction), on a trajectory towards the second Lagrangian point of the Earth-Sun system (L2). The orbit describes a Lissajous trajectory around L2 with a  $\sim 6$  month period that avoids crossing the Earth penumbra for at least 4 years. *Planck* started cooling down radiatively shortly after launch.

*Planck* utilises the two ESA deep-space ground stations in New Norcia (Australia) and Cebreros (Spain). The data are transferred to the mission operations control centre (MOC) located at ESOC in Darmstadt (Germany), where it is processed by redundant Mission Control Software (MCS) installations. All the data downloaded from the satellite, and processed products are made available each day for retrieval from the MOC by the LFI and HFI Data Processing Centres (DPCs), located in Trieste and Paris, respectively.

The Routine Operations phase of *Planck* started with the the First Light Survey (FLS; Figure 2.1) on 13 August of 2009. The FLS was conceived as a two-week period, between 13 and 27 August, during which *Planck* would be fully tuned up. It led to the conclusion that the *Planck* payload was operating stably and optimally, therefore the period of the FLS was accepted as a valid part of the first *Planck* survey.

*Planck* carries a scientific payload consisting of an array of 74 detectors sensitive to a range of frequencies between 30 and 857 GHz, which scan the sky simultaneously and continuously with an angular resolution varying between  $\sim 30$  arcminutes at the lowest frequencies and  $\sim 5$  arcminutes at the highest. The array is arranged into two instruments: the detectors of the Low Frequency Instrument (LFI; Bersanelli et al., 2010; Mennella et al., 2011) are radiometers, covering three bands centred at 30, 44, and 70 GHz; and the detectors of the High Frequency Instrument (HFI; Lamarre et al., 2010; The Planck HFI Core Team, 2011a) are bolometers, covering six bands centred at 100, 143, 217, 353, 545 and 857 GHz. The band centres are spaced approximately logarithmically (see Table 2.1). The LFI horns are situated in a ring around the HFI, see Figure 2.2. The 44 GHz receivers are widely separated in the *Planck* focal plane, allowing

## 2. THE *PLANCK* VIEW OF EXTRAGALACTIC SOURCES

---

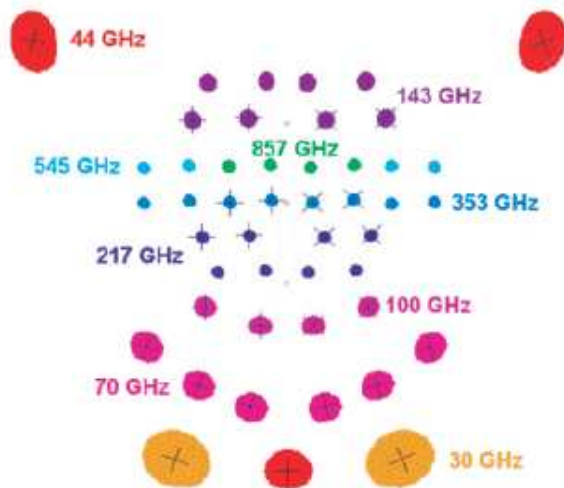


**Figure 2.2:** The footprint of the *Planck* field-of-view: the ellipticities seen are representative of the shape of the beam at full-width-half maximum. The black crosses indicate the orientation of the pairs of linearly polarised detectors within each horn (Planck Collaboration, 2006).

**Table 2.1:** *Planck* channels parameters.

<i>Planck</i> Channel [GHz]	Number of Detectors	Central Frequency [GHz]	Beam FWHM [arcmin]
30	4	28.5	32.65
44	6	44.1	27.92
70	12	70.3	13.01
100	8	100	9.37
143	11	143	7.04
217	12	217	4.68
353	12	353	4.43
545	3	545	3.80
857	3	857	3.67

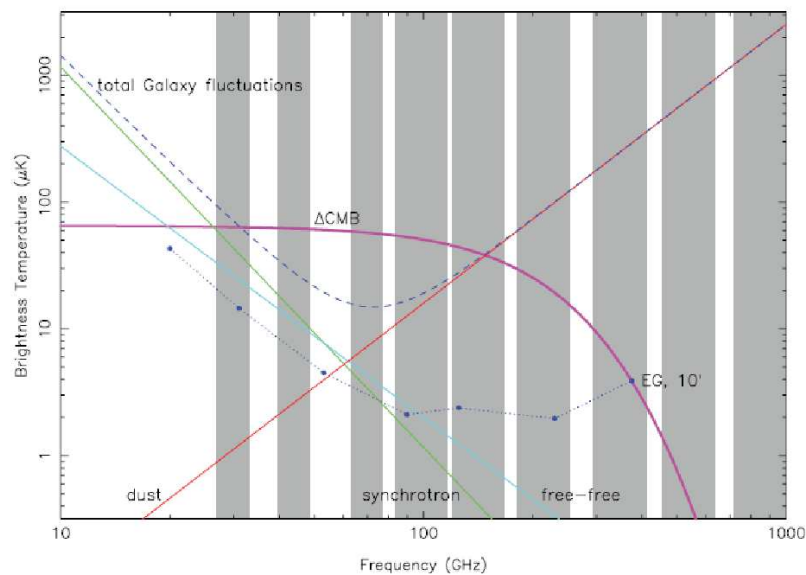


**Figure 2.3:** RMS of the CMB fluctuations, and the frequency coverage of the *Planck* channels. Also indicated are the spectra of other sources of fluctuations in the microwave sky. Dust, synchrotron, and free-free temperature fluctuation (i.e., unpolarized) levels correspond to the levels of fluctuations when the brightest part of the Galaxy (15%) has been cut out (*WMAP* Kp2 mask; Bennett et al., 2003b). The CMB and Galactic fluctuation levels depend on angular scale, and are shown for  $\sim 1^\circ$ . On small angular scales, extragalactic sources dominate. The minimum in diffuse foregrounds and the clearest window on CMB fluctuations occurs near 70 GHz. The highest HFI frequencies are primarily sensitive to dust (Planck Collaboration, 2006).

## 2. THE *PLANCK* VIEW OF EXTRAGALACTIC SOURCES

---

for the possibility of wider variation in the 44 GHz measurements. Each horn collects radiation from the telescope and feeds it to one or more detectors. Feeds at the same frequency are generally aligned along the same direction, except for the 44 GHz. All the LFI channels, and four of the HFI channels, can measure linear polarization as well as total intensity. The principal observational objective of *Planck* is to produce maps of the sky in nine frequency channels. The whole sky is scanned by *Planck* approximately twice per year and the mission anticipates  $\sim 4$  full sky surveys. The *Planck* maps will include not only the signal from the CMB, but also all other astrophysical foregrounds Galactic (free-free, synchrotron, and dust) and extragalactic (Figure 2.3). LFI covers well the frequency range where free-free and synchrotron emission from the Galaxy, and spinning dust emission (Planck Collaboration, 2011e), dominate the foreground radiation. HFI covers well the frequencies where dust emission dominates the foreground radiation. Taken together, they provide the frequency coverage necessary for accurate separation of the CMB and foreground radiation. The final scientific performance of the mission depends, therefore, not only on the instrumental behaviour, but also on the detailed nature of astrophysical foregrounds and the behaviour of many systematic effects which may produce spurious signals. Relevant systematic effects can be controlled by the appropriate choice of orbit and sky scanning strategy, described in Section 2.2.1.

At the time of writing *Planck* has completed three surveys of the whole sky and has released to the public its first set of scientific data: the Early Release Compact Source Catalogue (ERCSC), a list of unresolved and compact sources extracted from the first complete all-sky survey carried out by *Planck* (Planck Collaboration, 2011b) plus part of the second survey.

In this chapter we present the *Planck* scanning strategy and the *Planck* On-Flight Forecaster (Massardi and Burigana, 2010), software for predicting the region of the sky observed by the satellite at a given time, since it was used for planning ground-based observations (see Section 2.2). We also give an overview of the *Planck* early results concerning Extragalactic Radio Sources.

## 2.2 The *Planck* On-Flight Forecaster (POFF)

### 2.2.1 The *Planck* Scanning Strategy

*Planck* receivers observe the sky by continuously scanning nearly great circles on the

---

## 2.2 The *Planck* On-Flight Forecaster (POFF)

celestial sphere. The telescope’s field-of-view rotates at 1 rpm, while its spin axis is regularly updated, about 2.5 arcmin/hour in ecliptic longitude, with the constraint to remain within  $10^\circ$  from the anti-Sun direction. The Lissajous orbit is seen from the Earth as an approximately six monthly periodic path of the spin axis pointing sequence.

The specific scanning strategy has been chosen for *Planck* in order to minimize systematic effects and to achieve all-sky coverage for all the receivers. The scanning strategy is defined by a set of parameters, the chief one being the angle,  $\alpha$ , between the spacecraft spin axis and the telescope optical axis. Given the extension of the focal plane unit (see Section 2.2.2), each receiver actually points at its own specific angle,  $\alpha_r$ . The angle  $\alpha$  was fixed by design at  $85^\circ$  to achieve near all-sky coverage with the spacecraft spin axis kept always exactly along the anti-solar direction. This choice avoided the ‘degenerate’ case  $\alpha_r = 90^\circ$ , characterized by a concentration of the crossings of scan circles only at the ecliptic poles and the consequent degradation of the quality of de-stripping and map-making codes (Delabrouille et al., 1998; Janssen and Gulkis, 1992; Maino et al., 1999).

*Planck* scanning strategy is designed to minimize stray-light contamination from the Sun, Earth, and Moon (Burigana et al., 2001; Maffei et al., 2010; Sandri et al., 2010; Tauber et al., 2010), and as a consequence only limited spin axis deviations from the ecliptic plane are allowed. This small deviations from the ecliptic plane ensures maximization of sky coverage, actually keeping the solar aspect angle of the spacecraft constant for thermal stability reasons. The implemented *baseline* scanning strategy (Maris et al., 2006) makes use of this option: the spin axis performs a cycloidal motion, precessing around the nominal anti-Sun direction, with a semi-amplitude cone of  $7.5^\circ$ .

A cycloidal spin axis motion with a  $\sim 6$  month period satisfies the mission operational constraints, and avoids sharp gradients in the pixel hit count (Dupac and Tauber, 2005). Finally, this approach also spreads the crossings of scan circles over a wide region improving the quality of map-making, particularly for polarisation (Ashdown et al., 2007).

The last three scanning strategy parameters are: the sense of precession (clockwise or anti-clockwise); the initial spin axis phase along the precession cone; and the spacing between two consecutive spin axis repointings, chosen at  $2'$  to achieve four all-sky surveys with the available guaranteed number of spin axis manoeuvres.

## 2. THE *PLANCK* VIEW OF EXTRAGALACTIC SOURCES

---

The effective implementation of the scanning strategy of *Planck* is defined by the pre-programmed directions of the spin axis that are listed in two documents<sup>1</sup> :

- the Planned Pointing List (PPL), which contains a sequence of pointings for the *Planck* spin axis covering about one month period of the survey,
- the Long Term Preprogrammed Pointing List (LTPPL), which provides about one year of planned pointings and is based on the best survey information available at the time.

### 2.2.2 The Focal Plane

The focal plane is oriented at an  $85^\circ$  angle with respect to the spin axis, so that the scanning tracks pass close to the Ecliptic poles, but do not cross them exactly. The *Planck* telescope focuses radiation from the sky onto its focal plane, which is shared by the Low and High Frequency Instruments. The field of view of the ensemble of the *Planck* receivers has a total angular dimension of  $7.5^\circ$ .

Typically, horns at the same frequency, or subsets of them, observe the same scan circle for a given spin axis direction (see Figure 2.4), improving the sensitivity. These groups of aligned receivers at the same frequency are typically close to each other (Sandri et al., 2010; Tauber et al., 2010), except for the 44 GHz channel.

The Spacecraft Instrument Alignment Matrix (SIAM), originally estimated from ground calibration, provides the pointing direction and orientation of each receiver of the two *Planck* instruments with respect to the spacecraft functional reference frame. When bright sources (and, in particular, external planets) transit on the *Planck* field of view, they are used to better characterize the optical properties of each *Planck* beam, i.e. its shape, orientation, and, in particular, the pointing direction of its centre with respect to the spacecraft functional reference frame (Burigana et al., 2001). If the estimation of beam centre direction changes significantly through these observations the SIAM file is updated<sup>2</sup>.

---

<sup>1</sup>Their periodic updates can be downloaded from the web-page:  
<http://www.rssd.esa.int/index.php?project=Planck&page=Pointing>

<sup>2</sup>The most recent SIAM updates can be retrieved on the same web-page as the PPLs

## 2.2 The *Planck* On-Flight Forecaster (POFF)

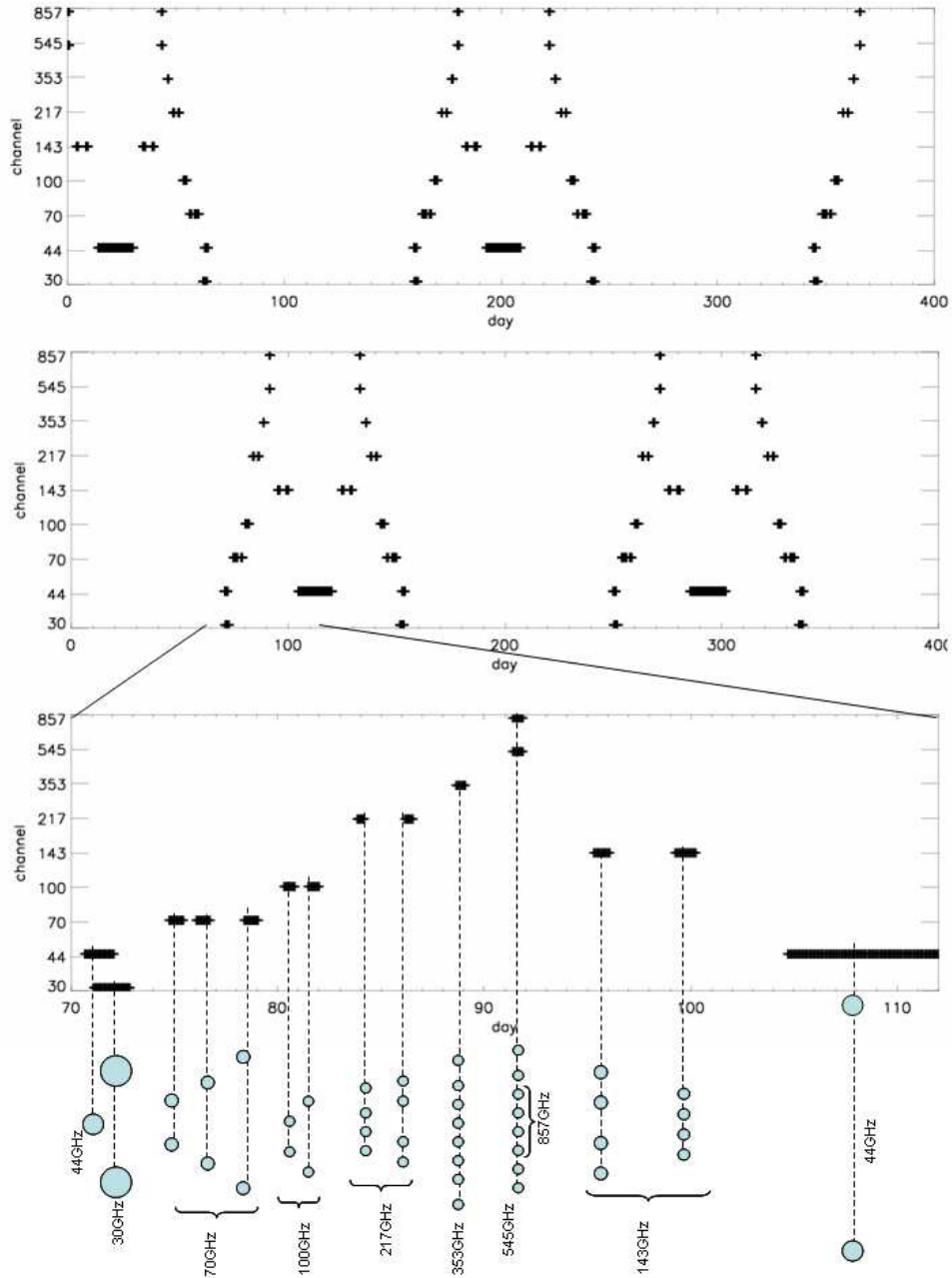


**Figure 2.4:** In the upper and middle panel the POFF output is shown as a function of time and *Planck* frequency channels for the South and North Ecliptic Pole positions, respectively. The lower panel is a zoom in the upper one for the first period of observability of the North Ecliptic Pole position. The scheme of the *Planck* focal plane has been plotted for comparison: the sequence of frequencies of observations corresponds to the sequence with which aligned beams scan through the sky position. Note that the distances between beams is not to scale for plotting purposes (Massardi and Burigana, 2010).

## 2. THE *PLANCK* VIEW OF EXTRAGALACTIC SOURCES

---

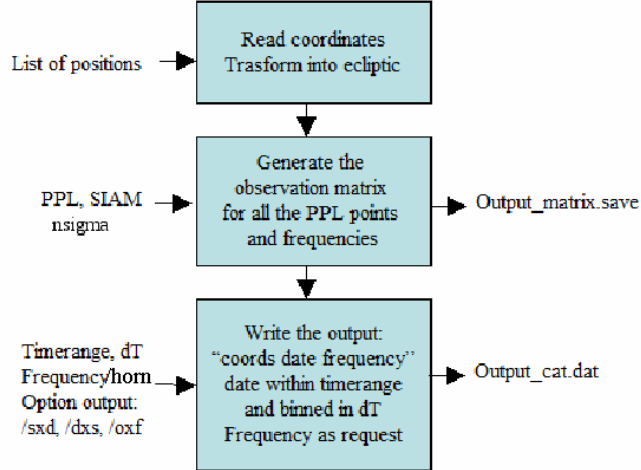


**Figure 2.5:** I/O flow chart of the POFF code by [Massardi and Burigana \(2010\)](#).

The first element of the part of the SIAM corresponding to a given receiver provides the cosine of the angle,  $\alpha_r$ , between the direction of the considered receiver and the direction of the spacecraft spin axis. This quantity is crucial for the POFF.

### 2.2.3 The Code

For a given spin axis direction, each receiver describes a circle on the sky defined by the corresponding angle  $\alpha_r$  from the spin axis. In reality, the spin axis direction is not exactly constant between two consecutive repointings (a pointing period), because of the complexity of spacecraft dynamics. The spread of the spin axis directions within a pointing period is of the order of 1 arcmin or less.

The POFF code by [Massardi and Burigana \(2010\)](#), adopts the nominal beam sizes given by [Planck Collaboration \(2006\)](#) i.e. the values 33, 28, 13, 9.5, 7.1 arcmin respectively for the FWHM at 30, 44, 70, 100, and 143 and 5 arcmin for all the channels between 217 and 857 GHz.

The *Planck* scanning strategy implies that positions close to the ecliptic poles will be observable throughout a long period (up to 3 months, see [Figure 2.4](#)), while objects close to the ecliptic equator remain in the region observed by the *Planck* focal plane at most for about one week during each survey.

---

## 2.3 The Early Release Compact Source Catalog (ERCSC)

The code is a combination of several IDL routines, and the input and output options are passed through a set of mandatory or optional keywords. Figure 2.5 shows the I/O flow chart of the code: the user provides the list of coordinates, POFF transforms them into Ecliptic coordinate where necessary and passes them to a routine that reads the PPL and SIAM files. The code determines for each pair of coordinates and for each of the *Planck* receivers whether the source position falls within the observable region during a whole rotation of the satellite around its spin axis for each PPL position.

The POFF is freely available<sup>1</sup> in IDL binary format (i.e. a ‘poff.sav’ file). To be executed it needs to be restored within an IDL environment (version 7.0 or later) and the calling sequence, with all the options, can be passed through the IDL command line or introduced in IDL scripts.

The pointings actually executed by *Planck* may differ from the pointings in the PPL in case of unpredictable re-pointing activities of the satellite in which case the discrepancies between the predictions and the observed pointings should not be larger than the satellite focal plane (i.e. the prediction is expected to be always correct within a week time); the corresponding accuracy of the LTPPL is lower because of the longer look-forward time-scale. Hence, if the user requires that the prediction is correct on shorter time scales, the short-term PPL, which are periodically updated, should be used.

An example of POFF output is given in Figure 2.6, which shows a scheme of observability of the PACO sources (see Section 3.2) according to the *Planck* scanning strategy. The importance of the POFF code is in the fact that it can predict when a region of the sky is observed by *Planck*, allowing the scheduling of ground-based observations of sources (see Chapter 3), simultaneously with the satellite. In such a way it is possible to reconstruct the SEDs of known sources in the range of frequencies given by the ground-based telescopes and *Planck* altogether, without being unduly affected by variability issues.

## 2.3 The Early Release Compact Source Catalog (ERCSC)

*Planck* is supplying flux density measurements of many hundreds of radio sources and of many thousands of dusty galaxies, providing us with the first all sky catalogue of

---

<sup>1</sup><http://web.oapd.inaf.it/rstools/poff/poff.html>

## 2. THE *PLANCK* VIEW OF EXTRAGALACTIC SOURCES

---

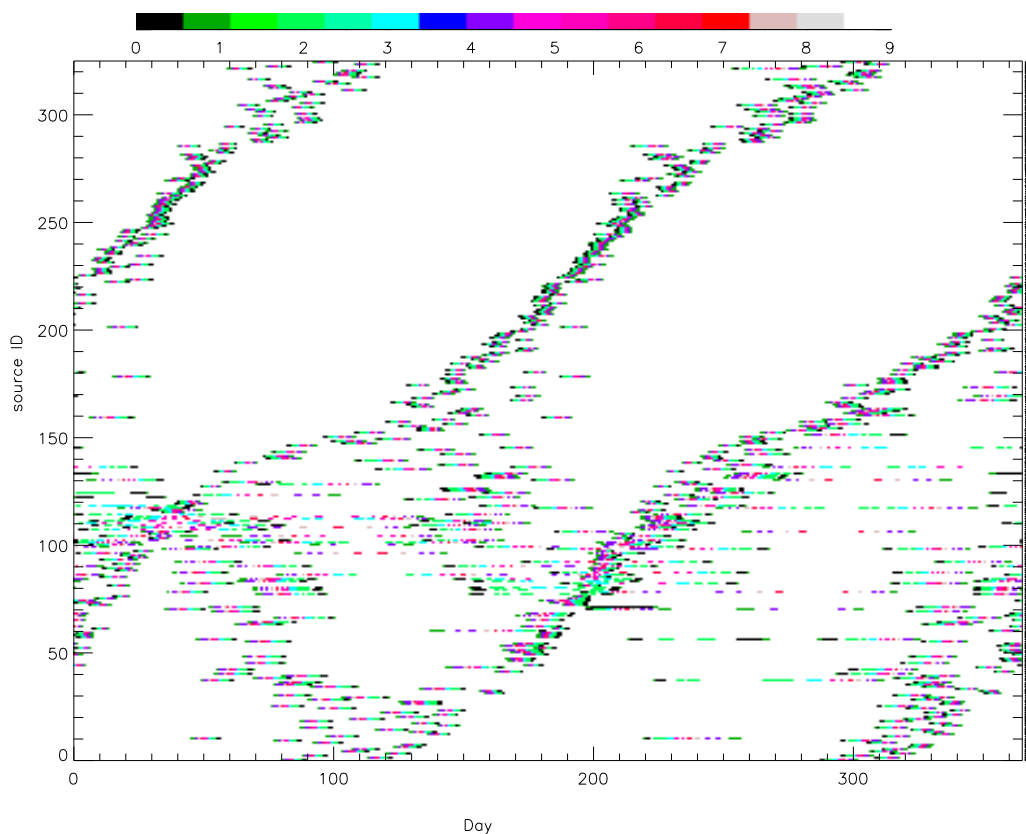


**Figure 2.6:** Scheme of observability of the PACO sources (see Section 3.2) according to the *Planck* scanning strategy. Different colours correspond to different *Planck* channels. Sources are sorted by right ascension from the bottom (0h) to the top of the scheme (24h). Notice the equatorial pole region over-density for  $4 < RA < 8$ . Day 0 corresponds to August 13th, 2009.

### 2.3 The Early Release Compact Source Catalog (ERCSC)

---

sub-millimetre sources (Planck Collaboration, 2011b). Due to *Planck*'s small telescope size (compared to millimetre and sub-millimetre antennas on the ground), its angular resolution and sensitivity to point sources are lower. However, *Planck* observes simultaneously at nine frequencies, covers the entire sky, and will be well-calibrated across all nine frequency bands: these advantages will allow us to find and study complete samples of bright, rare objects shining between 30 and 857 GHz, complementing both present and planned radio and sub-millimetre instruments, including measurements by the Atacama Large Millimetre Array (ALMA), which will produce deeper surveys over limited areas.

The frequency region spanned by the *Planck* detectors is poorly studied, hence the properties of sources at these frequencies are poorly understood. Moreover, there are classes of sources known to have spectra rather different from the typical ones: inverted spectra ( $\alpha > 0$ ) for frequencies up to tens of GHz, as well as other sources thought to be among the most recently formed and most luminous extragalactic radio sources. Many such sources are expected to be strongly variable. *Planck* permits study of the brightest of these objects with unprecedented frequency coverage and over a wide range of time domains.

The *Planck* ERCSC (Planck Collaboration, 2011b) lists positions and flux densities for the compact sources recovered from the *Planck* first 1.6 full sky survey maps. The ERCSC has been created by applying the PowellSnakes detection method (Carvalho et al., 2009) to the *Planck* full sky (dipole subtracted) anisotropy maps in the frequency channels from 30 to 143 GHz and the SExtractor package (Bertin and Arnouts, 1996) in the four channels at higher frequencies (from 217 to 857 GHz). The ERCSC flux densities have been calculated by aperture photometry, using the most recent definition of the beam shapes and sizes (The Planck HFI Core Team, 2011b; Zacchei et al., 2011). The *Planck* internal calibration at frequencies up to 353 GHz is based on the CMB dipole and on the modulation induced on it by the spacecraft orbital motion. In the highest frequency channels (545 and 857 GHz) it is based on a comparison with COBE/FIRAS. According to Zacchei et al. (2011) the absolute photometric calibration at LFI frequencies (30, 44 and 70 GHz) is at the 1% level and The Planck HFI Core Team (2011b) reports on a relative photometric accuracy, between the frequency channels from 100 to 353 GHz, better than 2% and, more likely, at the 1% level.

## 2. THE *PLANCK* VIEW OF EXTRAGALACTIC SOURCES

---

External validation (Planck Collaboration, 2011d) shows agreement to  $\pm 3\%$ ; see also Section 2.5.1.

A compact source is accepted in the ERCSC if it survived a set of primary and secondary selection criteria. The primary criterion utilized the feedback from the Monte Carlo Quality Assessment system and introduced a signal-to-noise ratio cut to ensure that  $> 90\%$  of the sources in the catalogue are reliable and have a flux density accuracy better than 30%. The secondary criterion comprised a set of cuts that removed the extended sources with an elongation  $> 3.0$  (the ratio between the major and minor axis, in pixels, of the detected source) and sources that could be potentially spurious. For instance a source is dropped whenever  $> 5\%$  of the pixels within  $2 \times FWHM$  of its position have invalid values (see the ERCSC Explanatory Supplement for more details). The overriding requirement in constructing the ERCSC is source reliability and not completeness.

The ERCSC also includes a sample of clusters detected through the Sunyaev-Zeldovich (SZ) effect and a catalogue of cold, molecular cloud cores with far-infrared colour temperatures cooler than the ambient temperature ( $\sim 18$  K) dust in our Galaxy. No polarisation information is provided for the sources at this time. One of the primary goals of the ERCSC is to provide an early catalogue of sources for follow-up observations with existing facilities.

The sources of noise vary significantly as a function of location on the sky as well as a function of frequency. Apart from the instrumental noise and emission from the Galaxy, at the lowest frequencies the dominant astrophysical source of noise is the CMB itself. At the highest frequencies, zodiacal dust and emission from the interstellar medium dominate. As a result, the flux density limits corresponding to the same reliability vary widely across the sky, with the sensitivity typically improving with increasing ecliptic latitude.

Table 2.2 shows the fraction of sky coverage, the beam FWHM and the sensitivity of the ERCSC after all cuts have been applied. Although the  $10\sigma$  values are quoted, sources which are up to a factor of  $\sim 2$  fainter and located in regions of low sky background are included in the ERCSC since they meet the high reliability criterion. As an illustration, Figure 2.7 shows the flux density limit of *Planck* both in the Galactic Plane ( $|b| < 10^\circ$ ) and at high Galactic latitude ( $|b| > 30^\circ$ ) relative to other wide area

### 2.3 The Early Release Compact Source Catalog (ERCSC)

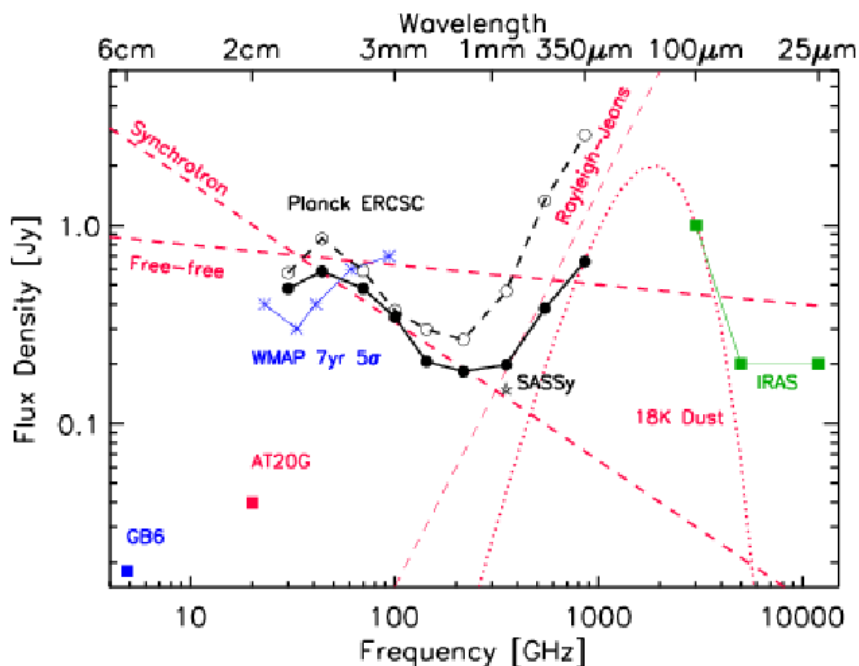


**Figure 2.7:** The *Planck* ERCSC flux density limit quantified as the faintest ERCSC source at  $|b| < 10^\circ$  (dashed black line) and at  $|b| > 30^\circ$  (solid black line) is shown relative to other wide area surveys. Also shown are the spectra of known sources of foreground emission as red lines; these include a  $F_\nu \sim \nu^{-0.7}$  synchrotron component,  $\nu^{-0.1}$  free-free component, a Rayleigh-Jeans component and a  $\nu^2$  emissivity of temperature 18 K. The ERCSC sensitivity is worse in the Galactic Plane due to the strong contribution of ISM emission especially at sub-millimetre wavelengths. In the radio regime, the effect is smaller. The faintest *WMAP* 7 year  $5\sigma$  sources are derived from the catalogue of [Gold et al. \(2011\)](#). Although the flux density limits of *WMAP* and *Planck* appear to be comparable at the lowest frequencies, the *Planck* ERCSC is more complete. The GB6 sensitivity value is from [Gregory et al. \(1996\)](#), the AT20G flux limit is from [Murphy et al. \(2010\)](#), the SCUBA-2 All Sky Survey (SASSy) limit is from the Joint Astronomy Centre website while the IRAS flux density limits are from the IRAS explanatory supplement ([Beichman et al., 1988](#)). From [Planck Collaboration \(2011b\)](#).

## 2. THE *PLANCK* VIEW OF EXTRAGALACTIC SOURCES

---

**Table 2.2:** *Planck* ERCSC characteristics. The tables gives, for each channel, both the nominal frequency and wavelength, the sky coverage, the total number of sources and the number of sources with Galactic latitude  $|b| < 30^\circ$ , the median flux density of the  $> 10\sigma$  sources at  $|b| > 30^\circ$  (where  $\sigma$  is the photometric uncertainty of the source), the flux density of the faintest  $> 10\sigma$  source at  $|b| > 30^\circ$ , and the flux density of the faintest source at  $|b| > 30^\circ$  (flux density limit) are also given.

Freq [GHz]	30	44	70	100	143	217	353	545	857
$\lambda[\mu m]$	10000	6818	4286	3000	2098	1382	850	550	350
Sky Coverage [%]	99.96	99.98	99.99	99.97	99.82	99.88	99.88	99.80	99.79
# of sources	705	452	599	1381	1764	5470	6984	7223	8988
# of $ b  > 30^\circ$ Sources	307	143	1576	332	420	691	1123	2535	4513
$10\sigma$ median [mJy]	1173	2286	2250	1061	750	807	1613	2074	2961
$10\sigma$ faintest [mJy]	487	1023	6736	500	328	280	249	471	813
Flux Density Limit [mJy]	480	585	481	344	206	183	198	381	655

surveys at comparable frequencies. Also shown are the spectrum of typical sources of foreground emission.

### 2.4 Extragalactic Radio Sources at *Planck* Frequencies

The primary emission mechanism in virtually all radio sources is synchrotron emission from relativistic electrons spiralling around magnetic fields in the source. If the electrons have a power law spectrum, with  $N(E) \propto E^{-p}$ , the synchrotron spectrum is also a power law with  $S \propto \nu^\alpha$  and  $\alpha = (1 - p)/2$ . For many, but not all, radio sources,  $-1.0 \lesssim \alpha \lesssim -0.5$ ; sources with  $\alpha > -0.5$  are referred to as flat spectrum sources, and those with  $\alpha > 0$  are referred to as inverted spectrum sources.

The observed spectra of radio sources frequently depart from simple power laws with fixed  $\alpha$ . One cause of a break  $\Delta\alpha$  in the spectral index is the steepening of the electron power law index  $p$  by 1.0 or more due to ageing: the higher the energy of an electron, the less time it takes to radiate a given fraction of that energy. Since high frequency synchrotron emission is dominated by the high energy electrons, the effect of ageing is to steepen the radio spectrum at high frequencies. Conversely, very young radio sources may have flatter than average radio spectra.

Another potential cause of curvature in the SEDs of radio sources is opacity: as the optical depth rises, the source spectra invert, with  $2 \leq \alpha \leq 2.5$  for fully opaque sources. The result is a peak in the SED at roughly the frequency where the optical

## 2.4 Extragalactic Radio Sources at *Planck* Frequencies

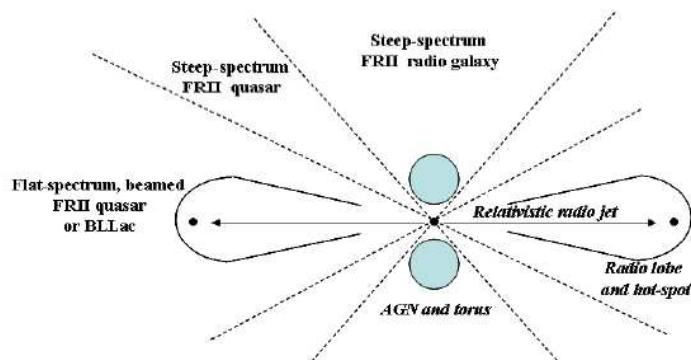


Figure 2.8: The unified model of radio sources (de Zotti et al., 2010).

depth reaches unity. The frequency at which this spectral peak occurs depends on both the physical parameters of the emitting/absorbing region and its age; younger, more compact sources display this spectral turnover at higher frequencies.

Synchrotron radiation is intrinsically highly polarized. Yet most radio sources observed at MHz or GHz frequencies are not. The lack of polarization may be due to random alignment of the magnetic fields in the source, or to Faraday depolarization of the emergent radiation. The latter effect is frequency dependent (the rotation measure RM varies as  $\nu^{-2}$ ). At *Planck* frequencies, Faraday depolarization will generally be small, so we will be able to measure the Faraday depth as well as to determine the intrinsic polarization of sources.

The so-called unification model of radio sources permits us to explain a wide variety of extragalactic discrete sources with a common scheme: an active galactic nucleus (AGN) with a black hole, an accretion disk around it, and axial jets, see Figure 2.8 (de Zotti et al., 2010). Many apparent differences between quasars, double-lobed radio sources, and other classes of radio source are then determined by the orientation of the line of sight to the jet axis. There is, first, Doppler boosting of photon energies along the jet axis. A bright blazar with strong variability is seen if the jet is viewed head-on, and a milder AGN with less dramatic features if the jet is viewed at a larger angle. Second, the appearance of the source may depend dramatically on the viewing angle at larger angles if the core is obscured by a dusty torus (Antonucci and Miller, 1985). The radio jets emit synchrotron radiation, and shocks moving in the jet create the typical flat spectrum of AGNs. At higher energies, the inverse Compton mechanism is at work. External photons (from, e.g., the accretion disk or clouds in the broad line region) or

## 2. THE *PLANCK* VIEW OF EXTRAGALACTIC SOURCES

---

synchrotron photons from the jet itself are scattered to higher energies by relativistic electrons in the jets, producing gamma-ray emission. The spectra of such sources have two similar peaks, the synchrotron peak at millimetre-to-optical frequencies and the inverse Compton peak at higher energies. It is clear that orientation to the line of sight cannot explain all apparent differences between classes of radio sources, nor should it be expected to. Intrinsic physical differences, including a variation of isotropic radio luminosity over at least five or six orders of magnitude, are known to exist as well. However, to disentangle the effects of orientation from those of physical differences, extreme cases provide an important diagnostic, and *Planck* is well suited to characterise extreme cases for its detection capabilities and frequency coverage.

### 2.4.1 Peaked Spectrum Sources

The GHz-Peaked Spectrum (GPS) sources are powerful ( $\log P_{1.4GHz} \geq 25 W Hz^{-1}$ ), compact ( $\lesssim 1 kpc$ ) radio sources with a convex spectrum peaking at GHz frequencies (O’Dea, 1998). The GPS phenomenon was originally thought to be associated with compact, putatively very young radio sources (O’Dea, 1998), and in fact many examples for this association have been found (Conway, 2002). Recent research, however, has shown that a large fraction of GHz peaked sources are not of this type, but associated with compact, beamed jet sources, commonly identified as blazars. Although these two classes produce slightly different spectral types (the former shows a rather narrow peak, while the latter seems to be rather broadly peaked), to date the only secure method to distinguish between them is VLBI observations, revealing the source morphology (Vollmer et al., 2008).

Some sources have been erroneously classified as GPS on the basis of multi-frequency observations made at different epochs. If a source happens to be flaring when a high frequency measurement is made, it can appear to have a GHz peak. For this reason *Planck* and ground based simultaneous multi-frequency measurements allow a straightforward, unambiguous characterisation of GPS sources.

#### 2.4.1.1 Compact Symmetric Objects

Compact Symmetric Objects (CSO) are thought to be either very young or very recently activated radio galaxies (Owsianik and Conway, 1998). Mapped with VLBI resolution, these sources show a typical, symmetric radio-double morphology, but with

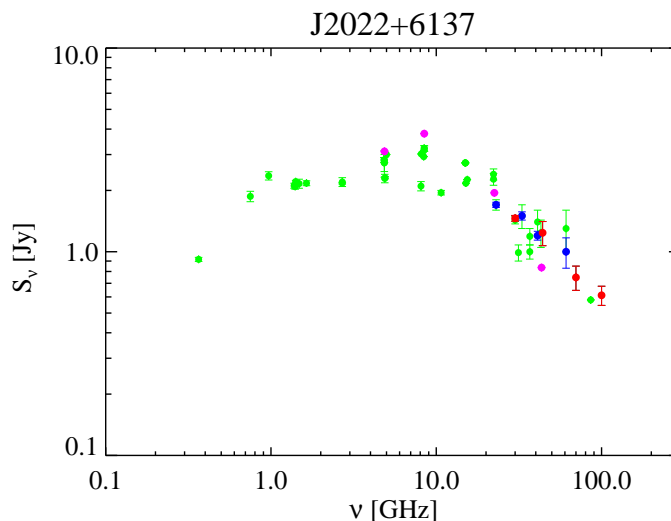


**Figure 2.9:** SED of a known CSO source, J2022+6137. *Planck* measurements are shown in red, *WMAP*-7yr flux densities in blue, new VLA measurements in pink, and archival data obtained from NED in green (Planck Collaboration, 2011d).

linear extensions of 1 kpc or less. They produce GPS type spectra by essentially single-zone synchrotron emission with synchrotron self-absorption causing a spectral turn-over at up to  $\nu > 1$  GHz (O’Dea, 1998). Unlike blazars, their emission is most likely not Doppler boosted, and they show no hint of fast variability, although their interpretation as young radio galaxies suggests that a spectral evolution over time scales of decades may be possible. There is also a well-established connection between the peak frequency of a CSO-type GPS source and its linear extent:  $\nu_b \simeq 0.62(d/\text{kpc})^{-0.65}$  GHz (O’Dea and Baum, 1997). Thus sources with peak frequencies in the *Planck* regime would point to objects of a few parsecs in linear size. Previously, populations of sources peaking above an observed frequency of 10 GHz (in the observer’s frame) might have been strongly under-represented because they are relatively faint at the low frequencies where most large surveys have been made. *Planck* opens the possibility of detecting such extreme GPS sources, or high frequency peakers in the nomenclature of Dallacasa et al. (2000). In addition, *Planck* allows the examination of the spectral decline of GPS sources at frequencies far above the peak frequency where optically thin synchrotron radiation is thought to dominate the emission. In Figure 2.9 (Planck Collaboration, 2011d), we show the spectrum of a known CSO source, J2022+6137 (B2021+614 from

## 2. THE *PLANCK* VIEW OF EXTRAGALACTIC SOURCES

---

Conway, 2002). *Planck* data have been combined with archival data as CSO sources are not expected to be variable.

### 2.4.1.2 Broad Peaked Radio Sources

As already mentioned, the alternative, and according to current observations more widespread, population of GHz peaked sources are radio sources with dominant compact jet emission, usually identified with blazars. At VLBI resolution, they generally appear as one-sided, compact, jet-like objects. The most likely explanation for the very flat, sometimes inverted, radio spectra of these sources is the overlay of synchrotron-self absorbed emission in a continuous jet (Marscher, 1977; Marscher and Gear, 1985). We may note at this point that the application of this mechanism to a standard Blandford-Konigl plasma jet (Blandford and Konigl, 1979) yields an optically thick spectral index for a simple blob along the jet  $\alpha \approx 0.5 - 1.0$ , depending on the electron spectral index and on the spatial profile of the magnetic field intensity (Marscher and Gear, 1985). The combination of the emission from different components, peaking at different frequencies, tends to flatten the overall spectrum.

Most of these objects are known to be strongly variable, on time scales down to one day (usually on week-month scale in the millimetre-regime, however). Variability and one-sided VLBI morphology give strong arguments in favour of beaming, i.e., the emission is strongly Doppler boosted, making the measured flux of the source at a given frequency depend on the Doppler factor. Therefore, small changes in the Doppler boosting can lead to strong variability, which would be expected to be achromatic, i.e., leaving the spectral shape unchanged. This can be distinguished from variability due to distortions in the jet, which is expected to be emphasized in a specific frequency range.

Figure 2.10 (Planck Collaboration, 2011d) shows two examples of sources of this kind: J1800+7828 shows a rather typical GHz-peaked blazar spectrum, with  $\alpha \approx 0.3$  below the break frequency at about 10 GHz, and steepening to  $\alpha \approx -0.17$  for  $\nu \leq 100$  GHz, with a further break to  $\alpha \approx -0.5$  at still higher frequencies. The more dome-like spectrum of J0423-0120, with  $\alpha \approx 1$  at lower frequencies, points to a more uniform component producing the radiation. Supporting, ground-based radio data from Effelsberg, Metsahovi and the VLA further suggest significant, achromatic variability

## 2.4 Extragalactic Radio Sources at *Planck* Frequencies

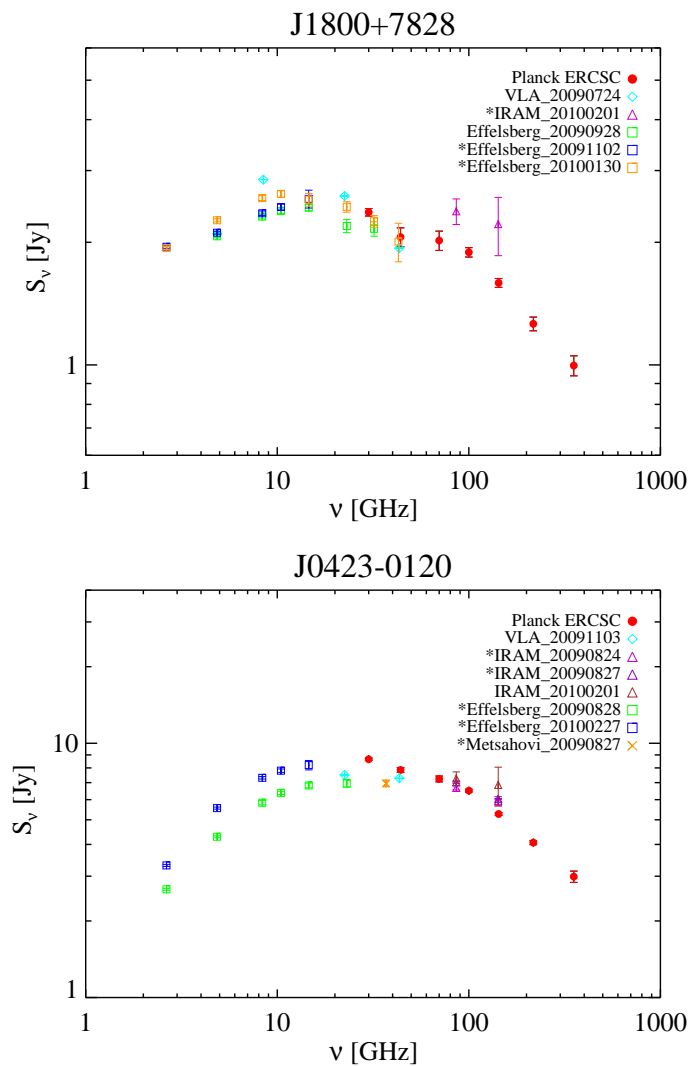


**Figure 2.10:** VLA, Metsahovi, IRAM, Effelsberg and *Planck* measurements of two known GHz-peaked blazars: J1800+782 (upper panel), and J0423-0120 (bottom panel). While the former shows only small signs of variability, the latter is clearly variable while preserving its spectral shape, pointing to helical or pressing jet. Asterisks identify epochs within 10 days from *Planck* observations at any of the LFI channels. For both sources, the *Planck* ERCSC data are a superposition of two scans separated by 3 and 6 months, respectively (Planck Collaboration, 2011d).

## 2. THE *PLANCK* VIEW OF EXTRAGALACTIC SOURCES

---

for this source, as would be expected from changes of the Doppler boosting in a jet. The high frequency spectrum has the same characteristics as J1800+7828.

### 2.4.2 Flat and Multicomponent Spectrum Sources

In the *Planck* Early Release Compact Source Catalog (ERCSC) a large number of sources with extended, flat, power law spectra has been found. There are also several sources with prominently zig-zag or bumpy spectra. In some cases the variation in flux density from one *Planck* band to the next was several times the associated errors. This could be caused by the superposition of emission from several components, as is probably the case in Figure 2.11 (Planck Collaboration, 2011d). However, it is important to recall that *Planck* multi-frequency observations were not exactly simultaneous. A source could sweep through the *Planck* beams at one frequency days before doing so at a neighbouring frequency (depending on position, it takes 7-10 days for a source to drift entirely across the focal plane). Hence fast variability on time-scales of days can contribute to irregularities in *Planck* spectra.

Spectra resulting from superposed radiation of at least two components have become the standard model to explain flaring blazars; this is known as a shock-in-jet model (Marscher and Gear, 1985). One component, the jet, produces a flat ( $\alpha \sim 0$ ) spectrum up to some break frequency, mostly between  $\sim 10$  and  $\sim 100$  GHz, above which the spectrum steepens to a typical index  $\alpha \sim -0.7$ . The second component, associated with an evolving shock, produces a self-absorbed synchrotron spectrum with a turnover frequency  $\sim 100$  GHz. Below this turnover frequency, the spectrum is strongly inverted. As the shock evolves, the turnover frequency and the flux of the shock component changes, and in some phases a detectable contribution of this component may not be present at all.

It should be noted that *Planck* allows us not only to make essentially simultaneous measurements of a given source in all frequency channels, thus providing single-epoch spectra (a true measure of the SED, unaffected by variability), but it also allows us to monitor variability frequency by frequency, since it is expected to perform at least four full sky surveys. It is therefore a powerful tool to distinguish variable from permanent spectral features, providing information on the size and evolution of extreme radio sources. For example, the flux is expected to vary coherently at all frequencies for GPS sources (Snellen et al., 1995). In contrast, the variability amplitude of flat-spectrum

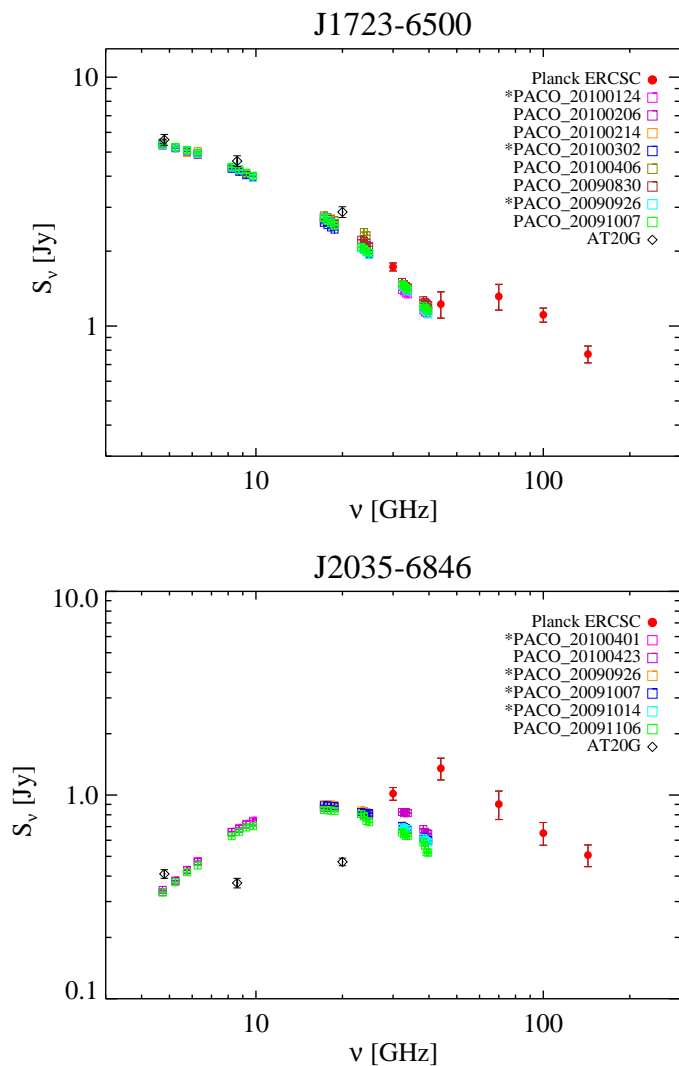


**Figure 2.11:** Two examples of clearly multi-component spectra. *Planck* measurements are shown by filled circles; AT20G data by open diamonds (Massardi et al., 2011b); PACO data, with their dense sampling in frequency space, are shown by open squares (Bonavera et al., 2011; Massardi et al., 2011a). Asterisks identify epochs within 10 days from *Planck* observations. The multi-valued spectra in J2035-6846 are a clear sign that this source is variable on time scales less than two weeks (see text) (Planck Collaboration, 2011d).

## 2. THE *PLANCK* VIEW OF EXTRAGALACTIC SOURCES

---

sources is generally found to increase with frequency, consistent with the fact that their SEDs are combinations of different components peaking at different frequencies, with the highest frequency components located closest to the nucleus and most compact.

### 2.4.3 Upturning Spectrum Sources

In many radio sources, synchrotron emission is dominated at high frequencies by re-emission from warm dust. Essentially no extragalactic *Planck* sources show this pattern at frequencies below 143 GHz. Of all the sources at  $|b| > 30^\circ$  that have *Planck* measurements at 30 to 217 GHz, only eleven show evidence of a significant increase of flux density even from 143 GHz to 217 GHz; three of them are shown in Figure 2.12 (Planck Collaboration, 2011d). The lack of upturn-spectrum sources in the ERCSC suggests that most of the sources detected by *Planck* are flat spectrum sources like blazars, with high enough synchrotron luminosity to swamp dust re-emission even up to 217 GHz.

The potential danger of apparently upturning spectra being produced by source confusion at high frequency should be stressed. At 545 and 857 GHz, in particular, the ERCSC catalogues are much richer, and these frequencies are in the Rayleigh-Jeans part of the spectra for most IR sources. The apparently upturning spectra may result from confusion of a radio source disappearing in the background with an IR source appearing within the positional error resulting from the large beam of *Planck*.

## 2.5 Radio Sources in the ERCSC

The ERCSC contains hundreds of extragalactic radio sources, many with an SED extending to frequencies of 143 GHz or higher. At frequencies  $> 100$  GHz, the *Planck* surveys are unique. At 30 and 70 GHz, the higher sensitivity and resolution offered by *Planck* allow us to detect more sources in a single sky survey than in seven years of survey by the *WMAP* satellite (Gold et al., 2011).

One of the findings of the ERCSC is the absence of compelling evidence for any new class of extragalactic radio sources. At 30 to 70 GHz, more than 90% of the extragalactic sources were reliably associated with radio sources in other large area surveys conducted at 8-20 GHz (Planck Collaboration, 2011b). Still others have plausible identifications in lower frequency radio catalogues. Many of the identified radio sources are blazars, some of them clearly variable (see a detailed discussion in Planck Collaboration, 2011c).

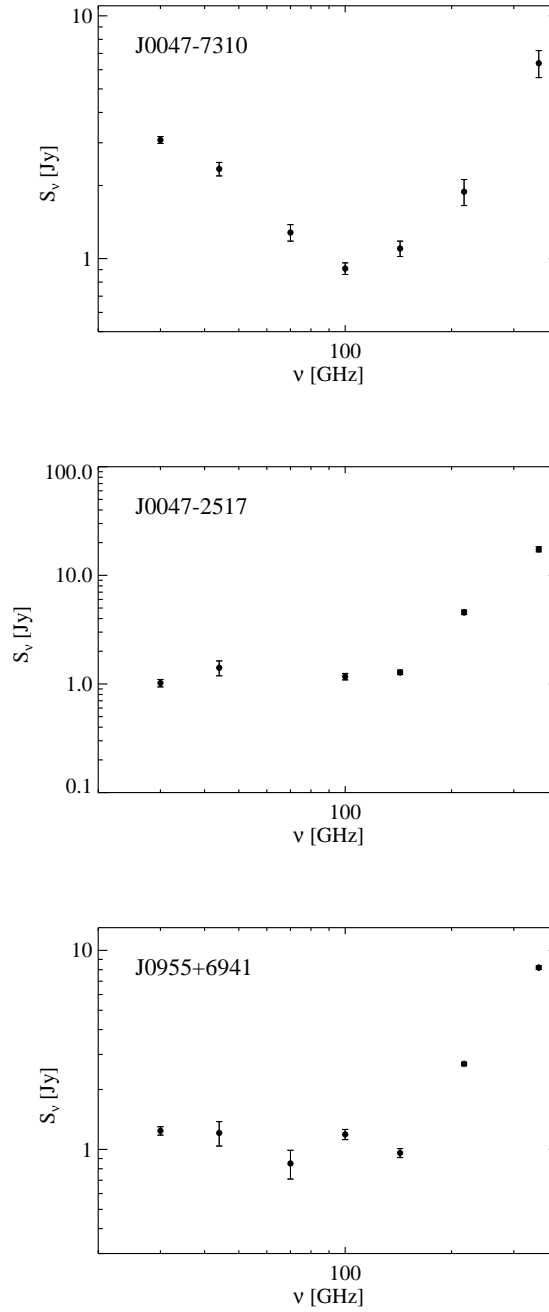


**Figure 2.12:** *Planck* sources with an upturn in the spectrum. Upper panel: J0047-7310 in the SMC. Central panel: *Planck* spectrum of a familiar star-forming system, NGC253. Bottom panel: The star-burst galaxy M82 ([Planck Collaboration, 2011d](#)).

## 2. THE *PLANCK* VIEW OF EXTRAGALACTIC SOURCES

---

A major finding from the analysis of ERCSC is that many bright radio sources have relatively flat ( $\alpha > -0.5$ ) radio spectra extending up to and sometimes beyond 143 GHz. The vast majority of the extragalactic sources detected at 100, 143 and 217 GHz are synchrotron-dominated radio sources and not dusty galaxies.

Since the data included in the ERCSC are taken from  $\sim 1.6$  full sky surveys, some sources have been covered twice with a time separation of  $\simeq 6$  months. It is thus important to keep in mind that the flux densities are averaged since this might affect the SEDs reconstruction. This is not, however, an issue when studying the statistical properties of extragalactic sources, offering the possibility to analyse them over a broad frequency range never fully explored by blind surveys and focusing in particular on the counts of extragalactic radio sources and on their spectral properties in the 30-217 GHz range.

### 2.5.1 Validation of the ERCSC

The validation process for the compact sources included in the *Planck* ERCSC was performed by two different teams, selected among members of the *Planck* Consortia: a Validation Team on radio sources (VTRS) and a Validation Team on far-IR sources. The two teams worked separately at first, but cross-checked their results in the second phase of the process. The processing steps and main outcomes are summarized in the Explanatory Supplement released with the ERCSC. For compact radio (i.e., synchrotron dominated) sources, the VTRS (see [Planck Collaboration, 2011d](#), for a more detailed discussion) has found that  $> 97\%$  of the ERCSC sources at 30 GHz have reliable counterparts in published catalogues at GHz frequencies (PMN: [Wright et al., 1996](#); GB6: [Gregory et al., 1996](#); NVSS: [Condon et al., 1998](#); SUMSS: [Mauch et al., 2003](#); AT20G: [Massardi et al., 2008](#); [Murphy et al., 2010](#)). Similar (although slightly lower) percentages were found for ERCSC sources detected at 44 and 70 GHz. At higher frequencies ( $\geq 100$  GHz) *Planck* detects an increasing fraction of dusty galaxies, undetected by low-frequency surveys. Therefore, the source reliability was confirmed by internal matches of sources detected in two neighbouring *Planck* frequency channels: i.e., 143 and 217 GHz, or 217 and 353 GHz, etc.. However, the validation of synchrotron-dominated sources is still relatively easy to perform, since all of them must be present in low-frequency catalogues.

The *WMAP* 7-year catalogue (Gold et al., 2011) contains a total of 471 sources detected in at least one frequency channel. Of these, 289, 281, 166 and 59 sources are detected as  $\geq 5\sigma$  peaks in the 33, 41, 61, and 94 GHz maps, respectively. The ERCSC catalogue includes 88%, 63%, 81%, and 95% of the  $5\sigma$  *WMAP* sources at 30, 44, 70, and 100 GHz, respectively. The median of the distribution of offsets between *WMAP* and *Planck* positions at each frequency are 2.5', 2.1', 1.7', and 1.0' at each frequency (see also Planck Collaboration, 2011d, for a more detailed discussion on this subject). Except for the 44 GHz channel, where *Planck* is known to be less sensitive, most *WMAP* sources that failed to be included in the *Planck* ERCSC (31 sources at 30 GHz) are generally at the faint end of the flux density distribution (i.e., near the detection threshold) and may have flux densities boosted by the Eddington bias or the effects of confusion, or may be spurious. The absence from the ERCSC of a few brighter *WMAP* sources (5 sources at 30 GHz) is probably caused by their variability.

Two main objective of the validation work of the ERCSC (Planck Collaboration, 2011b) are the accuracy of the identification of a source in the ERCSC and the consistency of the flux density scales. They must be ensured in order to construct SEDs that include measurements from both *Planck* and ground-based telescopes. The importance of these wide-range SEDs is extensively discussed in the next chapter.

### 2.5.2 Number Counts

Planck Collaboration (2011g) shows the normalized number counts of extragalactic radio sources at the six *Planck* frequencies from 30 to 217 GHz (see Figures 2.13 and 2.14). The sharp breaks in the number counts at approximately 1.0 Jy (30 GHz), 1.5 Jy (44 GHz), 1.1 Jy (70 GHz), 0.9 Jy (100 GHz), 0.5 Jy (143 GHz) and 0.4 Jy (217 GHz) signal the onset of incompleteness. The results of deeper surveys on small fractions of the sky and the *WMAP* differential number counts are also shown, for comparison. The agreement with *WMAP* data is very good. The differential counts at 30 and 70 GHz are somewhat deeper than the *WMAP* ones at 33 and 61 GHz, while at 44 GHz they are somewhat shallower than the ones calculated for the 41 GHz *WMAP* channel. Above the completeness limits they appear to join smoothly with those from deeper surveys. At frequencies of up to 100 GHz, the predictions of the de Zotti et al. (2005) cosmological evolution model, relying on extrapolations from lower frequency data and capable of providing a very good fit to almost all data on number counts as well as

## 2. THE *PLANCK* VIEW OF EXTRAGALACTIC SOURCES

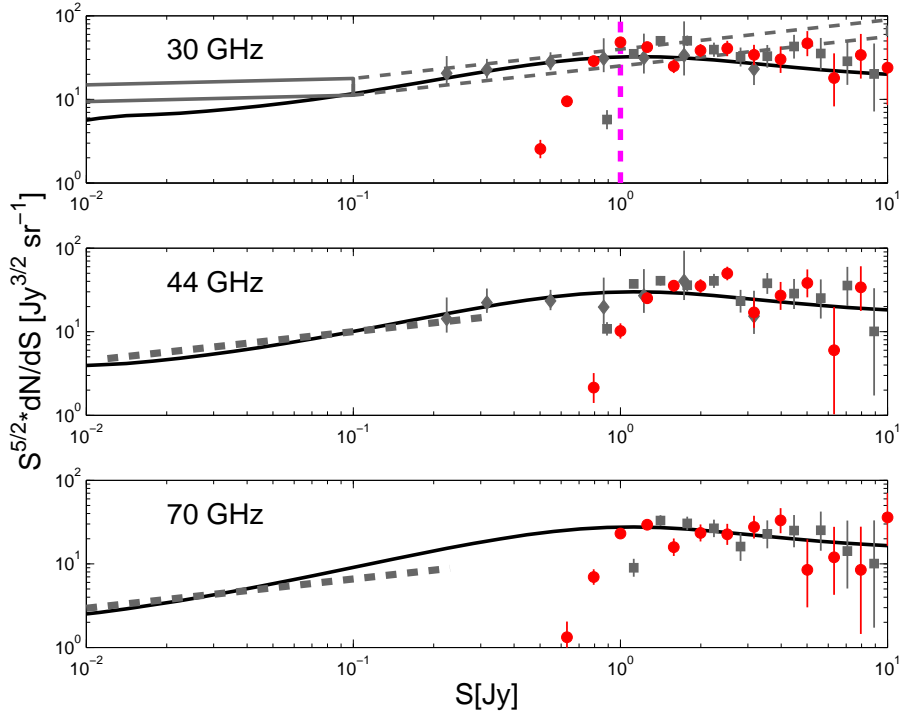


**Figure 2.13:** Euclidean normalized differential number counts at the LFI frequencies. The red circles with Poisson error bars show the counts of sources with counterparts in the reference 30 GHz sample. In each panel, the solid curves show the total number counts of extragalactic radio sources predicted by the *de Zotti et al. (2005)* model. Also shown are: the counts estimated at 31 GHz from DASI (grey dashed box; *Kovac et al., 2002*) and at 33 GHz from the VSA data (grey box; *Cleary et al., 2005*); the counts from the PACO (grey diamonds; *Bonavera et al., 2011*) and the *WMAP* 5-yr surveys (grey squares; *Massardi et al., 2009*), at the closest frequencies, and the counts estimated by *Waldram et al. (2007)* (grey dashed line), exploiting multi-frequency follow-up observations of the 15 GHz 9C sources. The vertical dashed magenta line in the upper panel indicates the estimated flux density completeness limit, 1.0 Jy (*Planck Collaboration, 2011g*).

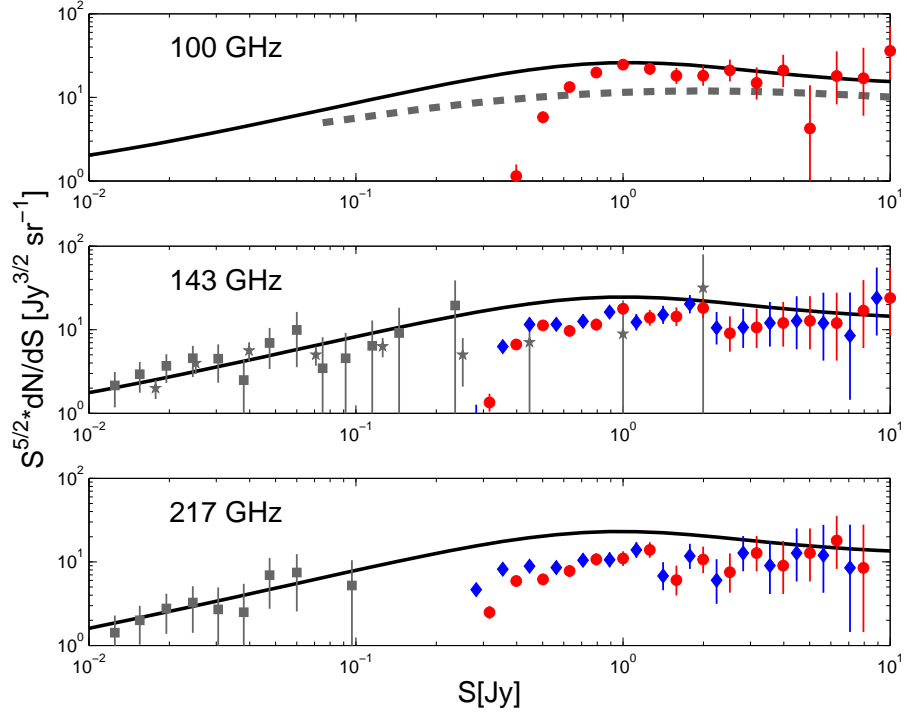


**Figure 2.14:** Euclidean normalized differential number counts at the HFI frequencies (100, 143, and 217 GHz). The red circles with Poisson error bars show the counts of sources with counterparts in the reference 30 GHz sample. At 143 and 217 GHz the blue diamonds (shifted to the left by half of the bin size, for clarity) show the counts obtained after removing sources with 143-217 GHz spectral index indicative of dust emission. Again, in each panel, the solid curves show the total number counts of extragalactic radio sources predicted by the [de Zotti et al. \(2005\)](#) evolution model (it should be noticed that the model fail at 100-1000 mJy). Also shown are the SPT (grey squares; [Vieira et al., 2010](#)) and ACT (grey stars; [Marriage et al., 2011](#)) counts of radio sources. At 100 GHz we also show the estimated counts by [Sadler et al. \(2008\)](#) from follow-up observations of a sample of sources selected from the 20 GHz ATCA survey (grey dashed line) ([Planck Collaboration, 2011g](#)).

## 2. THE *PLANCK* VIEW OF EXTRAGALACTIC SOURCES

---

on other statistics of radio sources at frequencies above 5 GHz, are generally in good agreement with the [Planck Collaboration \(2011g\)](#) findings. This result implies that no new radio source population shows up at bright flux densities. Very few extreme or inverted-spectrum compact radio sources are found in the *Planck* ERCSC. At higher frequencies (i.e., at 143 and 217 GHz) we also plot the number counts obtained by using the sample of radio sources selected at 143 and 217 with  $\alpha_{143}^{217} < 0.5$ , in order to avoid all possible sample contamination coming from a second population of sources dominated by thermal dust emission ( $\alpha_{143}^{217} > 1.0$ ). These number counts turn out to be in almost perfect agreement with the ones obtained from the sample selected at 30 GHz, with  $S \leq 1$  Jy.

Figure 2.14 shows that the [de Zotti et al. \(2005\)](#) model over-predicts the bright counts by a factor of about 2 at 143 GHz and about 2.6 at 217 GHz, while it is consistent with the fainter SPT ([Vieira et al., 2010](#)) and ACT ([Marriage et al., 2011](#)) counts. The discrepancy between the model and the current data is due to a steepening of the spectra of ERCSC sources above about 70 GHz, not predicted by the model but, at least partially, already suggested by other data sets (see Section 2.5.3). An implication of this result is that the contamination of the CMB angular power spectrum by extragalactic radio sources below the detection limit at 143 and 217 GHz is lower than predicted by the [de Zotti et al. \(2005\)](#) model. Since clustering effects are reduced to negligible values by the very broad luminosity function that strongly dilutes the clustering signal (e.g. [de Zotti et al., 2010](#); [Toffolatti et al., 2005](#)), the small scale fluctuation due to radio sources are dominated by the Poisson contribution (shot noise), whose power spectrum is independent of the multipole number. Its amplitude is given by:

$$C_l^{shot} = \int_0^{S_{cut}} S^2 \frac{dN}{dS} dS \quad (2.1)$$

where  $S$  is the source flux,  $dN/dS$  are the differential number counts and  $S_{cut}$  is the detection limit. The number counts can be directly measured or derived from evolution models of the relevant population of galaxies (dusty, star-forming and radio galaxies in our case). Taking into account the scaling factors listed above, the [de Zotti et al. \(2005\)](#) model yields the results listed in Table 2.3. The radio source contribution is sub-dominant, with respect to the one from dusty galaxies, at the frequencies ( $\geq 353$  GHz) relevant for Cosmic Infrared Background (CIB) anisotropy analysis ([Planck Collaboration, 2011a](#)).

**Table 2.3:** Flux cut from the ERCSC used in the 6 fields in which the CIBA power spectrum was estimated. The shot noise due to radio galaxies (both in  $Jy^2sr^{-1}$  and in  $\mu K_{CMB}^2$ ), appropriate for these cuts, is also shown. The computation is based on the radio galaxy evolution model by [de Zotti et al. \(2005\)](#). The values are given in two different units:  $Jy^2sr^{-1}$  and  $\mu K_{CMB}^2$ .

Frequency [GHz]	143	217	353	545	857
Flux cut [mJy]	245	160	325	540	710
shot noise [ $Jy^2sr^{-1}$ ]	7.1	4.0	<3.4	< 5.7	< 7.4
shot noise [ $\mu K_{CMB}^2$ ]	$5.2 \times 10^{-5}$	$1.7 \times 10^{-5}$	$4.1 \times 10^{-5}$	$< 1.7 \times 10^{-3}$	< 1.5

### 2.5.3 Spectral Index Distribution

[Planck Collaboration \(2011b\)](#) also show the distribution of spectral indices between adjacent bands for the sources at  $|b| > 30^\circ$  (see Figure 2.15). At the lower frequencies, the distribution of spectral indices is centred at  $\alpha = 0$  (flat spectrum sources). The spectral index distribution narrows between 30-100 GHz. At 143 and 217 GHz the radio source population continues to dominate although the infrared luminous galaxy population starts to become significant. It is also striking that even at 353 GHz, the radio source population continues to make a significant contribution. At the highest frequencies the sources show the behaviour expected from the Rayleigh-Jeans tail of dust emission.

[Planck Collaboration \(2011c\)](#) focused on a Northern sample of 104 extragalactic sources with extensive multi-frequency measurements simultaneous to *Planck* ones and studied the distributions of the spectral indices at low ( $\leq 70$  GHz) and high ( $> 70$  GHz) frequencies. They found that the low frequencies indices are fairly flat, with an average of -0.06. Their distribution is narrow, with 91% of the indices being in the range from -0.5 to 0.5. The high frequencies indices, computed on sources with at least three data points at HFI frequencies, are concentrated around -0.5, with an average value of -0.56. A large part of the high frequency index distribution is in the flat domain with  $\alpha_{HF} \geq -0.5$ .

[Planck Collaboration \(2011g\)](#) used the sample with  $S > 1$  Jy at 30 GHz to study the spectral properties of the extragalactic radio sources. They found a moderate steepening of spectral indices at higher frequencies (see Table 2.4). Hints in this direction were previously found by [González-Nuevo et al. \(2008\)](#) from their analysis of the NEWPS

## 2. THE *PLANCK* VIEW OF EXTRAGALACTIC SOURCES

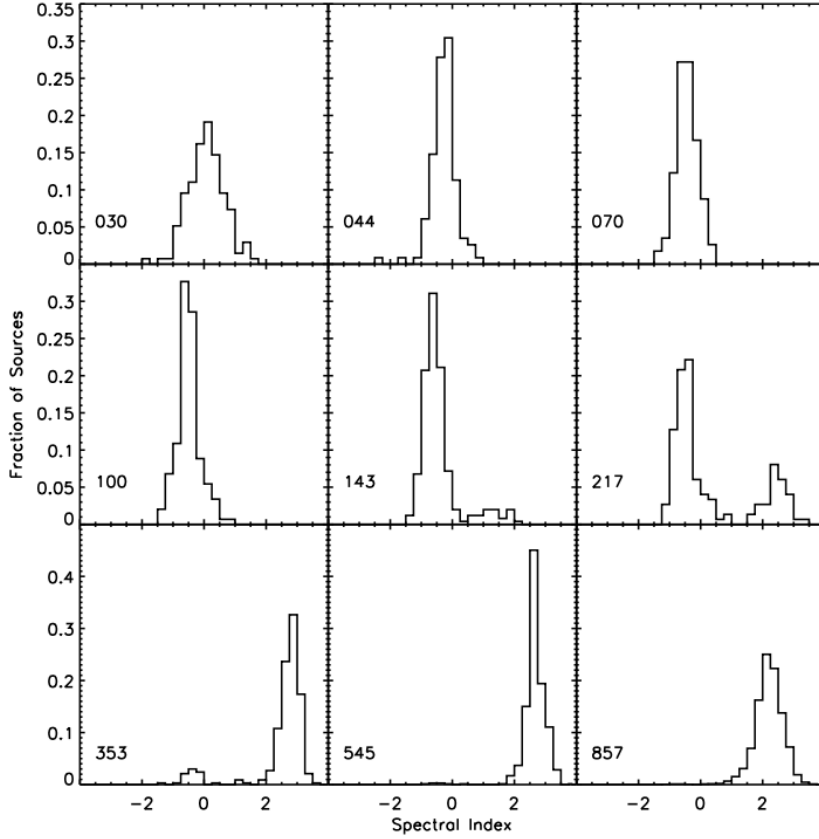


**Figure 2.15:** The distribution of spectral indices between adjacent *Planck* frequencies for sources above  $30^\circ$  of the Galactic Plane, likely to be dominated by extragalactic sources (Planck Collaboration, 2011b).

**Table 2.4:** Median and standard deviation of the spectral index distributions between 30 GHz and the selected frequency. We adopt the convention  $S_\nu \propto \nu^\alpha$ .

$\nu$ [GHz]	44	70	100	143	217
median	-0.06	-0.186	-0.28	-0.39	-0.37
error	0.01	0.01	0.01	0.01	0.01
$\sigma$	0.30	0.18	0.17	0.16	0.15

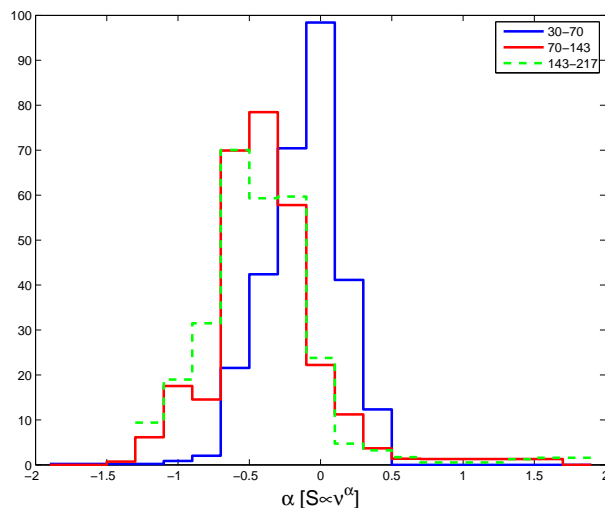


**Figure 2.16:** Spectral index distributions for different frequency intervals calculated by taking into account all sources selected at 30 GHz with  $S_\nu > 1$  Jy. There is clear evidence for a steepening above 70 GHz (Planck Collaboration, 2011g).

sample (López-Caniego et al., 2007) and also by Sadler et al. (2008). Planck Collaboration (2011g) found that the mean 30-100 GHz spectral index is close to the value  $\alpha \simeq -0.39$  found by Sadler et al. (2008) between 20 and 95 GHz, for a sample with 20 GHz flux density  $S > 150$  mJy. Moreover, the 30-143 GHz median spectral index is in very good agreement with the one found by Marriage et al. (2011) for their bright ( $S_\nu > 50$  mJy) 148 GHz-selected sample with complete cross-identifications from the AT20G, i.e.  $\alpha_{20}^{148} = -0.39 \pm 0.04$ . On the other hand, Vieira et al. (2010) find that their much fainter synchrotron emitting radio sources selected at 150 GHz are consistent with a flatter spectral behaviour (mean  $\alpha_5^{150} \simeq -0.1$ ) between 5 and 150 GHz. Massardi et al. (2011b) find mean spectral indices  $\alpha_5^{150} \simeq -0.17$  and  $\alpha_{20}^{150} \simeq -0.30$  for AT20G sources with 150 GHz flux density  $S > 50$  mJy. A flattening of the mean/median high-frequency spectral indices at flux densities fainter than the ones probed by the Planck ERCSC may help to account for the unusually flat normalized counts at 143 and 217 GHz. Planck Collaboration (2011g) also showed the distributions of spectral indices over different frequency intervals (see Figure 2.16). There is a clear shift toward steeper values above 70 GHz: the median values vary from  $\alpha_{30}^{70} = -0.18 \pm 0.01$  ( $\sigma = 0.18$ ) to  $\alpha_{70}^{143} = -0.52 \pm 0.01$  ( $\sigma = 0.22$ ). On the other hand, the distribution of spectral indices between 143 and 217 GHz is close to the one found for  $\alpha_{70}^{143}$  ( $\alpha_{143}^{217} = -0.46 \pm 0.01$ ;

## 2. THE *PLANCK* VIEW OF EXTRAGALACTIC SOURCES

---

$\sigma = 0.23$ ).

## Chapter 3

# Ground-based Observations

In planning the *Planck* mission, it was recognized that the science yield of *Planck* millimetre and FIR sky surveys would be increased if accompanying ground-based observations could be made. These include, but are not limited to, radio observations at frequencies below and overlapping *Planck* frequency bands, optical observations for source identification and both ground- and satellite-based X- and gamma-ray observations. The radio observations with ground-based telescopes were planned for those sources expected to be detected by *Planck*. They were performed at about the same time the sources pass through the *Planck* beam. The POFF software (Massardi and Burigana, 2010) was used to predict which sources would be seen by *Planck* at a given epoch. Obviously, only previously known sources can be observed in this way.

Because of the scanning strategy, described in Section 2.2.1, and the fact that, except for bright sources, the extraction of the flux densities of *Planck* sources is based on the analysis of frequency maps produced by optimally weighting the Time Ordered Data (TOD) in pixel space, observations are considered to be ‘simultaneous’ with *Planck* if performed within 10 days from the satellite observations at any of its frequencies (the same point in the sky is observed by all *Planck* channels within 7-10 days). This typical time sampling does not prevent the extraction of relevant variability information at least for the large majority of extragalactic sources, whose flux densities change appreciably on significantly longer time-scales.

In the Southern hemisphere, a substantial amount of time was obtained at the ATCA to make pre-emptive observations at a wide range of frequencies up to and overlapping with *Planck* ones. The PACO project (Massardi et al., 2011a) consists

### 3. GROUND-BASED OBSERVATIONS

---

of several-epoch observations of a compilation of sources selected from the AT20GHz survey (Murphy et al., 2010) with  $|b| > 5^\circ$ . Observations were made with the ATCA in the frequency range between 4.5 and 40 GHz at epochs close in time to the *Planck* observations over the interval July 2009 - August 2010. The PACO project includes complete flux density limited and spectrally selected samples over the whole Southern sky, described in Section 3.2.

In the Northern hemisphere, quasi-simultaneous cm/mm radio spectra for a large number of *Planck* blazars have been obtained within the framework of a Fermi-GST related monitoring program of  $\gamma$ -ray blazars (F-GAMMA program, Angelakis et al., 2008; Fuhrmann et al., 2007). Observations, made with the Effelsberg 100-m and IRAM 30-m telescopes, span the frequency range from 2.64 to 142 GHz. The Effelsberg measurements were conducted with receivers at 2.64, 4.85, 8.35, 10.45, 14.60, 23.05, 32.00 and 43.00 GHz. The IRAM30-m observations were carried out with the receivers operating at 86.2 and 142.3 GHz. Some more data also came from the Metsahovi 13.7-m radio telescope, in Finland. The measurements were made with the receiver centred at 36.8 GHz. Small amounts of time, scattered throughout the first 17 months of the *Planck* mission, were obtained at the Very Large Array (VLA) of the National Radio Astronomy Observatory (NRAO). Observations at the VLA began in late July 2009, slightly before the beginning of the *Planck* first sky survey and continued until the end of November 2010, with a gap between January and July 2010. The frequencies of observation are 4.86 GHz, 8.46 GHz, 22.46 GHz and 43.34 GHz. Finally, the SiMPIE project (Procopio et al., 2011), carried out with the Medicina 32-m single dish telescope, aims at observing at several frequencies and epochs, simultaneously with *Planck*, a sample of 263 objects. It is described in more details in Section 3.1.

## 3.1 The Simultaneous Medicina-*Planck* Experiment (SiMPIE)

### 3.1.1 The Sample

The selection is mostly based on the NEWPS catalogue (Massardi et al., 2008), based on WMAP data and therefore containing bright sources, likely to be detected by *Planck*.

Cross-matches of the Northern NEWPS sources with low-frequency wide-area surveys like the GB6 (Gregory et al., 1996) at 4.85 GHz or the NVSS (Condon et al.,

### 3.1 The Simultaneous Medicina-Planck Experiment (SiMPIE)

---

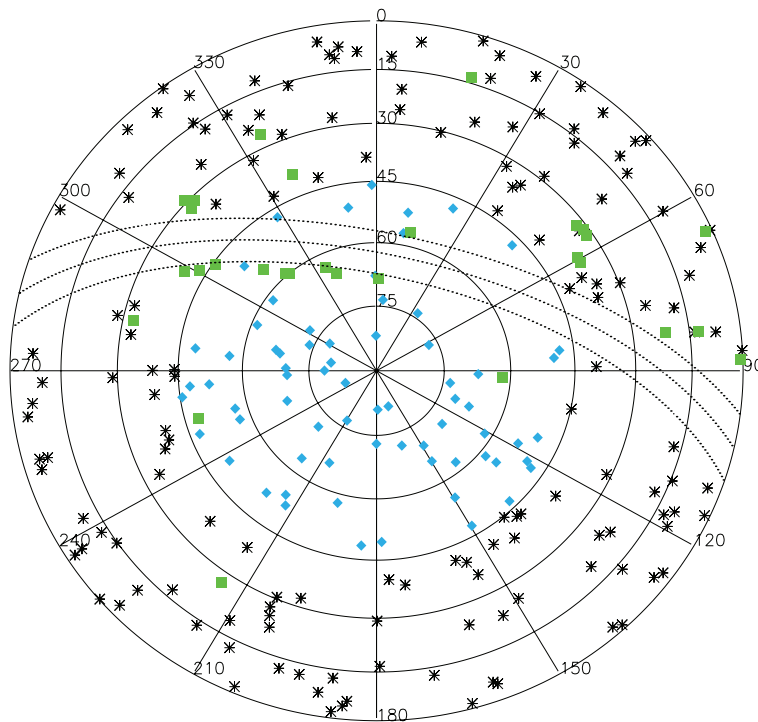


**Figure 3.1:** The SiMPIE sample: the Northern Sample (diamonds) covers the area with  $\delta > 45^\circ$ ; asterisks show the Southern Sample; squares indicate the central positions of the mapped sky patches (Procopio et al., 2011).

### 3. GROUND-BASED OBSERVATIONS

---

1998) at 1.4 GHz have identified candidate counterparts for 234 sources, 10 of which show multiple associations. According to the NASA Extragalactic Database (NED) 225 of them are classified as extragalactic objects and the remaining 9 as Galactic. 19 sources do not have counterparts in lower-frequency all-sky surveys with comparable flux densities and may be spurious.

Because of the large WMAP beam and, as a consequence, of the positional uncertainty of the NEWPS detections, in planning follow-up observations we have used the coordinates of the low frequency counterpart, where available, as target positions. In case of spurious sources or multiple associations we have chosen the WMAP positions as centres of regions that we have mapped at 5 GHz with the Medicina radio telescope in order to identify, in the case it was a compact radio source, the low-frequency counterpart of the WMAP detection. The SiMPIE observations will therefore help to assess precisely the reliability of the detection techniques that have been applied to the WMAP maps.

Comparisons of the NEWPS sample with the AT20G Bright Source Sample (Mas-sardi et al., 2008) data indicate that the NEWPS sample is almost 91% complete down to 1 Jy. The completeness of the sample refers to the epoch of the WMAP observations, and variability can alter it. However, the comparison with the coeval 30 GHz *Planck* observations, that reach somewhat fainter flux densities, will allow us to quantify the level of completeness of our sample at least at 22 GHz, once we properly account for the difference in frequency.

In summary, the SiMPIE sample contains 263 targets of which 253 are extracted from the NEWPS sample, the 10 sources not in the NEWPS catalogue are Galactic objects that may show strong outbursts during the *Planck* mission and are selected because of previously monitoring at the Noto observatory. Figure 3.1 shows the distribution on the Northern hemisphere of the observed sample. 79 objects have declination  $> 45^\circ$  and constitute the SiMPIE Northern sample.

#### 3.1.2 The observations

Observations of these objects began in 2009 with the Noto telescope at 43 GHz and continued at lower frequencies in Medicina, starting from June 2010. These observations covers at least 2 *Planck* surveys. The SiMPIE project obtained 33 observing runs in the period June 2010 - June 2011. Each run consists of up to 24 hours of observations. Only

### 3.1 The Simultaneous Medicina-Planck Experiment (SiMPIE)

**Table 3.1:** Observational details used to plan the cross scans; in each scan the time on-source is of about 2.5 s. The high system temperature of the 8.3 GHz receiver was due to malfunctions in the receiver cryogenic system.

Frequency	Beam size	Scan length	Scan speed	Usable bandwidth	Tsys	Instant rms
[GHz]	[ $\prime$ ]	[HPBW]	[ $\prime/min$ ]	[MHz]	[K]	[mJy]
5.0	7.5	5	180	2×80	30	74.1
8.3	4.8	5	120	2×230	80	132.7

one epoch was completely lost because of adverse weather conditions. In the first six months of the SiMPIE project no 22 GHz acquisitions could be achieved because of the insufficient sensitivity of the available K-band receiver. The temporary installation - for commissioning purposes - of a multi-feed 18-26 GHz receiver, whose final destination is the new Sardinia Radio Telescope, allowed us to carry out 22 GHz observations, together with new lower frequency ones, during the first semester of 2011. Details of the observations described in this thesis are reported in Table 3.1.

The scheduling procedure prioritised for each epoch the sources that were being observed by *Planck*, then the sources that in previous runs had been flagged out because of poor data quality, and, finally, all the other sources, in order to observe them as many times as possible.

Observations were carried out with the 32-m single dish of the Medicina radio telescope in the On-The-Fly (OTF) scan mode (Righini, 2008), exploiting both hardware devices and software tools recently developed. The number of cross-scans to be performed on each source was adjusted in real time during the observations, according to the actual system performances and weather conditions, in order to reach a SNR of at least 10 in the final integrated scans. This dynamical scheduling was possible thanks to an on-purpose-developed tool: the Positional On-the-flight-scan Planner (POP, Libardi et al., in prep.). As run-time execution of this tool completes in few seconds, POP allowed us to quickly produce new schedules whenever the weather and/or system conditions changed during an observing session. The only input required from the observer consists in the target coordinate list, the Local Sideral Time (LST) at which the schedule is supposed to be executed, the observing frequency and, optionally, the estimated flux density of the sources. POP schedules the sources after checking their visibility,

### 3. GROUND-BASED OBSERVATIONS

---

taking into account the telescope movement limits and duration in azimuth and elevation, sorting them in ascending RA, to minimise the slewing time between targets and maximise the number of observed targets during the allocated time. For each source POP calculates the minimum number of scans required to reach a noise level 10 times smaller than the 23 GHz WMAP flux density, provided in the input position list. If no flux density is provided, POP schedules for each target a number of scans equal to a user-defined value indicated in the software configuration settings; this is of use in case of bad weather conditions or instrumental failures when a longer integration time is needed.

#### 3.1.3 The data reduction

In optimal conditions for observations, each scan has the shape of the beam transfer function, i.e. a Gaussian with a FWHM corresponding to the beam size, overlapped with a baseline that corresponds to the off-source zero level of the signal. Along the scans, the fluctuations of amplitude are given by a Gaussian noise, dominated by instrument noise. However, cloudy weather, the presence of random contributions by Radio Frequency Interference (RFI) or digital noise heavily affected portions of the data, appearing as bumpy baselines or spike-like features. Hence, by fitting a Gaussian function and a linear baseline to the data it might be possible to assess the quality of each scan comparing the fitted value with the expected values and the overall goodness of the fit through a  $\chi^2$  analysis. A similar test allows one to get information about the Gaussian FWHM, the length of the baselines, the signal to noise ratio, the differences between the slopes of the two parts of the baseline (i.e. left and right with respect to the Gaussian). The broad variety of possible scan behaviours and the large number of parameters to be considered did not allow us to easily limit the parameter space.

The whole dataset was manually inspected to classify the scans according to their quality and to the features that affect them, if any is present. Hence, we have developed a tool that performs a Gaussian fit plus a linear baseline, showing it overlaid on the scan data (see Figure 3.2) as a reference for the visual inspection, to guarantee homogeneity to the flagging criteria. Bad weather conditions also reduce the signal-to-noise ratio (SNR), so that in the worst cases (i.e. faint sources with high noise level) the sources were completely embedded in the noise fluctuations. Averaging over several scans

### 3.1 The Simultaneous Medicina-Planck Experiment (SiMPIE)

---

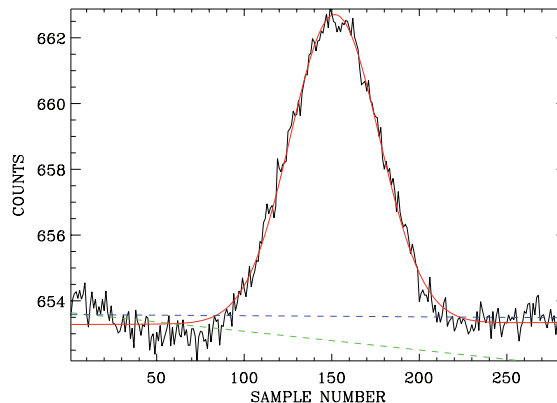


**Figure 3.2:** Fit of a sub-scan by a Gaussian (solid line) plus linear left and right baselines (dashed). From Procopio et al. (2011).

reduces the noise and amplifies the SNR; thus for these critical sources the analysis was performed also on the integrated scans.

The OTF Scan Calibration-Reduction (OSCaR) procedure was developed for the processing of calibrators and sources through the same tool. The procedures are developed in IDL language. A run of the entire pipeline does not require a large amount of memory or huge computational power: for about ten days of flagged data the complete process requires less than ten minutes. OSCaR was run after the manual inspection. The main steps of OSCaR are listed below:

- **The estimation of the factor to convert the counts to Jy units.** It is done by comparing the amplitude of Gaussian fits to the scans on calibrators to their known flux densities. The flux density/amplitude ratio is the counts-to-Jy factor valid for the observed elevation position. Then, whenever it is possible, we measure the flux density of other calibrators against the primary ones, exploiting the counts-to-Jy factors recovered on the primary calibrators. A time-line of the conversion factors is recovered along all the days of acquisitions.
- **The calculation of the source flux densities.** It is done by applying the correct counts-to-Jy factor, integrating the scans for a source, and fitting them with a Gaussian that reproduces the receiver response function. We obtain separate flux density estimates for the two acquisition channels and for each scan

### 3. GROUND-BASED OBSERVATIONS

---

direction. We firstly compute the flux density from the cross created by the integration of the RA-DEC scans in each channel, then through a weighted average we achieve a unique flux density for the considered source. Finally, each source is calibrated using a conversion factor recovered matching the acquisition epoch to the calibration time-line. In this way we ensure a short time distance between the observed source and the calibration factor, in order to minimise the possibility of weather or system variations.

- **The calculation of the source flux densities errors.** The error budget in the final flux density results from two main components: the calibration error  $S_{cal}$  and the noise error  $S_N$

$$\Delta S_{TOT} = \sqrt{\Delta S_{cal}^2 + \Delta S_N^2}. \quad (3.1)$$

The two terms have identical physical causes, although with different weights, and can be treated using a common formalism. The contribution to each component is given by:

$$\Delta S_i = \sqrt{\delta_{baseline}^2 + \delta_{Gauss}^2} \quad (3.2)$$

with  $i = cal, N$ . The baseline error ( $\delta_{baseline}$ ) is mainly due to the white instrumental and background noise and to the varying influence of the ground radiation, while the antenna is scanning at different angles. It has two spectral components: one showing a white spectrum (background, atmosphere, statistical uncertainty) and the other characterised by 1/f behaviour (long time drift of detectors and slow atmospheric changes between the telescope and the target). The ‘‘Gauss’’ error ( $\delta_{Gauss}$ ) represents the uncertainty on the amplitude of the Gaussian component of the fit. It can be ascribed either to white noise scatter effects affecting the whole scan or to local drops and spikes of the signal, mostly in correspondence of the tip. However, in most cases, the preliminary operation of data flagging is expected to have already prevented evident anomalies.

#### 3.1.4 The Northern Sample Catalogue

Procopio et al. (2011) presented the results for 79 sources at  $\delta \geq 45^\circ$  observed during the first six months of the SiMPLE project. The sample includes 69 NEWPS sources. In addition 10 regions around WMAP positions of candidate sources without low-frequency

---

## 3.2 The *Planck*-ATCA Co-eval Observations (PACO)

counterparts of comparable flux densities were mapped. Sources were detected at  $> 3\sigma$  in 5 out of the 10 regions mapped. Only 3 of these sources have detection significant at a  $\geq 5\sigma$  level. One of them was identified with HII region. On the whole 91% of NEWPS sources at  $\delta > 45^\circ$  were confirmed.

After the flagging and the removal of data points with signal-to-noise ratio lower than 5, 67 of the 69 NEWPS sources have reliable data at 5 GHz (the exceptions are # 179 and # 245 in the NEWPS catalogue for which all the data were flagged for bad weather conditions) and 59 sources have valid data also at 8 GHz in at least one epoch in the June-December runs.

## 3.2 The *Planck*-ATCA Co-eval Observations (PACO)

### 3.2.1 The Sample

The PACO sample is a combination of several sub-samples selected in order to maximize the scientific outcome in the allocated time. On the whole we have observed 482 AT20G extragalactic sources at Galactic latitude  $|b| > 5^\circ$  and outside a  $5^\circ$  radius circle centred at  $RA = 80.8939^\circ$ ,  $\delta = -69.7561^\circ$  (the LMC region). Of these, 344 sources form 3 partially overlapping complete sub-samples, selected for different purposes and organized as follows.

- The PACO faint sample, presented in [Bonavera et al. \(2011\)](#), is made of 162 sources with  $S_{20\text{GHz}} > 200$  mJy in the southern ecliptic pole region (ecliptic latitude  $< -75^\circ$ ) and with  $3\text{h} < RA < 9\text{h}$ ,  $\delta < -30^\circ$ . Near the ecliptic poles *Planck* scan circles intersect. Therefore the area is covered many times, and *Planck* sensitivity is maximal. Nevertheless, we expect that many sources in this sample will not be detected by *Planck*. On the other hand, Poisson fluctuations due to extragalactic sources below the detection limit, expected to be of 100-250 mJy in the range 100 – 353 GHz ([Leach et al., 2008](#)), are the main contaminant of *Planck* maps on angular scales smaller than  $20'$ - $30'$  at frequencies of up to  $\simeq 100$  GHz ([de Zotti et al., 1999](#); [Toffolatti et al., 1998, 1999](#)). It is therefore important to characterize as accurately as possible radio sources down to below the *Planck* detection limits at the time of *Planck* observations.

### 3. GROUND-BASED OBSERVATIONS

---

- The PACO spectrally-selected sample comprises the 69 sources with  $S_{20\text{GHz}} > 200$  mJy and spectra classified by [Massardi et al. \(2011b\)](#) as inverted or upturning in the frequency range 5-20 GHz, selected over the whole southern sky.
- The PACO bright sample presented in [Massardi et al. \(2011b\)](#), comprising the 189 sources with  $S_{20\text{GHz}} > 500$  mJy at  $\delta < -30^\circ$ .
- An additional sample (also partially overlapping with those defined above) is made of 63 bright southern blazars included in a long-term (up to 15 years) monitoring program at various frequencies with the Swedish-ESO Sub-millimetre Telescope (SEST, [Tornikoski et al., 1996](#)) and observed also with the LABOCA instrument on the APEX telescope. According to the source counts analysis, this sample seems to be 91 % complete down to the cut-off of 1 Jy at 90 GHz. These sources are of special interest because some of them may be flaring during the *Planck* mission. If this happens, the combination of *Planck* and ground-based observations will provide an unusually broad simultaneous frequency coverage of the flare.

The samples described above include 76 ATCA calibrators with 20 GHz flux density  $S_{20\text{GHz}} > 200$  mJy that showed more than 10% variability at this frequency in the last three years. Further 121 variable ATCA calibrators were added to the PACO sample, so that their total observed number is 197. Our data will also be included in the AT calibrator database.

Our observations allow us to characterize the source spectra in the range 5-40 GHz. *Planck* data may allow us to extend the spectral coverage up to 857 GHz, at least for the brightest flat-spectrum sources.

The classification as extragalactic objects and an indication of source extendedness up to 20 GHz were taken from the AT20G catalogue. AT20G positions were also used unless more precise coordinates were available, as is the case, e.g., for the AT calibrators whose positions are based on VLBI observations. A map of positions of sources in our sample is shown in Figure 3.3. As pointed out by [Massardi et al. \(2011b\)](#) the sample may still contain some Galactic sources, but they should be very few because the relatively high resolution 20 GHz observations preferentially select compact objects ( $< 30$  arcsec) and Galactic sources with  $|b| > 1.5^\circ$  are rarely that small, especially at bright flux density levels.

### 3.2 The *Planck*-ATCA Co-eval Observations (PACO)

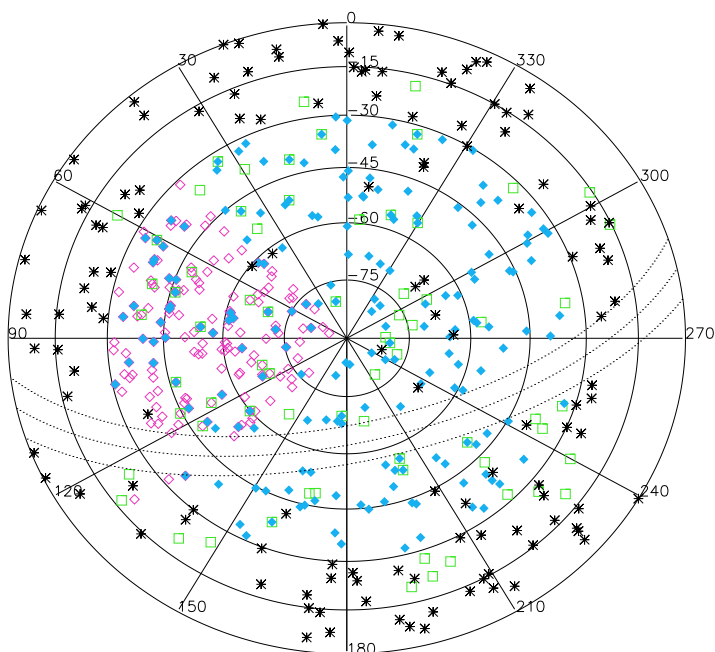


**Figure 3.3:** Polar projection of the Southern sky, showing the distribution of the PACO samples (RA=0 h is at the top and the RA increases counter-clockwise). The dotted lines indicate the Galactic plane and bound the area with Galactic latitude  $|b| < 5^\circ$ . Sources in these regions were excluded from the PACO samples. The PACO faint sample (open pink diamonds) occupies the area with  $3 < \text{RA} < 9$  h. The PACO bright sample (filled blue diamonds) covers the whole area at  $\delta < -30^\circ$ . The spectrally selected sample (green squares), the blazars and the Australia telescope calibrator sources (black asterisks) are spread over the whole southern sky. From [Massardi et al. \(2011a\)](#).

### 3. GROUND-BASED OBSERVATIONS

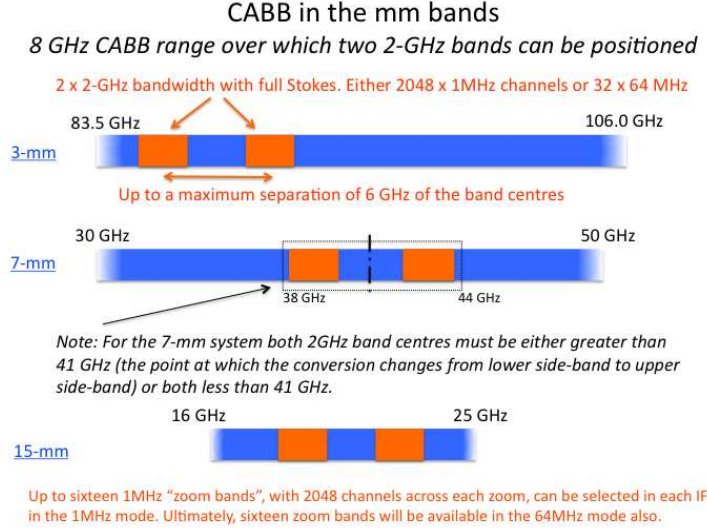


**Figure 3.4:** A schematic illustration of the CABB configurations in the ATCA receiver bands. The scheme is only for explanatory reasons, the channels in this figure are not the ones used in the PACO project. The blue bars correspond to the frequency coverage of each receiver band. The orange bars correspond to the CABB bands (2 GHz bandwidth). From [www.narrabri.atnf.csiro.au/observing/CABB.html](http://www.narrabri.atnf.csiro.au/observing/CABB.html)

#### 3.2.2 The Observations

The new ATCA CABB system allows  $2 \times 2$  GHz simultaneous bands in continuum (see Figure 3.4). Applied to the  $6 \times 22$  m antennas of the ATCA it gives a noise level reaching 0.5 mJy in 1 min on source in the 7 mm wavelength band. We chose to use the 7 mm receivers with bands centred at 33 and 39 GHz, to overlap the lower-frequency *Planck* channels, the 12 mm receiver with bands centred at 18 and 24 GHz to include the AT20G selection frequency, and we extended the SEDs to lower frequencies using the 3-6 cm receiver with bands at 5.5 and 9 GHz.

The AT20G catalogue is dominated by compact flat spectrum sources so the AT20G selection guarantees that most radio sources have small angular sizes so that the particular configuration of the ATCA is not crucial for flux density estimation. However we avoid observing equatorial sources at low frequency where the elongation of the beam can introduce spurious sources in the already bigger beam. Table 3.2 lists the characteristics of the array configurations that have been used in our observations.

### 3.2 The *Planck*-ATCA Co-eval Observations (PACO)

**Table 3.2:** Array configuration description: the first line of each row lists the array name and the stations for antennas 1 to 6 respectively; the second line lists the baseline lengths available for each configuration in metres, in ascending order.

1.5A	W100 W110 W147 W168 W196 W392
	153 321 429 566 719 750 888 1041 1316 1469 3000 3429 3750 4316 4469
1.5B	W111 W113 W163 W182 W195 W392
	31 199 291 490 765 796 1056 1087 1255 1286 3015 3214 3505 4270 4301
1.5D	W102 W109 W140 W182 W196 W392
	107 214 474 582 643 857 1117 1224 1332 1439 3000 3214 3857 4332 4439
750B	W98 W109 W113 W140 W148 W392
	61 122 168 230 413 474 536 597 643 765 3735 3857 4270 4332 4500
EW352	d W102 W104 W109 W112 W125 W392
	31 46 77 107 122 153 199 245 321 352 4087 4286 4332 4408 4439
H214	W98 W104 W113 N5 N14 W392
	82 92 132 138 138 144 240 217 230 247 4270 4378 4383 4408 4500
H168	W100 W104 W111 N7 N11 W392
	61 61 107 111 132 141 168 171 185 192 4301 4379 4381 4408 4469
H75	W104 W106 W109 N2 N5 W392
	31 31 43 46 46 55 77 77 82 89 4332 4378 4378 4378 4408

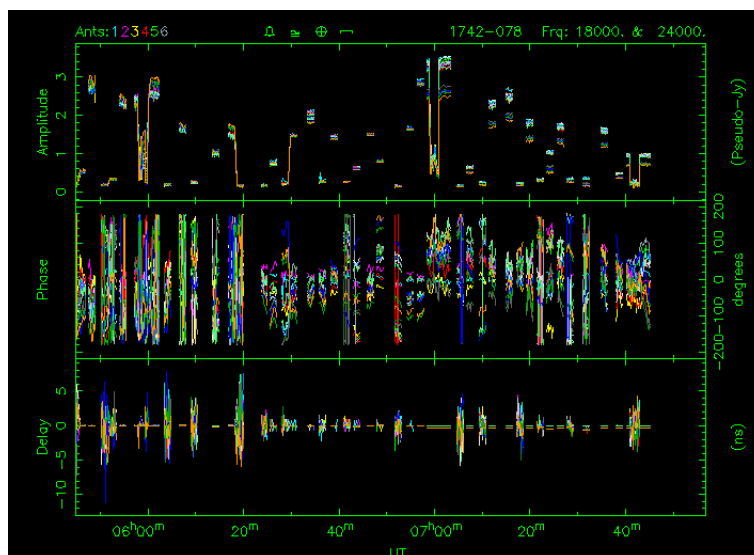


**Figure 3.5:** VIS display showing output during PACO observations.

### 3. GROUND-BASED OBSERVATIONS

---

Because of the risk of confusion with the highly elongated synthesized beam for sources with declination  $\delta > -10^\circ$ , they have not been observed at 3-6 cm. This is not a concern at shorter wavelengths where there is no confusion in the smaller primary beam. The observations were performed both remotely and on site. Figure 3.5 shows a screen-shot of the monitoring system while observations were running.

The scheduling process tries both to guarantee the simultaneity with the *Planck* observations following the satellite scanning strategy, and to minimize the slewing time, maximize the time on source and complete the measurements at the selected frequencies (i.e. including considerations about the weather, the array configuration in use and the minimization of the band switches).

The scheduling procedure is organized in the following phases:

- a run of the POFF code [Massardi and Burigana \(2010\)](#) on the sample identifies when each source will be observed by *Planck*;
- the code selects which sources may be observable by a given ATCA configuration at a given epoch of observation (i.e. LST range);
- the selected sub-sample for an observing epoch is divided according to their declination into a North and a South sub-sample (with respect to the zenithal position of the ATCA, i.e.  $-30^\circ$ ): this is necessary because of the wrapping limits of the antennas, minimizing the possibility to cross the limit, and thus sparing time of the antennas pirouettes to unwrap;
- the N and S sub-samples are sorted (and eventually splitted) according to the source hour angles;
- each hour angle-declination selected sub-sample is sorted to minimize the slewing time between sources;
- each hour angle-declination selected sub-sample is added into the schedule once for every frequency band at which should be observed (i.e. maximum 3 times); the order in which the various frequencies and sub-samples are observed is constrained by considerations about the presumed LST of observation, the configuration shadowing diagrams, the minimization of the frequency switches (it takes 2.5 min to move from 12 to 7 mm but only 10s from 3-6 cm to 12 mm).

## 3.2 The *Planck*-ATCA Co-eval Observations (PACO)

---

For each source (except the calibrators and Pictor A) we stay on source (`dwell` as type of observation) for 1.5 min. Despite every effort, the scheduling can predict only approximatively the duration of the run because the slewing time is seriously constrained by the LST at which the observation begins and by any unpredictable events which may affect the observations (e.g. failures, bad pointing to be repeated, longer calibration due to poor weather condition, ...).

### 3.2.3 The Calibrators

The calibration/set-up scheme during the observations is the following.

- A bright point source is chosen to make the set-up of the array for each frequency at the beginning of the observing run. Suitable sources are: 0537-441, 0823-500 (only at 3-6 cm), 1253-055 (only at 12 mm), 1921-293, 1934-638 (only at 3-6 cm), 2223-052.
- For each epoch and each frequency, a very bright compact object is used for bandpass calibration. Ideally it should be the brightest observed source and should be one of the sources in the previous list or any very bright point-like object. It should be observed for few minutes (in PACO observation it is observed at least for 5 minutes) at any stage of the observing run.
- PKS B1934-638 is the primary calibrator for all the frequencies. The spectral model for the primary calibrator that we have used in all the epochs is in Figure 3.6. Table 3.3 lists the model flux density values at the center of our observing frequency bands. At 7 mm we have sometimes observed Uranus and although it was always resolved at our longer baselines we could use the shorter baselines to transfer the calibration scale. By using the PKS 1934-638 flux densities to calibrate Uranus we note that there is a disagreement with the Uranus model by 18 and 16% at 33 and 39 GHz respectively. This is in agreement with what estimated on the basis of the on-going calibrator model update, as the absolute flux density scale at this frequency is still under investigation at both ATCA and VLA. Hence we applied these correction factors to all the 7 mm flux densities calibrated with the planet.

### 3. GROUND-BASED OBSERVATIONS

---

**Table 3.3:** The flux density values of the model for the primary calibrator PKS B1934-638 at the center of our observing frequency bands, as it is in the Miriad version we used.

Frequency [GHz]	Flux density [mJy]
5.5	4965
9.0	2701
18.0	1101
24.0	725
33.0	441
39.0	335

- No phase calibration is necessary because we are not interested in imaging. Thanks to the compactness and high signal to noise of most of the PACO sources neither imaging nor phase calibration is necessary. Since sources are self-calibrated we get good images when observing with hybrid arrays. We got a suitable flux density estimation from the visibilities using the triple-correlation techniques (see Section 3.2.6).
- A leakage calibrator selected among the polarized objects of the AT20G (a bright point-like unpolarized one should work as well) is observed at least 3 times at each frequency during each observing run, better if across the transit of the source. Suitable objects are: 0346-279, 0426-380, 0537-441, 1253-055, 1334-127, 1514-241, 1921-293.
- A  $S > 1Jy$  source is chosen as a pointing calibrator (this may constrain its position in the sorted sub-sample it belongs to) about once for every hour angle-declination block (at the beginning of it) at 12 mm, and more frequently at 7 mm (`update` type of pointing and `pointing` as type of observation); global solutions (`global` type of pointing and `dwell` as type of observation) for pointing are used at 3-6 cm. If pointing solutions look bad the pointing calibration is repeated.
- Each source at each frequency is observed for 1.5 min in a single pointing.

The project got  $\sim 460$  hours allocated over 65 epochs between July 2009 and August 2010 (i.e. during the time when *Planck* completed two all-sky surveys), of which 2

## 3.2 The *Planck*-ATCA Co-eval Observations (PACO)

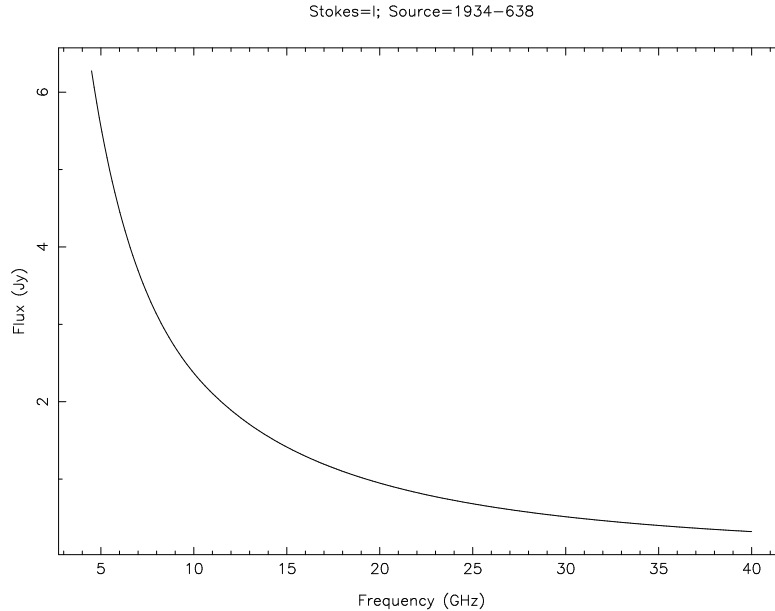


**Figure 3.6:** Model for PKS 1934-638 in the frequency range between 4.5 and 40 GHz, as it is in the Miriad version we used. From [Massardi et al. \(2011a\)](#).

epochs have been discarded for bad weather. Because of the high sensitivity in total intensity and the brightness of the sources in our sample we could observe on average 20 objects per run at all the 3 pairs of frequencies. Bad weather seriously affected some of the Austral summer epochs making it impossible to get the 7 mm data in a few runs. Table 3.4 summarizes the configurations, frequencies, and sky regions observed in each run.

### 3.2.4 The Data Reduction

Data reduction is performed by a C-shell coded pipeline which uses tasks from the MIRIAD software package ([Sault et al., 1995](#)) according to the scheme in Figure 3.7. As an example, Appendix A shows a script for running a general pipeline in the case in which PKS 1934-638 is both the bandpass and the primary calibrator, with the 3-6 cm receiver centred at 5.5 and 9 GHz.

#### 3.2.4.1 Loading the Raw Data

The data, initially in the RPFITS format, are converted in the MIRIAD format with the task ATLOD. Some options should be used at this stage in order to ease the subsequent

### 3. GROUND-BASED OBSERVATIONS

---

**Table 3.4:** The 63 good weather observational runs for the PACO project between July 2009 and August 2010.

Date	array	Allocated time [h]	Frequency Range	Date	array	Allocated time [h]	Frequency Range
2009-07-09	H75C	8.5	4.5-40 GHz	2010-02-07	6A	4.5	4.5-25 GHz
2009-07-10	H75C	5	17-40 GHz	2010-02-14	6A	9	4.5-25 GHz
2009-07-16	H75C	2	4.5-25 GHz	2010-02-28	750B	8.5	4.5-40 GHz
2009-07-18	H75C	1	32-40 GHz	2010-03-02	750B	4	4.5-25 GHz
2009-07-25	H75C	8	4.5-40 GHz	2010-03-06	H168	10	4.5-40 GHz
2009-07-26	H75C	7	4.5-40 GHz	2010-03-15	H168	8	4.5-40 GHz
2009-07-31	1.5A	7	4.5-40 GHz	2010-04-01	6A	12	4.5-40 GHz
2009-08-09	6D	6.5	4.5-40 GHz	2010-04-06	6A	4	4.5-25 GHz
2009-08-13	6D	8	4.5-40 GHz	2010-04-10	6A	5	4.5-40 GHz
2009-08-24	6D	2.5	17-40 GHz	2010-04-11	6A	6.5	4.5-40 GHz
2009-08-25	6D	3.5	17-40 GHz	2010-04-23	6A	7	4.5-40 GHz
2009-08-30	6D	6	4.5-40 GHz	2010-04-24	6A	7	4.5-40 GHz
2009-09-15	H214	8	4.5-40 GHz	2010-05-01	6A	4	4.5-40 GHz
2009-09-26	H75	14	4.5-40 GHz	2010-05-03	6A	4	4.5-40 GHz
2009-09-29	H75	4	4.5-40 GHz	2010-05-11	H214	4	4.5-40 GHz
2009-10-07	H75	6.5	4.5-40 GHz	2010-05-18	6C	7	4.5-40 GHz
2009-10-14	H168	10	4.5-40 GHz	2010-05-30	6C	12	4.5-40 GHz
2009-10-28	1.5B	4	4.5-40 GHz	2010-06-05	6C	7.5	4.5-40 GHz
2009-10-29	1.5B	4	4.5-40 GHz	2010-06-11	6C	4	4.5-40 GHz
2009-11-06	1.5B	14.5	4.5-40 GHz	2010-06-14	6C	12	4.5-40 GHz
2009-11-11	6B	4	4.5-40 GHz	2010-06-19	6C	14.5	4.5-40 GHz
2009-11-19	6B	11	4.5-40 GHz	2010-07-02	6C	4	4.5-40 GHz
2009-11-24	6B	4	4.5-40 GHz	2010-07-12	1.5D	5.5	4.5-40 GHz
2009-12-04	EW352	14	4.5-40 GHz	2010-07-16	EW352	5	4.5-40 GHz
2009-12-07	EW352	13	4.5-40 GHz	2010-07-31	H168	4	4.5-40 GHz
2009-12-17	6A	9.5	4.5-40 GHz	2010-08-10	H168	6	4.5-40 GHz
2009-12-29	6A	8	4.5-40 GHz	2010-08-13	H168	2	32-40 GHz
2010-01-03	6A	4.5	4.5-25 GHz	2010-08-14	H168	6.5	4.5-40 GHz
2010-01-17	6A	4	4.5-25 GHz	2010-08-15	H168	6.5	4.5-40 GHz
2010-01-24	6A	7	4.5-40 GHz	2010-08-20	H168	10	4.5-40 GHz
2010-01-27	6A	4	4.5-25 GHz	2010-08-21	H168	10	4.5-40 GHz
2010-02-06	6A	12	4.5-25 GHz				

## 3.2 The *Planck*-ATCA Co-eval Observations (PACO)

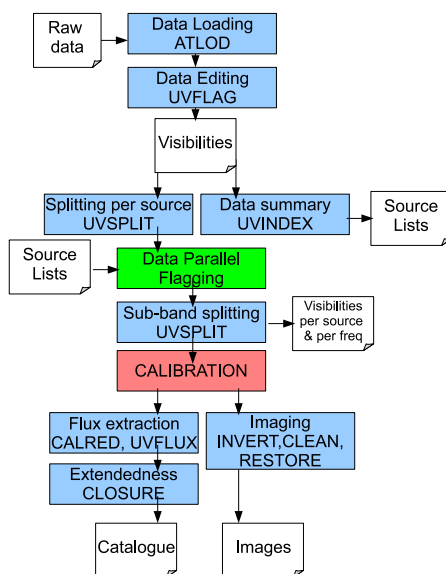


**Figure 3.7:** Data reduction pipeline diagram. Names in capital letters indicate the Miriad tasks used. From [Massardi et al. \(2011a\)](#).

reduction.

- The `birdie` option to flag, when loading CABB data, those channels that are affected by self-generated interference from the 640 MHz CABB clock.
- The `rfiflag` option to automatically flag out frequency bands that are known to be heavily affected by RFI.
- The `xycorr` option to correct the measured XY phase of the ATCA.
- The `noauto` option to flag the autocorrelations (i.e. correlations between two detector of the same antenna) since by default, CABB records them from each of the antennas that are being used. They are not useful since we are interested in the cross-correlations. In principle their presence is not a problem for the MIRIAD routines during the reduction, but can be source of confusion when examining the data.

### 3.2.4.2 Editing

The purpose of editing is to remove instrumental and atmospheric effects including radio interference or equipment malfunction. The weather was good for most of the

### 3. GROUND-BASED OBSERVATIONS

---

observing runs. Only in the last period the higher temperature may have affected the highest frequency channels, due to the presence of water vapour that decreases the sensitivity of the observations and atmospheric turbulence that causes decorrelation. Time intervals affected by bad weather or antenna misbehaving have to be flagged with the task UVFLAG.

Also data affected by shadowing have to be flagged. In an interferometer array the antennas may shadow each other when observing in particular regions if the antennas are close-by each other. If the measured visibilities are in a shadowed region, their amplitudes will be reduced and the phases are offset, resulting in an error in the position of the phase center and in the flux density estimation. Shadowing scheme for different array configurations are shown in Figure 3.8. The flagging for shadowing is done by the task UVFLAG with keyword `select=shadow(d)`, which selects data that would be shadowed by an antenna of diameter "d" meters (for PACO d=22 m).

After loading the data into a MIRIAD dataset, it is usually most convenient to split this into many sub-datasets, each containing an individual source at a single central frequency. This is done using the UVSPLIT task.

Even if the `birdie` and `rfiflag` options are given to ATLOD, it can happen that RFI and internal noise produce spikes in some of the frequency band channels or at some time during the observation period which have to be flagged. In particular, calibrator data must be as good as possible in order to avoid bad effects in the calibration of the whole data-set. Automatic procedures identify among the 2048 channels which constitute the 2.048 GHz bandwidth for each IF, those that exceed by  $5\sigma$  the mean value for each baseline for each source. Typically less than 1% of the band is flagged.

#### 3.2.4.3 Calibration

In the CABB era the ATCA calibration strategy has been refined to deal with wide bandwidth and to be as accurate as possible. The CABB system allows us to break up the 2 GHz CABB bandwidth into smaller chunks with the task UVSPLIT and the `maxwidth` parameter with which the bandwidth is specified (in GHz). In order to properly define the detailed source spectral behaviour we have split each 2 GHz band into  $4 \times 512$  MHz sub-bands, and calibrated each sub-band independently. As a drawback, we lost a factor of 2 in the S/N ratio per sub-band.

### 3.2 The *Planck*-ATCA Co-eval Observations (PACO)

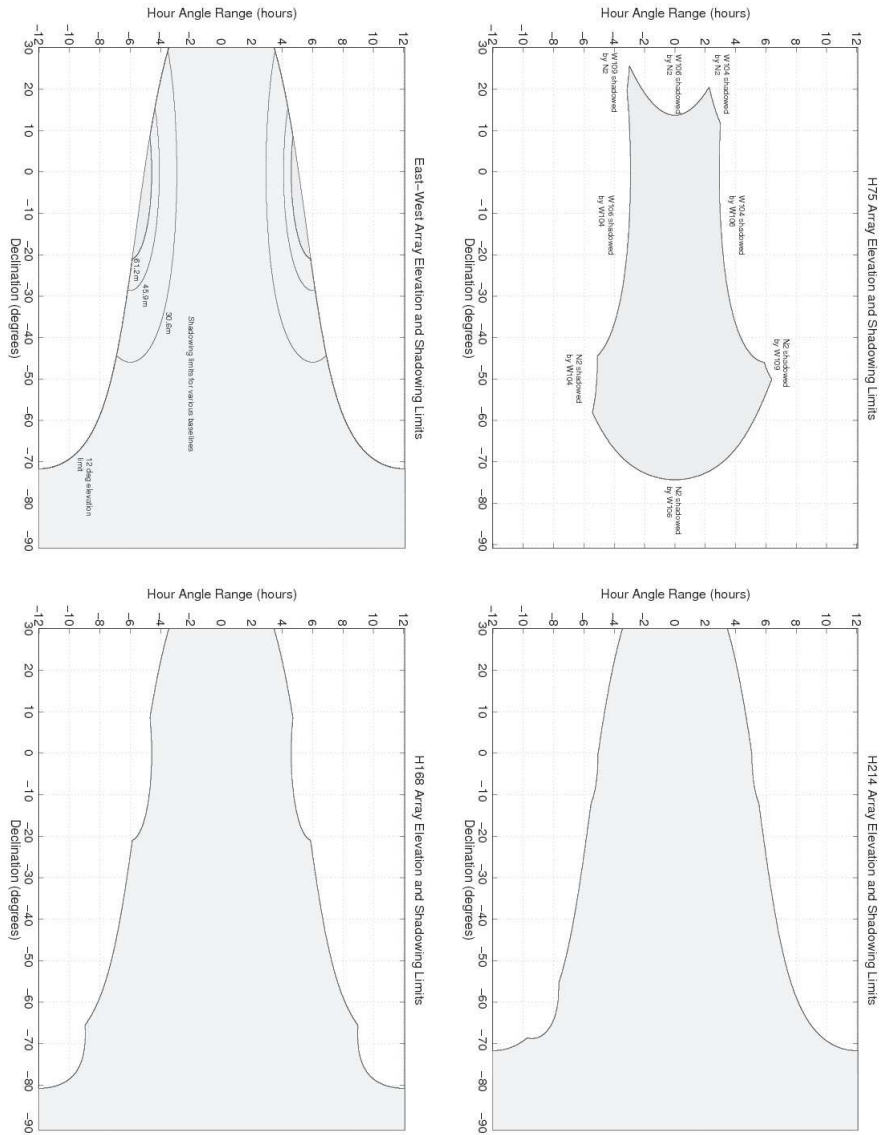


**Figure 3.8:** Shadowing scheme for different array configurations: the blue area shows the region (hour angle and declination) not affected by shadowing. From ATCA User Guide ([www.narrabri.atnf.csiro.au/observing/users\\_guide/](http://www.narrabri.atnf.csiro.au/observing/users_guide/)).

### 3. GROUND-BASED OBSERVATIONS

---

**General calibration.** Before describing the details of the PACO calibration and flux densities estimations, we sketch out the general approach for calibration.

- The bandpass calibrator is used to correct for the bandpass shape, i.e. to determine the instrumental response to the incoming spectrum. Given a flat spectrum (i.e. equal flux density at all frequencies), the ideal instrument would produce a flat bandpass shape, but any real instrument responds to different frequencies in an unequal way, and this gives rise to the bandpass shape which is solved for by the task MFCAL.
- The flux calibrator, commonly chosen between PKS 1934-638 and the planet Uranus, is used as a reference to know how much the measured flux has to be scaled in order to obtain the true value.
- The target source is the source of interest.
- The phase calibrator is a source observed almost contemporaneously with the target source. There should be at least as many cuts of the phase calibrator as of the target source. This calibrator is not necessary if we can rely on self-calibration. The phase calibrator must be a point source, with as little confusion and defects as possible. It is used to solve for the phases (or more accurately, the complex gains) of the cross-correlations: they usually change with time due to atmospheric conditions, system temperature variations, elevation of the antenna etc. For this reason it should be an unchanging point source, observed throughout the observations. The phase calibrator was not observed during the PACO observations, since our sources are bright enough to allow us to self-calibrate.

The same source can be used for more than one of these roles. For example, 1934-638 can be used as a flux calibrator and as a bandpass calibrator at 3-6 cm as in the case of the pipeline presented in Appendix A.

The first step is to solve for the bandpass solution, using the task MFCAL on the bandpass calibrator. After having solved for the bandpass function, MFCAL produces a tables of the bandpass solutions (i.e. amplitude scaling factors as a function of frequency) that is associated to the visibility dataset, without modifying the data. MFCAL also determines antenna gains (i.e. amplitude scaling factor as a function of

### 3.2 The *Planck*-ATCA Co-eval Observations (PACO)

---

time for each antenna). As the bandpass calibrator is assumed to be a point-like object phases are self-calibrated.

The next step is to copy the bandpass solution to the flux calibrator, using the task `GPCOPY`.

Then the calibration procedure should determine the antenna gains and instrumental polarisation from the flux calibrator, using the task `GPCAL`. It will use the bandpass determined by `MFCAL` to partially correct the data. If the flux calibrator is 1934-638, the only options turned on should be `xyvaryis`. It solves for the XY phases as a function of time. The task `GPCAL` will report the instrumental polarisation parameters (leakages), for which typical values are 1 – 2%, or 4% under bad conditions and they are quite constant with time and modestly frequency dependent. This task scales the average flux of the entire band to the known flux of 1934-638 at the centre frequency of the band.

Afterwards the same action is performed on the phase calibrator using `GPCAL` again, but this time solving for the Stokes Q and U values for the source, which are not known a-priori. To do this we add the `qusolve` option.

At this point, the flux and phase calibrators have the same bandpass solution, but different flux scalings. The goal is to get the phase calibrator calibrated so that it has the correct bandpass shape and slope, the correct flux scaling, and a useful phase solution.

If the flux calibrator is not a planet, `GPBOOT` must be used to correct the phase calibrator’s flux scale. This task takes two inputs: `vis`, which is a dataset with a flux scale that needs correcting, and `cal`, which is a dataset with the reference or the correct flux scale. In principle, for this purpose the observations of the phase and flux calibrators should have been taken at the same time and elevation, because atmospheric opacity affects the amplitude gain calibration. It is not always possible and the further apart the observations are in time and elevation, the less accurate the flux calibration will be, especially at high frequencies. The output of `GPBOOT` will indicate how large the scaling adjustment is, with 1.000 being no adjustment at all. If the flux calibrator is a planet, `GPCAL` must be used to transfer the gain scaling from the phase calibrator to the flux one, using as reference flux scale the one of the phase calibrator. This step is necessary because the task that adjusts the flux scales using a planet requires that

### 3. GROUND-BASED OBSERVATIONS

---

all the input datasets (which will be the flux and phase calibrators) have the same flux scale to begin with.

Finally the task MFBOOT corrects both the bandpass slope of the phase calibrator, and the flux scaling, performing the following steps: it constructs a model, for a known flux calibrator, of what the flux should be on each baseline and for all frequencies across the band; it determines by how much the gains must be scaled to make the observed flux at the centre of the band match the model value; it scales all the datasets it has been given by that factor; it calculates the slope of the model between two points either side of the band centre, and corrects the bandpass table to make the observed spectrum match that slope. All that remains is to transfer the calibration tables to the program source, using GPCOPY.

**PACO calibration.** The calibration used in PACO is slightly different from the one described above. Instead of using a phase calibrator, we did self-calibrate, due to the fact the our sources are bright enough and imaging is not our primary product. Our procedure can be summarized as follows.

First MFCAL generates bandpass reference calibration tables using the bandpass calibrator. The bandpass tables are then copied to the primary and leakage calibrators using the task GPCOPY. Leakage tables are generated using MFCAL with the `nopassol` option to ensure that we don't solve for the bandpass shape. The bandpass tables, copied from the bandpass calibrator, are already present in the visibility data-set and will be applied to the data. The GPCAL task is applied to the leakage calibrator with the usual options `qsolve` and `xyvary`. At this point the leakage tables are copied, with the task GPCOPY, to the target sources. MFCAL (option `nopassol`) is applied on the primary calibrator. This task is not performed when Uranus is used. The gain tables are then copied on the target source (GPCOPY). The target source flux density is then scaled to that of the primary calibrator with MFCAL and GPBOOT, when PKS 1934-638 is the primary calibrator, or MFBOOT, when Uranus is the primary calibrator. The steps for calibration are plotted in Figure 3.9.

#### 3.2.5 Extended Sources

Compact objects are expected to show higher levels of variability than extended sources. For this reason in order to investigate the variability properties we have confined our-

### 3.2 The *Planck*-ATCA Co-eval Observations (PACO)

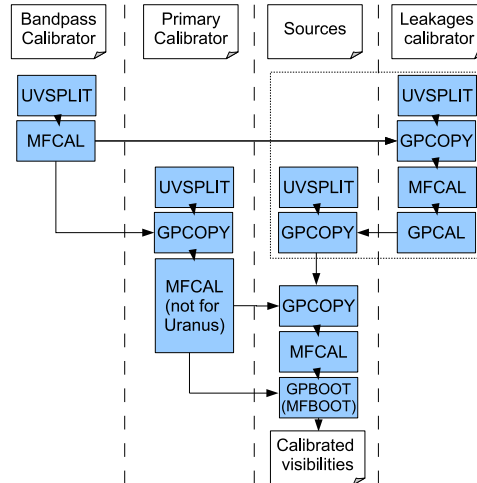


**Figure 3.9:** Scheme of the calibration performed with MIRIAD tasks. The indications in parenthesis refer to the case of Uranus as primary calibrator. The steps included in the dotted square have been applied only when a suitable leakage calibrator has been observed. (Massardi et al., 2011a).

selves to well selected samples of compact objects. Also, to estimate the flux density properties of our samples we need to distinguish extended from compact objects in order to apply the right method to estimate the flux density for each source.

We expect that the AT20G analysis for extendedness already identifies all the extended sources up to 20 GHz. We have therefore done the analysis only for the 7 mm data, applying the automatic procedure used by Massardi et al. (2008) for the AT20G bright sample to distinguish between point-like and extended sources.

This method is based on the closure phase technique that, as demonstrated by the AT20G analysis, distinguishes between extended and point-like sources accounting for effects due to noise in the beam, but is independent from the position of the object within the beam. Closure effects are relationships between visibility values for baselines that form a closed triangle with antennas as vertices.

For three antennas  $m$ ,  $n$  and  $p$  the phase closure is:

$$\phi_c = \phi_{mn} + \phi_{np} - \phi_{pm}. \quad (3.3)$$

For a point source the phase closure rms should be zero and is independent of atmospheric and instrumental effects. For these reasons it is used to define an extendedness

### 3. GROUND-BASED OBSERVATIONS

---

parameter: we use the ratio between the observed phase closure rms and the theoretical one corrected for the effects of noise. We used it to define the extendedness parameter  $ep$ :

$$ep = P_{cl\ obs}/P_{cl\ th} \quad (3.4)$$

where

$$P_{cl\ th} = \sqrt{P_{th\ rms}^2 + (\arctan(V_{rms}k/S)^h)^2}. \quad (3.5)$$

Here  $P_{th\ rms}$  is given by the CLOSURE task of MIRIAD and coincides with the theoretical estimate of the phase closure rms for the given array;  $V_{rms}$  is the V-Stokes rms that we assume to be an estimate of the noise in our beam;  $S$  is the triple product,  $k = 50$  and  $h = 2.5$  are the values estimated for 20 GHz data for the AT20G. When the ratio of actual to theoretical phase closure rms is larger than 3 the source should be considered extended (this is a semi-empirical formula, already used in the AT20G analysis; [Massardi et al., 2008](#); [Murphy et al., 2010](#)). We have used this ratio as an indication of extension for the sources that appear to be extended at 7 mm and were not identified as extended in the AT20G catalogue.

#### 3.2.6 Flux Density Estimation

To estimate the flux densities for point sources we have used the triple product (i.e. the geometrical average of the amplitude over a closure triangle averaged over all the possible triangles, given by the MIRIAD task CALRED; for a reference see [Thompson et al., 2001](#)). Our flux density estimation techniques are well suited for point sources. To estimate the flux densities in the case of extended sources, we adopted the amplitude of the shortest spacings for the array configuration used (see Tables [3.4](#) and [3.5](#)), given by the MIRIAD task UVFLUX, as the best estimate of flux densities. This approach underestimates the flux densities for sources more extended than  $D_{max} = 15(100\text{m}/b_{\min})(39\text{GHz}/\nu)$  arcsec, where  $b_{\min}$  is the shortest baseline for any used configuration. Thus our flux densities are increasingly underestimated and, as a consequence, our samples are increasingly incomplete for more and more extended sources. Table [3.5](#) lists the shortest baselines ( $b_{\min}$ ), the primary and synthesized beam sizes for the central frequencies of our observing runs and  $D_{max}$  for all the array configurations used.

### 3.2 The *Planck*-ATCA Co-eval Observations (PACO)

**Table 3.5:** The array configurations and their resolution properties.

Array Configuration	Shortest Baseline [m]	frequency IF1 - IF2[GHz]	Primary beam FWHM [arcmin]	Beam IF1 [arcsec]	Beam IF2 [arcsec]	$D_{\max}$ [arcmin]
H75c	31 (1-4,2-4)	5.5 - 9	8.7 - 5.3	115.51 x 115.51	70.59 x 70.59	6.0 - 3.7
		18 - 24	2.6 - 2.0	35.29 x 35.29	26.47 x 26.47	1.8 - 1.4
		33 - 39	1.5 - 1.2	19.25 x 19.25	16.29 x 16.29	1.0 - 0.9
H168d	61 (1-4,2-4)	5.5 - 9	8.7 - 5.3	50.23 x 50.23	30.69 x 30.69	3.1 - 1.9
		18 - 24	2.6 - 2.0	15.35 x 15.35	11.51 x 11.51	0.9 - 0.7
		33 - 39	1.5 - 1.2	8.37 x 8.37	7.08 x 7.08	0.5 - 0.4
H214c	82 (2-4)	5.5 - 9	8.7 - 5.3	38.9 x 38.9	23.78 x 23.78	2.3 - 1.4
		18 - 24	2.6 - 2.0	11.89 x 11.89	8.92 x 8.92	0.7 - 0.5
		33 - 39	1.5 - 1.2	6.48 x 6.48	5.49 x 5.49	0.4 - 0.3
1.5A	153 (1-2)	5.5 - 9	8.7 - 5.3	7.2 x 8.31	4.4 x 5.08	1.2 - 0.7
		18 - 24	2.6 - 2.0	2.2 x 2.54	1.65 x 1.91	0.4 - 0.3
		33 - 39	1.5 - 1.2	1.2 x 1.39	1.02 x 1.17	0.2 - 0.2
1.5B	31 (1-2)	5.5 - 9	8.7 - 5.3	7.2 x 8.31	4.4 x 5.08	6.0 - 3.7
		18 - 24	2.6 - 2.0	2.2 x 2.54	1.65 x 1.91	1.8 - 1.4
		33 - 39	1.5 - 1.2	1.2 x 1.39	1.02 x 1.17	1.0 - 0.9
6B	214 (4-5)	5.5 - 9	8.7 - 5.3	2.48 x 2.86	1.51 x 1.75	0.9 - 0.5
		18 - 24	2.6 - 2.0	0.76 x 0.87	0.57 x 0.65	0.3 - 0.2
		33 - 39	1.5 - 1.2	0.41 x 0.48	0.35 x 0.4	0.1 - 0.1
6D	77 (4-5)	5.5 - 9	8.7 - 5.3	2.48 x 2.86	1.51 x 1.75	2.4 - 1.5
		18 - 24	2.6 - 2.0	0.76 x 0.87	0.57 x 0.65	0.7 - 0.6
		33 - 39	1.5 - 1.2	0.41 x 0.48	0.35 x 0.4	0.4 - 0.3

### 3. GROUND-BASED OBSERVATIONS

---

The noise terms of the flux density errors for point sources are calculated as the rms of the triple product amplitudes over all the possible triangles of antennas. For extended sources the rms of the triple product has been multiplied by  $\sqrt{n_b}$  where  $n_b$  is the number of baselines of the used configuration. An analysis of the gain term of the flux density error including systematics and calibration uncertainties will be discussed in Section 3.2.7.1

#### 3.2.7 Quality Assessment

By running the data reduction pipeline previously described we have generated a preliminary catalogue for each observing epoch. This catalogue was then processed through a quality assessment procedure. Depending on the results of the assessment, we either proceeded to create the final catalogue for the considered epoch or we carried out further investigations in order to improve the results.

The quality assessment step is needed because each observation can be affected by different problems (bad weather conditions, some antenna correlations to be rejected, residual spikes, etc.) which could not be addressed by the automatic pipeline run. It is designed to identify the major flaws that the catalogue of each observing epoch may have and to perform an a-posteriori flagging of the bad data.

The quality check assumes that the true SEDs do not contain discontinuities; those observed are interpreted as due to residual spikes in the data or to calibration errors. The smoothness of the spectra is checked by comparing the data points with a fitting polynomial function with degree equal to the number of 2 GHz bands observed. We stress that, at this stage, the fit is done for flagging purposes only.

For each SED of the considered epoch we compute the fractional rms divergence,  $\sigma$ , of the data points from the fitting line. Next we exclude those points (if any) that are more than  $4\sigma$  off and recompute the fractional divergence over all the other points. The procedure is iterated until the value of  $\sigma$  converges. To get rid of particularly bad epochs, if the final  $\sigma$  is higher than 0.02, which corresponds to  $\simeq 2\times$  the median rms fractional divergence for all the observing epochs, we do one more iteration with  $\sigma = 0.02$ . Whenever two data points within the same 2 GHz band are discarded, it is likely that some problem is affecting the whole band, and we flag it for the considered source.

---

## 3.2 The *Planck*-ATCA Co-eval Observations (PACO)

When the fraction of good data for a given observing epoch exceeds 90% (and this happens in most cases) we directly create the final catalogue of the unflagged data. All the other cases are inspected in order to identify the problems and new runs of the data reduction pipeline with improved specifications are performed aiming at reducing the data loss to no more than 10 – 15%. The recovery succeeded in most cases. The exceptions are due to problems affecting observations of the flux density calibrator for some bands. In a few cases the calibrator could not be recovered to a satisfactory level and the whole target sample was rejected. After the quality assessment process, we are left with more than 85% of our data.

### 3.2.7.1 Flux Density Error Estimation

The gain term of the noise for each epoch has been estimated as the rms fractional divergence between the data and the fit, re-calculated as discussed in the previous section after all the flagged data have been removed. For the days with less than 10 good fits available we have used  $\sigma_g = 0.012$  equal to the median of the rms fractional divergence calculated over all the epochs for point sources only. The gain term, calculated with our procedure, includes also flux density errors due to pointing errors. Hence, the final error bars for each point-source in each epoch have been estimated as the square root of the quadratic sum of the gain term  $\sigma_g$  multiplied by the source flux density plus the noise term  $\sigma_s$  (estimated as discussed in Section 3.2.6). Since our flux density estimation technique is tailored for point sources, we have increased the gain term of the noise for extended sources to a minimum of  $\sim 5\%$  of their flux density. This value has been obtained by scaling the rms fractional divergence calculated over all the epochs by  $\sqrt{r_b}$  where  $r_b = 15/1$  is the ratio between the number of baselines used in case of point sources and in case of extended sources. This term does not account for any missing flux density of extended objects.

The gain term does not include any scaling error due to deficiencies in the absolute calibration which should affect equally all the frequencies calibrated with the same calibrator source (generally PKS 1934-638). The comparison with *Planck* CMB-dipole calibrated flux densities will allow us to estimate this bias and correct it.

### 3. GROUND-BASED OBSERVATIONS

---

#### 3.2.8 Catalogues

Two among the PACO extended sources (AT20GJ051926-454554 and AT20GJ051949-454643) correspond to the core and to the western lobe of PictorA. We have performed a dedicated observation in total intensity and polarization at 18, 24, 33 and 39 GHz. The region of the western lobe, the brightest and the more polarized one (Burke-Spolaor et al., 2009) one, have been mosaicked. These sources will be discussed in a future paper and were left out from the analysis in Section 4.1 and from the catalogue.

Of the other 187 sources comprised in the PACO bright sample, 11 are flagged as extended in the AT20G catalogue and 2 more were found to be extended by our 7 mm data analysis. Of the 157 sources in the PACO faint sample, 9 were found to be extended, only 4 of which were classified as extended in the AT20G catalogue.

After the data reduction, 7 extended sources in the PACO bright sample and 5 in the PACO faint sample turned out to have unreliable flux density estimates at all the frequencies and for all the days of observations. This is mostly due to having used too extended array configurations, so that the sensitivity on the observed scale was poor. They have therefore not been included in the present catalogue.

For all the extended objects in the catalogues, the estimated flux densities represent a lower limit of the integrated flux densities. Those which passed all the quality checks have nevertheless been included in the catalogue, with flux densities listed as lower limits, but have been excluded from further analysis.

Both the bright and the faint PACO catalogues in the on-line version are organized as follows:

- 1 AT20G name;
- 2-3 J2000 equatorial coordinates;
- 4 epoch of observation as [yymmdd];
- 5 flag ‘s’ for simultaneity within 10 days from the *Planck* observations. The epochs before February 2010 overlap with the *Planck* first survey, whereas the following epochs overlap with the second survey.
- 6 flag ‘e’ for extended sources;

### **3.2 The *Planck*-ATCA Co-eval Observations (PACO)**

---

**7-31** flux densities in mJy at the 24 frequencies between 4732 and 39768 MHz in which our 6×2-GHz bands have been divided;

**32-55** flux density errors;

**56-60** fit parameters,  $S_0$ ,  $\nu_0$ , a, b.

### **3. GROUND-BASED OBSERVATIONS**

---

## Chapter 4

# Data Analysis

Figures 4.1 and 4.2 show the SEDs for the point-like sources in the PACO bright and faint samples. Different colours correspond to different observing epochs. Figure 4.3 shows, as an example, images at each frequency for the point source AT20GJ053850-440508. For the epochs observed with hybrid arrays, as in this case, good quality images could be obtained even with only one cut per source. This is possible thanks to the brightness of the sources in our sample. The figure is a clear illustration of the quality of our observations and of the beam size at the different frequencies.

### 4.1 Spectral Analysis

Even though a power-law is a poor description for the majority of the spectra, conventional spectral indices are still useful for practical purposes. For example, they provide the easiest way to extrapolate the observed counts or model prediction from one frequency to another.

As our observations cover a wide frequency range (4.5-40 GHz), over which a single power-law is not enough to describe the spectral behaviour of the sources, we have studied the spectral energy distributions of our point-like sources by fitting the observed data with a double power law:

$$S(\nu) = S_0/[(\nu/\nu_0)^{-\alpha} + (\nu/\nu_0)^{-\beta}], \quad (4.1)$$

where  $\nu$  is the frequency in GHz,  $S$  the flux density in Jy and  $S_0$ ,  $\nu_0$ ,  $\alpha$  and  $\beta$  are free parameters related to the spectral indices, but not equal to them. We considered

## 4. DATA ANALYSIS

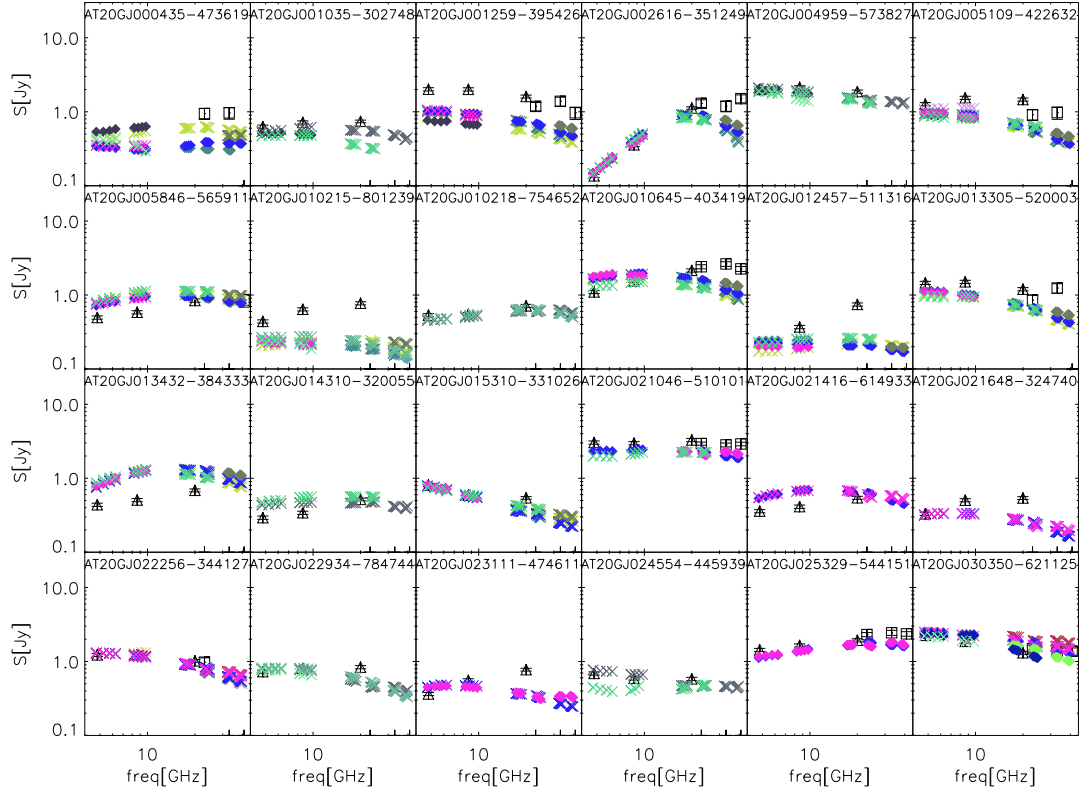


**Figure 4.1:** SEDs of the sources in PACO bright sample. Asterisks of different colours correspond to different observing epochs. To avoid overcrowding we have not plotted the error bars that are in all the cases smaller than the symbol size. For comparison, the AT20G data (triangles) and, when available, *WMAP* data taken from the NEWPS\_5yr catalogue (squares; [Massardi et al., 2009](#)) are also shown. From [Massardi et al. \(2011a\)](#).

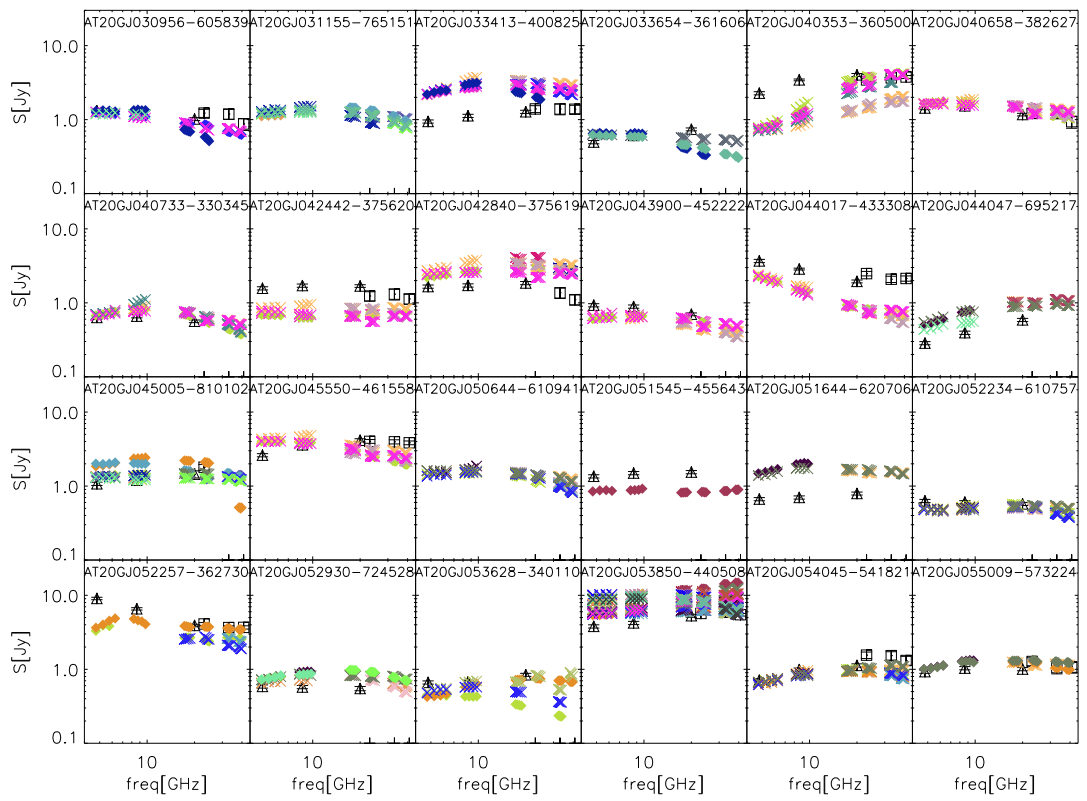


Figure 4.1: Continue.

## 4. DATA ANALYSIS

---

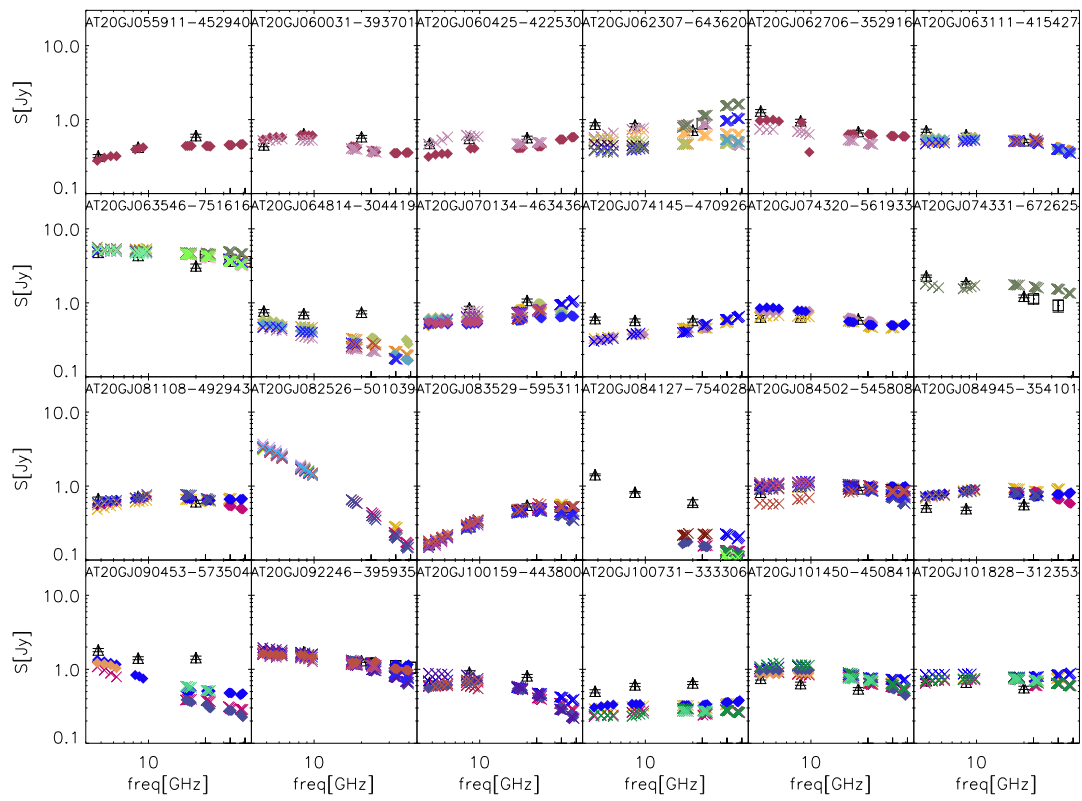


Figure 4.1: Continue.

## 4.1 Spectral Analysis

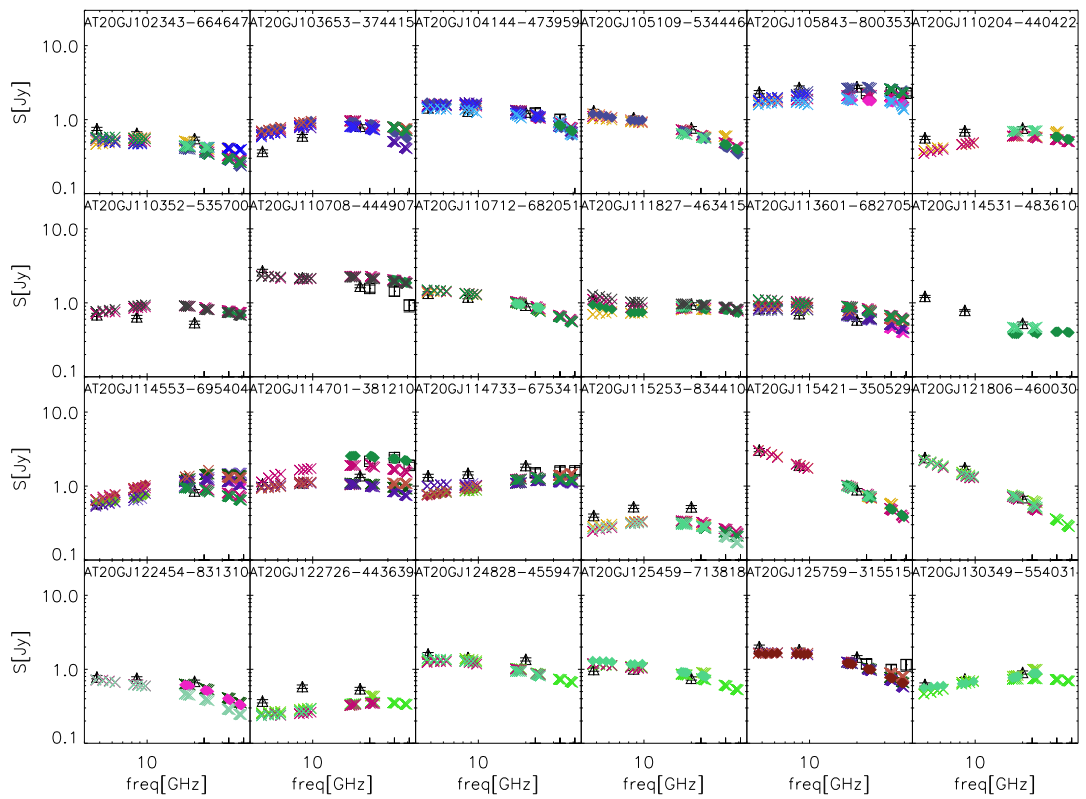


Figure 4.1: Continue.

## 4. DATA ANALYSIS

---

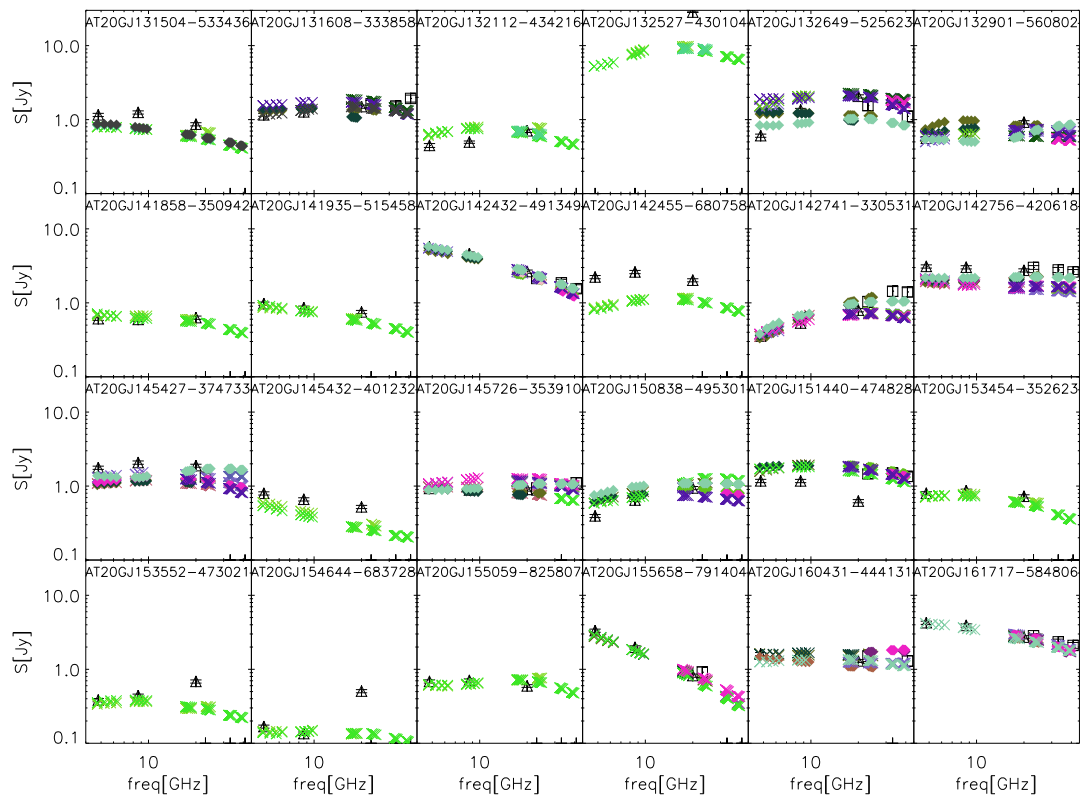


Figure 4.1: Continue.

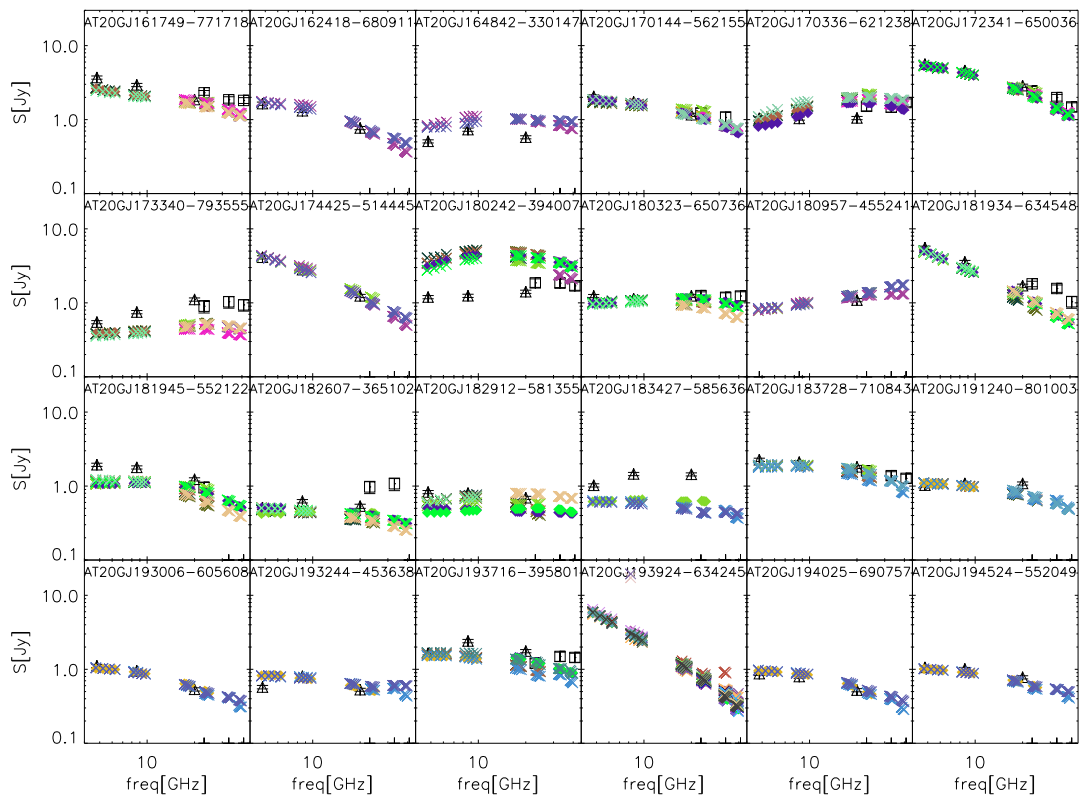


Figure 4.1: Continue.

## 4. DATA ANALYSIS

---

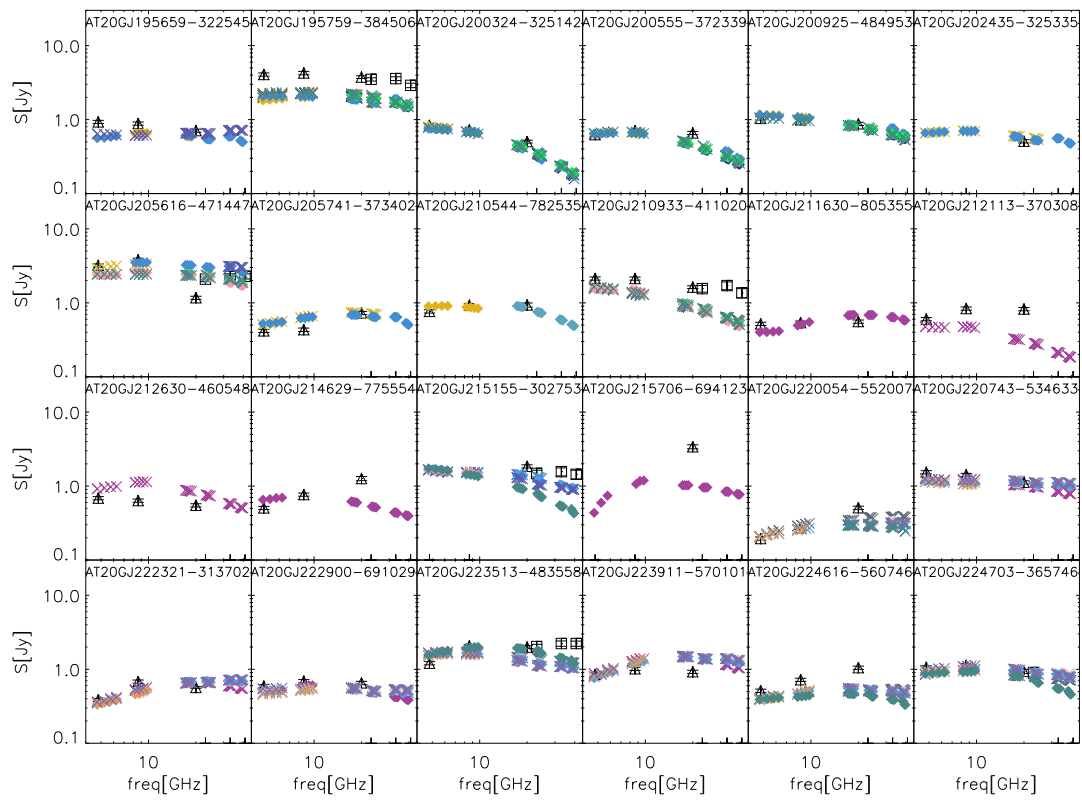


Figure 4.1: Continue.

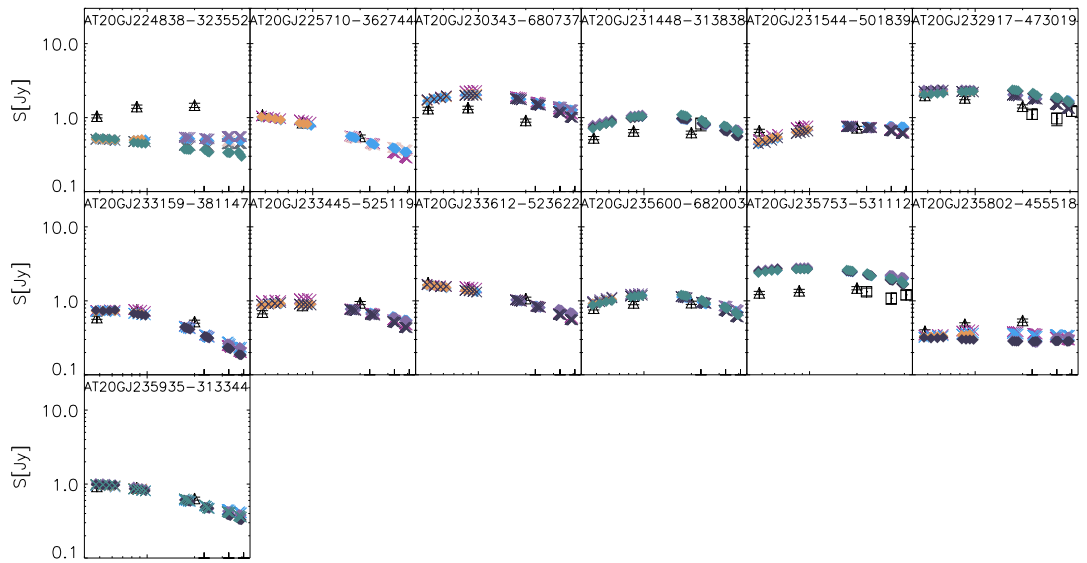
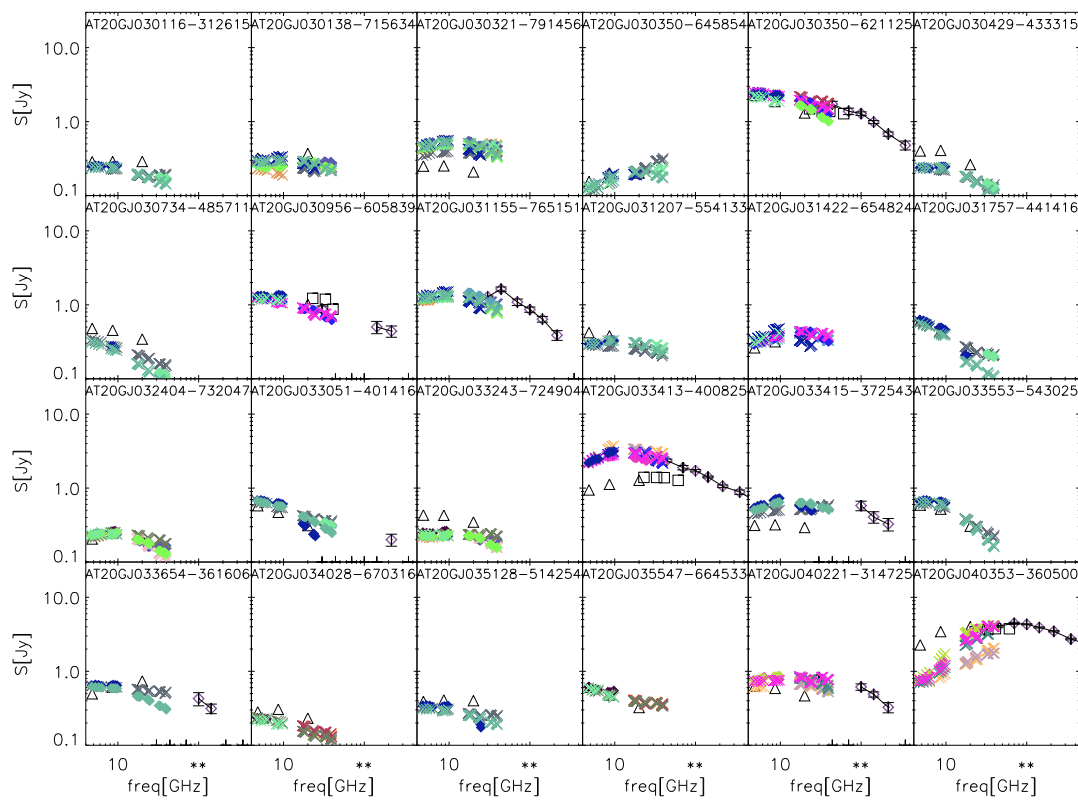


Figure 4.1: Continue.

## 4. DATA ANALYSIS



**Figure 4.2:** Same of the previous figure, but for the PACO faint sample.

## 4.1 Spectral Analysis

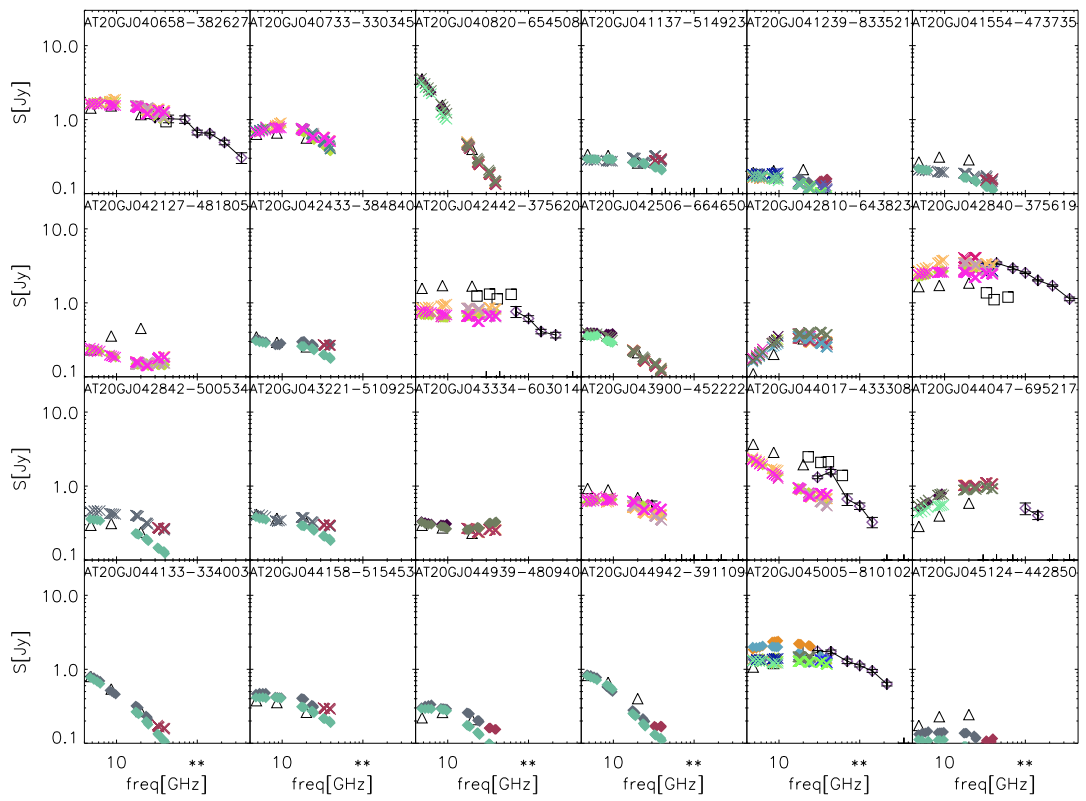


Figure 4.2: Continue.

## 4. DATA ANALYSIS

---

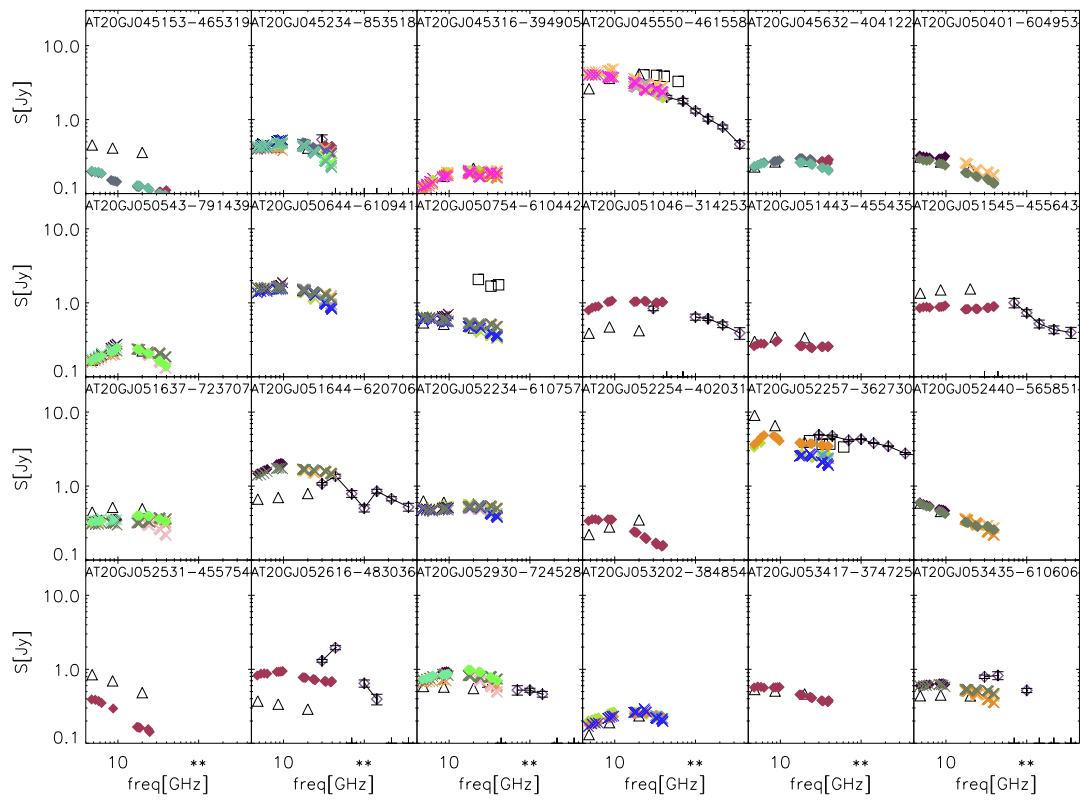


Figure 4.2: Continue.

## 4.1 Spectral Analysis

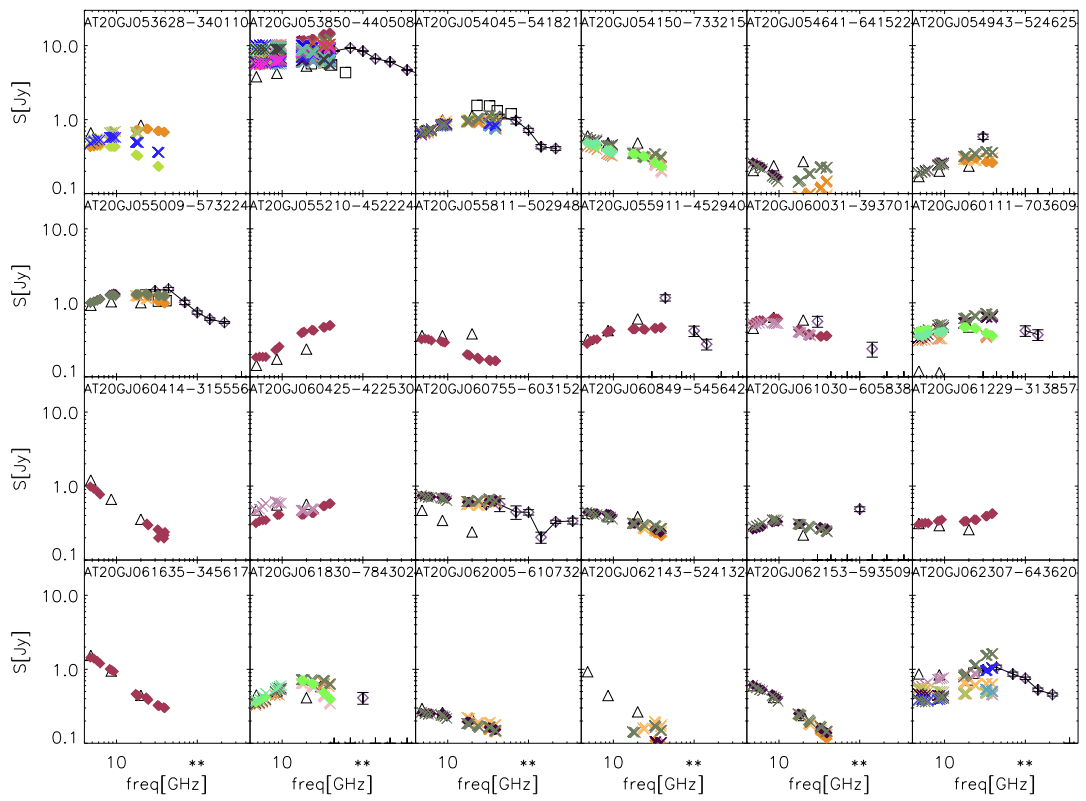


Figure 4.2: Continue.

## 4. DATA ANALYSIS

---

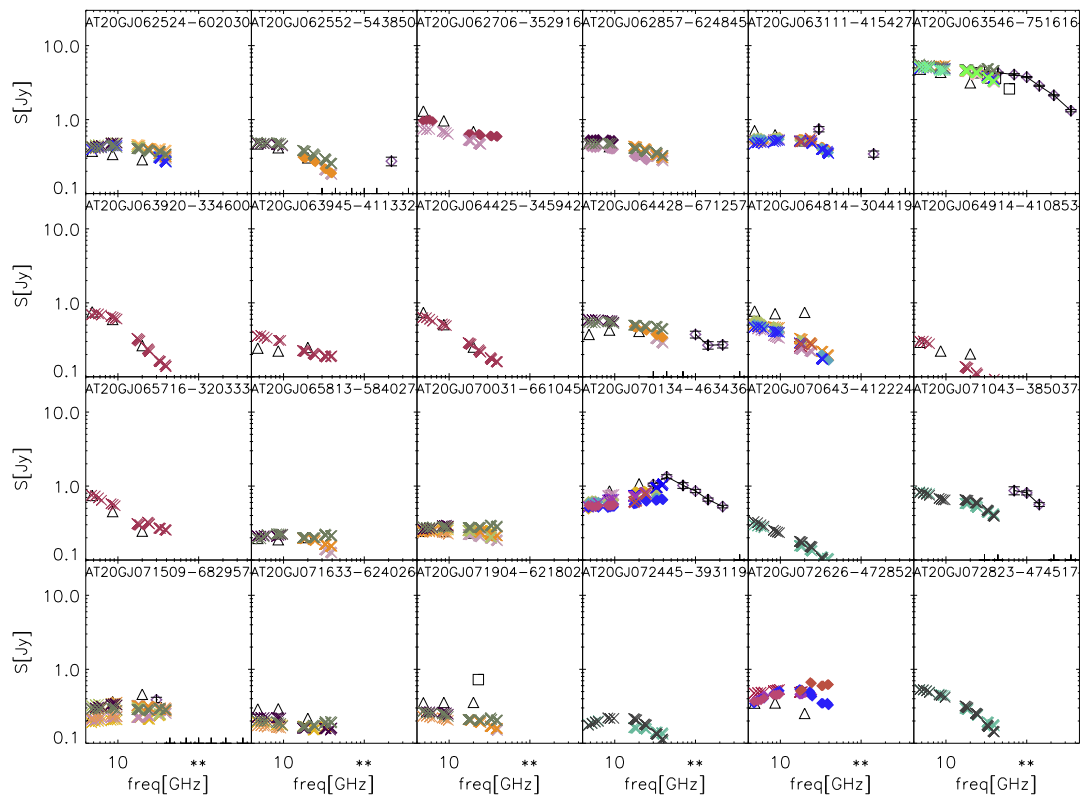


Figure 4.2: Continue.

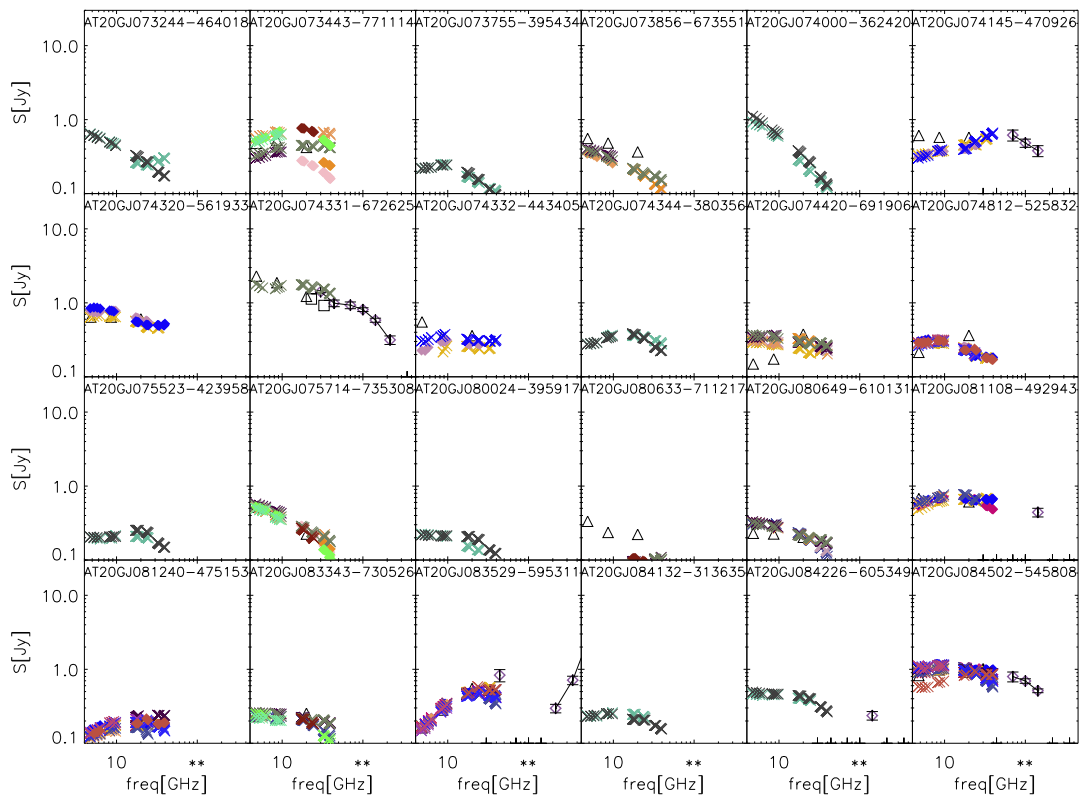


Figure 4.2: Continue.

## 4. DATA ANALYSIS

---

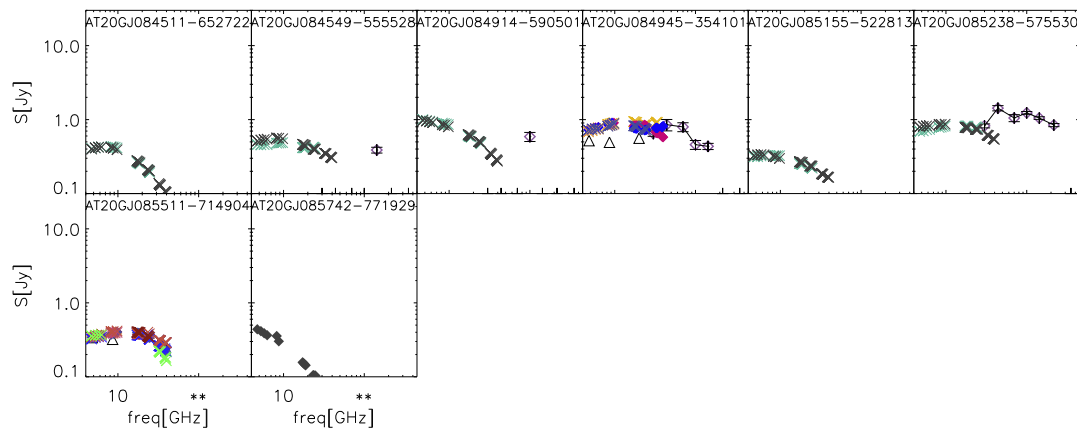
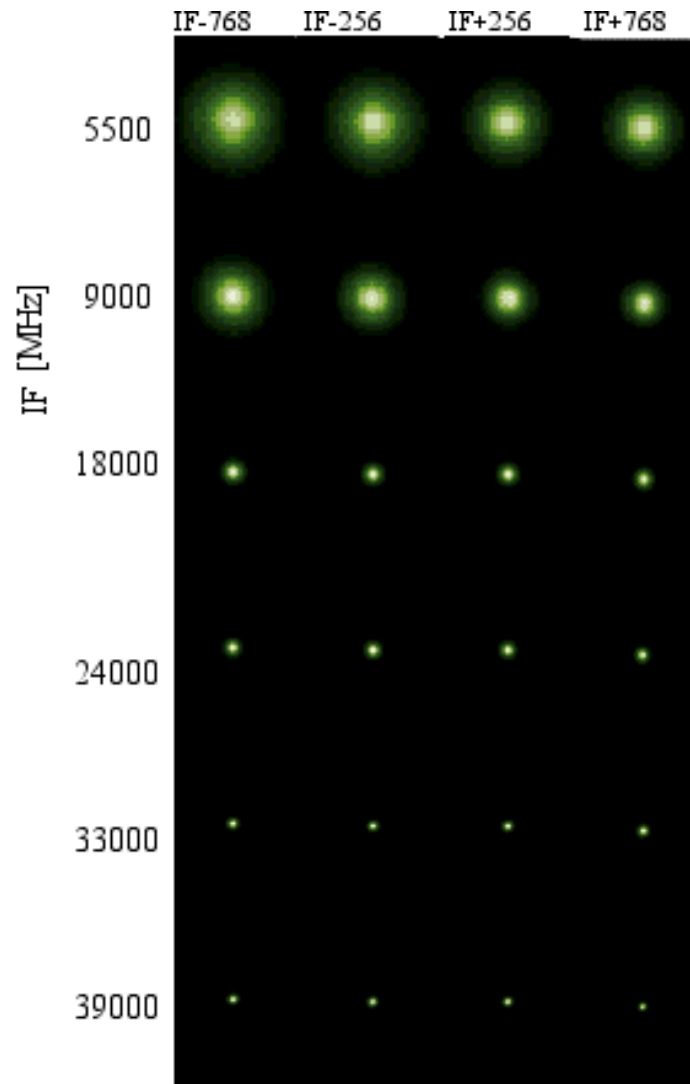


Figure 4.2: Continuum.



**Figure 4.3:** Images at each frequency for 0537-441 as observed on July 26th 2009 with the hybrid configuration H75, as an example of the quality of our data and a representation of the beam. Each panel measures  $6 \times 6$  arcmin. Every 512-MHz sub-band for a given IF band is in a different column, so that frequencies increase from the left to the right and from the top to the bottom. From [Massardi et al. \(2011a\)](#).

## 4. DATA ANALYSIS

---

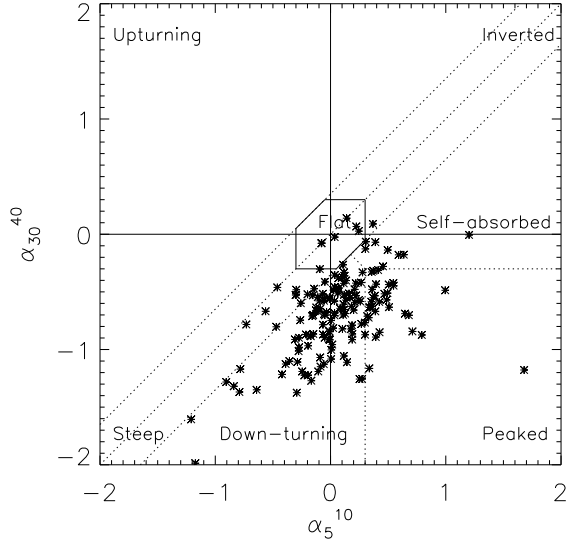


**Figure 4.4:** Colour-colour plot comparing the spectral indices in the ranges 5-10 and 30-40 GHz for the PACO bright sample. The dotted lines show the boundaries adopted for our spectral classification. From [Massardi et al. \(2011a\)](#).

only the sources for which we had at least 4 data points for each of the  $2 \times 2$  GHz bands considered. The fit has been performed in logarithmic units by minimizing the  $\chi^2$  with a non-linear optimization technique based on an implementation of the Generalised Reduced Gradient optimisation method (GRG; [Windward Technologies, 1997](#)). The allowed ranges for the parameters are:  $4.5 \leq \nu_0[\text{GHz}] \leq 40$ ,  $\alpha \geq -3$ ,  $\beta \leq 3$ .

We have considered as bad fits those with  $\chi^2 - \langle \chi^2 \rangle > 3\sigma_\chi$  where  $\langle \chi^2 \rangle = 1.3$  and  $\sigma_\chi = 0.54$  are the mean and the standard deviation of the Gaussian fit of the  $\chi^2$  distribution of the fits over the whole PACO sample.

For 4 of the 174 point-like sources in the bright sample and for 2 of the 143 in the faint sample, we do not have enough data to obtain meaningful values of the parameters, while in 5 cases for the bright sample and 9 for the faint sample, Equation (4.1) does not yield an acceptable fit ( $\chi^2$  above the threshold). The fit was not successful for those sources that show an irregular spectrum that could not be described by the fitting formula. In most cases the irregularities of the spectrum seem to be due to residual calibration problems. For the remaining sources (165 in the bright sample and 132 in the faint sample) we have classified the spectral shape according to the values

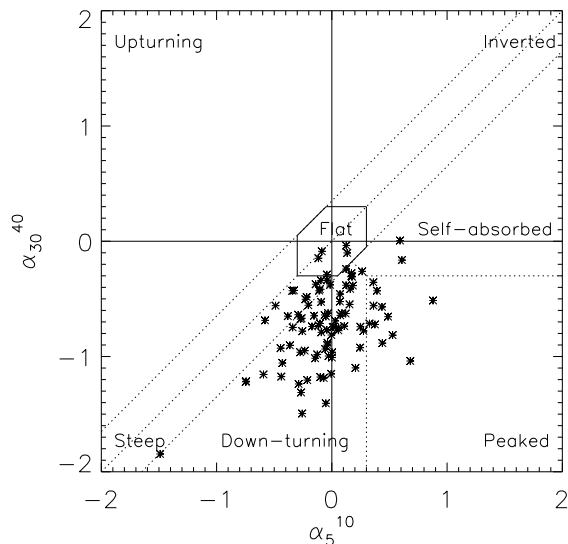


**Figure 4.5:** Distribution of PACO faint sources with  $200 \text{ mJy} \leq S_{\text{AT20G}} < 500 \text{ mJy}$  in the  $\alpha_5^{10}$ - $\alpha_{30}^{40}$  plane. The dotted lines show the boundaries for the various spectral types. From [Bonavera et al. \(2011\)](#).

of the low- and high-frequency spectral indices  $\alpha_5^{10}$  and  $\alpha_{30}^{40}$  ( $S \propto \nu^\alpha$ ) defined in the ranges 5-10 GHz and 30-40 GHz and calculated using the fitting formula. Moreover in the case of the faint sample we have restricted the analysis to the 98 sources with  $S_{20\text{GHz}} < 500 \text{ mJy}$ , since the sources with  $S_{20\text{GHz}} > 500 \text{ mJy}$  are already present in the bright sample. The distribution of these spectral indices is shown in Figure 4.4 and in Figure 4.5.

When  $|\alpha_5^{10} - \alpha_{30}^{40}| < 0.35$  the source spectrum is classified as ‘single power law’, further subdivided in:

- ‘steep’ with  $\alpha_5^{10}, \alpha_{30}^{40} < -0.3$ ,
- ‘flat’ with  $|\alpha_5^{10}|, |\alpha_{30}^{40}| \leq 0.3$ ,
- ‘inverted’ for  $\alpha_5^{10}, \alpha_{30}^{40} > 0.3$ .

The other sources have been classified as follows:

- ‘downturning’ if  $\alpha_{30}^{40} \leq \min(\alpha_5^{10} - 0.35, -\alpha_5^{10})$ ,

## 4. DATA ANALYSIS

---

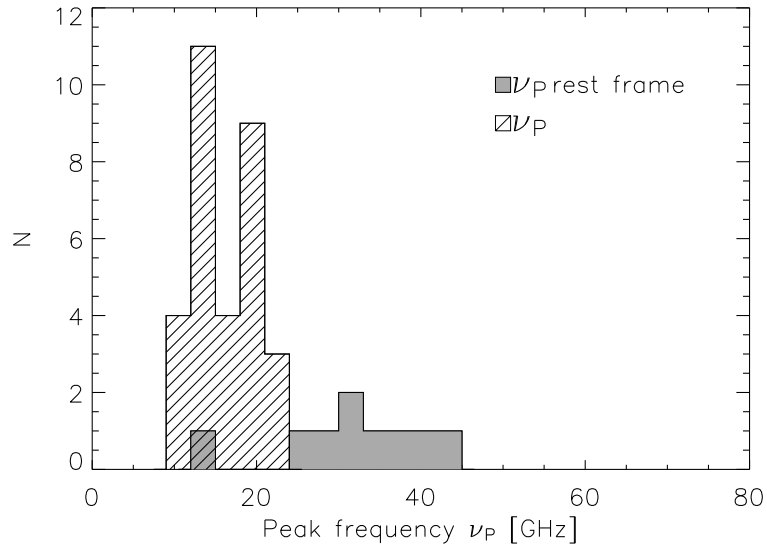
**Table 4.1:** Percentages of sources of each spectral type in the PACO faint sample ( $200 \text{ mJy} \leq S_{\text{AT20G}} < 500 \text{ mJy}$ ) and in the bright sample ( $S_{\text{AT20G}} \geq 500 \text{ mJy}$ ).

Type	$200\text{mJy} \leq S_{20\text{GHz}} < 500\text{mJy}$	$S_{20\text{GHz}} \geq 500\text{mJy}$
	per cent	per cent
flat	5.1	10.3
steep	13.3	3.6
inverted	0	0.6
peaked	11.2	14.5
down turning	65.3	66
self absorbed	5.1	4.8
upturning	0	0

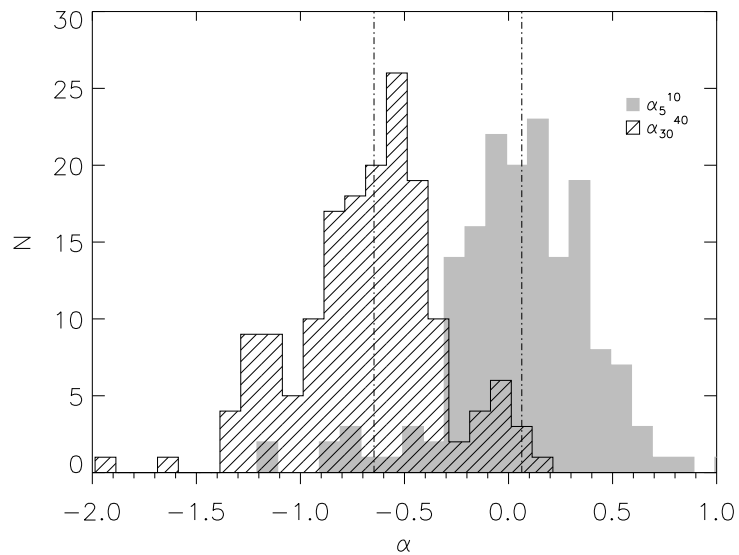
- ‘peaked’ if  $\alpha_5^{10} > 0.3$ ,  $\alpha_{40}^{30} < -0.3$ ,
- ‘self-absorbed’ if  $\alpha_5^{10} - 0.35 \geq \alpha_{40}^{30} \geq \max(-0.3, -\alpha_5^{10})$ .

Remarkably, we don’t find any ‘upturning’ source ( $\alpha_5^{10} < \alpha_{30}^{40}$ ). It is worth noticing that in a similar work, [Sajina et al. \(2011\)](#) did find some, although few, ‘upturning’ sources. The difference can be due to our highest frequency spectral index selection. The fractions of sources of each spectral type are listed in Table 4.1. The main difference between the faint and the bright sample is the larger fraction of steep-spectrum sources in the former, mostly at the expenses of peaked- and flat-spectrum sources.

The peak frequency of ‘peaked’ sources is  $\nu_p = \nu_0(-b/a)^{1/(b-a)}$ . The distribution of  $\nu_p$  in the observer’s frame for the bright sample is shown by the solid histogram in Figure 4.6. The mean value is 16.4 GHz with a standard deviation of 3.5 GHz. The median is 15.5 GHz with inter-quartile range 14.0-19.7 GHz. The figure also shows the distribution of peak frequencies in the source frame for the 9 sources for which redshifts are available ([Mahony et al., 2011](#); [Massardi et al., 2011a](#)), for these the mean is 32.1 GHz with dispersion of 8.8 GHz; the median is 32.2 GHz with inter-quartile range of 27.7-38.9 GHz. For the 11 peaked sources with  $200 \leq S_{20\text{GHz}} \leq 500 \text{ mJy}$  we found a median value of 16.6 GHz, a mean of 17.2 GHz and a dispersion of 3.7 GHz. For the 64 down-turning sources in the same flux density range we found a median break frequency value of 31.8 GHz, a mean of 26.2 GHz and a dispersion of 14.1. We note that 28 sources have a value of  $\nu_0$  at the border of our frequency range and therefore not reliably estimated. This does not affect the value of the median.



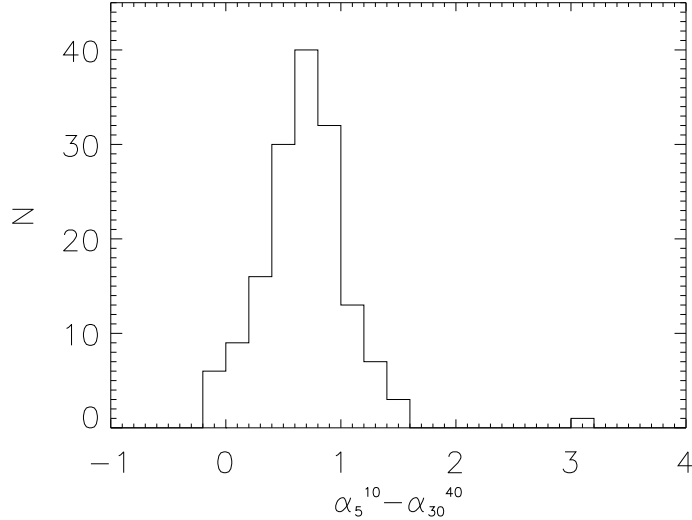
**Figure 4.6:** Distribution of peak frequencies of sources in the bright sample in the observer's frame (hatched histogram) and in the source frame (shaded) for sources with measured redshift. From [Massardi et al. \(2011a\)](#).



**Figure 4.7:** Distribution of  $\alpha_5^{10}$  (shaded area) and  $\alpha_{30}^{40}$  (hatched area) for the PACO bright sample.

#### 4. DATA ANALYSIS

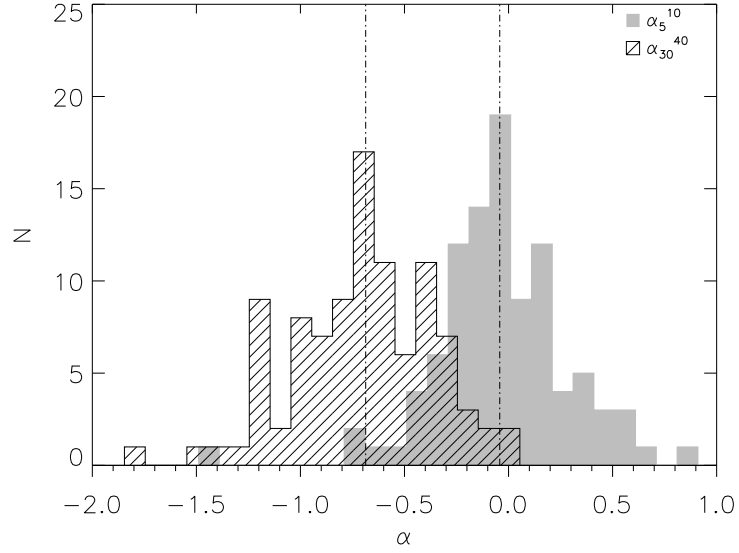
---



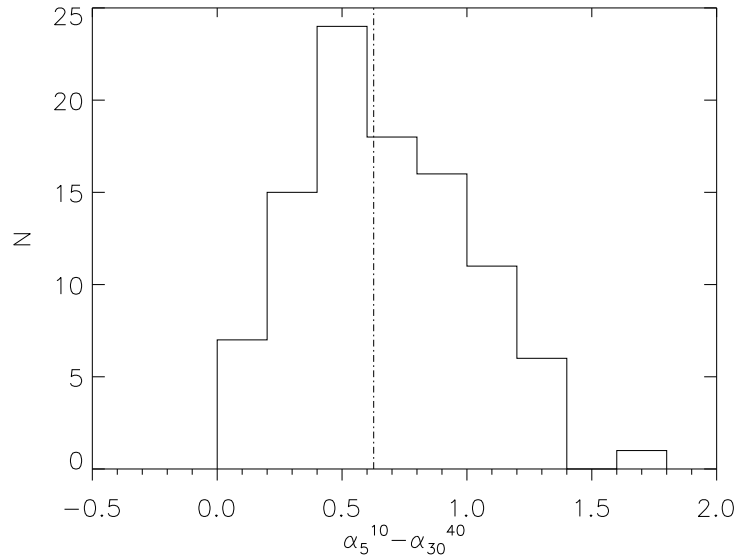
**Figure 4.8:** Distribution of the differences between low- and high- frequency spectral indices ( $\alpha_5^{10} - \alpha_{30}^{40}$ ) for the PACO bright sample. From [Massardi et al. \(2011a\)](#).

Figure 4.7 shows the spectral index distributions for  $\alpha_5^{10}$  and  $\alpha_{30}^{40}$  for the bright sample. The median is 0.064 and -0.65 for  $\alpha_5^{10}$  and  $\alpha_{30}^{40}$  respectively, with interquartile ranges  $[-0.12, 0.30]$  and  $[-0.87, -0.48]$ . The distribution of the differences between low- and high-frequency spectral indices ( $\alpha_5^{10} - \alpha_{30}^{40}$ ) is shown in Figure 4.8. There is a clear steepening of the spectra at high frequency. The mean difference is 0.75 with a standard deviation of 0.37. The median difference is 0.73 with inter-quartile range  $[0.52, 0.97]$ .

The distributions of spectral indices  $\alpha_5^{10}$  and  $\alpha_{30}^{40}$  for the PACO faint sample with  $200 \leq S_{20GHz} \leq 500$  mJy are shown in Figure 4.9. The median values are  $-0.04$  for  $\alpha_5^{10}$  and  $-0.69$  for  $\alpha_{30}^{40}$ , with interquartile ranges  $[-0.22; 0.15]$  and  $[-0.93; -0.43]$  respectively, showing that the spectra are mainly flat at lower frequencies and steepen at higher ones. The distribution of the differences between the two spectral indices, shown in Figure 4.10, has mean value of  $0.67 \pm 0.04$  and standard deviation of 0.35; the median value is  $0.63 \pm 0.04$ . A steepening of the spectral indices between 20 and 90 GHz has also been reported by [Sajina et al. \(2011\)](#), based on VLA observations of a sample selected from the AT20G survey. Moreover, a steepening of spectral indices at higher frequencies is also shown in the analysis of the NEWPS sample ([González-Nuevo](#)



**Figure 4.9:** Distributions of  $\alpha_5^{10}$  (shaded area) and of  $\alpha_{30}^{40}$  (hatched area) for the PACO faint sample ( $200 \leq S_{20GHz} \leq 500$  mJy). From [Bonavera et al. \(2011\)](#).



**Figure 4.10:** Distribution of the difference  $\alpha_5^{10} - \alpha_{30}^{40}$  for the PACO faint sample ( $200 \leq S_{20GHz} \leq 500$  mJy). From [Bonavera et al. \(2011\)](#).

## 4. DATA ANALYSIS

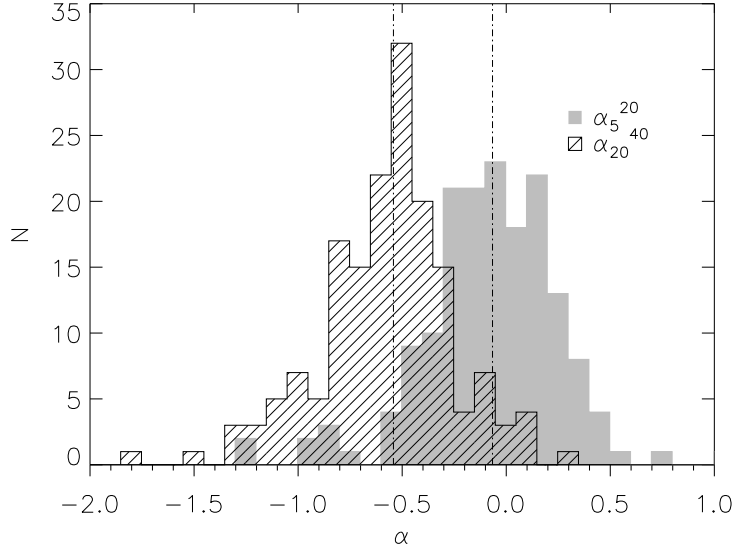


**Figure 4.11:** Distributions of spectral indices between 5 and 20 GHz (shaded) and between 20 and 40 GHz (hatched) for the PACO bright sample.

et al., 2008) and the ERCSC sample (Planck Collaboration, 2011g).

Figure 4.11 and Figure 4.12 show the distributions of spectral indices between 5 and 20 GHz and between 20 and 40 GHz (we refer to 20 GHz since it is the selection frequency of the PACO sample) for the bright and the faint PACO sample respectively. The mean value of  $\alpha_5^{20}$  is -0.07 for the bright sample and -0.16 for the faint sample, with standard deviations of 0.32 and 0.31 respectively. The mean  $\alpha_{20}^{40}$  is -0.55 for the bright sample and -0.60 for the faint sample, with standard deviations of 0.34 and 0.31 respectively. It should be noted that the 20 GHz selection favours sources that are brighter at this frequency. Therefore a positive value of  $\alpha_5^{20} - \alpha_{20}^{40}$  is, at least partly, due to a selection effect. These values for the two samples are similar, although not equal. This indicates that the overall spectral behaviour up to 40 GHz is not strongly dependent on flux density in the range covered by these samples, especially between 20 and 40 GHz.

Finally, Table 4.2 and Table 4.3 (for the bright and faint sample respectively) summarize the median spectral indices calculated from the fitting double power-law function among couples of frequencies in the range covered by our observations. Since spectra are complex, spectral indices were computed only for relatively narrow frequency intervals.

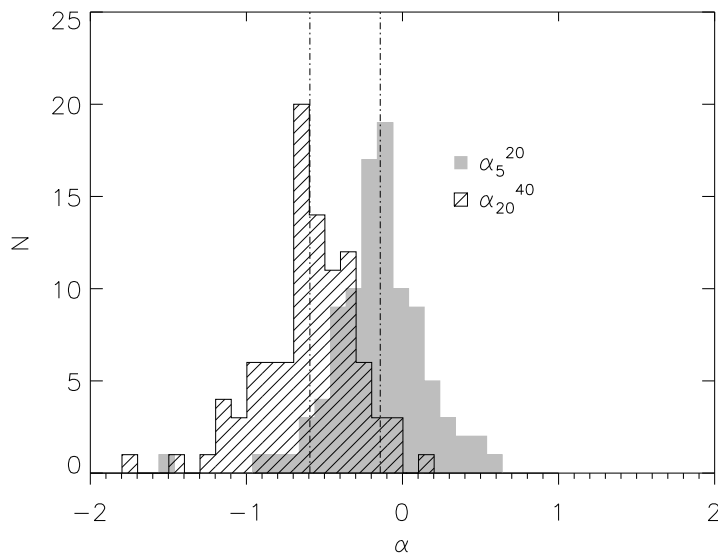


**Figure 4.12:** Distributions of  $\alpha_5^{20}$  (shaded area) and of  $\alpha_{20}^{40}$  (hatched area) for the PACO faint sample ( $200 \leq S_{20GHz} \leq 500$  mJy).

**Table 4.2:** Matrix of median spectral indices calculated from the fitting double power-law function for the PACO bright sample.

Frequency [GHz]	10	15	20	30	40
5	0.04	-0.02	-0.07	-	-
10	-	-0.12	-0.19	-	-
15	-	-	-0.25	-0.38	-
20	-	-	-	-0.45	-0.55
30	-	-	-	-	-0.70

**Table 4.3:** Matrix of median spectral indices calculated from the fitting double power-law function for the PACO faint sample.

Frequency [GHz]	10	15	20	30	40
5	0.01	-0.06	-0.09	-	-
10	-	-0.15	-0.21	-	-
15	-	-	-0.29	-0.39	-
20	-	-	-	-0.44	-0.53
30	-	-	-	-	-0.65

## 4. DATA ANALYSIS

---

**Table 4.4:** Fractions of PACO sources with  $\simeq 19$  GHz (more precisely, at 18.768 GHz) flux densities (mJy) within the bins indicated in the first column, found in the 32.768 (upper panel) and 39.768 GHz (lower panel) bins listed in the first row. The values in parenthesis are the number of sources in each 19 GHz bin.

$S_{19\text{GHz}} \backslash S_{33\text{GHz}}$	200-250	250-400	400-750	750-1000	1000-1500	1500-2000	2000-5000
200-250 (23)	0.11	0.	0.	0.	0.	0.	0.
250-400 (38)	0.45	0.39	0.	0.	0.	0.	0.
400-750 (68)	0.03	0.37	0.59	0.	0.	0.	0.
750-1000 (28)	0.	0.	0.85	0.15	0.	0.	0.
1000-1500 (35)	0.	0.	0.17	0.45	0.38	0.	0.
1500-2000 (15)	0.	0.	0.	0.	0.60	0.40	0.
2000-5000 (11)	0.	0.	0.	0.	0.07	0.33	0.60
$S_{19\text{GHz}} \backslash S_{40\text{GHz}}$	200-250	250-400	400-750	750-1000	1000-1500	1500-2000	2000-5000
200-250 (23)	0.11	0.	0.	0.	0.	0.	0.
250-400 (38)	0.26	0.29	0.	0.	0.	0.	0.
400-750 (68)	0.07	0.56	0.32	0.	0.	0.	0.
750-1000 (28)	0.	0.12	0.85	0.03	0.	0.	0.
1000-1500 (35)	0.	0.	0.34	0.45	0.21	0.	0.
1500-2000 (15)	0.	0.	0.	0.	0.70	0.30	0.
2000-5000 (11)	0.	0.	0.	0.	0.13	0.47	0.40

### 4.2 Source Counts

We use a combination of the faint and bright PACO measurements to estimate the distribution of flux densities at 33 or 40 GHz of sources with 19 GHz flux density within a given interval. Using the results in Table 4.4, we derive from the 20 GHz AT20G counts (Massardi et al., 2011b), the counts at 33 and 40 GHz.

Table 4.4 suggests that additional, albeit small, contributions to the counts in the lowest and in the highest 33 or 40 GHz flux density bins could come from sources outside the flux density range covered by the PACO samples. Thus, strictly speaking, the derived counts in these bins are lower limits. While at low flux densities the incompleteness arises from the flux density limit of the faint sample, at high flux densities it may be due to the limited sky coverage.

Figure 4.13 compares the present estimates of source counts (listed in Table 4.5) with those obtained from the *Planck* ERCSC (Planck Collaboration, 2011g) and from

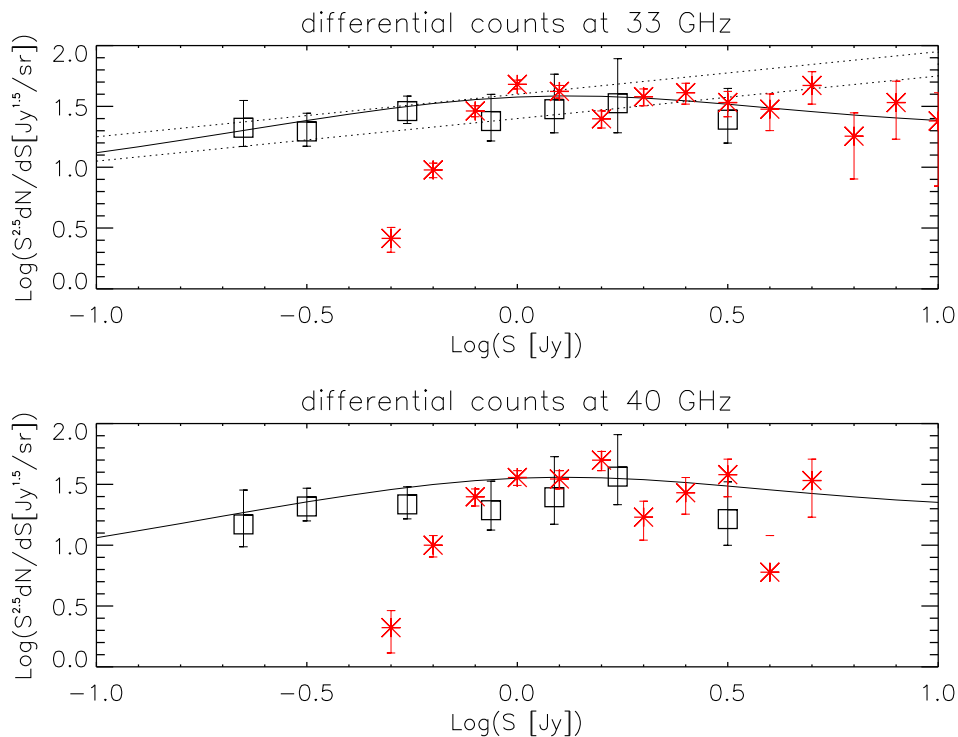


**Figure 4.13:** Differential source counts at 33 and 40 GHz (squares) compared with the *Planck* counts (Planck Collaboration, 2011g) at 30 and 44 GHz (red asterisks), and with the DASI estimate (Kovac et al., 2002) at 31 GHz (region bounded by dotted lines). The solid lines show the predictions of the de Zotti et al. (2005) model. From Bonavera et al. (2011).

the DASI experiment (Kovac et al., 2002). The agreement is very good in the region of overlap, and our data extend the counts downwards in flux density by a substantial factor compared to those obtained by Planck Collaboration (2011g). The predictions of the de Zotti et al. (2005) model are nicely consistent with these data.

The extension of the counts downwards in flux density is important to quantify the fluctuations in CMB maps due to sources below the detection limit,  $S_l$ . Since the differential counts below the completeness limits of the ERCSC ( $\simeq 1$  Jy at 30 GHz and  $\simeq 1.5$  Jy at 44 GHz) go roughly as  $dN/dS \propto S^{-2.2}$ , the amplitude of the power spectrum of Poisson fluctuations due to sources fainter than  $S_l$  goes as (de Zotti et al.,

## 4. DATA ANALYSIS

---

**Table 4.5:** Source counts at 32.744 (second column) and 39.768 GHz(third column), with their errors, obtained by extrapolating the AT20G source counts.

$\log(S)$ [Jy]	$\log(S^{2.5}dN/dS)_{33\text{GHz}}$ [Jy <sup>1.5</sup> /sr]	$\log(S^{2.5}dN/dS)_{40\text{GHz}}$ [Jy <sup>1.5</sup> /sr]
-0.65	1.32 (+0.22, -0.15)	1.17 (+0.28, -0.17)
-0.50	1.29 (+0.15, -0.12)	1.32 (+0.15, -0.12)
-0.26	1.46 (+0.12, -0.10)	1.33 (+0.15, -0.13)
-0.06	1.38 (+0.22, -0.16)	1.29 (+0.24, -0.16)
0.09	1.48 (+0.29, -0.19)	1.39 (+0.33, -0.22)
0.24	1.53 (+0.37, -0.24)	1.56 (+0.35, -0.23)
0.50	1.39 (+0.26, -0.19)	1.21 (+0.31, -0.22)

1996):

$$C = \Omega \int_0^{S_l} \frac{dN}{dS} S^2 dS \propto S_l^{0.8}, \quad (4.2)$$

where  $\Omega$  is the beam solid angle. This means that more than 70% of the residual point source fluctuations in *Planck* 30 and 44 GHz maps, after subtraction of directly detected sources, are contributed by sources in the flux density range covered by the PACO survey. Note that fluctuations due to clustering, not taken into account in the above equation, are negligible in the case of radio sources because of the strong dilution due to the broadness of the luminosity function.

The effect of an assessment of the counts down to fainter flux limits on the contribution to the power spectrum of radio sources below the detection limit is shown in Figure 4.14. Here the dotted line refers to the completeness limits of the ERCSC (Planck Collaboration, 2011b), 1 Jy at 33 GHz and 1.5 Jy 40 GHz (Planck Collaboration, 2011g). The present assessment of the counts down to 200 mJy decreases the amplitude of the extragalactic source power spectrum as shown by the dashed lines.

### 4.3 Variability

#### 4.3.1 The PACO Bright Sample

Most of the sources in this sample have been observed several times to monitor the flux density variations between the first two *Planck* surveys, carried out six months apart. Thus we typically re-observed each source after 6 months. More frequent monitoring

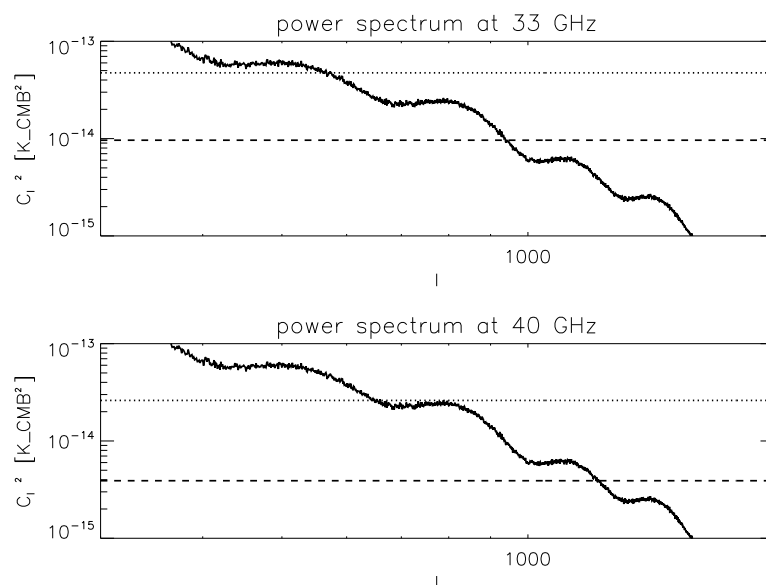


**Figure 4.14:** Contribution of extragalactic point sources to the CMB power spectrum (black solid line) for different flux density limits. In each panel the upper (dot-dashed) line refers to the ERCSC completeness limit (1 Jy at 33 GHz and 1.5 Jy 40 GHz), while the lower (dashed line) refers to the flux density limit of the PACO faint sample (200 mJy). From [Bonavera et al. \(2011\)](#).

**Table 4.6:** Median variability index of the PACO bright sample at varying frequency and time lag range.

Time lag[d]	5.5 GHz	9 GHz	18 GHz	24 GHz	33 GHz	39 GHz
90	3.5±0.8	6.3±1.2	5.2±1.4	5.7±1.2	6.7±1.3	7.5±0.9
180	5.4±1.0	5.8±1.1	5.4±1.0	7.6±1.1	6.3±1.5	7.5±1.2
270	8.3±1.8	5.0±2.0	9.2±1.3	8.4±1.3	10.6±2.3	11.3±2.4

## 4. DATA ANALYSIS

---

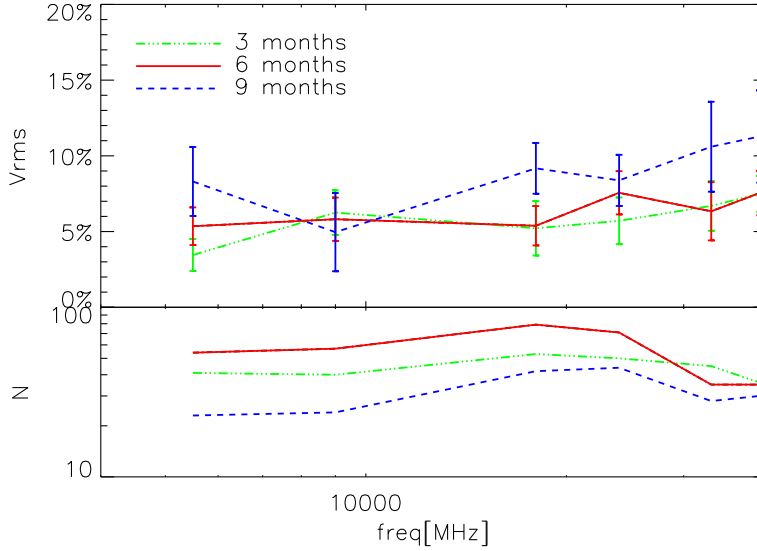


**Figure 4.15:** Top: median variability index of the sample as a function of frequency; error bars are  $\sigma/\sqrt{N-1}$ . Bottom: number of pairs. From [Massardi et al. \(2011a\)](#).

was carried out only if spare time was available. Therefore observations with time lags shorter or longer than 6 months were done only for limited sub-samples.

Following [Sadler et al. \(2006\)](#) we define the variability index as:

$$V_{rms} = \frac{100}{\langle S \rangle} \sqrt{\frac{\sum [S_i - \langle S \rangle]^2 - \sum \sigma_i^2}{N}}, \quad (4.3)$$

where  $S_i$  are the flux densities of a given sources measured at different epochs,  $\sigma_i$  are the associated errors,  $N$  is the number of measurements, and  $\langle S \rangle$  is the mean flux density.

To estimate the variability over a certain time interval we have selected for each source of the sample only the pairs of observations (i.e.,  $n=2$ ) spaced by the same time interval within  $\pm 20\%$ . For each pair we computed the variability index according to the previous relation, ( $\langle S \rangle$  being the mean over all the available measurements, and thus our best estimate of the mean source flux density) and then averaged over all the pairs obtained for the same source. In [Figure 4.15](#) we show the median variability index for the sample of sources as a function of frequency for time intervals of 3, 6, and 9 months (upper panel) and the number of pairs obtained for those time intervals (lower panel).

We find, as expected (Ciarabella et al., 2004; Impey and Neugebauer, 1988), a trend toward an increase of the variability amplitude with frequency (see Table 4.6 and Figure 4.15). There is also a marginal indication of higher variability for the longer time lag, consistent with earlier results (Ciarabella et al., 2004). On the other hand, around 20 GHz the median variability index for a 9 months lag is  $\simeq 9 \pm 1.7\%$ , slightly larger than that found by Sadler et al. (2006) over a one year time-scale (6.9%) for a somewhat fainter sample (flux density limit of 100 mJy). The distribution of  $V_{rms}$ , however is similar to that found by Sadler et al. (2006), for example  $37 \pm 9\%$  of our sources show a variability index larger than 10% to be compared with  $42 \pm 7\%$  for the Sadler et al. (2006) sample.

#### 4.3.2 Comparison of PACO with AT20G measurements

The AT20G flux densities have been collected in several epochs between 2004 and 2008. Therefore, the time lag between the AT20G and the PACO observations ranges from several months to several years. Since variable sources are more likely to meet the detection limit of a blind survey if they are in a bright phase, it is not surprising that, on average, AT20G flux densities are slightly higher than the PACO ones. After correcting for the small frequency difference between the PACO and AT20G observations, using our measured spectral indices between 18.768 and 23.232 GHz, we find  $\langle \log_{10}(S_{AT20G}/S_{PACO}) \rangle = 0.043$ , where the PACO flux density is scaled to 20 GHz. A comparison of the two flux densities is shown in Figure 4.16. The least-squares linear relationship is  $S_{PACO}[Jy] = (0.89 \pm 0.04) \cdot S_{AT20G}[Jy] + (0.05 \pm 0.05)$ , showing no statistically significant deviations from a constant ratio between the two flux densities.

It is important to note, in this respect, that the observations have been performed with the same front-end system, but the back-end has changed. Last, but not least, the new CABB system requires a more careful account of the spectral behaviour of the sources during the analysis, because of the broader bands. Our findings add to a series of indications of the high performance of the new system and show that there are no obvious instrumental effects that may complicate the comparison with measurements obtained before its upgrade.

Since both the PACO and the AT20G measurement errors are negligibly small, the variability at  $\simeq 20$  GHz can be estimated as the standard deviation of the distribution of  $S_{PACO}/S_{AT20G}$  or of  $\log_{10}(S_{PACO}/S_{AT20G})$ . The distribution of the latter quantity

#### 4. DATA ANALYSIS

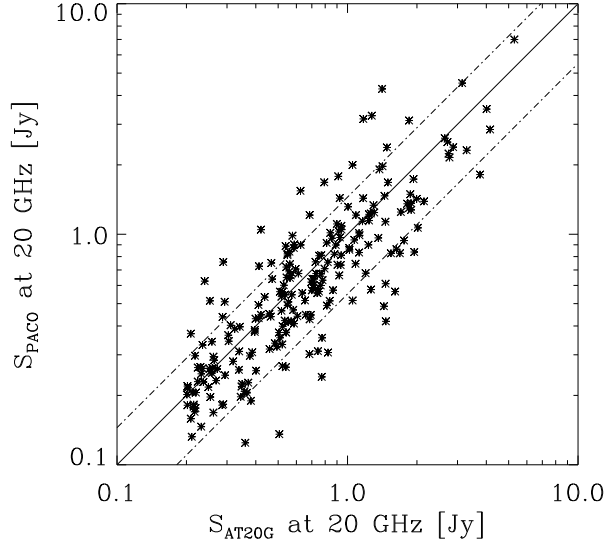


**Figure 4.16:** Comparison between the AT20G flux densities at 20 GHz and the PACO ones scaled to 20 GHz. The solid line corresponds to  $S_{\text{AT20G}} = S_{\text{PACO}}$  and the dot-dashed lines correspond to  $S_{\text{PACO}} = S_{\text{AT20G},20\text{GHz}}(1 \pm \sigma_v)$ . From [Bonavera et al. \(2011\)](#).

is better fitted by a Gaussian than that of the former one, see Figure 4.17. The dotted line is the Gaussian best-fit, centred at  $-0.03$  with  $\text{FWHM} = 0.34$ , and the dashed lines are the mean and the mean  $\pm \sigma$  of the distribution. The mean and the standard deviation,  $\sigma$ , of  $\log_{10}(S_{\text{PACO}}/S_{\text{AT20G}})$  are  $-0.043$  and  $0.18$ , respectively, corresponding to a dispersion  $\sigma_v = \sigma(S_{\text{PACO}}/S_{\text{AT20G}}) \simeq 0.40$ , on a time-scale of a few years. For comparison [Sajina et al. \(2011\)](#) found for the ratio  $S_{\text{AT20G}}/S_{\text{VLA}}$  a mean value of  $1.23$  and a standard deviation of  $0.27$ . Our result is consistent with earlier indications (i.e., [Ciaramella et al., 2004](#)) that the variability increases with the time lag, for lags of up to several years.

An inspection of Figure 4.16 suggests that the dispersion  $\sigma_v$  may be somewhat lower at the fainter flux densities. For the flux density interval  $0.2 \leq S_{\text{AT20G}} < 0.4 \text{ Jy}$  we find  $\langle \log_{10}(S_{\text{PACO}}/S_{\text{AT20G}}) \rangle = -0.03$  and  $\sigma[\log_{10}(S_{\text{PACO}}/S_{\text{AT20G}})] = 0.17^{+0.01}_{-0.02}$ , while for  $S_{\text{AT20G}} \geq 0.4 \text{ Jy}$  we have  $\langle \log_{10}(S_{\text{PACO}}/S_{\text{AT20G}}) \rangle = -0.05$  and  $\sigma[\log_{10}(S_{\text{PACO}}/S_{\text{AT20G}})] = 0.19^{+0.01}_{-0.01}$ . The 68% confidence errors on  $\sigma$  have been computed following [Danese et al. \(1980\)](#). The difference however is not statistically significant, as confirmed by a KS

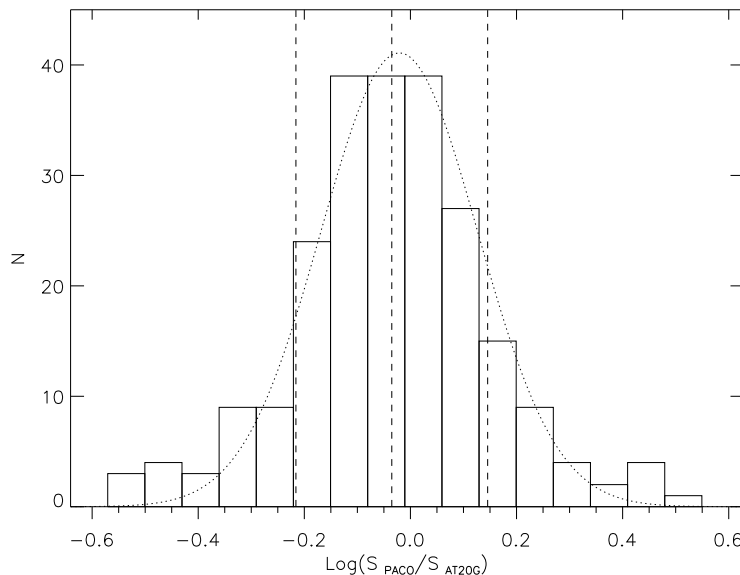


**Figure 4.17:** Distribution of  $\log_{10}(S_{\text{PACO}}/S_{\text{AT20G}})$  at  $\simeq 20$  GHz. The dotted line is the Gaussian best-fit. The dashed lines are the mean and the mean  $\pm\sigma$  of the distribution. From [Bonavera et al. \(2011\)](#).

test that yields 3.8% probability that the two distributions come from the same parent population.

We have made the same analysis at lower frequency by comparing  $S_{\text{PACO},4.7\text{GHz}}$  with the flux densities at 4.8 GHz measured in the AT20G follow-up observations. The least square linear relation between the two sets of observations (see Figure 4.18) gives  $S_{\text{PACO}}[Jy] = (0.92 \pm 0.03) \cdot S_{\text{AT20G}}[Jy] + (0.05 \pm 0.04)$ , confirming the pre- and post-CABB compatibility also at these frequencies. The variability ( $\sigma_v$ ) is 38% and the mean and standard deviation of the  $\log_{10}(S_{\text{PACO}}/S_{\text{AT20G}})$  distribution are -0.006 and 0.15 respectively.

An estimate of the variability at 33 and 40 GHz can be obtained comparing the distribution of spectral indices  $\alpha_{19}^{33}$  or  $\alpha_{19}^{40}$ , based on simultaneous PACO observations with those obtained replacing the  $\sim 19$  GHz PACO flux densities with the AT20G 20 GHz ones. Variability enhances the dispersion of the distribution of spectral indices based on non simultaneous observations. Let  $f$  be the ratio between the flux density at the frequency  $\nu$  of a source at the time of AT20G 20 GHz observations and that

#### 4. DATA ANALYSIS

---

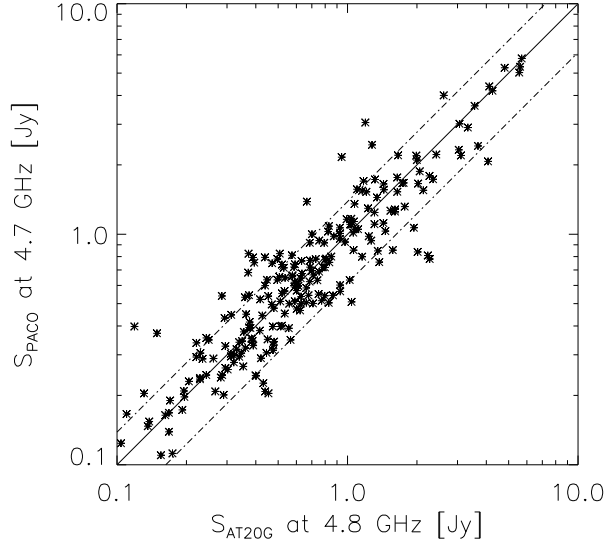


**Figure 4.18:** Comparison between the AT20G flux densities at 4.8 GHz and the PACO ones at 4.744 GHz. The solid line corresponds to  $S_{\text{AT20G}} = S_{\text{PACO}}$  and the dot-dashed lines correspond to  $S_{\text{PACO},4.7\text{GHz}} = S_{\text{AT20G},4.8\text{GHz}}(1 \pm \sigma_v)$ . From [Bonavera et al. \(2011\)](#).

at the moment of PACO observations,  $\alpha_s$  the spectral index between  $\sim 19$  GHz and  $\nu$  determined from the simultaneous PACO observations, and  $\alpha_{ns}$  the non-simultaneous spectral index between 20 GHz and  $\nu$  obtained combining the AT20G measurements at 20 GHz with the PACO measurements at  $\nu$ . Then, neglecting the effect of the small frequency difference between AT20G 20 GHz and PACO  $\sim 19$  GHz observations, we have:

$$\left(\frac{\sigma(f)}{f}\right)^2 = \ln^2(\nu/20 \text{ GHz}) [\sigma^2(\alpha_{ns}) - \sigma^2(\alpha_s)]. \quad (4.4)$$

For  $\nu = 33$  GHz we get  $\sigma(\alpha_{ns}) = 0.91$ ,  $\sigma(\alpha_s) = 0.34$ , whence  $\sigma(f)/f = 0.42$  or  $\sigma[\log_{10}(f)] = 0.18$ . The results for  $\nu = 40$  GHz are similar:  $\sigma(\alpha_{ns}) = 0.70$ ,  $\sigma(\alpha_s) = 0.34$ , whence, again,  $\sigma(f)/f = 0.42$  or  $\sigma[\log_{10}(f)] = 0.18$ . This hints at an increase of the variability amplitude from 20 GHz to 33 or 40 GHz, consistent with earlier results ([Ciaramella et al., 2004](#); [Impey and Neugebauer, 1988](#)).

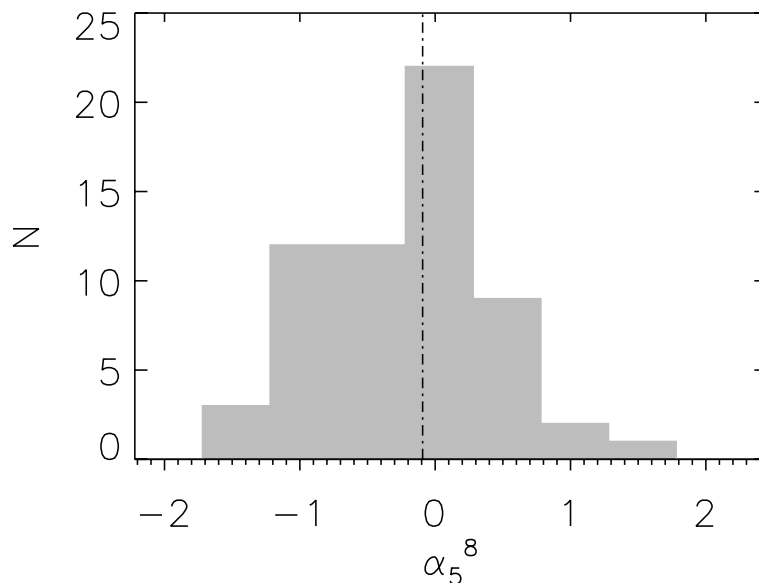


**Figure 4.19:** Distribution of spectral indices in the 5-8 GHz frequency ranges for the SiMPIE sample. From [Procopio et al. \(2011\)](#).

#### 4.4 The SiMPIE Northern Sample

The sample consists of 79 objects with declination  $> 45^\circ$ . Of these, 69 are selected in the NEWPS catalogue and 10 are Galactic objects that may show strong outbursts during the *Planck* mission and selected because of previous monitoring at the Noto observatory.

For each source we have identified the best epoch of observations as the one with measurements both 5 and 8.3 GHz. In case of multiple epochs with both frequencies we have chosen those having higher signal-to-noise ratio at both frequencies. We thus have a sample of 61 sources for which we estimated the spectral indices  $\alpha_5^{8.3}$  ( $S \propto \nu^\alpha$ ). The median spectral index is -0.09 with a standard deviation of 0.62 (see Figure 4.19). This is compatible with the 5-10 GHz spectral index found for the PACO samples (median value of 0.064 and interquartile range [-0.12, 0.30] for the bright sample and median value of -0.04 and interquartile range [-0.87, -0.48] for the faint sample).

33 sources have a counterpart in the *Planck* ERCSC ([Planck Collaboration, 2011b](#)). The median of the 5-30 GHz spectral index is -0.07 (see Figure 4.20). For this sample the 30-70 GHz spectral index, based on ERCSC data, is -0.16.

We have compared our sample flux densities with the 4.85 GHz GB6 catalogue

## 4. DATA ANALYSIS

---

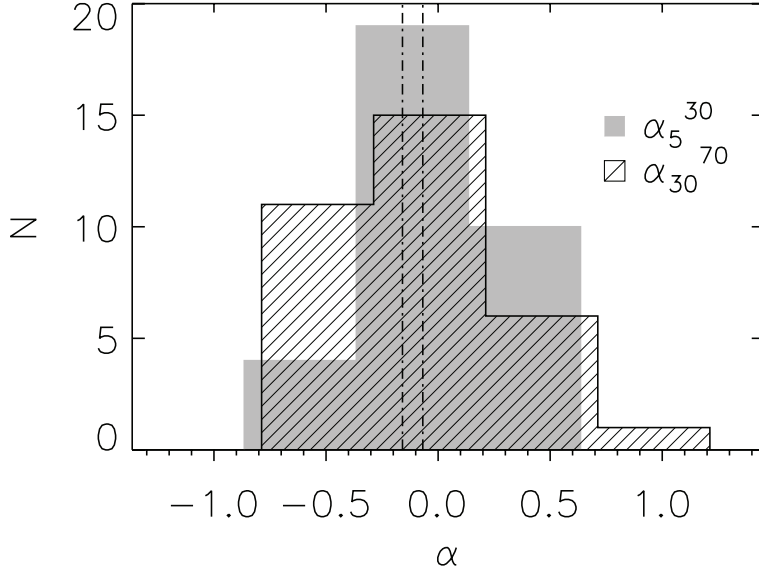


**Figure 4.20:** Distribution of spectral indices in the 5-30 (shaded area) and 30-70 GHz (hatched area) frequency ranges for the SiMPIE sample. From [Procopio et al. \(2011\)](#).

([Gregory et al., 1996](#)). 60 objects in the Northern sample have a counterpart in the GB6 catalogue. As stated in Section 3.1, of the 79 sources in the SiMPIE northern sample, 10 have no counterparts in existing catalogues, two do not have reliable SiMPIE measurements at 5 GHz and 7 lie in the  $\delta > 75^\circ$  region not covered by the GB6 survey.

### 4.5 Calibration Issues

The flux density scale for the ATCA is well determined for frequencies up to 20 GHz but there are known problems at higher frequencies. The difficulty occurs because interferometers (such as the ATCA and CARMA), which can make the most precise flux measurements at high frequencies, need point sources to calibrate and the strong point sources at those frequencies are highly variable AGNs. This has led to the use of the planets, Mars and Uranus, as primary calibrators. Their flux estimation relies on complex atmospheric models. In particular it is known for Uranus that there is an orbital change in flux: during the Uranian year our view changes from equatorial to polar angles.

The absolute calibration of the *Planck* detectors up to 353 GHz is derived from the annual modulation of the CMB dipole by the satellite orbit around the Sun. An

absolute measurement of the dipole is obtained by differentiating along a spin period. The CMB dipole direction is expected to be recovered to better than  $\sim 2$  arcmin, and its amplitude to better than 0.5% (Planck Collaboration, 2006). The goal of *Planck* is to obtain a photometric calibration better than 1% for all frequency channels up to 353 GHz. As discussed in López-Caniago et al. (2007) the main limitation to the accuracy of *Planck* flux densities is confusion due to faint sources within the beam. Leach et al. (2008) estimated typical rms fluctuations  $\sim 100$  mJy for the 30 and 44 GHz channels at high Galactic latitude. This corresponds to a few percent of the flux density of the brightest extragalactic sources. At 100 GHz, the smaller beam size and the relatively steep spectrum of the average confusing source makes confusion much less important. The confusion level at this frequency should be comparable to or smaller than the variability error.

Thus ground based observations, simultaneous with *Planck* and at approximately the same frequencies, of very bright sources can be used to assess the absolute flux densities of calibrators for ground based telescopes. This is considered by the *Planck* Science Team as one of the contributions of the satellite to the scientific community. The PACO project has enough observations to determine the relative flux density scale between *Planck* and the ATCA.

Table 4.7 lists the 7 mm PACO flux densities measured in epochs simultaneous to *Planck* observations for the 6 bright compact sources in the PACO sample, selected as those having 20 GHz flux density  $S_{AT20G} > 5$  Jy and unflagged observations simultaneous to the *Planck* satellite that could be used for calibration of the flux densities (note that, with the only exception of AT20GJ053850-440508, they do not belong to the bright sample because of their position). All of them are well-known highly variable blazars. Two of them are equatorial sources and are currently used in some ad-hoc observational runs for cross-calibration between Southern and Northern hemisphere telescopes, in order to assure that the *Planck* absolute calibration could be shared with all the major ground-based facilities.

As noted above, the ERCSC (Planck Collaboration, 2011b) fluxes are unsuitable for calibrating ground-based telescopes. A proper comparison with *Planck* flux density scales will be possible, and will be done, when *Planck* time ordered data will become available.

**Table 4.7:** The 7 mm flux densities for the point-like calibrators in the PACO sample selected as those having  $S_{AT20G} > 5\text{Jy}$  as observed in epochs simultaneous to the *Planck* satellite observations.

AT20G name	RA	$\delta$	Observing	$S_{32.2\text{GHz}}$	$S_{32.7\text{GHz}}$	$S_{33.2\text{GHz}}$	$S_{33.7\text{GHz}}$	$S_{38.2\text{GHz}}$	$S_{38.7\text{GHz}}$	$S_{39.2\text{GHz}}$	$S_{39.7\text{GHz}}$
	[hr]	[deg]	Date	[mJy]							
AT20G053850-440508	5.6473226	-44.0858154	2010-02-28	9506	9483	9385	9356	8962	8921	8864	8893
				118	118	117	117	112	111	110	111
AT20G053850-440508	5.6473226	-44.0858154	2010-03-15	14278	14210	14135	14137	14848	14620	14639	14814
				187	186	185	185	195	192	192	194
AT20G053850-440508	5.6473226	-44.0858154	2009-09-15	6344	6352	6339	6339	6192	6156	6177	6141
				92	92	92	92	89	89	89	89
AT20G125611-054721	12.9364349	-5.7893119	2010-07-16	14740	14665	14669	14659	14041	13956	14064	14089
				126	126	126	126	120	120	121	121
AT20G133739-125724	13.6277171	-12.9568596	2010-07-16	4228	4197	4188	4181	3974	3955	3922	3876
				36	36	36	35	34	34	33	33
AT20G183339-210341	18.5610881	-21.0611248	2009-09-26	3256	3210	3174	3132	2750	2714	2674	2639
				16	16	16	16	14	13	13	13
AT20G192451-291430	19.4141825	-29.2417011	2010-04-01	17111	17807	17451	17748	0	0	0	0
				196	204	200	203	0	0	0	0
AT20G192451-291430	19.4141825	-29.2417011	2010-04-10	14571	14696	14686	14357	14007	13782	13723	13891
				213	215	215	210	205	202	201	203
AT20G192451-291430	19.4141825	-29.2417011	2009-09-26	14028	13876	13789	13663	12490	12393	12263	12127
				71	71	70	69	63	63	62	62
AT20G192451-291430	19.4141825	-29.2417011	2009-10-07	15333	15248	15083	14820	14380	14225	14341	14617
				60	60	59	58	56	56	56	57
AT20G192451-291430	19.4141825	-29.2417011	2009-10-14	13728	13641	13475	13267	12282	12179	12076	12078
				122	122	120	118	110	109	108	108
AT20G222547-045701	22.4297933	-4.9503870	2009-11-06	6177	6098	5929	5905	5557	5337	5009	4978
				105	103	101	100	94	90	85	84
AT20G222547-045701	22.4297933	-4.9503870	2009-11-19	5589	5524	5469	5417	4910	4840	4794	4743
				110	109	108	107	97	95	94	93

## Chapter 5

# Multi-frequency SEDs of PACO Sources

### 5.1 Combining PACO with ERCSC data

As illustrated in Figure 5.1, the comparison between ATCA and ERCSC flux densities at the nearest frequencies (30 and 44 GHz, respectively), shows a reassuringly close agreement, the linear fit to  $y = mx + q$  for flux densities greater than 1 Jy and 1.5 Jy (at 30 and 44 GHz respectively) gives  $m = 1.03 \pm 0.01$  and  $q = 0.05 \pm 0.01$  at 30 GHz and  $m = 0.83 \pm 0.04$  and  $q = 0.20 \pm 0.04$  at 44 GHz. The faintest ERCSC flux densities are obviously enhanced by the effect of the Eddington bias, the boosting of estimated fluxes due to positive noise plus confusion fluctuations, which is further enhanced in the 44 GHz *Planck* channel, where the noise level is higher.

The results of the cross-match between PACO and ERCSC sources in all *Planck* channels are summarized in Table 5.1, where we also list the adopted search radii and the rms values of the distances between *Planck* and PACO positions in each channels. We also present the results for the PACO bright sample sources only. The rms values are much lower than the search radii, and consistent with the rms positional errors being lower than FWHM/5, as found in [Planck Collaboration \(2011b\)](#). The distribution of angular distances between PACO and ERCSC positions are given in Figure 5.2 for all the *Planck* channels except for the one at 857 GHz for which the number of common sources is very small. Figure 5.3 shows the positional difference in  $\Delta_{RA} \cos(\delta_{ERCSC})$  and  $\Delta_{\delta}$  for each PACO sources detected in *Planck*. The red circle corresponds to the

## 5. MULTI-FREQUENCY SEDS OF PACO SOURCES

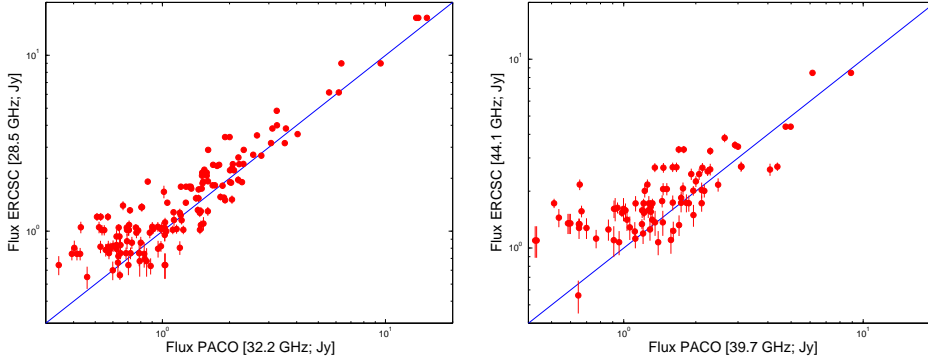


**Figure 5.1:** Comparison between the ERCSC flux densities at 30 GHz (left panel) and at 44 GHz (right panel) with the almost simultaneous ATCA measurements (PACO project) at 32.2 and 39.7 GHz, respectively. No correction for the slightly different frequencies has been applied. From [Planck Collaboration \(2011g\)](#).

**Table 5.1:** Number of PACO sources present in the ERCSC and rms distances between ERCSC and PACO positions, for each frequency channel.

freq (GHz)	search radius (arcmin)	number of sources-all PACO	rms distance all PACO (arcmin)	number of sources-bright sample	rms distance bright sample (arcmin)
30	15	203	2.6	111	2.7
44	12	112	2.5	63	2.4
70	7	117	1.4	64	1.4
100	5	198	1.0	102	1.0
143	4	214	0.8	112	0.8
217	3	160	0.4	83	0.4
353	3	67	0.6	34	0.7
545	3	18	0.6	10	-
857	3	8	-	6	-

## 5.1 Combining PACO with ERCSC data

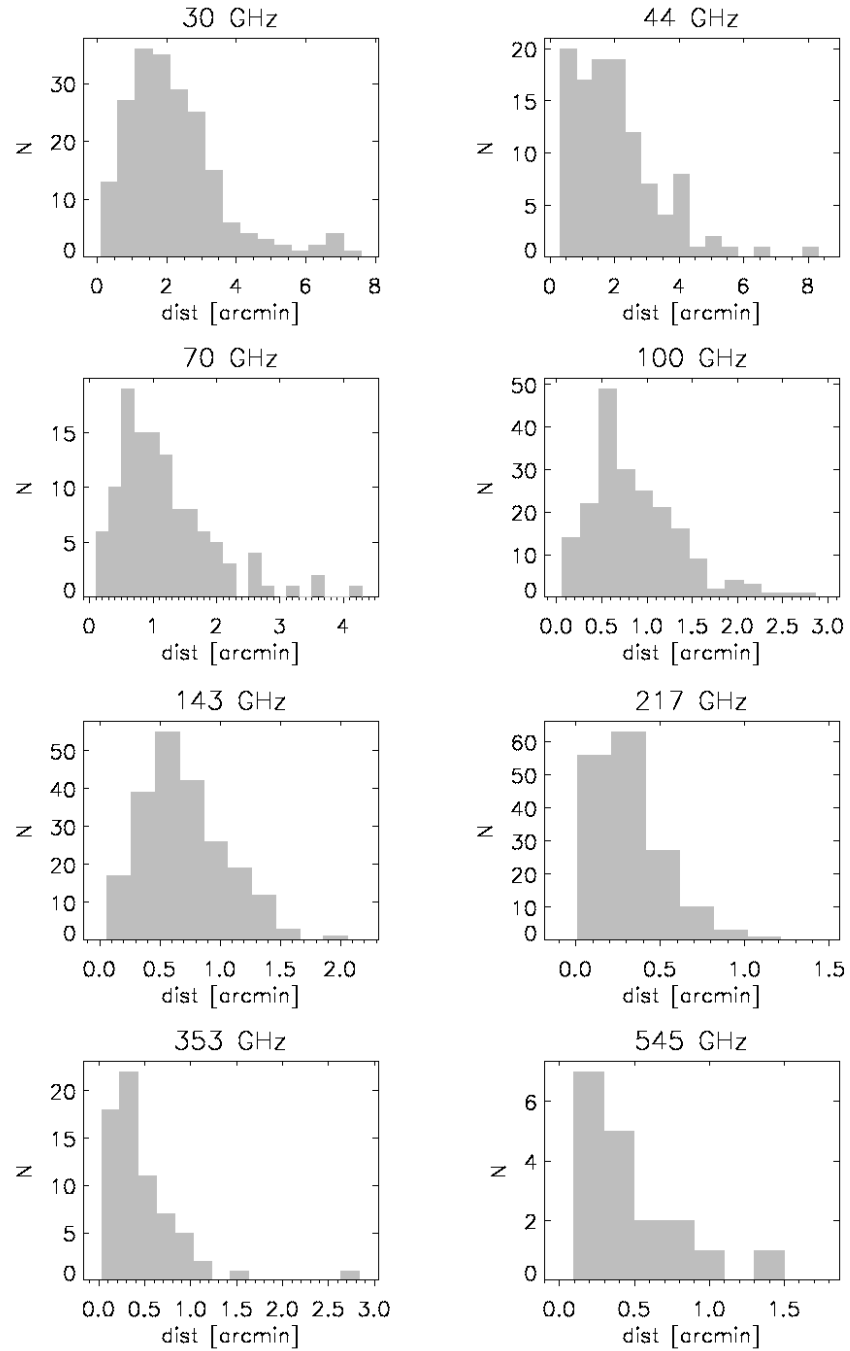


**Figure 5.2:** Distribution of the angular distances (in arcmin) between the PACO and the ERCSC positions of PACO sources detected in the *Planck* channels.

## 5. MULTI-FREQUENCY SEDS OF PACO SOURCES

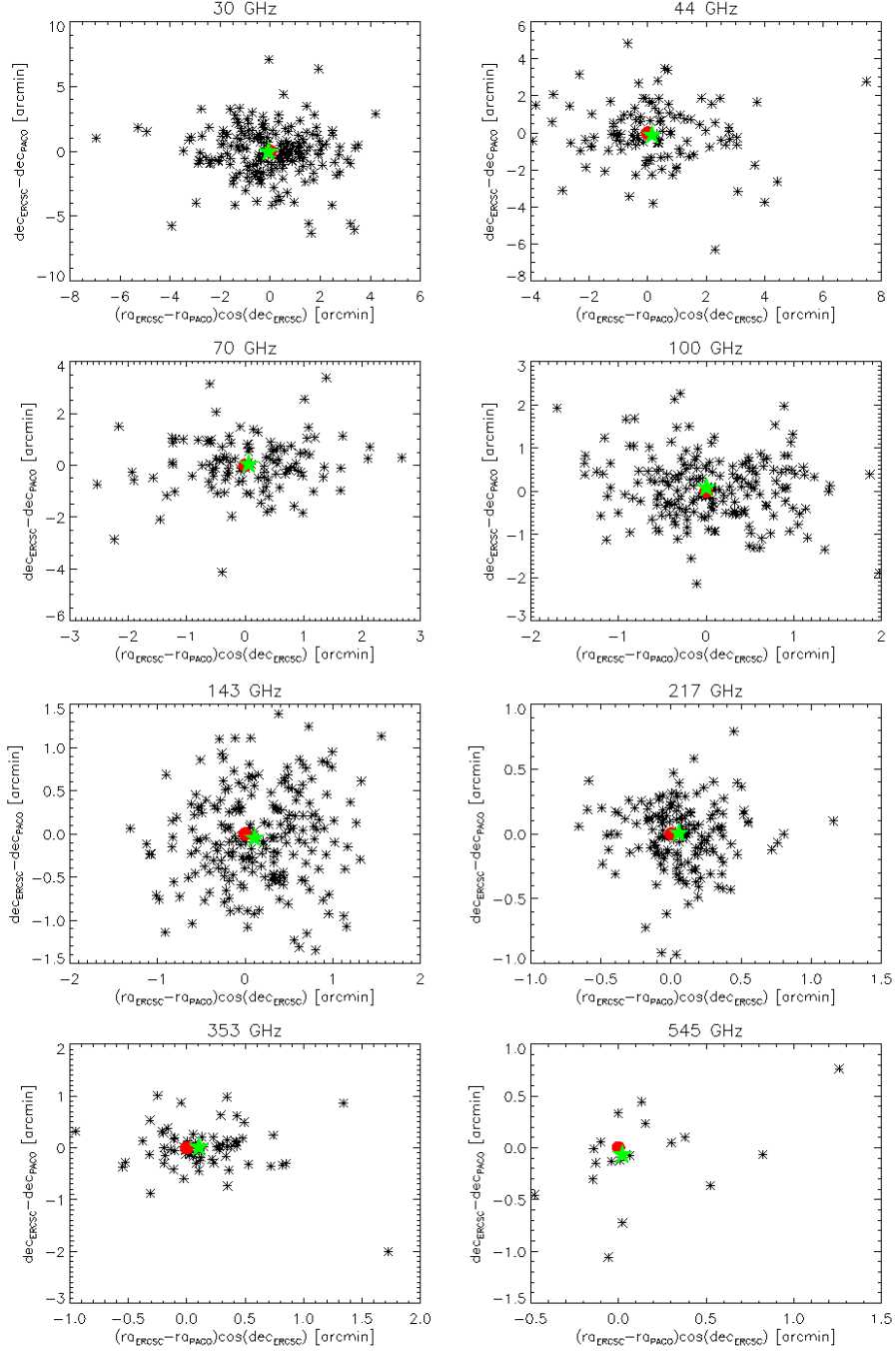


**Figure 5.3:** Plot of the  $\Delta_{RA} \cos(\delta_{ERCSC})$  and  $\Delta_{\delta}$  (in arcmin) between the PACO and the ERCSC positions of PACO sources detected in the *Planck* channels (black asterisks). The red circle corresponds to the ideal case of  $\Delta_{RA} \cos(\delta_{ERCSC}) = \Delta_{\delta} = 0$  and the green star to the median values of  $\Delta_{RA} \cos(\delta_{ERCSC})$  and  $\Delta_{\delta}$ .

## 5.1 Combining PACO with ERCSC data

---

ideal case of  $\Delta_{RA} \cos(\delta_{ERCSC}) = \Delta_{\delta} = 0$  and the green star to the median values of  $\Delta_{RA} \cos(\delta_{ERCSC})$  and  $\Delta_{\delta}$ . The mean, median and  $\sigma$  values for these quantities are listed in Table 5.2

We show in Figure 5.4 the spectra determined combining the PACO (black asterisks) and ERCSC (red diamonds) data for sources with ERCSC flux densities in at least three *Planck* channels.

In the case of the PACO faint sample, 57 sources are in the ERCSC (see Table 5.3 for each single *Planck* channel). We plot in Figure 5.5 the spatial distribution of sources together with the distribution of ERCSC sources, for the channels up to 70 GHz, in the same area and in neighbouring regions. The crosses are the PACO faint sample sources, the circles are the ERCSC sources. At 30 GHz there are 16 ERCSC sources within the region bounded by the dashed lines, not included in the present sample. Twelve lie either within regions excluded from the PACO sample, i.e. within the Large Magellanic Cloud (PLCKERC030 G276.20-33.22, PLCKERC030 G277.16-36.06, PLCKERC030 G277.62-32.14, PLCKERC030 G278.40-33.32, PLCKERC030 G279.49-31.67) or at  $|b| < 5^\circ$  (PLCKERC030 G252.05+03.28, PLCKERC030 G260.67-03.20, PLCKERC030 G263.73-03.72, PLCKERC030 G265.14+01.48, PLCKERC030 G267.93-01.02, PLCKERC030 G253.63-00.23, PLCKERC030 G248.44-04.00) areas. Three (PLCKERC030 G271.21-09.56, PLCKERC030 G249.07-05.17, PLCKERC030 G251.04-05.33) are at low Galactic latitude and were not detected by the AT20G survey, suggesting that they are extended Galactic sources or peaks of the Galactic diffuse emission. Two of them have a counterpart in NEWPS catalogue. The last one (PLCKERC030 G240.02-56.83) is Fornax A, missed by the AT20G because its core emission at 20 GHz is below the detection limit and its extended emission has a size exceeding the ATCA field-of-view (Massardi et al., 2008). Thus there is one potentially spurious source out of 42 at 30 GHz in the ERCSC in the PACO faint area, namely a fraction  $\leq 2\%$ . The PACO bright sample is not suitable for this analysis because of its higher flux density limit with respect to the PACO faint. In fact it turns out that the ERCSC contains ten 30 GHz sources that are included in the PACO faint sample but not in the PACO bright one. This is mostly the effect of variability. Seven of these sources had 18.7 GHz flux densities  $> 500$  mJy at the moment of PACO observations while they had 20 GHz flux densities  $< 500$  mJy in the AT20G catalogue. We performed the same analysis also at 44 and 70 GHz, finding three possibly spurious sources out of 30 at 40 GHz,

## 5. MULTI-FREQUENCY SEDS OF PACO SOURCES

---

**Table 5.2:** Mean, median and  $\sigma$  values for  $\Delta_{RA} \cos(\delta_{ERCSC})$  and  $\Delta_\delta$  for all *Planck* channels.

freq (GHz)		$\Delta_{RA} \cos(\delta_{ERCSC})$ (arcmin)	$\Delta_\delta$ (arcmin)
30	mean	-0.06	-0.09
	median	-0.07	-0.04
	$\sigma$	1.6	1.9
44	mean	0.2	-0.07
	median	0.1	-0.1
	$\sigma$	1.8	1.7
70	mean	0.05	0.02
	median	0.06	0.04
	$\sigma$	0.9	1.0
100	mean	0.05	0.07
	median	0.002	0.08
	$\sigma$	0.7	0.7
143	mean	0.1	-0.03
	median	0.1	-0.05
	$\sigma$	0.6	0.5
217	mean	0.07	-0.01
	median	0.06	0.006
	$\sigma$	0.3	0.3
353	mean	0.1	-0.009
	median	0.1	0.01
	$\sigma$	0.4	0.4
545	mean	0.1	-0.08
	median	0.02	-0.07
	$\sigma$	0.4	0.4

## 5.1 Combining PACO with ERCSC data

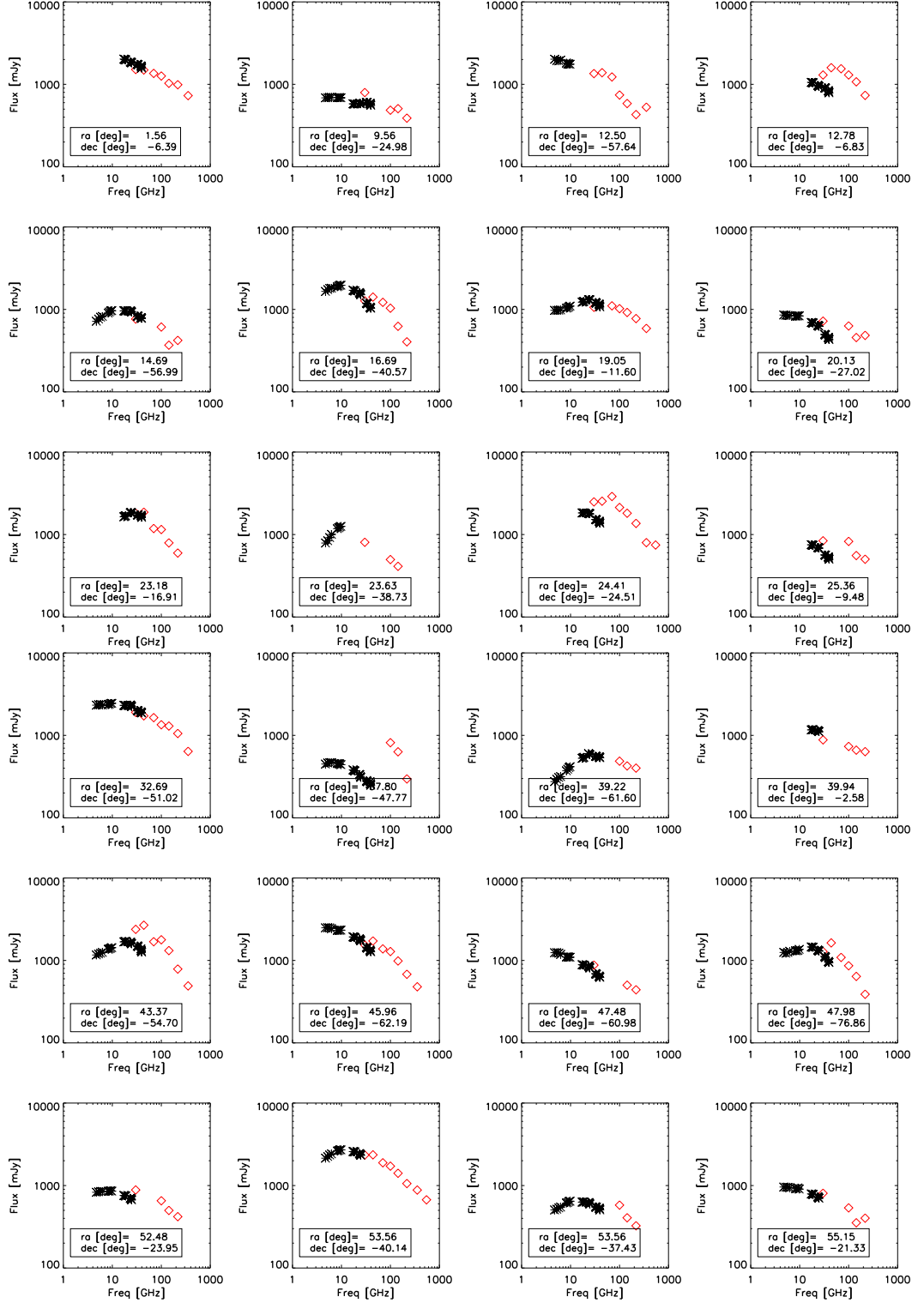


**Figure 5.4:** SEDs determined combining the PACO (black asterisks) and ERCSC (red diamonds) data sets of sources for which ERCSC flux densities in at least three *Planck* channels are available. The position of each source is also specified according to PACO RA and DEC coordinates.

## 5. MULTI-FREQUENCY SEDS OF PACO SOURCES

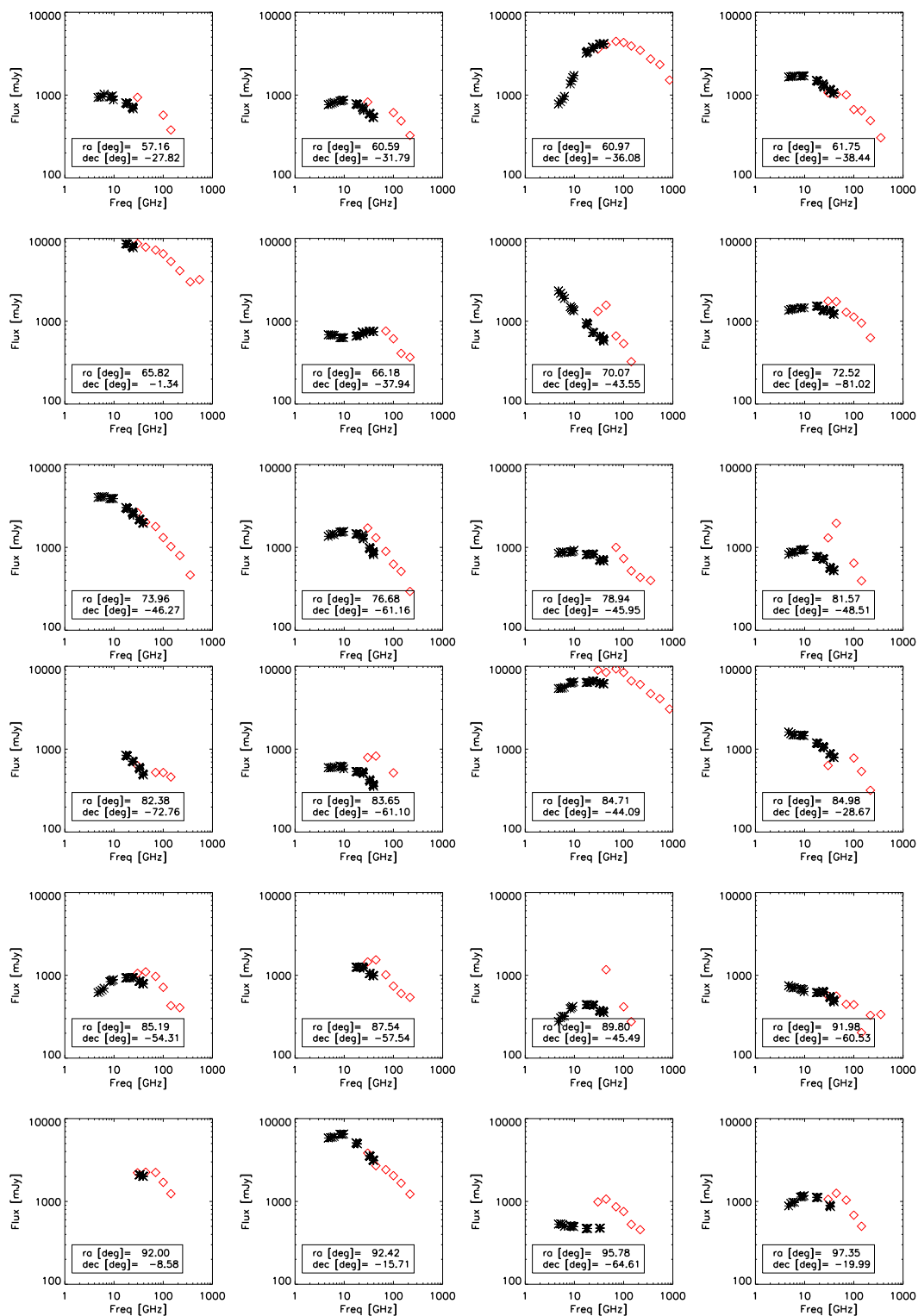


Figure 5.4: Continue.

## 5.1 Combining PACO with ERCSC data

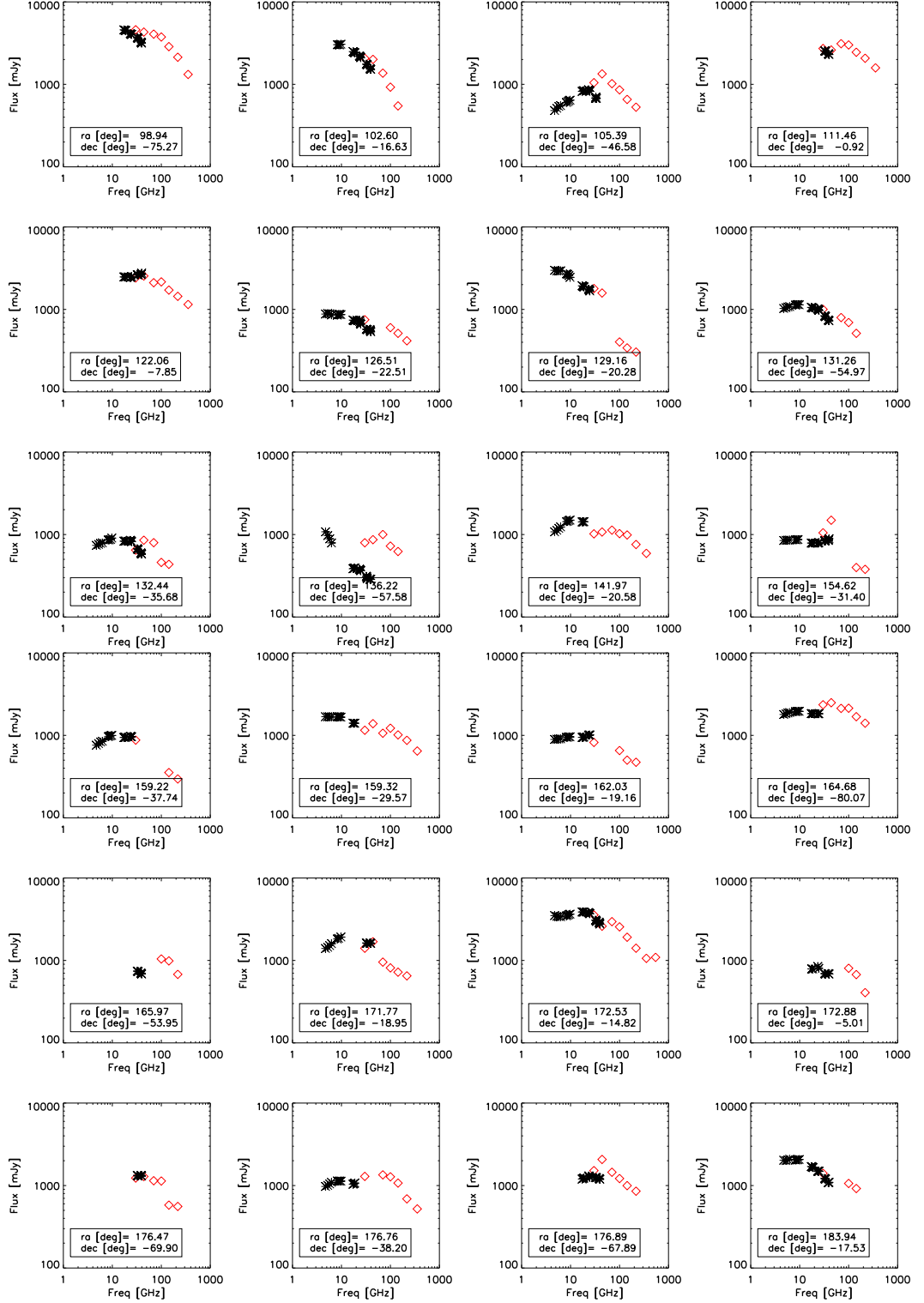


Figure 5.4: Continue.

## 5. MULTI-FREQUENCY SEDS OF PACO SOURCES

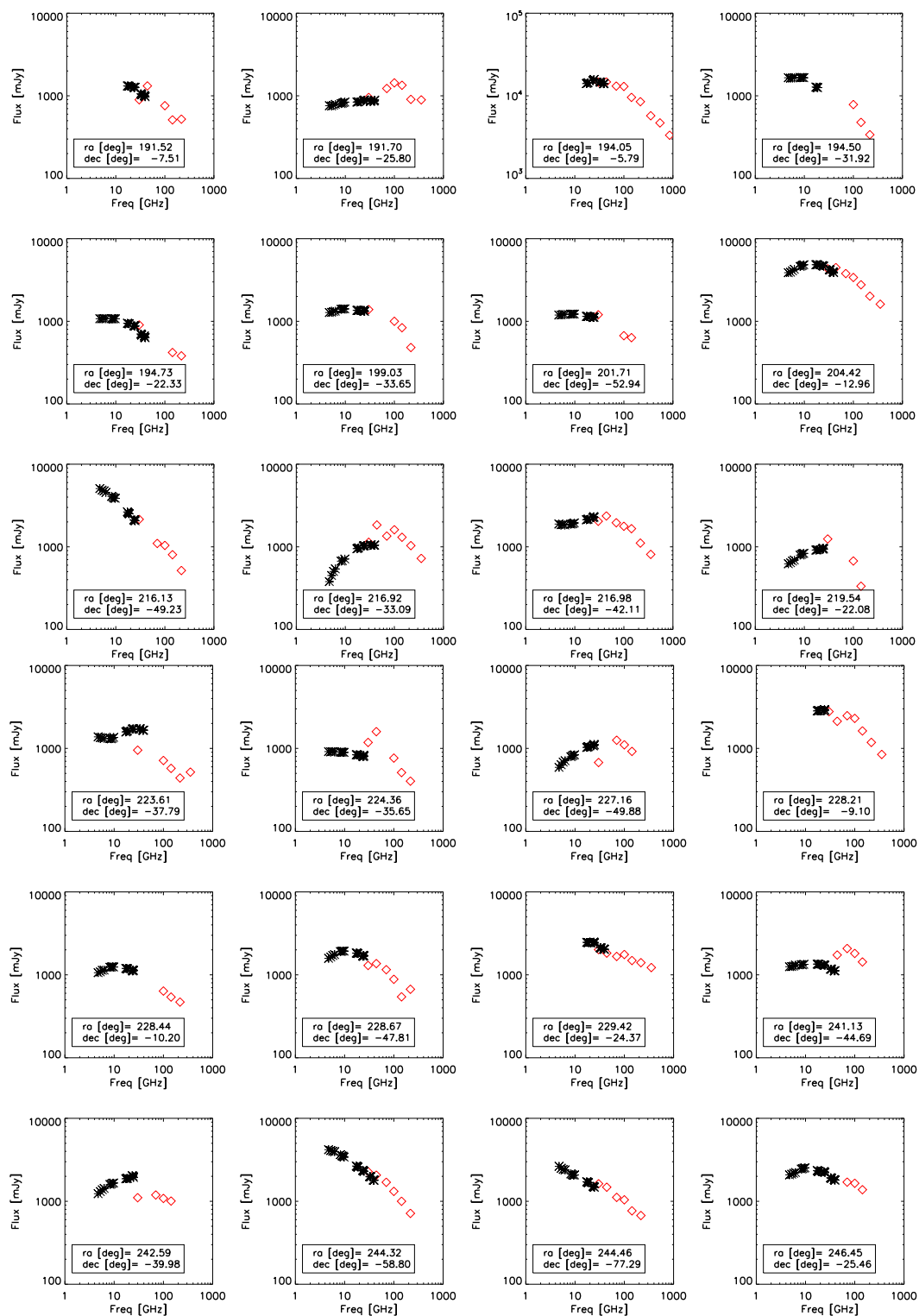


Figure 5.4: Continue.

## 5.1 Combining PACO with ERCSC data

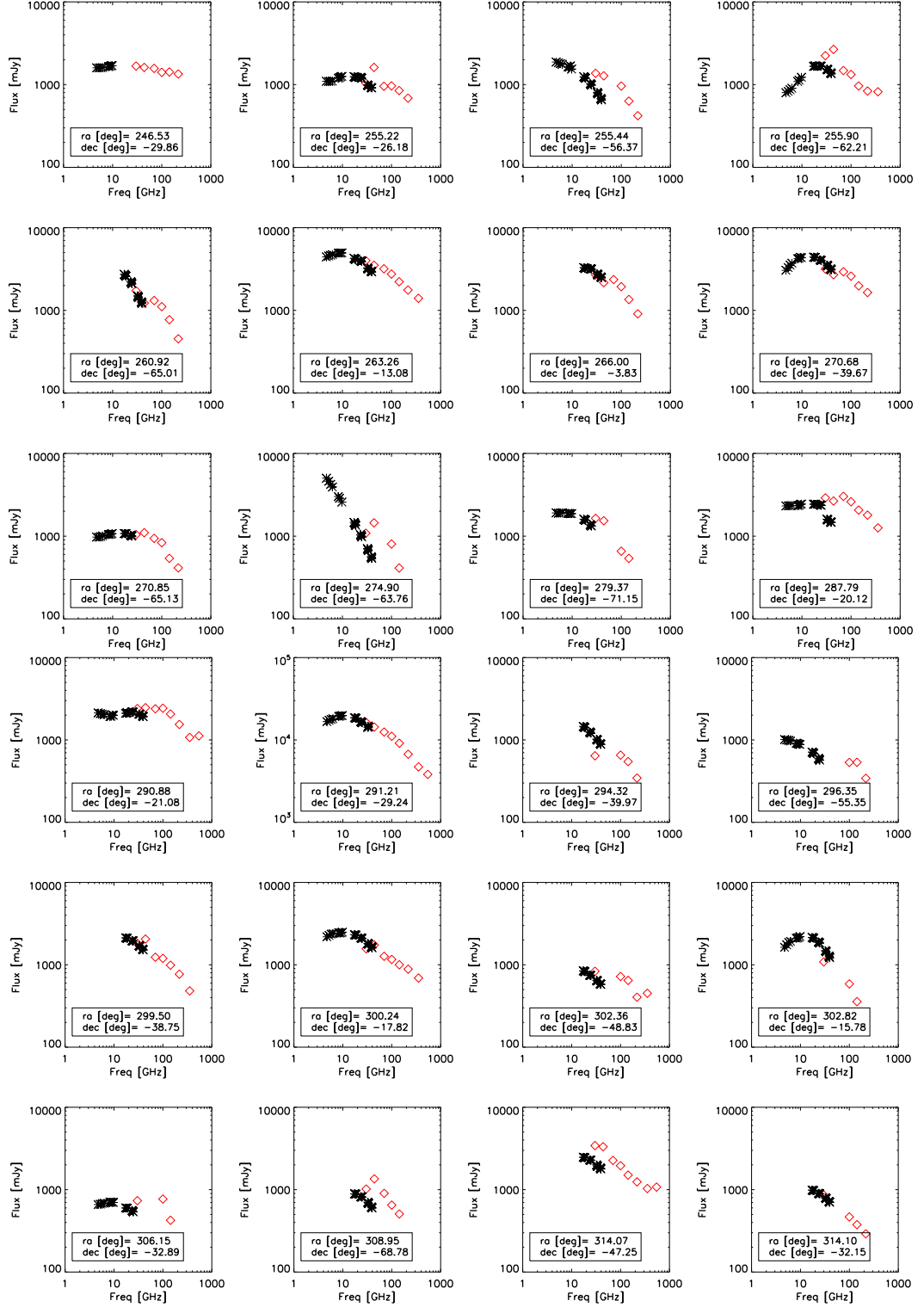


Figure 5.4: Continue.

## 5. MULTI-FREQUENCY SEDS OF PACO SOURCES

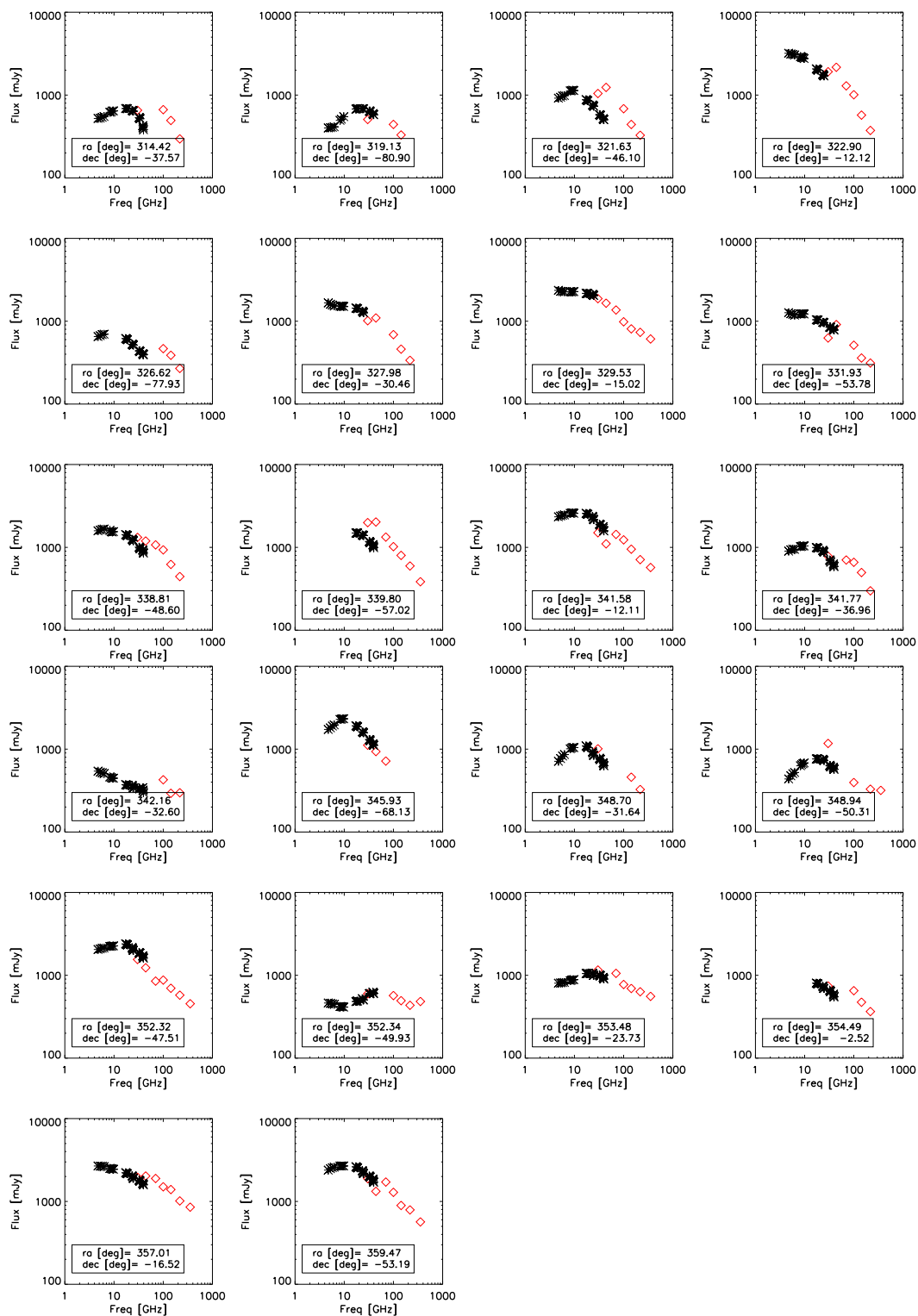


Figure 5.4: Continue.

**Table 5.3:** We give, for each *Planck* channel, the number of PACO faint sources in the ERCSC, the number of PACO faint sources in the ERCSC but not in the PACO bright sample, those which that have  $S_{PACO} > 500$  mJy at 18.7 GHz, the percentage of missed sources when using the bright sample only.

frequency [GHz]	# FS sources in the ERCSC	# FS sources in the ERCSC not in the BS	# of sources with $S_{PACO} > 500$ mJy	% missed sources when using BS
30	39	10	7	~26%
44	27	4	4	~15%
70	29	3	3	~10%
100	42	13	11	~31%
143	44	11	8	~25%
217	31	8	5	~26%
353	15	2	2	~13%
545	5	0	-	-
857	3	0	-	-

two of which have a counterpart in the NEWPS catalogue ( $\leq 3\%$ ), and 2 out of 31 at 70 GHz ( $\leq 6\%$ ). These values are in agreement with those found during the validation of the ERCSC (Planck Collaboration, 2011b). At frequencies  $\geq 100$  GHz, the number of ERCSC sources not in the PACO sample is higher, due to the presence of dusty galaxies.

## 5.2 Global SEDs of Blazars

Blazars are the most extreme and powerful AGNs. They are characterized by an electromagnetic emission spanning from the radio to the gamma rays, attributed to plasma moving relativistically along a jet aligned with the line of sight. The non-thermal emission is amplified by Doppler boosting and dominates with respect to the sources of thermal emissions (i.e. the ones from the accretion disks, the dust heated by the AGN and the interstellar matter of the host galaxy).

### 5.2.1 Sample Selection

The PACO bright sample has been cross-matched with the Third Edition (April 2011) of the Multi-frequency Catalogue of Blazars by Massaro et al. (2009). This catalogue classifies the blazars in three main groups, according to their observational properties: BL Lac objects (BZB) are objects with a featureless optical spectrum or only with

## 5. MULTI-FREQUENCY SEDS OF PACO SOURCES

---

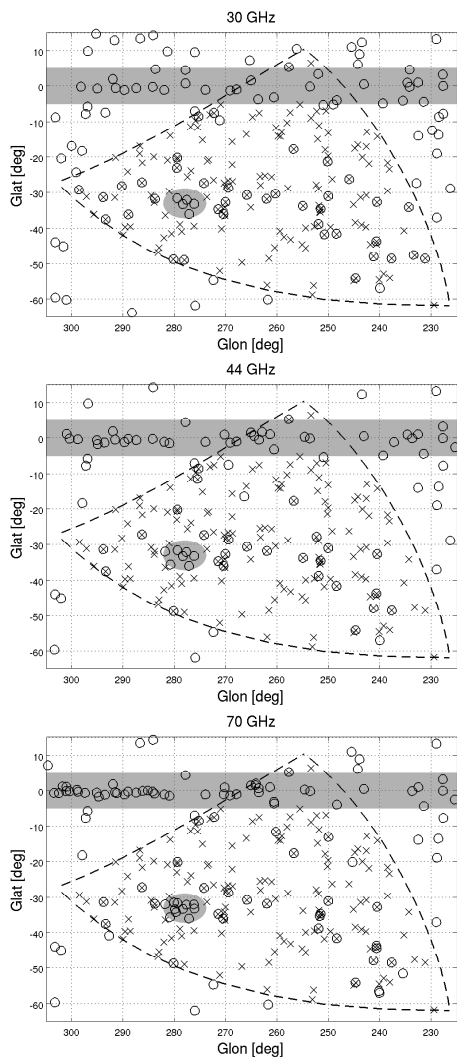


**Figure 5.5:** The area covered by the PACO faint sample is that bounded by the dashed lines, excluding the grey areas, i.e. the Galactic plane region ( $|b| \leq 5^\circ$ ) and the Large Magellanic Cloud (LMC) region (a circle of  $4^\circ$  radius). The crosses show the positions of PACO sources, the circles those of ERCSC sources at 30, 44 and 70 GHz.

absorption lines and weak and narrow emission lines; flat spectrum radio quasars (BZQ) are objects with an optical spectrum showing broad emission lines; objects of uncertain type (BZU) are sources with peculiar characteristics but also showing blazar activity. For each source the catalogue reports the J2000 coordinates, the redshift (if available) and a large collection of photometric data.

It turns out that 105 of the 180 sources in the PACO bright sample have a match in the Multi-frequency Catalogue of Blazars catalogue. The distributions of the flux densities at 20 GHz in the AT20G catalogue (where the original selection has been performed) of these sources is plotted in Figure 5.6.

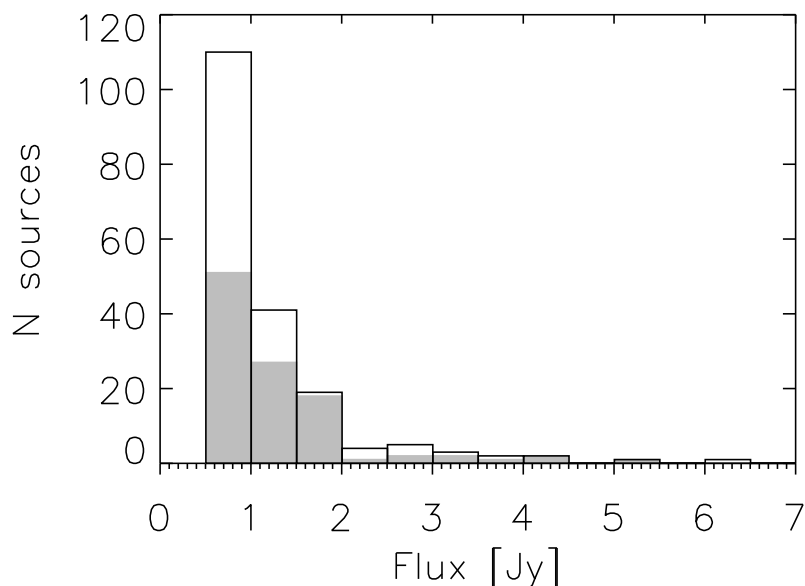


**Figure 5.6:** Distributions of the flux densities at 20 GHz in the AT20G catalogue of the PACO bright sample sources (white histogram) and of the bright sample sources with a match in the blazars catalogue (grey histogram).

To maximize the fraction of bright sample sources classified as blazars, we consider the 27 sources with  $S > 1.5$  Jy, that correspond to the 73%. Most of these (78%) are classified as BZQ, 11% as BZB and 11% as BZU. We reconstruct the SED of these blazars with the ASDC SED Builder (see Figure 5.7), that combines data from several missions and experiments, both ground and space-based, together with catalogues and

## 5. MULTI-FREQUENCY SEDS OF PACO SOURCES

---

archival data (e.g. *Swift*, *AGILE*, *Fermi*, *Planck*, NED, 2MASS, Sloan, etc.), covering the whole electromagnetic spectrum, from radio to TeV energies. Unfortunately these data are generally non simultaneous and are therefore affected by variability. Anyway most of the SEDs in Figure 5.7 show the typical broad double bump. The first peak is attributed to synchrotron radiation and the second to inverse Compton emission.

### 5.2.2 Analysis

For most of the sources (23) it was possible to fit the data with a third degree polynomial function in the part dominated by Synchrotron emission. In this way we estimated the peak frequency and the corresponding flux. For 13 sources we have enough data to perform a similar fit in order to find also the Compton peak frequency and flux. Since all these sources have measured cosmological redshift, the peak frequencies in the source rest frame could be computed. The results are summarized in Table 5.4.

The redshifts of all but one of these sources are below 2 (Figure 5.8).

Figure 5.9 shows the distributions of the synchrotron (top panel) and Compton (bottom panel) peak frequencies in both the observer- (hatched histogram) and source rest-frame (grey histogram). [Abdo et al. \(2010\)](#) classify the non thermal dominated AGNs as follows.

- Low synchrotron peaked blazars (LSP): this kind of sources have the synchrotron power peak at low energy (i.e. in the far-IR or IR band or  $\nu_{peak} \lesssim 10^{14} Hz$ ) and therefore their X-ray emission is flat ( $\alpha_x \approx 0.4 - 0.7$ ) and due to the rising part of the inverse Compton component. At these relatively low energies the inverse Compton scattering occurs in the Thomson regime.
- Intermediate synchrotron peaked blazars (ISP): sources where the synchrotron emission peaks at intermediate energies ( $10^{14} \lesssim \nu_{peak} \lesssim 10^{15} Hz$ ). In this case, the X-ray band includes both the tail of the synchrotron emission and the rise of the inverse Compton component.
- High synchrotron peaked blazars (HSP): sources where the emitting particles are accelerated at much higher energies than in LSPs so that the peak of the synchrotron power reaches UV or higher energies ( $\nu_{peak} \gtrsim 10^{15} Hz$ ). Under these conditions the synchrotron emission dominates the observed flux in the X-ray band and the inverse Compton scattering occurs in the Klein Nishina regime.

## 5.2 Global SEDs of Blazars

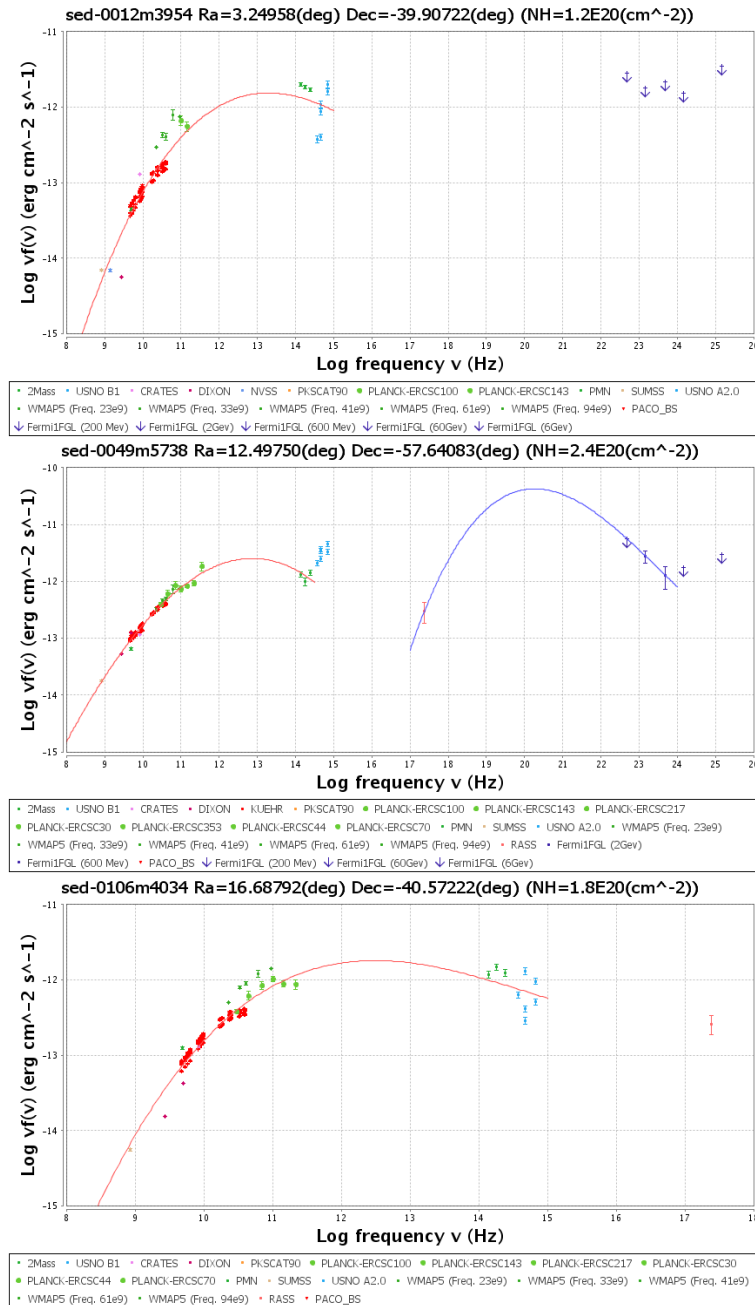


**Figure 5.7:** SEDs constructed using the ASDC SED Builder tool. The red line is the fit to a third degree polynomial.

## 5. MULTI-FREQUENCY SEDS OF PACO SOURCES

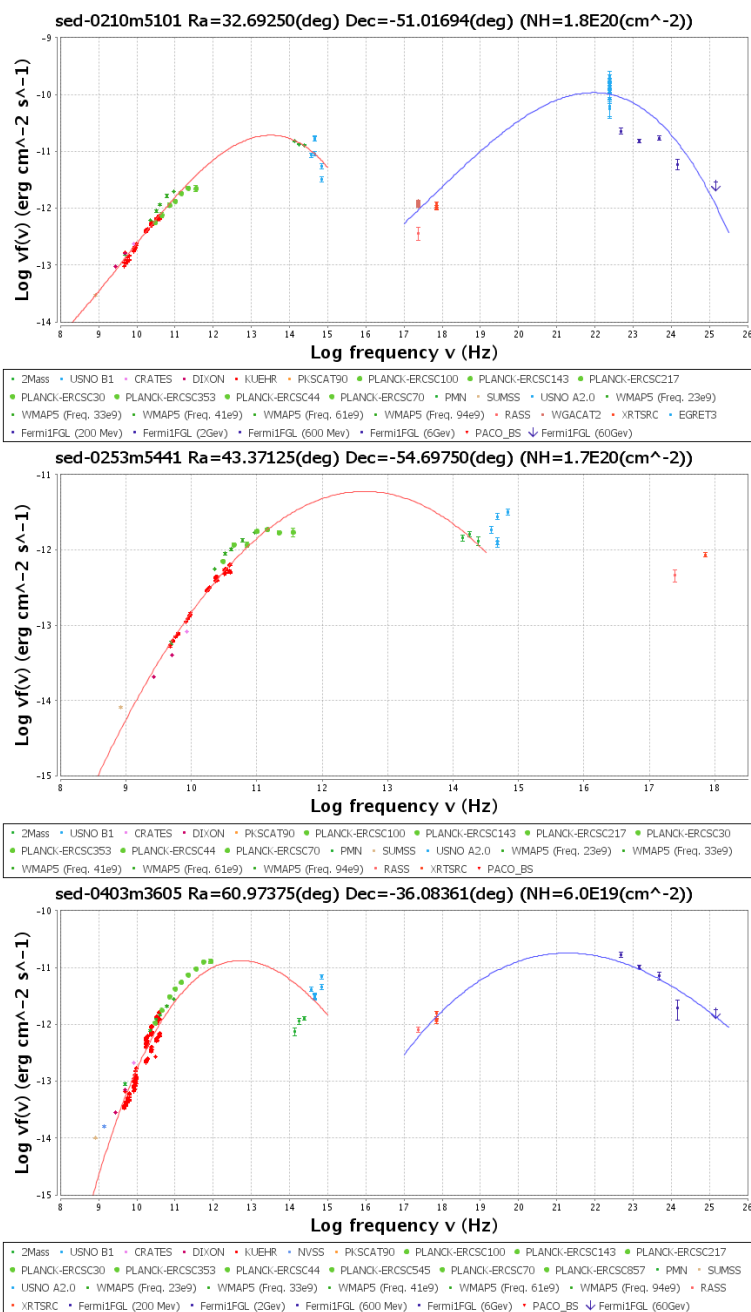


Figure 5.7: Continue.

## 5.2 Global SEDs of Blazars

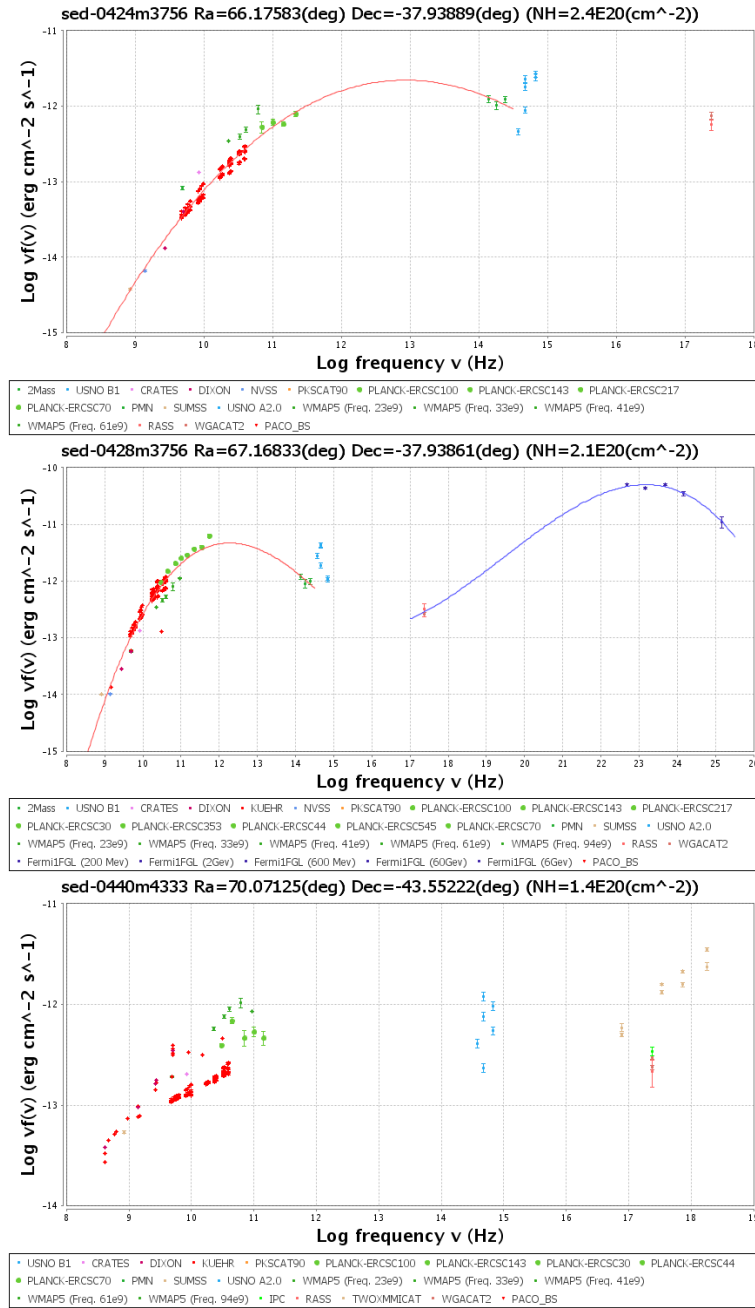


Figure 5.7: Continue.

## 5. MULTI-FREQUENCY SEDS OF PACO SOURCES

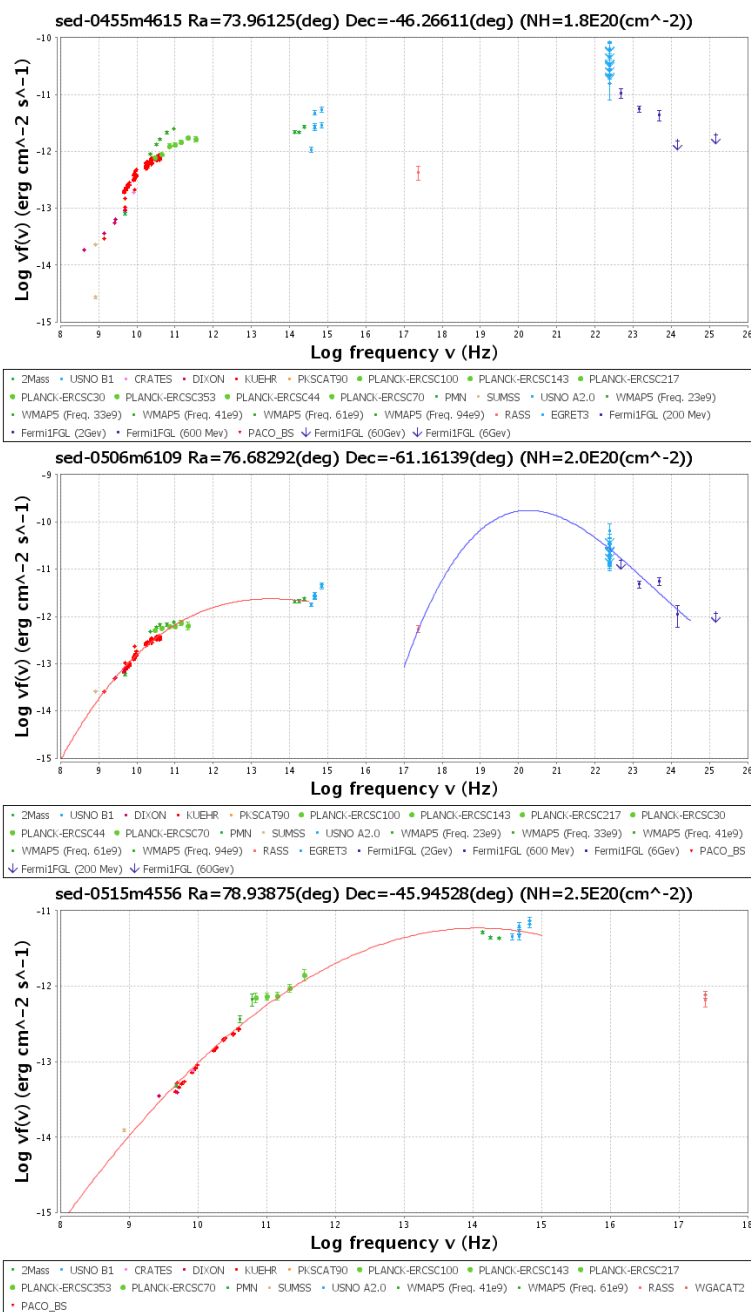


Figure 5.7: Continue.

## 5.2 Global SEDs of Blazars

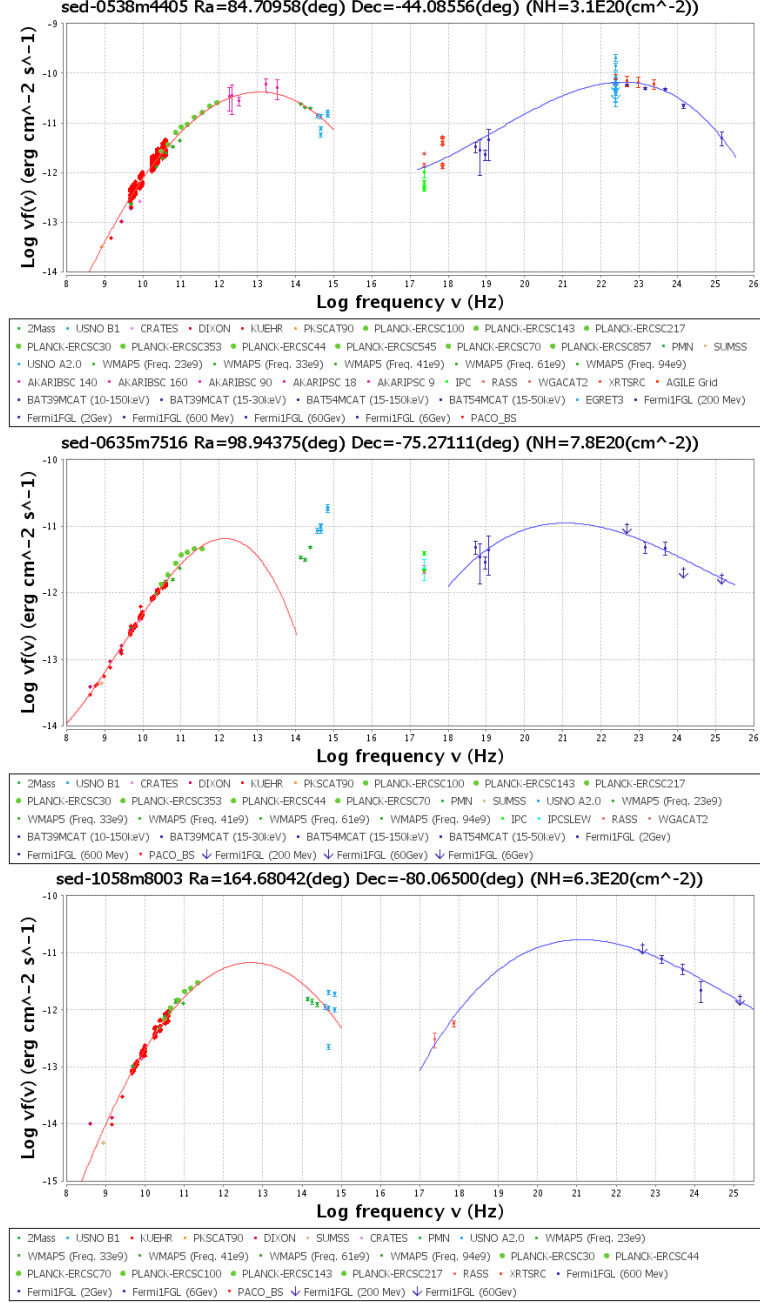


Figure 5.7: Continue.

## 5. MULTI-FREQUENCY SEDS OF PACO SOURCES

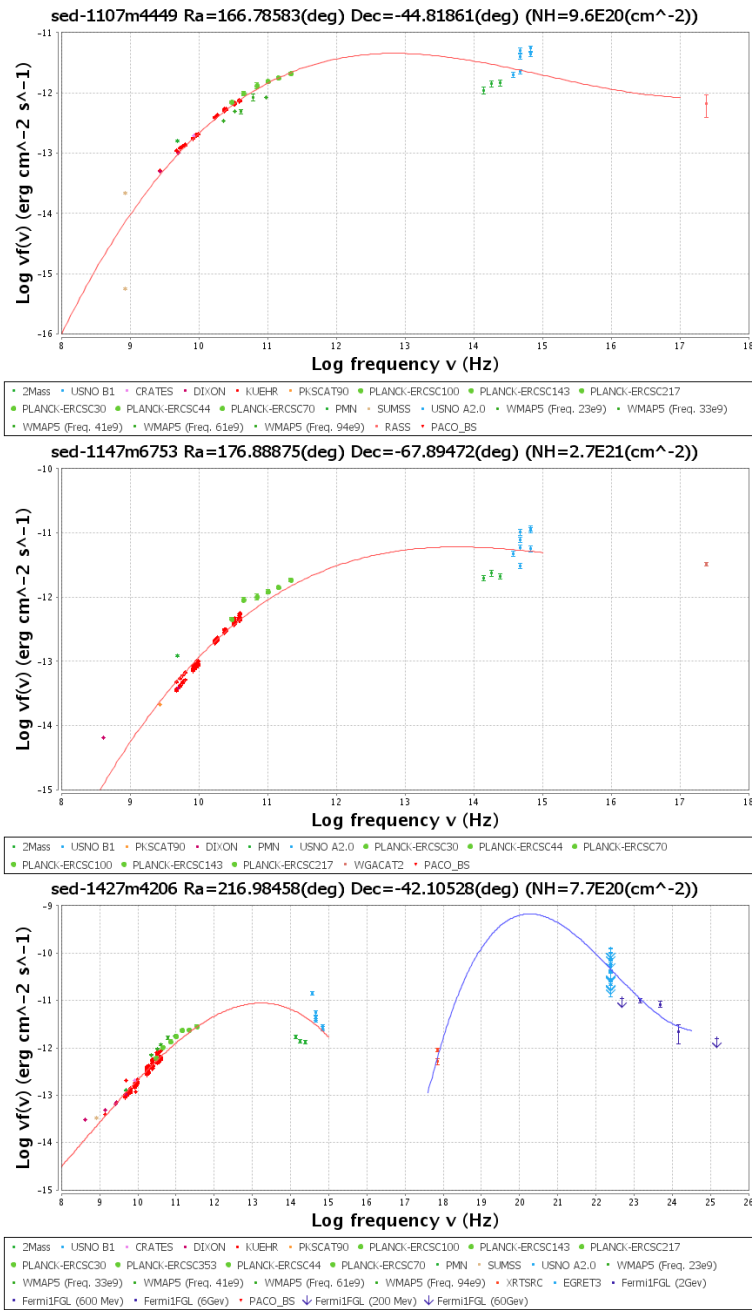


Figure 5.7: Continue.

## 5.2 Global SEDs of Blazars

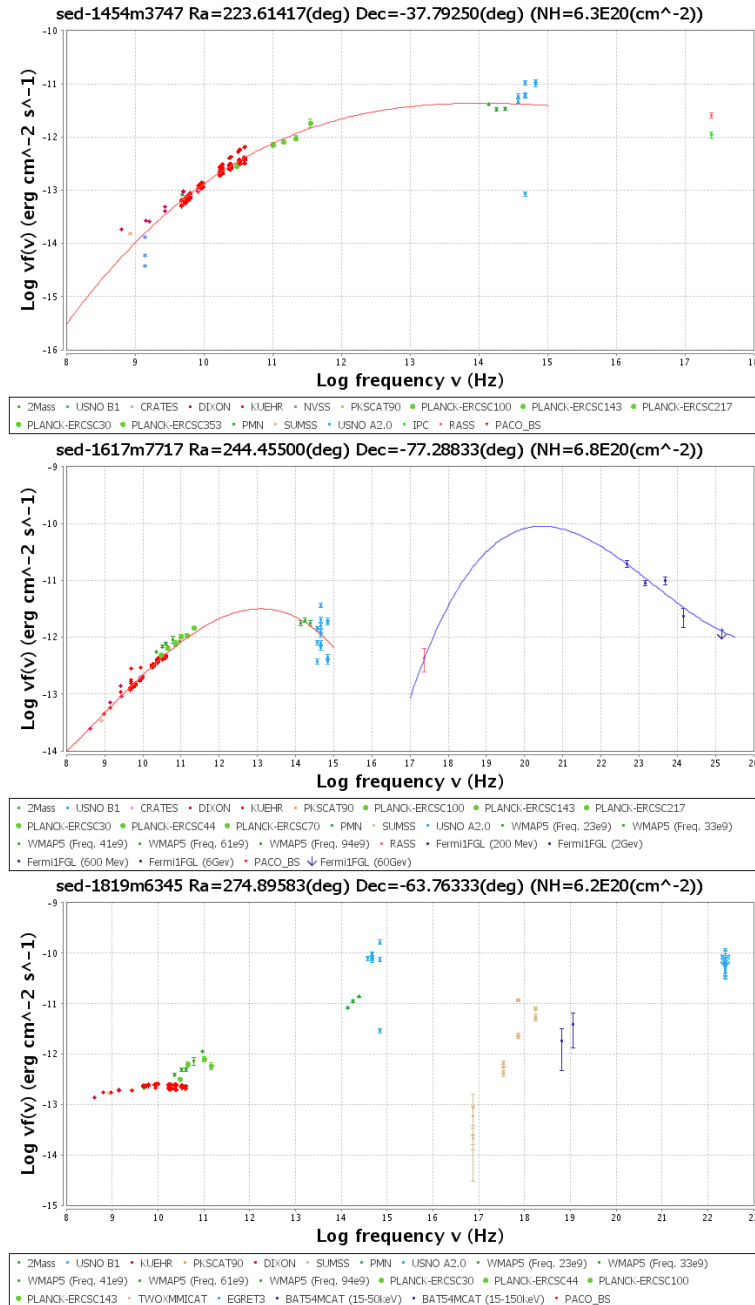


Figure 5.7: Continue.

## 5. MULTI-FREQUENCY SEDS OF PACO SOURCES

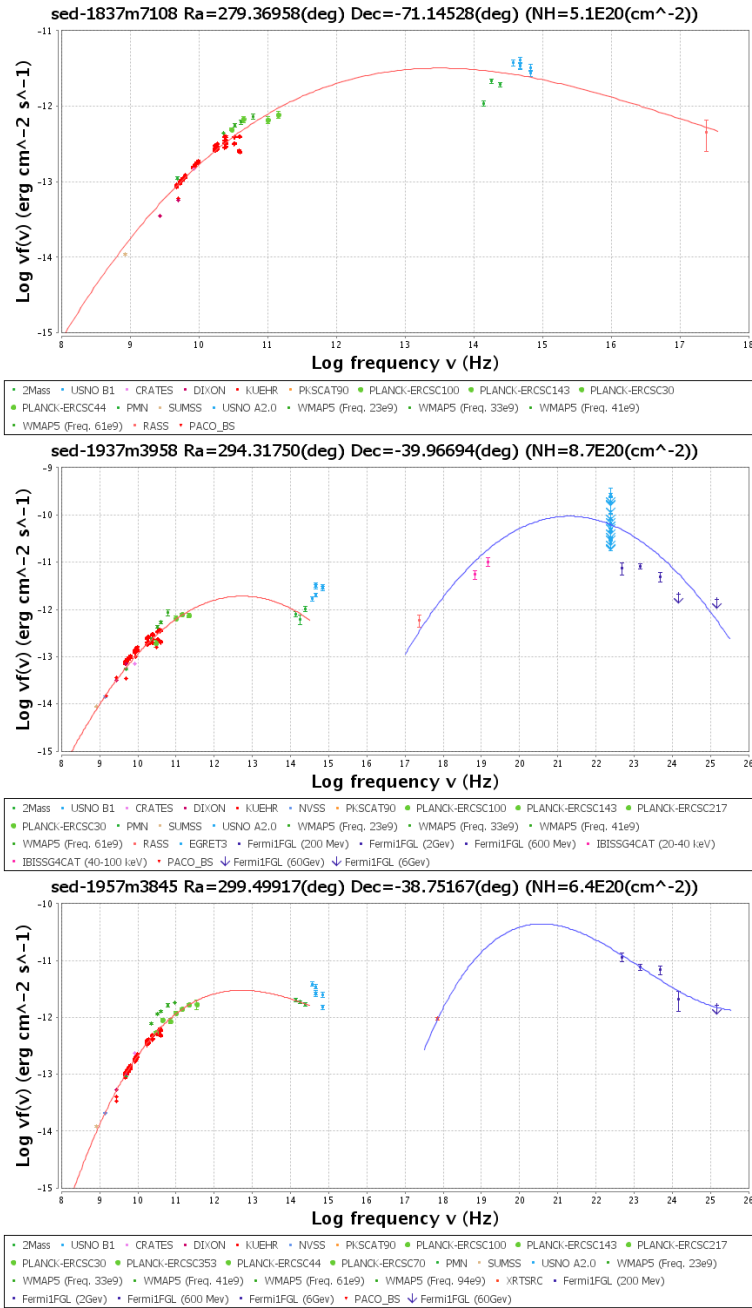


Figure 5.7: Continue.

## 5.2 Global SEDs of Blazars

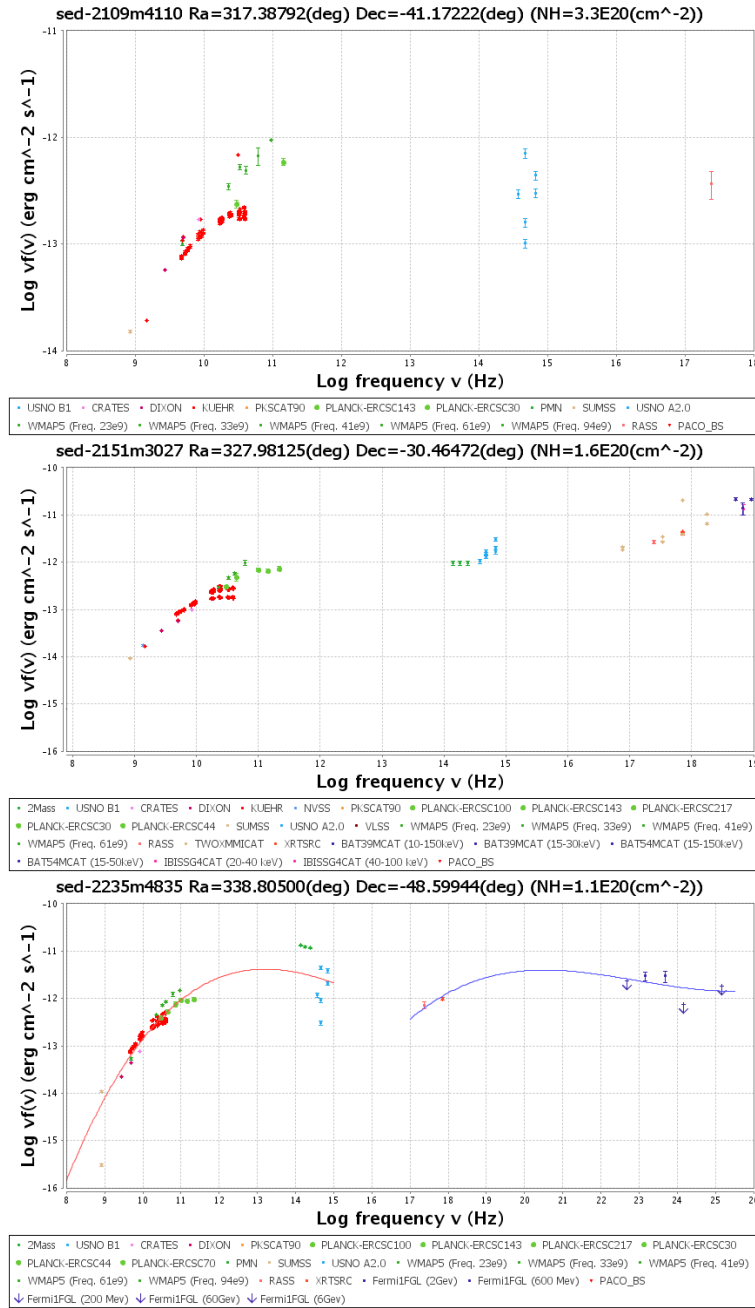
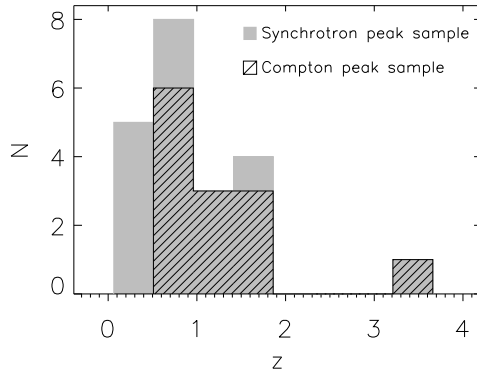


Figure 5.7: Continue.

## 5. MULTI-FREQUENCY SEDS OF PACO SOURCES



**Figure 5.8:** Redshift distribution of the sources for which it was possible to determine the synchrotron (grey histogram) and the Compton (hatched histogram) peak frequencies.

Following the [Abdo et al. \(2010\)](#) classification, we find that in our sample blazars are mainly LSP. This is not surprising because of the high radio frequency selection. The mean, median and sigma values of  $\log \nu_{peaks}$  [Hz] are 13.06, 13.08, 0.52 (synchrotron case) and 21.14, 21.08, 0.93 (Compton case) in the observer frame and 13.31, 13.29, 0.47 (synchrotron case) and 21.46, 21.29, 0.99 (Compton case) in the source rest-frame.

The Figure 5.10 shows that there is little evidence for a correlation between the synchrotron and Compton peak frequencies. If anything this thesis is a hint for an anti-correlation (the correlation coefficient is -0.33). Although the sample is too small to allow us to reach definite conclusion, we note that a positive correlation is expected in the framework of the blazar sequence model (see Fig.12 of [Fossati et al., 1998](#)).

Figure 5.11 shows the synchrotron (top panel) and the Compton (bottom panel) rest-frame peak frequencies. Again, no indication of a correlation shows up (the correlation coefficients are 0.24 and 0.28 for the synchrotron and Compton case, respectively). This does not support the claim by [Fossati et al. \(1998\)](#) of an anti-correlation between the synchrotron peak luminosity and the peak frequency. We caution, however that not only is the sample small, but also the range of  $\nu_{peak}^S$  is very limited.

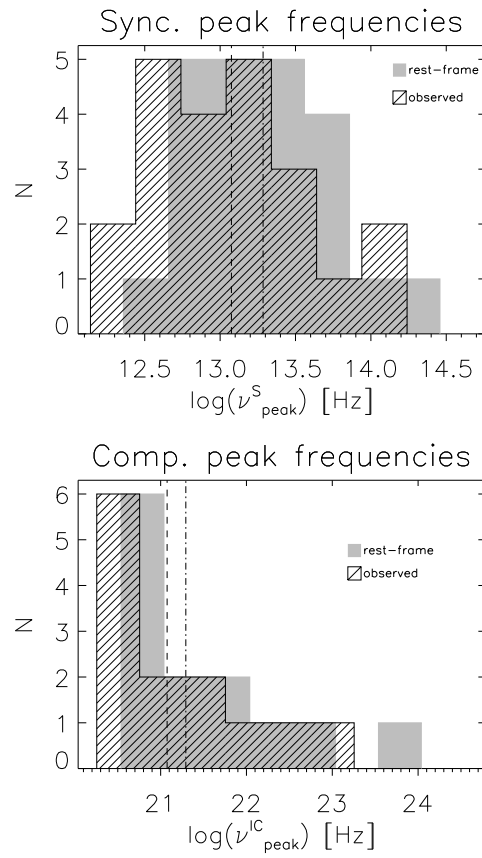


**Figure 5.9:** Distributions of the observed (hatched histogram) and rest-frame (grey histogram) synchrotron (top panel) and Compton (bottom panel) peak frequencies. The observed (dashed) and the rest-frame (dot-dashed) median values are also shown.



**Table 5.4:** Summary of the properties of the bright sample sources with a match in the BZcat (Massaro et al., 2009) and  $S_{AT20G}$  at 20 GHz greater than 1.5 Jy.

AT20G name	BZcat name	BZcat classification	positional distance [arcsec]	redshift	$\log \nu_S$ [Hz]	$\log \nu_S F_{\nu_S}$ [ $erg\,cm^{-2}\,s^{-1}$ ]	$\log \nu_C$ [Hz]	$\log \nu_C F_{\nu_C}$ [ $erg\,cm^{-2}\,s^{-1}$ ]
AT20GJ001259-395426	BZBJ0012-3954	BL Lac Candidate	1.4044	0	13.285	-11.811	-	-
AT20GJ004959-573827	BZQJ0049-5738	QSO RLoud flat radio sp.	1.141	0.92	12.875	-11.596	20.255	-10.372
AT20GJ010645-403419	BZQJ0106-4034	QSO RLoud flat radio sp.	0.822	0.584	12.480	-11.742	-	-
AT20GJ021046-510101	BZUJ0210-5101	Blazar Uncertain type	1.153	1.003	13.495	-10.715	21.9725	-9.966
AT20GJ025329-544151	BZQJ0253-5441	QSO RLoud flat radio sp.	2.382	0.539	12.648	-11.223	-	-
AT20GJ040353-360500	BZQJ0403-3605	QSO RLoud flat radio sp.	1.581	1.417	12.725	-10.878	21.293	-10.746
AT20GJ042442-375620	BZQJ0424-3756	QSO RLoud flat radio sp.	0.624	0.782	12.940	-11.655	-	-
AT20GJ042840-375619	BZBJ0428-3756	QSO RLoud flat radio sp.	1.688	3.317	12.258	-11.329	23.163	-10.301
AT20GJ044017-433308	BZQJ0440-4333	QSO RLoud flat radio sp.	2.111	0.109	-	-	-	-
AT20GJ045550-461558	BZQJ0455-4615	QSO RLoud flat radio sp.	1.908	0.858	-	-	-	-
AT20GJ050644-610941	BZQJ0506-6109	QSO RLoud flat radio sp.	1.411	1.093	13.525	-11.628	20.263	-9.757
AT20GJ051545-455643	BZQJ0515-4556	QSO RLoud flat radio sp.	2.131	0.194	14.090	-11.230	-	-
AT20GJ053850-440508	BZBJ0538-4405	BL Lac	1.921	0.892	13.075	-10.381	22.554	-10.178
AT20GJ063546-751616	BZQJ0635-7516	QSO RLoud flat radio sp.	0.457	0.653	12.140	-11.184	21.075	-10.951
AT20GJ105843-800353	BZBJ1058-8003	BL Lac	0.261	0.581	12.690	-11.172	21.122	-10.772
AT20GJ110708-444907	BZQJ1107-4449	QSO RLoud flat radio sp.	1.470	1.598	12.830	-11.344	-	-
AT20GJ114733-675341	BZQJ1147-6753	QSO RLoud flat radio sp.	1.971	0.21	13.775	-11.219	-	-
AT20GJ142756-420618	BZQJ1427-4206	QSO RLoud flat radio sp.	1.508	1.522	13.215	-11.055	20.257	-9.175
AT20GJ145427-374733	BZQJ1454-3747	QSO RLoud flat radio sp.	1.864	0.314	14.020	-11.365	-	-
AT20GJ161749-771718	BZQJ1617-7717	QSO RLoud flat radio sp.	1.188	1.71	13.075	-11.499	20.443	-10.049
AT20GJ181934-634548	BZUJ1819-6345	Blazar Uncertain type	1.218	0.063	13.510	-11.495	-	-
AT20GJ183728-710843	BZQJ1837-7108	QSO RLoud flat radio sp.	1.120	1.356	-	-	-	-
AT20GJ193716-395801	BZUJ1937-3958	Blazar Uncertain type	1.396	0.965?	12.745	-11.718	21.293	-10.029
AT20GJ195759-384506	BZQJ1957-3845	QSO RLoud flat radio sp.	1.280	0.63	12.713	-11.523	20.58	-10.355
AT20GJ210933-411020	BZQJ2109-4110	QSO RLoud flat radio sp.	0.821	1.058	-	-	-	-
AT20GJ215155-302753	BZQJ2151-3027	QSO RLoud flat radio sp.	1.272	2.345	-	-	-	-
AT20GJ223513-483558	BZQJ2235-4835	QSO RLoud flat radio sp.	2.016	0.51	13.215	-11.381	20.528	-11.401

## **5. MULTI-FREQUENCY SEDS OF PACO SOURCES**

---

## Chapter 6

# Conclusions

This thesis is focused on two major projects of ground-based radio observations, simultaneous with *Planck*: the *Planck*-ATCA Coeval Observations (PACO) and the Simultaneous Medicina-*Planck* Experiment (SiMPIE).

The PACO project consists of observations with ATCA of three complete samples in three pairs of  $2 \times 2$  GHz bands centred at 5.5 and 9 GHz, 18 and 24 GHz, 33 and 39 GHz. The observations were carried out in several epochs between July 2009 and August 2010 for a total of  $\simeq 460$  hours. At least one observation was made within 10 days from the *Planck* satellite observations in any of the LFI channels (30, 44, 70 GHz). The three samples are defined as follows. The PACO bright sample presented in [Massardi et al. \(2011b\)](#) comprises the 189 sources with  $S_{20\text{GHz}} > 500$  mJy at  $\delta < -30^\circ$ . The PACO faint sample, presented in [Bonavera et al. \(2011\)](#), is made of 162 sources with  $S_{20\text{GHz}} > 200$  mJy in the southern ecliptic pole region (ecliptic latitude  $< -75^\circ$ ) with  $3\text{h} < \text{RA} < 9\text{h}$ ,  $\delta < -30^\circ$ . The PACO spectrally-selected sample comprises the 69 sources with  $S_{20\text{GHz}} > 200$  mJy and spectra classified by [Massardi et al. \(2011b\)](#) as inverted or upturning in the frequency range 5-20 GHz, selected over the whole southern sky. An additional sample (also partially overlapping with those defined above) is made of 63 bright southern blazars included in a long-term (up to 15 years) monitoring program at various frequencies with the Swedish-ESO Sub-millimetre Telescope (SEST, [Tornikoski et al., 1996](#)) and observed also with the LABOCA instrument on the APEX.

The SiMPIE project complements the PACO project in the Northern Hemisphere. It has targeted 253 objects in the NEWPS sample plus 10 Galactic objects, not in the NEWPS catalogue, that may show strong outbursts during the *Planck* mission and were

## 6. CONCLUSIONS

---

previously monitored at the Noto observatory (Procopio et al., 2011). The observations were carried out between June 2010 - June 2011 for a total of 33 runs ( $\simeq 790$  hours). In this thesis we have presented the results obtained for a sub-sample of 79 sources with  $\delta \geq 45^\circ$  observed in 22 runs in the period June-December 2010, at 5 and 8.3 GHz. Data for 2 of them have been flagged for bad weather conditions.

The spectra of the PACO bright and faint sample show a similar overall phenomenology. In both cases, adopting the classification in Section 4.1 (frequency range 4 – 40 GHz), most of the sources (more than 65%) show a down-turning behaviour,  $\sim 10\text{--}14\%$  show a peaked spectrum, very few ( $\sim 5\%$ ) a self-absorbed spectrum, less than 1% (0% and 0.6% for the bright and the faint sample respectively) an inverted spectrum and none of the sources shows an upturning spectrum in either sample. The main difference between the two samples is in the fraction of flat (5.1% and 10.3% for the bright and faint sample respectively) and steep (13.3% and 3.6% for the bright and the faint sample respectively) sources.

In the case of the SiMPIE Northern sample the spectral analysis has been performed exploiting the ERCSC flux densities for the 33 sources in common to compute the spectral indices between 5 and 30 GHz and 30 and 70 GHz. Our analysis confirms that sources are mostly composed by flat-spectrum objects up to 30 GHz, showing an overall steepening in the spectrum in the frequency range 30-70 GHz.

The PACO short term (3, 6 and 9 months) variability analysis shows a trend towards an increase of the variability amplitude with frequency. This trend however is not apparent when we compare with the AT20G with the PACO data, we found a variability  $\simeq 40\%$  at 20 GHz and  $\simeq 38\%$  at  $\simeq 5$  GHz for a time lag of a few years.

The PACO data have allowed us to extrapolate the 20 GHz source counts to 33 and 40 GHz, down to  $\simeq 200$  mJy, that is a factor  $\geq 5$  below current estimates from *Planck* data at nearby frequencies (30 and 44 GHz). Our counts are in very good agreement with the *Planck* ones in the region of overlap and are well accounted for by the de Zotti et al. (2005) model. The assessment of the counts down to faint flux density limits substantially improves the control of fluctuations due to unresolved sources in *Planck* maps.

The *Planck* ERCSC (Planck Collaboration, 2011b) reports the detection at least at one frequency of 257 PACO sources, 138 of which are in the PACO bright sample, 57 in the PACO faint sample (but only 20 of which are not common with the PACO

---

bright sample, i.e. have  $S_{AT20G} < 500$  mJy) and 99 in the inverted and blazars samples. 142 PACO sources have flux density measurements in at least 3 *Planck* channels. We present the SEDs obtained combining the PACO and ERCSC data, showing different spectral behaviours in the broad frequency range obtained combining ground-based and satellite observations. There are some evidences of artefacts in the ERCSC spectra that can be due, for variable sources, to the fact that ERCSC flux densities represent the average over two scans, or during one scan, to the fact that it requires 7-10 days or more for the *Planck* focal plane to cross a point source. Obviously this will improve when it will be possible to get data for individual detectors.

Many more sources should be detected by *Planck* as new surveys are completed and the data analysis improves. Additional constraints on the source spectra at *Planck* frequencies will be extracted from *Planck* maps, when they become available, by a stacking analysis.

The analysis of the angular distances between ATCA and ERCSC positions, performed on the whole PACO sample, confirms that the positional error in the ERCSC is less than FWHM/5, as found in [Planck Collaboration \(2011b\)](#).

There are three ERCSC sources at 30 GHz within the PACO faint area not included in our sample. They are at low Galactic latitudes and were not detected by the AT20G survey (flux density limit of 40 mJy, 93% complete above 100 mJy; [Massardi et al., 2011b](#)). Two of them have a counterpart in the NEWPS catalogue ([López-Caniego et al., 2007](#)). Thus, since the number of 30 GHz ERCSC sources in the PACO faint area is 42, the fraction of potentially spurious 30 GHz ERCSC sources is  $\leq 2\%$ . The same analysis at 44 and 70 GHz gives  $\leq 3\%$  (three undetected sources, two of which are in NEWPS, out of a total of 30) and  $\leq 6\%$  (two out of 31) possibly spurious sources respectively, in agreement with the results presented by [Planck Collaboration \(2011b\)](#).

The comparison between PACO and *Planck* data has shown a good consistency at flux densities higher than  $\sim 1$  Jy at 30 GHz and  $\sim 1.5$  Jy at 44 GHz. Below these limits the *Planck* flux densities are no longer reliable because of the Eddington bias.

Finally we have carried out an analysis of the global SEDs of a well-defined sample of blazars selected from the PACO bright sample and included in the ERCSC. For most of the sources with flux density  $> 1.5$  Jy at 20 GHz in the AT20G catalogue, it was possible to determine the synchrotron peak frequency and flux density, and for more than half of the selected blazars it was also possible to obtain the Compton peak

## 6. CONCLUSIONS

---

frequency and flux density. Our analysis in general does not support the claims in [Fossati et al. \(1998\)](#) of an anti-correlation between the synchrotron peak luminosity and the peak frequency. We stress however that our sample is small and the range of  $\nu_{peak}$  is very limited.

The catalogues and the analysis for the spectrally selected and blazar PACO samples are in preparation. Additionally, once the satellite time-ordered data will be available, the accurate PACO flux density measurements, simultaneous with *Planck*, can be used to exploit the excellent absolute calibration achieved by *Planck* to re-assess the high-frequency calibration of ground-based telescopes and to improve models for planets and other sources used as calibrators at mm wavelengths.

Moreover, when both *Planck* and PACO polarization data will be available, it will be possible to investigate high frequencies polarization properties of different source populations. Polarization fluctuations due to extragalactic radio sources are the dominant foreground contamination of CMB maps on small angular scales at frequencies up to  $\simeq 100$  GHz ([Tucci et al., 2005](#)). PACO data will allow us to control them with substantially better accuracy than would be possible with *Planck* data alone.

## Appendix A

# Script for a general ATCA-CABB Continuum Data Reduction Pipeline

The following script is an example for running a general pipeline in the case in which PKS 1934-638 is both the bandpass and the primary calibrator, with the 3-6 cm receiver centred in 5.5 and 9 GHz.

```
#!/bin/bash

#Bandpass and Primary calibrator=1934-638
#target source=$1
#phase calibrator=$2
#reference antenna=$3

# GENERAL EDITING
cd p_$1
rm -rf p_$1.uv
atlod in="*.C1741" out=p_$1.uv options=noauto,birdie,xycorr,rfiflag
uvflag vis=p_$1.uv select="shadow(22)" flagval=flag
rm -rf p_$1.uvindex
uvindex vis="p_$1.uv" log=p_$1.uvindex
rm -rf *.*00
uvsplit vis="p_$1.uv"
```

## A. SCRIPT FOR A GENERAL ATCA-CABB CONTINUUM DATA REDUCTION PIPELINE

---

```
cd ..

# CHANNELS FLAGGING
cd p_$1
rm -rf *.list
rm -rf *.flag
for freq in 5500 9000
do
    mfcalf vis=1934-638.$freq interval=1 refant=$3
    gpcopy vis=1934-638.$freq out=$2.$freq
    gpcopy vis=$2.$freq out=$1.$freq
done
#generate channels' amplitude list
for k in 1934-638 $2 $1
do
    for freq in 5500 9000
    do
        for ant1 in 'seq 6'
        do
            for ant2 in 'seq 6'
            do
                if test $ant1 -lt $ant2
                then
                    uvspec vis=$k.$freq axis=channel,amp \
select="ant($ant1)($ant2)" \
stokes=i log=$k.$ant1$ant2.$freq.list
                fi
            done
        done
    done
done
cd ..
#search for channels to be flagged
for k in 1934-638 $2 $1
do
    nsigma=5.
```

---

```

    idl <<EOF
.comp readcol.pro
.comp ch2flag.pro
ch2flag,'p_$1/', '$k', $nsigma, 5500, 9000, ''
EOF
done
#flag selected channels
cd p_$1
for freq in 5500 9000
do
    for k in 1934-638 $2 $1
    do
for j in `cat $k.$freq.flag`
do
    chfch=`echo $j | awk -F : '{print $2}'`
    chwid=`echo $j | awk -F : '{print $3}'`
    ant1=`echo $j | awk -F : '{print $4}'`
    ant2=`echo $j | awk -F : '{print $5}'`
        # bp and prim calibrator flagging
        uvflag vis=1934-638.$freq line="chan,$chwid,$chfch" \
select="ant($ant1)($ant2)" flagval=flag
        # phase calibrator flagging
        uvflag vis=$2.$freq line="chan,$chwid,$chfch" \
select="ant($ant1)($ant2)" flagval=flag
        # surce flagging
        uvflag vis=$1.$freq line="chan,$chwid,$chfch" \
select="ant($ant1)($ant2)" flagval=flag
    done
    done
done
cd ..

# CALIBRATION
cd p_$1
for freq in 5500 9000
do

```

## A. SCRIPT FOR A GENERAL ATCA-CABB CONTINUUM DATA REDUCTION PIPELINE

---

```
mfcal vis=1934-638.$freq interval=1 refant=$3
gpcopy vis=1934-638.$freq out=$2.$freq
gpical vis=$2.$freq options=xyvary,qusolve interval=0.1, refant=$3
gpical vis=1934-638.$freq options=xyvary interval=0.1 refant=$3
gpboot vis=$2.$freq cal=1934-638.$freq
mfboot vis=1934-638.$freq,$2.$freq select=source"(1934-638)"
gpcopy vis=$2.$freq out=$1.$freq
done
cd ..

# IMAGING
cd p_$1
rm -rf ./im
mkdir ./im
for freq in 5500 9000
do
    invert vis=$1.$freq map=./im/$1.$freq.map beam=./im/$1.$freq.beam \
robust=0.5 stokes=i options=mfs,sdb
    clean map=./im/$1.$freq.map beam=./im/$1.$freq.beam \
out=./im/$1.$freq.clean gain=0.1 niters=500
    restor model=./im/$1.$freq.clean map=./im/$1.$freq.map \
beam=./im/$1.$freq.beam out=./im/$1.$freq.out
done
cd ..
```

# References

- A. A. Abdo, M. Ackermann, I. Agudo, M. Ajello, H. D. Aller, M. F. Aller, E. Angelakis, A. A. Arkharov, M. Axelsson, U. Bach, and et al. The Spectral Energy Distribution of Fermi Bright Blazars. *Astrophysical Journal*, 716:30–70, June 2010. doi: 10.1088/0004-637X/716/1/30. [126](#), [136](#)
- E. Angelakis, L. Fuhrmann, N. Marchili, T. P. Krichbaum, and J. A. Zensus. Monitoring the radio spectra of selected blazars in the Fermi-GST era. The Effelsberg 100-m telescope covering the cm band. *Mem. Societa Astronomica Italiana*, 79:1042+, 2008. [42](#)
- R. R. J. Antonucci and J. S. Miller. Spectropolarimetry and the nature of NGC 1068. *Astrophysical Journal*, 297:621–632, October 1985. doi: 10.1086/163559. [23](#)
- M. A. J. Ashdown, C. Baccigalupi, A. Balbi, J. G. Bartlett, J. Borrill, C. Cantalupo, G. de Gasperis, K. M. Górski, V. Heikkilä, E. Hivon, E. Keihänen, H. Kurki-Suonio, C. R. Lawrence, P. Natoli, T. Poutanen, S. Prunet, M. Reinecke, R. Stompor, and B. Wandelt. Making maps from Planck LFI 30 GHz data. *Astronomy and Astrophysics*, 471:361–380, August 2007. doi: 10.1051/0004-6361:20077312. [13](#)
- C. A. Beichman, G. Neugebauer, H. J. Habing, P. E. Clegg, and T. J. Chester, editors. *Infrared astronomical satellite (IRAS) catalogs and atlases. Volume 1: Explanatory supplement*, volume 1, 1988. [viii](#), [21](#)
- C. L. Bennett, G. F. Smoot, M. Janssen, S. Gulks, A. Kogut, G. Hinshaw, C. Backus, M. G. Hauser, J. C. Mather, L. Rokke, L. Tenorio, R. Weiss, D. T. Wilkinson, E. L. Wright, G. de Amici, N. W. Boggess, E. S. Cheng, P. D. Jackson, P. Keegstra, T. Kelsall, R. Kummerer, C. Lineweaver, S. H. Moseley, T. L. Murdock, J. Santana, R. A. Shafer, and R. F. Silverberg. COBE differential microwave radiometers - Calibration techniques. *Astrophysical Journal*, 391:466–482, June 1992. doi: 10.1086/171363. [7](#)
- C. L. Bennett, M. Bay, M. Halpern, G. Hinshaw, C. Jackson, N. Jarosik, A. Kogut, M. Limon, S. S. Meyer, L. Page, D. N. Spergel, G. S. Tucker, D. T. Wilkinson, E. Wollack, and E. L. Wright. The Microwave Anisotropy Probe Mission. *Astrophysical Journal*, 583:1–23, January 2003a. doi: 10.1086/345346. [7](#)
- C. L. Bennett, M. Halpern, G. Hinshaw, N. Jarosik, A. Kogut, M. Limon, S. S. Meyer, L. Page, D. N. Spergel, G. S. Tucker, E. Wollack, E. L. Wright, C. Barnes, M. R. Greason, R. S. Hill, E. Komatsu, M. R. Nolta, N. Odegard, H. V. Peiris, L. Verde, and J. L. Weiland. First-Year Wilkinson Microwave Anisotropy Probe (WMAP) Observations: Preliminary Maps and Basic Results. *Astrophysical Journal, Supplement*, 148:1–27, September 2003b. doi: 10.1086/377253. [vii](#), [7](#), [11](#)
- M. Bersanelli, N. Mandolesi, R. C. Butler, A. Mennella, F. Villa, B. Aja, E. Artal, E. Artina, C. Baccigalupi, M. Balasini, G. Baldan, A. Banday, P. Bassia, P. Battaglia, T. Bernardino, E. Blackhurst, L. Boschini, C. Burigana, G. Cafagna, B. Cappellini, F. Cavaliere, F. Colombo, G. Crone, F. Cuttaia, O. D’Arcangelo, L. Danese, R. D. Davies, R. J. Davis, L. de Angelis, G. C. de Gasperis, L. de La Fuente, A. de Rosa, G. de Zotti, M. C. Falvella, F. Ferrari, R. Ferretti, L. Figini, S. Fogliani, C. Franceschet, E. Franceschi, T. Gaier, S. Garavaglia, F. Gomez, K. Gorski, A. Gregorio, P. Guzzi, J. M. Herreros, S. R. Hildebrandt, R. Hoyland, N. Hughes, M. Janssen, P. Jukkala, D. Kettle, V. H. Kilpiä, M. Laaninen, P. M. Lapolla, C. R. Lawrence, D. Lawson, J. P. Leahy, R. Leonardi, P. Leutenegger, S. Levin, P. B. Lilje, S. R. Lowe, P. M. Lubin, D. Maino, M. Malaspina, M. Maris, J. Marti-Canales, E. Martinez-Gonzalez, A. Mediavilla, P. Meinhold, M. Miccolis, G. Morgante, P. Natoli, R. Nesti, L. Pagan, C. Paine, B. Partridge, J. P. Pascual, F. Pasian, D. Pearson, M. Pecora, F. Perrotta, P. Platania, M. Pospieszalski, T. Poutanen, M. Prina, R. Rebolo, N. Roddis, J. A. Rubiño-Martin, M. J. Salmon, M. Sandri, M. Seiffert, R. Silvestri, A. Simonetto, P. Sjöman, G. F. Smoot, C. Sozzi, L. Stringhetti, E. Taddei, J. Tauber, L. Terenzi, M. Tomasi, J. Tuovinen, L. Valenziano, J. Varis, N. Vittorio, L. A. Wade, A. Wilkinson, F. Winder, A. Zachei, and A. Zonca. Planck pre-launch status: Design and description of the Low Frequency Instrument. *Astronomy and Astrophysics*, 520:A4+, September 2010. doi: 10.1051/0004-6361/200912853. [9](#)
- E. Bertin and S. Arnouts. SExtractor: Software for source extraction. *Astronomy and Astrophysics, Supplement*, 117:393–404, June 1996. [19](#)
- R. D. Blandford and A. Konigl. Relativistic jets as compact radio sources. *Astrophysical Journal*, 232:34–48, August 1979. doi: 10.1086/157262. [26](#)
- L. Bonavera, M. Massardi, A. Bonaldi, J. González-Nuevo, G. de Zotti, and R. D. Ekers. The Planck-ATCA Co-eval Observations project: the faint sample. *Monthly Notices of the RAS*, 416:559–566, September 2011. doi: 10.1111/j.1365-2966.2011.19070.x. [ix](#), [x](#), [xii](#), [xiii](#), [xiv](#), [29](#), [34](#), [49](#), [91](#), [95](#), [99](#), [101](#), [104](#), [105](#), [106](#), [141](#)
- C. Burigana, D. Maino, K. M. Górski, N. Mandolesi, M. Bersanelli, F. Villa, L. Valenziano, B. D. Wandelt, M. Maltoni, and E. Hivon. PLANCK LFI: Comparison between Galaxy Straylight Contamination and other systematic effects. *Astronomy and Astrophysics*, 373:345–358, July 2001. doi: 10.1051/0004-6361:20010538. [13](#), [14](#)
- S. Burke-Spolaor, R. D. Ekers, M. Massardi, T. Murphy, B. Partridge, R. Ricci, and E. M. Sadler. Wide-field imaging and polarimetry for the biggest and brightest in the 20-GHz southern sky. *Monthly Notices of the RAS*, 395:504–517, May 2009. doi: 10.1111/j.1365-2966.2009.14556.x. [70](#)
- P. Carvalho, G. Rocha, and M. P. Hobson. A fast Bayesian approach to discrete object detection in astronomical data sets - PowellSnakes I. *Monthly Notices of the RAS*, 393:681–702, March 2009. doi: 10.1111/j.1365-2966.2008.14016.x. [19](#)

## REFERENCES

---

- A. Ciaramella, C. Bongardo, H. D. Aller, M. F. Aller, G. De Zotti, A. Lähteenmaki, G. Longo, L. Milano, R. Tagliaferrri, H. Teräsraanta, M. Tornikoski, and S. Urpo. A multifrequency analysis of radio variability of blazars. *Astronomy and Astrophysics*, 419:485–500, May 2004. doi: 10.1051/0004-6361:20035771. [103](#), [104](#), [106](#)
- K. A. Cleary, A. C. Taylor, E. Waldram, R. A. Battye, C. Dickinson, R. D. Davies, R. J. Davis, R. Genova-Santos, K. Grainge, M. E. Jones, R. Kneissl, G. G. Pooley, R. Rebolo, J. A. Rubiño-Martín, R. D. E. Saunders, P. F. Scott, A. Slosar, D. Titterton, and R. A. Watson. Source subtraction for the extended Very Small Array and 33-GHz source count estimates. *Monthly Notices of the RAS*, 360:340–353, June 2005. doi: 10.1111/j.1365-2966.2005.09037.x. [x](#), [34](#)
- J. J. Condon, W. D. Cotton, E. W. Greisen, Q. F. Yin, R. A. Perley, G. B. Taylor, and J. J. Broderick. The NRAO VLA Sky Survey. *Astronomical Journal*, 115:1693–1716, May 1998. doi: 10.1086/300337. [32](#), [42](#)
- J. E. Conway. Compact symmetric objects-newborn radio galaxies? *New Astronomy Review*, 46:263–271, May 2002. doi: 10.1016/S1387-6473(01)00191-9. [24](#), [26](#)
- D. Dallacasa, C. Stanghellini, M. Centonza, and R. Fanti. High frequency peakers. I. The bright sample. *Astronomy and Astrophysics*, 363:887–900, November 2000. [25](#)
- L. Danese, G. de Zotti, and G. di Tullio. On velocity dispersions of galaxies in rich clusters. *Astronomy and Astrophysics*, 82:322–327, February 1980. [104](#)
- G. de Zotti, A. Franceschini, L. Toffolatti, P. Mazzei, and L. Danese. Extragalactic Backgrounds: I. General Formalism. *Astrophysical Letters Communications*, 35:289–+, 1996. [99](#)
- G. de Zotti, L. Toffolatti, F. Argüeso, R. D. Davies, P. Mazzotta, R. B. Partridge, G. F. Smoot, and N. Vittorio. The Planck Surveyor mission: astrophysical prospects. In L. Maiani, F. Melchiorri, & N. Vittorio, editor, *3K cosmology*, volume 476 of *American Institute of Physics Conference Series*, pages 204–223, May 1999. doi: 10.1063/1.59327. [49](#)
- G. de Zotti, R. Ricci, D. Mesa, L. Silva, P. Mazzotta, L. Toffolatti, and J. González-Nuevo. Predictions for high-frequency radio surveys of extragalactic sources. *Astronomy and Astrophysics*, 431:893–903, March 2005. doi: 10.1051/0004-6361:20042108. [x](#), [xiii](#), [xvii](#), [33](#), [34](#), [35](#), [36](#), [37](#), [99](#), [142](#)
- G. de Zotti, M. Massardi, M. Negrello, and J. Wall. Radio and millimeter continuum surveys and their astrophysical implications. *Astronomy and Astrophysics Reviews*, 18:1–65, February 2010. doi: 10.1007/s00159-009-0026-0. [viii](#), [23](#), [36](#)
- J. Delabrouille, J. . Puget, R. Gispert, and J. . Lamarre. Scanning strategies for the Planck mission. *ArXiv Astrophysics e-prints*, October 1998. [13](#)
- X. Dupac and J. Tauber. Scanning strategy for mapping the Cosmic Microwave Background anisotropies with Planck. *Astronomy and Astrophysics*, 430:363–371, January 2005. doi: 10.1051/0004-6361:20041526. [13](#)
- A. S. Eddington. On a formula for correcting statistics for the effects of a known error of observation. *Monthly Notices of the RAS*, 73:359–360, March 1913. [2](#)
- Wilson W. E. Ferris, R. H. . *URSI XXVIII GA, Maastricht*, 2002. [3](#)
- G. Fossati, L. Maraschi, A. Celotti, A. Comastri, and G. Ghisellini. A unifying view of the spectral energy distributions of blazars. *Monthly Notices of the RAS*, 299:433–448, September 1998. doi: 10.1046/j.1365-8711.1998.01828.x. [136](#), [144](#)
- L. Fuhrmann, J. A. Zensus, T. P. Krichbaum, E. Angelakis, and A. C. S. Readhead. Simultaneous Radio to (Sub-)mm-Monitoring of Variability and Spectral Shape Evolution of potential GLAST Blazars. In S. Ritz, P. Michelson, & C. A. Meehan, editor, *The First GLAST Symposium*, volume 921 of *American Institute of Physics Conference Series*, pages 249–251, July 2007. doi: 10.1063/1.2757314. [42](#)
- P. Giommi, G. Polenta, A. Lähteenmaki, D. J. Thompson, M. Capalbi, S. Cutini, D. Gasparrini, J. Gonzalez-Nuevo, J. Leon-Tavares, M. Lopez-Caniego, M. N. Mazzotta, C. Monte, M. Perri, S. Raino, G. Tosti, A. Tramacere, F. Verrecchia, H. D. Aller, M. F. Aller, E. Angelakis, D. Bastieri, A. Berdyugin, A. Bonaldi, L. Bonavera, C. Burigana, D. N. Burrows, S. Buson, E. Cavazuti, G. Chincarini, S. Colafrancesco, L. Costamante, F. Cuttaia, F. D’Ammando, G. de Zotti, M. Frailis, L. Fuhrmann, S. Galeotta, F. Gargano, N. Gehrels, N. Giglietto, F. Giordano, M. Giroletti, E. Keihanen, O. King, T. P. Krichbaum, A. Lasenby, N. Lavonen, C. R. Lawrence, C. Leto, E. Lindfors, N. Mandolesi, M. Massardi, W. Max-Moerbeck, P. F. Michelson, M. Mingaliev, P. Natoli, I. Nestoras, E. Nieppola, K. Nilsson, B. Partridge, V. Pavlidou, T. J. Pearson, P. Procopio, J. P. Rachen, A. Readhead, R. Reeves, A. Reimer, R. Reintal, S. Ricciardi, J. Richards, D. Riquelme, J. Saarinen, A. Sajina, M. Sandri, P. Savolainen, A. Sievers, A. Sillanpaa, Y. Sotnikova, M. Stevenson, G. Tagliaferrri, L. Takalo, J. Tammi, D. Tavagnacco, L. Terenzi, L. Toffolatti, M. Tornikoski, C. Trigilio, M. Turunen, G. Umana, H. Ungerechts, F. Villa, J. Wu, A. Zachei, J. A. Zensus, and X. Zhou. Simultaneous Planck, Swift, and Fermi observations of X-ray and gamma-ray selected blazars. *ArXiv e-prints*, August 2011. [2](#)
- B. Gold, N. Odegard, J. L. Weiland, R. S. Hill, A. Kogut, C. L. Bennett, G. Hinshaw, X. Chen, J. Dunkley, M. Halpern, N. Jarosik, E. Komatsu, D. Larson, M. Limon, S. S. Meyer, M. R. Nolte, L. Page, K. M. Smith, D. N. Spergel, G. S. Tucker, E. Wollack, and E. L. Wright. Seven-year WMAP catalog (Gold+), 2011). *VizieR Online Data Catalog*, 219:20015–+, March 2011. [viii](#), [1](#), [21](#), [30](#), [33](#)
- J. González-Nuevo, M. Massardi, F. Argüeso, D. Herranz, L. Toffolatti, J. L. Sanz, M. López-Caniego, and G. de Zotti. Statistical properties of extragalactic sources in the New Extragalactic WMAP Point Source (NEWPS) catalogue. *Monthly Notices of the RAS*, 384:711–718, February 2008. doi: 10.1111/j.1365-2966.2007.12733.x. [37](#), [94](#)
- P. C. Gregory, W. K. Scott, K. Douglas, and J. J. Condon. The GB6 Catalog of Radio Sources. *Astrophysical Journal, Supplement*, 103:427–+, April 1996. doi: 10.1086/192282. [viii](#), [21](#), [32](#), [42](#), [108](#)
- D. W. Hogg. Confusion Errors in Astrometry and Counterpart Association. *Astronomical Journal*, 121:1207–1213, February 2001. doi: 10.1086/318736. [2](#)

- D. W. Hogg and E. L. Turner. A Maximum Likelihood Method to Improve Faint-Source Flux and Color Estimates. *Publications of the ASP*, 110:727–731, June 1998. doi: 10.1086/316173. [2](#)
- C. D. Impey and G. Neugebauer. Energy distributions of blazars. *Astronomical Journal*, 95:307–351, February 1988. doi: 10.1086/114638. [103](#), [106](#)
- M. A. Janssen and S. Gulkis. Mapping the sky with the COBE differential microwave radiometers. In M. Signore & C. Dupraz, editor, *NATO ASIC Proc. 359: The Infrared and Submillimetre Sky after COBE*, pages 391–408, 1992. [13](#)
- A. Kogut, G. F. Smoot, C. L. Bennett, E. L. Wright, J. Aymon, G. de Amici, G. Hinshaw, P. D. Jackson, E. Kaita, P. Keegstra, C. Lineweaver, K. Loewenstein, L. Rokke, L. Tenorio, N. W. Boggess, E. S. Cheng, S. Gulkis, M. G. Hauser, M. A. Janssen, T. Kelsall, J. C. Mather, S. Meyer, S. H. Moseley, T. L. Murdock, R. A. Shafer, R. F. Silverberg, R. Weiss, and D. T. Wilkinson. COBE Differential Microwave Radiometers - Preliminary systematic error analysis. *Astrophysical Journal*, 401:1–18, December 1992. doi: 10.1086/172033. [7](#)
- J. M. Kovac, E. M. Leitch, C. Pryke, J. E. Carlstrom, N. W. Halverson, and W. L. Holzapfel. Detection of polarization in the cosmic microwave background using DASI. *Nature*, 420:772–787, December 2002. doi: 10.1038/nature01269. [x](#), [xiii](#), [34](#), [99](#)
- J.-M. Lamarre, J.-L. Puget, P. A. R. Ade, F. Bouchet, G. Guyot, A. E. Lange, F. Pajot, A. Arondel, K. Benabed, J.-L. Beney, A. Benoît, J.-P. Bernard, R. Bhatia, Y. Blanc, J. J. Bock, E. Bréelle, T. W. Bradshaw, P. Camus, A. Catalano, J. Charra, M. Charra, S. E. Church, F. Couchot, A. Coulais, B. P. Crill, M. R. Crook, K. Dassel, P. de Bernardis, J. Delabrouille, P. de Marcillac, J.-M. Delouis, F.-X. Désert, C. Dumesnil, X. Dupac, G. Efstathiou, P. Eng, C. Evesque, J.-J. Fourmond, K. Ganga, M. Giard, R. Gispert, L. Guglielmi, J. Haissinski, S. Henrot-Versillé, E. Hivon, W. A. Holmes, W. C. Jones, T. C. Koch, H. Lagardère, P. Lami, J. Landé, B. Leriche, C. Leroy, Y. Longval, J. F. Macías-Pérez, T. Maciaszek, B. Maffei, B. Mansoux, C. Marty, S. Masi, C. Mercier, M.-A. Miville-Deschênes, A. Moneti, L. Montier, J. A. Murphy, J. Narbonne, M. Nexon, C. G. Paine, J. Pahn, O. Perdereau, F. Piacentini, M. Piat, S. Plaszczyński, E. Pointecouteau, R. Pons, N. Ponthieu, S. Prunet, D. Rambaudo, G. Roucoure, C. Renault, I. Ristorcelli, C. Rosset, D. Santos, G. Savini, G. Serra, P. Stassi, R. V. Sudiwala, J.-F. Sygnet, J. A. Tauber, J.-P. Torre, M. Tristram, L. Vibert, A. Woodcraft, V. Yurchenko, and D. Yvon. Planck pre-launch status: The HFI instrument, from specification to actual performance. *Astronomy and Astrophysics*, 520:A9+, September 2010. doi: 10.1051/0004-6361/200912975. [9](#)
- S. M. Leach, J.-F. Cardoso, C. Baccigalupi, R. B. Barreiro, M. Betoule, J. Bobin, A. Bonaldi, J. Delabrouille, G. de Zotti, C. Dickinson, H. K. Eriksen, J. González-Nuevo, F. K. Hansen, D. Herranz, M. Le Jeune, M. López-Cañiego, E. Martínez-González, M. Massardi, J.-B. Melin, M.-A. Miville-Deschênes, G. Patanchon, S. Prunet, S. Ricciardi, E. Salerno, J. L. Sanz, J.-L. Starck, F. Stivoli, V. Stolyarov, R. Stompor, and P. Vielva. Component separation methods for the PLANCK mission. *Astronomy and Astrophysics*, 491:597–615, November 2008. doi: 10.1051/0004-6361:200810116. [1](#), [49](#), [109](#)
- M. López-Cañiego, J. González-Nuevo, D. Herranz, M. Massardi, J. L. Sanz, G. De Zotti, L. Toffolatti, and F. Argüeso. Nonblind Catalog of Extragalactic Point Sources from the Wilkinson Microwave Anisotropy Probe (WMAP) First 3 Year Survey Data. *Astrophysical Journal, Supplement*, 170:108–125, May 2007. doi: 10.1086/512678. [39](#), [109](#), [143](#)
- B. Maffei, F. Novello, J. A. Murphy, P. A. R. Ade, J.-M. Lamarre, F. R. Bouchet, J. Brossard, A. Catalano, R. Colgan, R. Gispert, E. Gleeson, C. V. Haynes, W. C. Jones, A. E. Lange, Y. Longval, I. McAuley, F. Pajot, T. Peacock, G. Pisano, J.-L. Puget, I. Ristorcelli, G. Savini, R. Sudiwala, R. J. Wylde, and V. Yurchenko. Planck pre-launch status: HFI beam expectations from the optical optimisation of the focal plane. *Astronomy and Astrophysics*, 520:A12+, September 2010. doi: 10.1051/0004-6361/200912999. [13](#)
- E. K. Mahony, E. M. Sadler, S. M. Croom, R. D. Ekers, K. W. Bannister, R. Chhetri, P. J. Hancock, H. M. Johnston, M. Massardi, and T. Murphy. Optical Properties of High-Frequency Radio Sources from the Australia Telescope 20 GHz (AT20G) Survey. *ArXiv e-prints*, July 2011. [92](#)
- D. Maino, C. Burigana, M. Maltoni, B. D. Wandelt, K. M. Górski, M. Malaspina, M. Bersanelli, N. Mandolesi, A. J. Banday, and E. Hivon. The Planck-LFI instrument: Analysis of the 1/f noise and implications for the scanning strategy. *Astronomy and Astrophysics, Supplement*, 140:383–391, December 1999. doi: 10.1051/aas:1999429. [13](#)
- M. Maris, M. Bersanelli, C. Burigana, B. Cappellini, X. Dupac, G. Morgante, F. Pasian, M. Sandri, A. Sinigaglia, L. Terenzi, and the PLANCK collaboration. The Flexible Planck Scanning Strategy. *Memorie della Societa Astronomica Italiana Supplementi*, 9:460–+, 2006. [13](#)
- T. A. Marriage, J. Baptiste Juin, Y.-T. Lin, D. Marsden, M. R. Nolta, B. Partridge, P. A. R. Ade, P. Aguirre, M. Amiri, J. W. Appel, L. F. Barrientos, E. S. Battistelli, J. R. Bond, B. Brown, B. Burger, J. Chervenak, S. Das, M. J. Devlin, S. R. Dicker, W. Bertrand Doriese, J. Dunkley, R. Dünner, T. Essinger-Hileman, R. P. Fisher, J. W. Fowler, A. Hajian, M. Halpern, M. Hasselfield, C. Hernández-Monteagudo, G. C. Hilton, M. Hilton, A. D. Hincks, R. Hlozek, K. M. Huffenberger, D. Handel Hughes, J. P. Hughes, L. Infante, K. D. Irwin, M. Kaul, J. Klein, A. Kosowsky, J. M. Lau, M. Limon, R. H. Lupton, K. Martocci, P. Mauskopf, F. Menanteau, K. Moodley, H. Moseley, C. B. Netterfield, M. D. Niemack, L. A. Page, L. Parker, H. Quintana, B. Reid, N. Sehgal, B. D. Sherwin, J. Sievers, D. N. Spergel, S. T. Staggs, D. S. Swetz, E. R. Switzer, R. Thornton, H. Trac, C. Tucker, R. Warne, G. Wilson, E. Wollack, and Y. Zhao. The Atacama Cosmology Telescope: Extragalactic Sources at 148 GHz in the 2008 Survey. *Astrophysical Journal*, 731:100–+, April 2011. doi: 10.1088/0004-637X/731/2/100. [x](#), [35](#), [36](#), [39](#)
- A. P. Marscher. Effects of nonuniform structure on the derived physical parameters of compact synchrotron sources. *Astrophysical Journal*, 216:244–256, August 1977. doi: 10.1086/155467. [26](#)
- A. P. Marscher and W. K. Gear. Models for high-frequency radio outbursts in extragalactic sources, with application to the early 1983 millimeter-to-infrared flare of 3C 273. *Astrophysical Journal*, 298:114–127, November 1985. doi: 10.1086/163592. [26](#), [28](#)

## REFERENCES

- M. Massardi and C. Burigana. The Planck On-the-Flight Forecaster (POFF). *New Astronomy*, 15:678–687, November 2010. doi: 10.1016/j.newast.2010.05.001. **viii**, **12**, **15**, **16**, **41**, **54**
- M. Massardi, R. D. Ekers, T. Murphy, R. Ricci, E. M. Sadler, S. Burke, G. de Zotti, P. G. Edwards, P. J. Hancock, C. A. Jackson, M. J. Kesteven, E. Mahony, C. J. Phillips, L. Staveley-Smith, R. Subrahmanyam, M. A. Walker, and W. E. Wilson. The Australia Telescope 20-GHz (AT20G) Survey: the Bright Source Sample. *Monthly Notices of the RAS*, 384:775–802, February 2008. doi: 10.1111/j.1365-2966.2007.12751.x. **32**, **42**, **44**, **65**, **66**, **115**
- M. Massardi, M. López-Caniego, J. González-Nuevo, D. Heranz, G. de Zotti, and J. L. Sanz. Blind and non-blind source detection in WMAP 5-yr maps. *Monthly Notices of the RAS*, 392:733–742, January 2009. doi: 10.1111/j.1365-2966.2008.14084.x. **x**, **xii**, **1**, **34**, **74**
- M. Massardi, A. Bonaldi, L. Bonavera, M. López-Caniego, G. de Zotti, and R. D. Ekers. The Planck-ATCA Co-eval Observations project: the bright sample. *Monthly Notices of the RAS*, 415:1597–1610, August 2011a. doi: 10.1111/j.1365-2966.2011.18802.x. **ix**, **xi**, **xii**, **xiii**, **29**, **41**, **51**, **57**, **59**, **65**, **74**, **89**, **90**, **92**, **93**, **94**, **102**
- M. Massardi, R. D. Ekers, T. Murphy, E. Mahony, P. J. Hancock, R. Chhetri, G. de Zotti, E. M. Sadler, S. Burke-Spolaor, M. Calabretta, P. G. Edwards, J. A. Ekers, C. A. Jackson, M. J. Kesteven, K. Newton-McGee, C. Phillips, R. Ricci, P. Roberts, R. J. Sault, L. Staveley-Smith, R. Subrahmanyam, M. A. Walker, and W. E. Wilson. The Australia Telescope 20 GHz (AT20G) Survey: analysis of the extragalactic source sample. *Monthly Notices of the RAS*, 412:318–330, March 2011b. doi: 10.1111/j.1365-2966.2010.17917.x. **ix**, **29**, **39**, **50**, **98**, **141**, **143**
- E. Massaro, P. Giommi, C. Leto, P. Marchegiani, A. Maselli, M. Perri, S. Piranomonte, and S. Scavi. Roma-BZCAT: a multifrequency catalogue of blazars. *Astronomy and Astrophysics*, 495:691–696, February 2009. doi: 10.1051/0004-6361:200810161. **xix**, **123**, **139**
- J. C. Mather, E. S. Cheng, R. E. Eplee, Jr., R. B. Isaacman, S. S. Meyer, R. A. Shafer, R. Weiss, E. L. Wright, C. L. Bennett, N. W. Boggess, E. Dwek, S. Gulkis, M. G. Hauser, M. Janssen, T. Kelsall, P. M. Lubin, S. H. Moseley, Jr., T. L. Murdock, R. F. Silverberg, G. F. Smoot, and D. T. Wilkinson. A preliminary measurement of the cosmic microwave background spectrum by the Cosmic Background Explorer (COBE) satellite. *Astrophysical Journal Letters*, 354:L37–L40, May 1990. doi: 10.1086/185717. **7**
- J. C. Mather, D. J. Fixsen, R. A. Shafer, C. Mosier, and D. T. Wilkinson. Calibrator Design for the COBE Far-Infrared Absolute Spectrophotometer (FIRAS). *Astrophysical Journal*, 512:511–520, February 1999. doi: 10.1086/306805. **7**
- T. Mauch, T. Murphy, H. J. Buttery, J. Curran, R. W. Hunstead, B. Piestrzynski, J. G. Robertson, and E. M. Sadler. SUMSS: a wide-field radio imaging survey of the southern sky - II. The source catalogue. *Monthly Notices of the RAS*, 342:1117–1130, July 2003. doi: 10.1046/j.1365-8711.2003.06605.x. **32**
- A. Mennella, M. Bersanelli, R. C. Butler, A. Curto, F. Cuttaia, R. J. Davis, J. Dick, M. Frailis, S. Galeotta, A. Gregorio, H. Kurki-Suonio, C. R. Lawrence, S. Leach, J. P. Leahy, S. Lowe, D. Maino, N. Mandolesi, M. Maris, E. Martínez-González, P. R. Meinhold, G. Morgante, D. Pearson, F. Perrotta, G. Polenta, T. Poutanen, M. Sandri, M. D. Seiffert, A. . Suur-Uski, D. Tavagnacco, L. Terenzi, M. Tomasi, J. Valiviita, F. Villa, R. Watson, A. Wilkinson, A. Zacchei, A. Zonca, B. Aja, E. Artal, C. Baccigalupi, A. J. Banday, R. B. Barreiro, J. G. Bartlett, N. Bartolo, P. Battaglia, K. Bennett, A. Bonaldi, L. Bonavera, J. Borrill, F. R. Bouchet, C. Burigana, P. Cabella, B. Cappellini, X. Chen, L. Colombo, M. Cruz, L. Danese, O. D’Arcangelo, R. D. Davies, G. de Gasperis, A. de Rosa, G. de Zotti, C. Dickinson, J. M. Diego, S. Donzelli, G. Efstathiou, T. A. Enßlin, H. K. Eriksen, M. C. Falvela, F. Finelli, S. Foley, C. Franceschet, E. Franceschi, T. C. Gaier, R. T. Génova-Santos, D. George, F. Gómez, J. González-Nuevo, K. M. Górski, A. Gruppuso, F. K. Hansen, D. Heranz, J. M. Herreros, R. J. Hoyland, N. Hughes, J. Jewell, P. Jukkala, M. Juvela, P. Kangaslahti, E. Keihänen, R. Kesitalo, V. . Kilpia, T. S. Kisner, J. Knoche, L. Knox, M. Laaninen, A. Lähteemäki, J. . Lamarre, R. Leonardi, J. León-Tavares, P. Leutenegger, P. B. Lilje, M. López-Caniego, P. M. Lubin, M. Malaspina, D. Marínucci, M. Massardi, S. Matarrese, F. Matthai, A. Melchiorri, L. Mendes, M. Miccolis, M. Migliaccio, S. Mitra, A. Moss, P. Natoli, R. Nesti, H. U. Nørgaard-Nielsen, L. Pagano, R. Paladini, D. Paoletti, B. Partridge, F. Pasian, V. Pettorino, D. Pietrobon, M. Pospieszalski, G. Prézeau, M. Prina, P. Procopio, J. . Puget, C. Quercellini, J. P. Rachen, R. Rebolo, M. Reinecke, S. Ricciardi, G. Robbers, G. Rocha, N. Roddis, J. A. Rubiño-Martín, M. Savelainen, D. Scott, R. Silvestri, A. Simonetto, P. Sjoman, G. F. Smoot, C. Sozzi, L. Stringhetti, J. A. Tauber, G. Tofani, L. Toffolatti, J. Tuovinen, M. Türler, G. Umana, L. Valenziano, J. Varis, P. Vielva, N. Vittorio, L. A. Wade, C. Watson, S. D. M. White, and F. Winder. Planck early results: First assessment of the Low Frequency Instrument in-flight performance. *ArXiv e-prints*, January 2011. **9**
- T. Murphy, E. M. Sadler, R. D. Ekers, M. Massardi, P. J. Hancock, E. Mahony, R. Ricci, S. Burke-Spolaor, M. Calabretta, R. Chhetri, G. de Zotti, P. G. Edwards, J. A. Ekers, C. A. Jackson, M. J. Kesteven, E. Lindley, K. Newton-McGee, C. Phillips, P. Roberts, R. J. Sault, L. Staveley-Smith, R. Subrahmanyam, M. A. Walker, and W. E. Wilson. The Australia Telescope 20 GHz Survey: the source catalogue. *Monthly Notices of the RAS*, 402:2403–2423, March 2010. doi: 10.1111/j.1365-2966.2009.15961.x. **viii**, **21**, **32**, **42**, **66**
- C. P. O’Dea. The Compact Steep-Spectrum and Gigahertz Peaked-Spectrum Radio Sources. *Publications of the ASP*, 110:493–532, May 1998. doi: 10.1086/316162. **24**, **25**
- C. P. O’Dea and S. A. Baum. Global Properties of GPS and CSS Sources: Constraints on Evolution. In I. A. G. Snellen, R. T. Schilizzi, H. J. A. Roettgering, & M. N. Bremer , editor, *Gigahertz Peaked Spectrum and Compact Steep Spectrum Radio Sources*, pages 241–251, 1997. **25**
- I. Owsianik and J. E. Conway. First detection of hotspot advance in a Compact Symmetric Object. Evidence for a class of very young extragalactic radio sources. *Astronomy and Astrophysics*, 337:69–79, September 1998. **24**
- Planck Collaboration. The Scientific Programme of Planck. *ArXiv Astrophysics e-prints*, April 2006. **vii**, **1**, **10**, **11**, **16**, **109**

## REFERENCES

- Planck Collaboration. Planck Early Results: The Power Spectrum Of Cosmic Infrared Background Anisotropies. *ArXiv e-prints*, January 2011a. [36](#)
- Planck Collaboration. Planck Early Results: The Early Release Compact Source Catalog. *ArXiv e-prints*, January 2011b. [viii](#), [x](#), [2](#), [3](#), [12](#), [19](#), [21](#), [30](#), [33](#), [37](#), [38](#), [100](#), [107](#), [109](#), [111](#), [123](#), [142](#), [143](#)
- Planck Collaboration. Planck early results: Spectral energy distributions and radio continuum spectra of northern extragalactic radio sources. *ArXiv e-prints*, January 2011c. [2](#), [30](#), [37](#)
- Planck Collaboration. Planck Early Results: ERCSC Validation and Extreme Radio Sources. *ArXiv e-prints*, January 2011d. [ix](#), [20](#), [25](#), [26](#), [27](#), [28](#), [29](#), [30](#), [31](#), [32](#), [33](#)
- Planck Collaboration. Planck Early Results XX: New Light on Anomalous Microwave Emission from Spinning Dust Grains. *ArXiv e-prints*, January 2011e. [12](#)
- Planck Collaboration. Planck Early Results: The Planck mission. *ArXiv e-prints*, January 2011f. [1](#), [2](#), [9](#)
- Planck Collaboration. Planck Early Results: Statistical properties of extragalactic radio sources in the Planck Early Release Compact Source Catalogue. *ArXiv e-prints*, January 2011g. [x](#), [xi](#), [xiii](#), [xiv](#), [2](#), [33](#), [34](#), [35](#), [36](#), [37](#), [39](#), [96](#), [98](#), [99](#), [100](#), [112](#)
- P. Procopio, M. Massardi, S. Righini, A. Zanichelli, S. Ricciardi, P. Libardi, C. Burigana, F. Cuttaia, K.-H. Mack, L. Terenzi, F. Villa, L. Bonavera, G. Morgante, C. Triguilio, T. Trombetti, and G. Umana. The Simultaneous Medicina-Planck Experiment: data acquisition, reduction and first results. *Monthly Notices of the RAS*, pages 1300–+, August 2011. doi: 10.1111/j.1365-2966.2011.19334.x. [xi](#), [xiv](#), [42](#), [43](#), [47](#), [48](#), [107](#), [108](#), [142](#)
- S. Righini. IRA internal report 425/08, 2008. [45](#)
- E. M. Sadler, R. Ricci, R. D. Ekers, J. A. Ekers, P. J. Hancock, C. A. Jackson, M. J. Kesteven, T. Murphy, C. Phillips, R. F. Reinfrank, L. Staveley-Smith, R. Subrahmanyan, M. A. Walker, W. E. Wilson, and G. de Zotti. The properties of extragalactic radio sources selected at 20GHz. *Monthly Notices of the RAS*, 371:898–914, September 2006. doi: 10.1111/j.1365-2966.2006.10729.x. [102](#), [103](#)
- E. M. Sadler, R. Ricci, R. D. Ekers, R. J. Sault, C. A. Jackson, and G. de Zotti. The extragalactic radio-source population at 95GHz. *Monthly Notices of the RAS*, 385:1656–1672, April 2008. doi: 10.1111/j.1365-2966.2008.12955.x. [x](#), [35](#), [39](#)
- A. Sajina, B. Partridge, T. Evans, S. Steff, N. Vechik, S. Myers, S. Dicker, and P. Korngut. High-frequency Radio Spectral Energy Distributions and Polarization Fractions of Sources in an Atacama Cosmology Telescope Survey Field. *Astrophysical Journal*, 732:45–+, May 2011. doi: 10.1088/0004-637X/732/1/45. [92](#), [94](#), [104](#)
- M. Sandri, F. Villa, M. Bersanelli, C. Burigana, R. C. Butler, O. D’Arcangelo, L. Figini, A. Gregorio, C. R. Lawrence, D. Maino, N. Mandolesi, M. Maris, R. Nesti, F. Perrotta, P. Platania, A. Simonetto, C. Sozzi, J. Tauber, and L. Valenziano. Planck pre-launch status: Low Frequency Instrument optics. *Astronomy and Astrophysics*, 520:A7+, September 2010. doi: 10.1051/0004-6361/200912891. [13](#), [14](#)
- R. J. Sault, P. J. Teuben, and M. C. H. Wright. A Retrospective View of MIRIAD. In R. A. Shaw, H. E. Payne, & J. J. E. Hayes, editor, *Astronomical Data Analysis Software and Systems IV*, volume 77 of *Astronomical Society of the Pacific Conference Series*, pages 433–+, 1995. [57](#)
- G. F. Smoot, C. L. Bennett, A. Kogut, E. L. Wright, J. Aymon, N. W. Boggess, E. S. Cheng, G. de Amici, S. Gulkis, M. G. Hauser, G. Hinshaw, P. D. Jackson, M. Janssen, E. Kaita, T. Kelsall, P. Keegstra, C. Lineweaver, K. Loewenstein, P. Lubin, J. Mather, S. S. Meyer, S. H. Moseley, T. Murdock, L. Rokke, R. F. Silverberg, L. Tenorio, R. Weiss, and D. T. Wilkinson. Structure in the COBE differential microwave radiometer first-year maps. *Astrophysical Journal, Letters*, 396:L1–L5, September 1992. doi: 10.1086/186504. [7](#)
- I. A. G. Snellen, M. Zhang, R. T. Schilizzi, H. J. A. Roettgering, A. G. de Bruyn, and G. K. Miley. Faint radio sources with peaked spectra. I. VLA observations of a new sample with intermediate flux-densities. *Astronomy and Astrophysics*, 300:359–+, August 1995. [28](#)
- J. A. Tauber, N. Mandolesi, J.-L. Puget, T. Banos, M. Bersanelli, F. R. Bouchet, R. C. Butler, J. Charra, G. Crone, J. Dodsworth, and et al. Planck pre-launch status: The Planck mission. *Astronomy and Astrophysics*, 520:A1+, September 2010. doi: 10.1051/0004-6361/200912983. [13](#), [14](#)
- The Planck HFI Core Team. Planck early results: first assessment of the High Frequency Instrument in-flight performance. *ArXiv e-prints*, January 2011a. [9](#)
- The Planck HFI Core Team. Planck Early Results: The High Frequency Instrument data processing. *ArXiv e-prints*, January 2011b. [1](#), [19](#)
- A. R. Thompson, J. M. Moran, and G. W. Swenson, Jr. *Interferometry and Synthesis in Radio Astronomy, 2nd Edition*. 2001. [66](#)
- L. Toffolatti, F. Argüeso Gomez, G. de Zotti, P. Mazzei, A. Franceschini, L. Danese, and C. Burigana. Extragalactic source counts and contributions to the anisotropies of the cosmic microwave background: predictions for the Planck Surveyor mission. *Monthly Notices of the RAS*, 297:117–127, June 1998. doi: 10.1046/j.1365-8711.1998.01458.x. [49](#)
- L. Toffolatti, G. De Zotti, F. Argüeso, and C. Burigana. Extragalactic Radio Sources and CMB Anisotropies. In A. de Oliveira-Costa & M. Tegmark, editor, *Microwave Foregrounds*, volume 181 of *Astronomical Society of the Pacific Conference Series*, pages 153–+, 1999. [49](#)
- L. Toffolatti, M. Negrello, J. González-Nuevo, G. de Zotti, L. Silva, G. L. Granato, and F. Argüeso. Extragalactic source contributions to arcminute-scale Cosmic Microwave Background anisotropies. *Astronomy and Astrophysics*, 438:475–480, August 2005. doi: 10.1051/0004-6361:20042158. [36](#)
- M. Tornikoski, E. Valtaoja, H. Teraesranta, K. Karlamaa, M. Lainela, K. Nilsson, J. Kotilainen, S. Laine, A. Lahteenmaeki, L. B. G. Knee, and L. C. L. Botti. SEST observations of extragalactic radio sources at 3mm and 1.3mm. *Astronomy and Astrophysics, Supplement*, 116:157–165, March 1996. [50](#), [141](#)

## REFERENCES

---

- M. Tucci, E. Martínez-González, P. Vielva, and J. Delabrouille. Limits on the detectability of the CMB B-mode polarization imposed by foregrounds. *Monthly Notices of the RAS*, 360:935–949, July 2005. doi: 10.1111/j.1365-2966.2005.09123.x. 144
- J. D. Vieira, T. M. Crawford, E. R. Switzer, P. A. R. Ade, K. A. Aird, M. L. N. Ashby, B. A. Benson, L. E. Bleem, M. Brodwin, J. E. Carlstrom, C. L. Chang, H.-M. Cho, A. T. Crites, T. de Haan, M. A. Dobbs, W. Everett, E. M. George, M. Gladders, N. R. Hall, N. W. Halverson, F. W. High, G. P. Holder, W. L. Holzapfel, J. D. Hrubes, M. Joy, R. Keisler, L. Knox, A. T. Lee, E. M. Leitch, M. Lueker, D. P. Marrone, V. McIntyre, J. J. McMahon, J. Mehl, S. S. Meyer, J. J. Mohr, T. E. Montroy, S. Padin, T. Plagge, C. Pryke, C. L. Reichardt, J. E. Ruhl, K. K. Schaffer, L. Shaw, E. Shirokoff, H. G. Spieler, B. Stalder, Z. Staniszewski, A. A. Stark, K. Vanderlinde, W. Walsh, R. Williamson, Y. Yang, O. Zahn, and A. Zenteno. Extragalactic Millimeter-wave Sources in South Pole Telescope Survey Data: Source Counts, Catalog, and Statistics for an 87 Square-degree Field. *Astrophysical Journal*, 719:763–783, August 2010. doi: 10.1088/0004-637X/719/1/763. x, 35, 36, 39
- B. Vollmer, T. P. Krichbaum, E. Angelakis, and Y. Y. Kovalev. Quasi-simultaneous multi-frequency observations of inverted-spectrum GPS candidate sources. *Astronomy and Astrophysics*, 489:49–55, October 2008. doi: 10.1051/0004-6361:20078857. 24
- E. M. Waldram, R. C. Bolton, G. G. Pooley, and J. M. Riley. Some estimates of the source counts at Planck Surveyor frequencies, using the 9C survey at 15 GHz. *Monthly Notices of the RAS*, 379:1442–1452, August 2007. doi: 10.1111/j.1365-2966.2007.12025.x. x, 34
- W. E. Wilson, R. H. Ferris, P. Axtens, A. Brown, E. Davis, G. Hampson, M. Leach, P. Roberts, S. Saunders, B. S. Koribalski, J. L. Caswell, E. Lenc, J. Stevens, M. A. Voronkov, M. H. Wieringa, K. Brooks, P. G. Edwards, R. D. Ekers, B. Emonts, L. Hindson, S. Johnston, S. T. Maddison, E. K. Mahony, S. S. Malu, M. Massardi, M. Y. Mao, D. McConnell, R. P. Norris, D. Schnitzeler, R. Subrahmanyan, J. S. Urquhart, M. A. Thompson, and R. M. Wark. The Australia Telescope Compact Array Broadband Backend: description and first results. *Monthly Notices of the RAS*, 416:832–856, September 2011. doi: 10.1111/j.1365-2966.2011.19054.x. 3
- Windward Technologies. *GRG2 Users's Guide*, 1997. 90
- A. E. Wright, M. R. Griffith, A. J. Hunt, E. Troup, B. F. Burke, and R. D. Ekers. Source catalog for the PMN zenith survey (Wright+ 1996). *VizieR Online Data Catalog*, 210:30145–, September 1996. 32
- E. L. Wright, S. S. Meyer, C. L. Bennett, N. W. Boggess, E. S. Cheng, M. G. Hauser, A. Kogut, C. Lineweaver, J. C. Mather, G. F. Smoot, R. Weiss, S. Gulkis, G. Hinshaw, M. Janssen, T. Kelsall, P. M. Lubin, S. H. Moseley, Jr., T. L. Murdock, R. A. Shafer, R. F. Silverberg, and D. T. Wilkinson. Interpretation of the cosmic microwave background radiation anisotropy detected by the COBE Differential Microwave Radiometer. *Astrophysical Journal Letters*, 396:L13–L18, September 1992. doi: 10.1086/186506. 7
- A. Zacchei, D. Maino, C. Baccigalupi, M. Bersanelli, A. Bonaldi, L. Bonavera, C. Burigana, R. C. Butler, F. Cuttaia, G. de Zotti, J. Dick, M. Frailis, S. Galeotta, J. González-Nuevo, K. M. Górski, A. Gregorio, E. Keihänen, R. Kesitalo, J. Knoche, H. Kurki-Suonio, C. R. Lawrence, S. Leach, J. P. Leahy, M. López-Cañiego, N. Mandolesi, M. Maris, F. Matthai, P. R. Meinhold, A. Mennella, G. Morgante, N. Morisset, P. Natoli, F. Pasian, F. Perrotta, G. Polenta, T. Poutanen, M. Reinecke, S. Ricciardi, R. Rohlfs, M. Sandri, A. Suur-Uski, J. A. Tauber, D. Tavagnacco, L. Terenzi, M. Tomasi, J. Valiviita, F. Villa, A. Zonca, A. J. Banday, R. B. Barreiro, J. G. Bartlett, N. Bartolo, L. Bedini, K. Bennett, P. Binko, J. Borrill, F. R. Bouchet, M. Bremer, P. Cabella, B. Cappellini, X. Chen, L. Colombo, M. Cruz, A. Curto, L. Danese, R. D. Davies, R. J. Davis, G. de Gasperis, A. de Rosa, G. de Troia, C. Dickinson, J. M. Diego, S. Donzelli, U. Dörl, G. Efstathiou, T. A. Enßlin, H. K. Eriksen, M. C. Falvella, F. Finelli, E. Franceschi, T. C. Gaier, F. Gasparo, R. T. Génova-Santos, G. Giardino, F. Gómez, A. Gruppuso, F. K. Hansen, R. Hell, D. Herranz, W. Hovest, J. Jewell, M. Juvela, T. S. Kisner, L. Knox, A. Lähteenmäki, J. Lamarre, R. Leonardi, J. León-Tavares, P. B. Lilje, P. M. Lubin, G. Maggio, D. Marinucci, E. Martínez-González, M. Massardi, S. Matarrese, M. T. Meharga, A. Melchiorri, M. Migliaccio, S. Mitra, A. Moss, H. U. Nørgaard-Nielsen, L. Pagano, R. Paladini, D. Paoletti, B. Partridge, D. Pearson, V. Pettorino, D. Pietrobon, G. Prézeau, P. Procopio, J. Puget, C. Quercellini, J. P. Rachen, R. Rebolo, G. Robbers, G. Rocha, J. A. Rubino-Martín, E. Salerno, M. Savelainen, D. Scott, M. D. Seiffert, J. I. Silk, G. F. Smoot, J. Sternberg, F. Stivoli, R. Stompor, G. Tofani, J. Tuovinen, M. Türlér, G. Umata, P. Vielva, N. Vittorio, C. Vuerli, L. A. Wade, R. Watson, S. D. M. White, and A. Wilkinson. Planck Early Results: The Low Frequency Instrument data processing. *ArXiv e-prints*, January 2011. 1, 19